

Multinary Metal Oxides for Solar Water Splitting: Towards High Efficiency and High Stability

vorgelegt von

Master of Engineering, South China University of Technology

Fuxian Wang

geb. in Dawu, Hubei, China

Von der Fakultät II – Mathematik und Naturwissenschaften

der Technischen Universität Berlin

zur Erlangung des akademischen Grades

Doktor der Naturwissenschaften

- Dr. rer. nat -

genehmigte Dissertation

Promotionsausschuss:

Vorsitzender: Prof. Dr. Arne Thomas

Gutachter: Prof. Dr. Roel van de Krol

Gutachter: Dr. Roland Marschall

Tag der wissenschaftlichen Aussprache: 11. Dezember 2017

Berlin 2017

It takes a strong man to save himself, and it takes a great man to save another.
—to myself, and my direct supervisor Sean P. Berglund.

Abstract

The world has experienced an exponential increase in the demand for energy primarily coming from the consumption of fossil fuels, which is accompanied by the inevitable emission of carbon dioxide, causing global warming. Developing renewable and carbon-free sources is essential to reduce carbon dioxide emission and mitigate global warming. Among the renewable energy sources, solar energy has the greatest potential to meet our future energy demands. One crucial problem of solar energy utilization is its intermittency due to day and night cycles as well as fluctuations in weather. Solar water splitting provides a possible route to convert solar energy into more storable chemical energy—hydrogen. To ensure good efficiency and stability in photoelectrochemical water splitting, the photoelectrode materials must satisfy critical thermodynamic and kinetic requirements. Unfortunately, so far no material in nature can meet all these requirements. Therefore, exploring new materials and modifying the properties of the existing materials are the crucial tasks ahead for materials scientists. In this thesis, we demonstrate the development of CuBi_2O_4 as a photocathode material for hydrogen production and BiVO_4 as a photoanode material for water oxidation. A new spray pyrolysis recipe is developed to deposit homogeneous CuBi_2O_4 . The key to the synthesis is to use additives including (1) triethyl orthoformate to avoid rapid hydrolysis of the bismuth precursor in the spray solution and (2) polyethylene glycol to improve the spreading behavior of the droplets over the substrates. A comprehensive investigation of the structure, optical, electrical, and morphological properties of CuBi_2O_4 demonstrates its potential to be used as a photocathode material with the main limitations being poor charge separation efficiency and photo-corrosion. To address these limitations, we explore a new strategy of gradient self-doping by introducing a Cu vacancy gradient using a two-step-diffusion assisted spray pyrolysis process. The flat-band of the CuBi_2O_4 photocathodes can be tailored by varying the Cu : Bi ratio. Introducing a Cu : Bi gradient inside the film leads to a gradient in Cu vacancies and therefore a built-in electric field, which in turn enhances or reduces the photoelectrochemical performance depending on the direction of the gradient. Applying CdS/TiO_2 as protection layers and Pt as a catalytic layer significantly improves the stability of the forward gradient CuBi_2O_4 photocathode. We also explore direct current magnetron sputtering as a potential scaling-up technique for the economical deposition of BiVO_4 photoanodes. The role of stoichiometry on structure, grain size, diffusion length, and photoelectrocatalytic performance is investigated, revealing a strong relationship between the grain size and the electronic properties. Our self-designed solvent capture technique combined with attenuated total reflection infrared (ATR-IR) spectroscopy can be useful for in-situ analysis of the reaction mechanisms in solution. The strategies we utilized

to improve the solution chemistry by adding additives might be applicable for developing solution-based recipe for the synthesis of other metal oxides. The concept of using self-gradient-doping to improve the charge separation efficiency in CuBi_2O_4 can be easily applied to other multinary metal oxide photoelectrodes. In addition, we demonstrate the potential of using direct current magnetron sputtering, a highly scalable technique, to produce multinary oxide photoelectrodes at high deposition rate and low cost.

Kurzfassung

Der exponentiell ansteigende Weltenergiebedarf wird zurzeit hauptsächlich durch Fossile Brennstoffe gedeckt. Dies hat den unvermeidlichen Ausstoß von Kohlenstoffdioxid zur Folge, welches für den Klimawandel verantwortlich ist. Die Erschließung von erneuerbaren und kohlenstofffreien Energiequellen ist daher essenziell für die Reduktion des Kohlenstoffdioxidausstoßes und der Abschwächung des Klimawandels. Unter den erneuerbaren Energiequellen besitzt die Solarenergie das größte Potential den kommenden Bedarf zu decken. Die schwankende Verfügbarkeit von Solarenergie durch den Tag-/Nachtzyklus oder Wettereinflüsse stellt jedoch ein großes Problem dar. Die solare Wasserspaltung könnte dieses Problem lösen, indem die Sonnenenergie in den besser speicherbaren chemischen Brennstoff Wasserstoff umgewandelt wird. Um eine hohe Effizienz und Stabilität bei der solaren Wasserspaltung zu gewährleisten, müssen die Materialien für die Photoelektroden wichtige thermodynamische und kinetische Anforderungen erfüllen. Leider kann bisher kein Material diese Vielzahl von Bedingungen erfüllen. Daher ist das Erforschen von neuen und die Modifikation von bestehenden Photoelektrodenmaterialien eine der wichtigsten Aufgaben für Materialwissenschaftler im Feld der solaren Wasserspaltung. In dieser Arbeit demonstrieren wir die Entwicklung von CuBi_2O_4 als Photokathodenmaterial für die Wasserstoffproduktion und BiVO_4 als Photoanodenmaterial für die Sauerstofferzeugung. Ein neues Spray-Pyrolyse Rezept entwickelt, das die Herstellung von homogenen CuBi_2O_4 -Schichten ermöglicht. Die entscheidenden Schritte sind das Hinzufügen von (1) Triethyl-Orthoformiat, das die schnelle Hydrolyse von Bismut im Präkursor verhindert und (2) Polyethylenglykol, das das Verteilungsverhalten der Tropfen auf dem Substrat verbessert. Ein intensives Erforschen der Struktur, der optischen, elektrischen und morphologischen Eigenschaften von CuBi_2O_4 -Schichten zeigt zum einen das Potential und zum anderen die limitierenden Eigenschaften für die Nutzung des Materials als Photokathode auf. Letztere liegen hauptsächlich im Bereich der Ladungstrennung und der Photokorrosion. Um diese Limitationen zu umgehen untersuchen wir die neue Strategie einer graduellen Selbst-Dotierung mittels einem Kupfer-Fehlstellen-Gradienten, der mit einem zweistufigen diffusionsgestützten Spray-Pyrolyse Prozess hergestellt wird. Das Flachbandpotential der Schichten kann durch Variation der Cu : Bi Verhältnisses kontrolliert werden. Das Einstellen eines Cu : Bi-Gradienten innerhalb des Films führt zu einem Kupfer-Fehlstellen-Gradienten und damit einem elektrischen Feld, das die photoelektrochemischen Eigenschaften je nach Richtung des Gradienten verbessert oder verschlechtert. Das Abscheiden von CdS/TiO_2 als Schutzschichten und Pt als Katalysator verbessert die Stabilität der Vorwärts-Gradienten- CuBi_2O_4 -Photokathode. Des Weiteren wurde Magnetron Sputtern als potentiell Scale-Up

Verfahren für die wirtschaftliche Herstellung von BiVO_4 -Schichten untersucht. Der Einfluss der Stöchiometrie auf die Struktur, die Korngröße, Diffusionslänge und der photoelektrokatalytischen Leistung wurde näher betrachtet und eine starke Verknüpfung zwischen Korngröße und elektrischen Eigenschaften festgestellt. Unsere selbstentwickelte Lösemittelabscheidung Technik kombiniert mit ATR-IR Spektroskopie kann für die In-Situ Betrachtung von Reaktionsmechanismen innerhalb der Lösung hilfreich sein. Die verwendeten Strategien zur Beeinflussung der chemischen Vorgänge in der Lösung durch die Zugabe von Additiven könnten auf andere lösungsbasierte Synthesen von Metalloxiden übertragen werden. Das Konzept der selbst-dotierenden-Gradienten-Elektroden für die Verbesserung der Trennung von Ladungsträgern in CuBi_2O_4 könnte auch auf andere Mehrmetalloxide angewandt werden. Darüber hinaus demonstrieren wir das Potential des Gleichstrom-Magnetron-Sputterns als leicht skalierbare Herstellungsmethode von Mehrmetalloxid-Photoelektroden mit hohen Depositionsraten und geringen Kosten.

Table of Contents

Chapter 1. Introduction	1
Global Energy Crisis, CO ₂ Emission and Climate Change	1
Renewable and Carbon-Free Energy Sources	3
Photoelectrochemical Water Splitting as a Solution.....	5
Chapter 2. Research Background	6
PEC Cell-Overview.....	6
Requirements for the Semiconductor.....	7
Quantum Physics and Semiconductor Basics.....	7
Band Gap and Band Edges Positions	13
Semiconductor/Electrolyte Interface.....	17
PEC Cell under Operating Conditions.....	19
Quasi Fermi Level and Photovoltage.....	19
Photo-corrosion under Illumination	20
Energy Conversion Efficiencies.....	22
Photoelectrode Materials	24
The Hydrogen Evolution Reaction-Photocathode Materials.....	24
The Oxygen Evolution Reaction-Photoanode Materials	26
This thesis	27
Chapter 3. Spray Pyrolysis of CuBi ₂ O ₄ Photocathodes: Improved Solution Chemistry for Highly Homogeneous Thin Films 28	
Introduction	30
Experimental.....	31
Material Synthesis.....	31
Material Characterization	32
Precursor Solution Characterization	34
Electrochemical and Photoelectrochemical Measurements	35
Results and Discussion	37
Development of a Spray Pyrolysis Recipe for CuBi ₂ O ₄	37
PEC Performance and Optical Properties.....	53
Conclusions	64
Chapter 4. Gradient Self-doped CuBi ₂ O ₄ with Highly Improved Charge Separation Efficiency.....	66
Introduction	68
Experimental.....	69
Material Synthesis.....	69

Material Characterization	70
Electrochemical and PEC Measurements	72
Results and Discussion	75
Crystal Structure, Morphology and Composition	75
PEC Performance and Optical Properties	81
Improving Charge Separation by Gradient Self-doping	85
Hydrogen Production and Stability under Operation	90
Conclusions	96
Chapter 5. Direct Current Magnetron Sputtering of Photoactive BiVO ₄ : Role of Stoichiometry on Grain Size, Structure, Carrier Mobility and Lifetime	97
Introduction	99
Experimental	101
Film Preparation	101
Film Characterization	103
PEC Measurements	104
Results and Discussion	104
Photocurrent at Different V : Bi ratios	104
Charge Carrier Mobility, Lifetime, and Diffusion Length	105
Crystal Structure and Preferential Growth	107
Morphology and Grain Size	109
Phase Segregation	112
Conclusions	114
Summary and Outlook	115
Appendix A: Supplemental Information for Spray Pyrolysis of CuBi ₂ O ₄ Photocathodes: Improved Solution Chemistry for Highly Homogeneous Thin Films	118
Appendix B: Supplemental Information for Gradient Self-doped CuBi ₂ O ₄ with Highly Improved Charge Separation Efficiency	125
Appendix C: Supplemental Information for Direct Current Magnetron Sputtering of Photoactive BiVO ₄ : Role of Stoichiometry on Grain Size, Structure, Carrier Mobility and Lifetime	135
List of Publications	143
Acknowledgement	144
Bibliography	145

Chapter 1. Introduction

Global Energy Crisis, CO₂ Emission and Climate Change

The world has experienced an exponential increase in the demand for energy, especially since the industrial revolution. This has been accompanied by a large increase in the world's population. Currently, the world population is estimated to be ~7.5 billion, and will likely increase to ~9 billion in 2050. By then, the world will need 50 TW if the average per capita usage of energy is one-half of the United States.¹ As illustrated in **Figure 1.1**, so far most of the world's energy needs are met by fossil fuels such as coal, natural gas and oil, and the amount of power consumption keeps increasing with time.

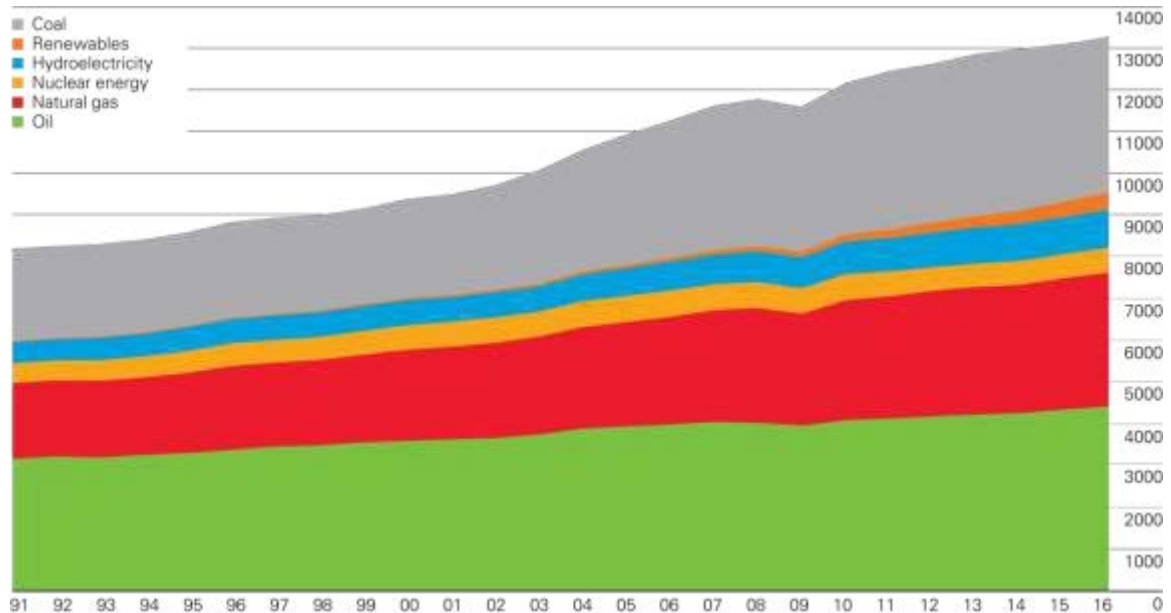


Figure 1.1. Primary energy world consumption in Million tonnes oil equivalent per year. This figure was adapted from reference ².

Fossil fuels, as the name suggests, come from very old fossils and take millions of years to form. The reserves of fossil fuels are limited. According to 2017 BP Statistical Review of World Energy, global total reserve levels, by fossil fuels, are now 1139.3 billion tonnes of coal, 186.6 trillion cubic meters of natural gas, and 1706.7 billion barrels of crude oil. The estimated years of extraction remaining are 53 years, 54 years and 109 years for oil, natural gas and coal, respectively.²

Moreover, the use of fossil fuels is accompanied by the inevitable emission of greenhouse gases into the atmosphere, particularly carbon dioxide (CO₂). CO₂ in the atmosphere can increase the optical depth of infrared

radiation emitted by the ground to traverse through the atmosphere, and therefore cause an increase in the average temperature on earth.³ CO₂ emissions are the most important cause of global warming. CO₂ emissions have been dramatically increased within the last decades and are projected to continue increasing by almost 3 % each year. Consequently, the CO₂ concentration has increased from 280 ppm in pre-industrial times to 404 ppm in 2016, as shown in **Figure 1.2**.⁴ The rate of CO₂ concentration change is estimated to be 2.4 ppm/year.

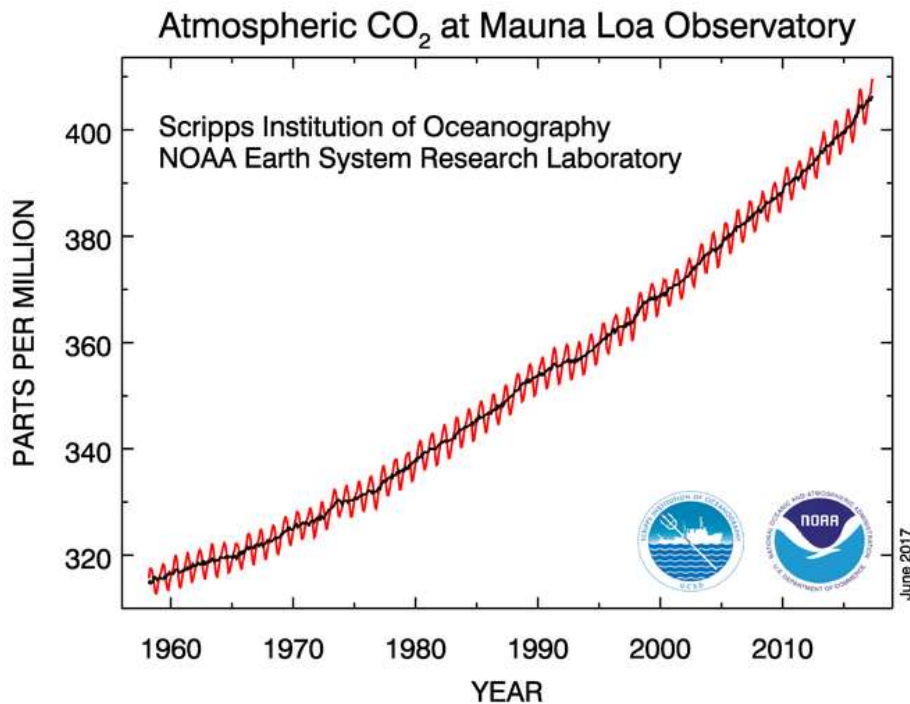


Figure 1.2. Trends in atmosphere CO₂ concentration, reproduced from reference ⁴.

As shown in **Figure 1.3**, the Earth's average temperature has increased by ~ 1.2 to 1.9 °C since 1880 and the anthropogenic increase in CO₂ concentration most certainly contributes to this increase in temperature. Global warming can result in variety of devastating consequences including the melting of land ice, a rise in sea level, retreating of glaciers, bleaching of coral reefs, and an increase in the frequency of intense hurricanes.⁵ According to the IPCC report,⁶ the temperature increase caused by global warming must not exceed 2 °C and the CO₂ concentration has to be kept below 450 ppm in order to avoid a catastrophe. To accomplish this, annual global CO₂ emissions have to be reduced from the current 32 gigatonnes to 20 gigatonnes by 2050. One should also keep in mind that the world population will likely grow to about 9 billion people in 2050, and the industrialization in developing countries will lead to a large increase in energy consumption, which will cause CO₂ emissions if this energy comes from fossil fuels.⁷

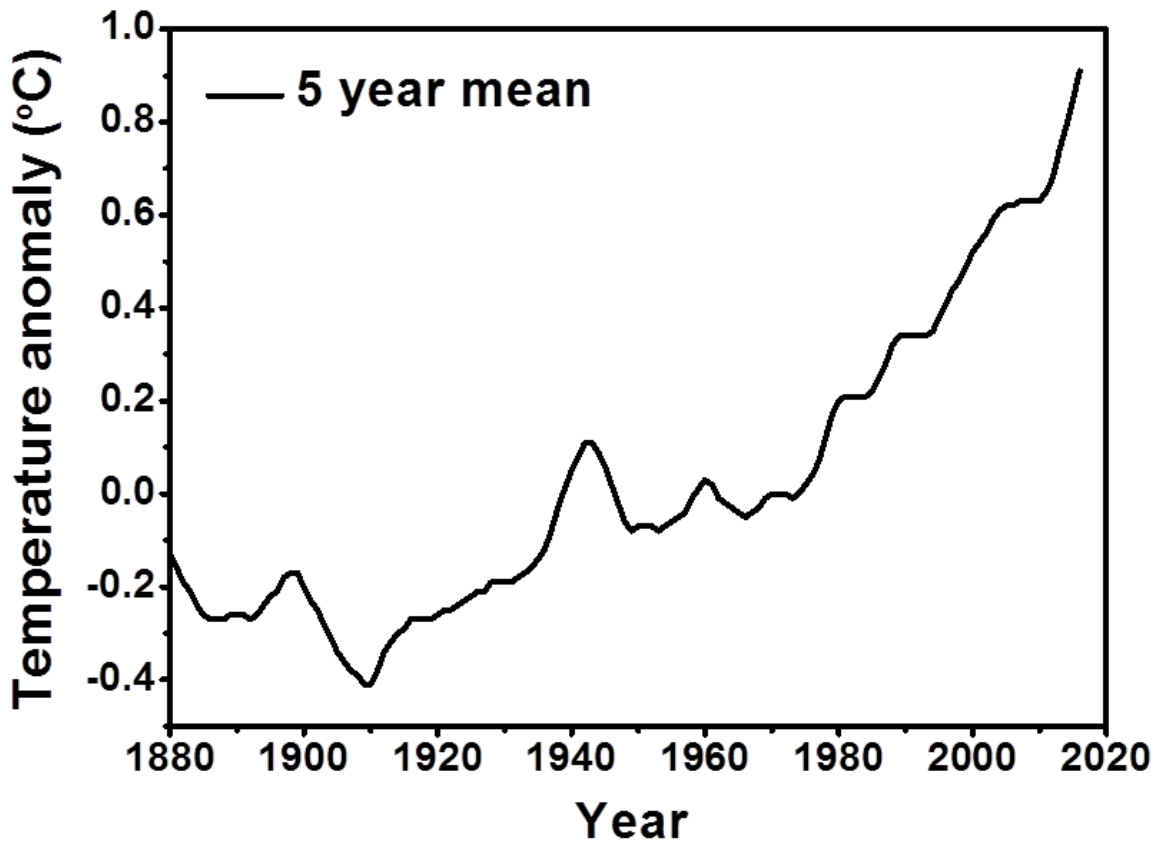


Figure 1.3. Global temperature increase since 1880. Data source ⁸.

Renewable and Carbon-Free Energy Sources

To address global warming, practical solutions to significantly reduce CO₂ emissions have been proposed.⁹ One way to reduce CO₂ emissions is to use carbon-free energy sources such as solar power, wind power, geothermal and hydroelectric energy, nuclear power, etc. Collectively, these renewable energy sources have the potential to meet the world's energy demand. In contrast to conventional sources such as gas, coal, and oil which are geographically concentrated, renewable energy sources are more evenly distributed globally. .

Table 1.1 shows the estimated global power generation capacities of a variety of renewable energy sources. However, there are certain limitations for most of the renewable energy sources. For example, electricity generated by wind turbines is challenging to store; hydropower requires high-cost dam construction; geothermal energy is a continuous source, but it is limited in lifetime and has high operation expenses.¹⁰⁻¹¹ Of all the available renewable energy sources, solar energy has the greatest potential to meet our future energy demands, as shown by the enormous power of > 20 TW that could be obtained by covering only 0.16 % of the earth's surface with 10 % efficient solar cells.

Table 1.1. Global power generating capacities of several renewable energy sources.¹²⁻¹³

Energy source	Power (TW)	Remarks
Solar	> 20	Requires 0.16 % of the earth' surface to be covered with 10 % efficient solar cells
Wind	4	Represents 10-15 of global potential for on- and off- shore installations
Geothermal	12	Only a small fraction of this can be exploited
Hydroelectric	1-2	Remaining untapped potential is 0.5 TW
Biomass	10	Requires 10 % of the Earth's surface to be covered in switch grass

Several technologies can be used to convert solar energy into more useable forms of energy, among which the most prevalent are solar cells comprised of semiconducting materials exhibiting the photovoltaic effect. Currently the photovoltaic (PV) industry is one of the world's fastest growing markets, expanding 35-40 % per year. It is estimated that solar energy will be the largest source of electricity ahead of fossil fuels, wind, hydro and nuclear.¹⁴ However, as the PV capacity increases, it will become difficult for the electrical grid to cope with the intermittent nature of solar power since the light intensity depends on geographical position, day, time, and season.¹⁵⁻¹⁶ At a certain stage, electrical grid-based storage capacities will be exceeded and the implementation of alternative large-scale energy storage will be needed. One possible solution is to convert solar energy into chemical energy in the form of chemical fuels such as hydrogen, methane, methanol, gasoline, diesel, etc. Nearly all of these chemical fuels contain carbon and do not help reducing CO₂ emission, with the exception hydrogen. Hydrogen is an advantageous chemical fuel because it is: (1) abundant in various sustainable resources (e.g., water); (2) combustible with high energy yield; (3) carbon free; and (4) high in storage capability by mass.¹⁷⁻¹⁸ Moreover, hydrogen can be easily converted to electricity and back with fuel cells and electrolyzers. Hydrogen can also be produced directly from water and sunlight using photoelectrolysis or photoelectrochemical water splitting, which will be described below. Therefore, it is possible to establish a future energy infrastructure based on sunlight, hydrogen, and electricity, as illustrated in **Figure 1.4**.^{12, 19-20}

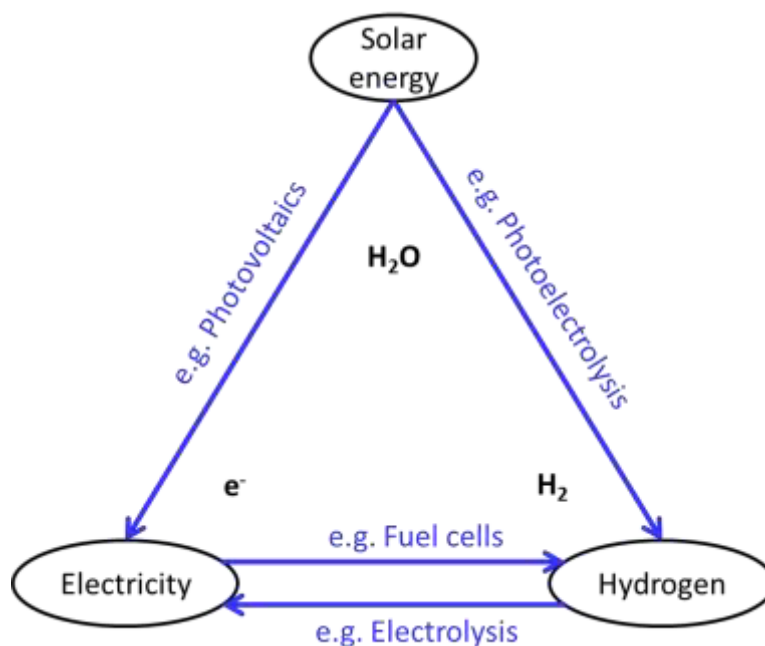


Figure 1.4. Illustration of the possible future triangle energy system.

Photoelectrochemical Water Splitting as a Solution

As discussed above, hydrogen is an ideal alternative source of energy. However, technological developments are needed to efficiently convert solar energy into hydrogen. So far, several pathways have been developed for this process such as photoelectrochemical (PEC) water splitting, photocatalytic water splitting, electrolysis, thermochemical conversion, photobiological methods, molecular artificial photosynthesis, etc.²¹⁻²² Among those different pathways, semiconductor based PEC water splitting is appealing due to its' attractive characteristics. First of all, hydrogen and oxygen are generated separately at a photocathode and photoanode, respectively. This avoids the safety concern of mixing hydrogen with oxygen and allows for easy gas separation.²³ Secondly, it can be carried out at room temperature and, unlike solar thermal power plants, solar concentrators are not needed for its application on large scale. Thirdly, low-cost earth-abundant inorganic materials such as metal oxides are ubiquitous in their employment in PEC devices, which may significantly lower the cost for hydrogen production to the range of 3-5 \$/kg, while hydrogen produced by PV-electrolyzer systems currently costs ~8 \$/kg.²⁴⁻²⁵ What's more, in PEC devices the current can be spread across the large area of photoelectrodes so that the current density is only 10-20 mA/cm², which is much lower than that for PV electrolysis (~1 A/cm²). Therefore, the required overpotential for PEC water splitting is substantially lower. In addition, a PEC water splitting device requires fewer components (e.g., wires, frames, glass) than a PV-electrolyzer system. This may lead to easier construction and a lower balance-of-system cost for hydrogen production.

Chapter 2. Research Background

Semiconductor-based solar water splitting offers a straightforward route towards renewable solar-to-chemical energy conversion. Before introducing our efforts on the development of CuBi_2O_4 as a photocathode material and BiVO_4 as a photoanode material, the working principle of a PEC cell is briefly summarized in this section.

PEC Cell-Overview

Figure 2.1 shows a simplified energy diagram of a PEC cell based on a photocathode and a metal anode. More complicated configurations will be discussed later. The main component in PEC cell is the semiconductor, which absorbs light converting incident photons to electron-hole pairs. The photogenerated electrons and holes are separated and used for the reduction and oxidation reactions, respectively.

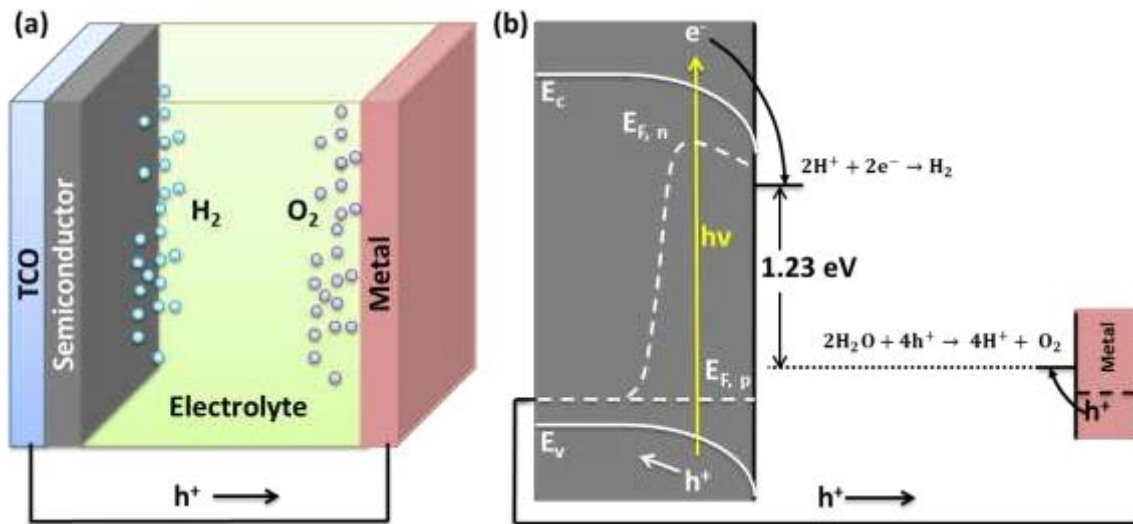
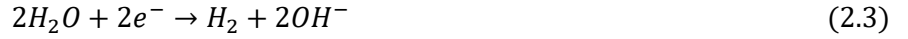


Figure 2.1. (a) Illustration of a PEC cell that consists of a semiconducting photocathode and a metal anode and (b) The corresponding energy diagram. Note that 1.23 eV is the thermodynamic energy for water splitting reaction, in reality at least 1.9 eV is required due to the overpotentials and energy losses.

In an acidic electrolyte, the reduction and oxidation half reactions can be written as:



In alkaline electrolyte they are:

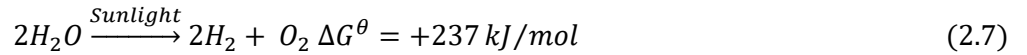


The redox potentials for the reduction and oxidation half reactions are pH dependent as follows:

$$E_{reduction}^{\theta} = +0.000 V - 0.059V \cdot pH \text{ (vs. NHE)} \quad (2.5)$$

$$E_{oxidation}^{\theta} = +1.229 V - 0.059V \cdot pH \text{ (vs. NHE)} \quad (2.6)$$

In any case, the overall water splitting reaction can be expressed as:



Here $\Delta G^{\theta} = +237 \text{ kJ/mol}$ is the Gibbs free energy which corresponds to a thermodynamic water splitting potential of $\Delta E^{\theta} = -1.23 \text{ V}$ according the following relationship:

$$\Delta G^{\theta} = -nF\Delta E^{\theta} \quad (2.8)$$

where n is the number of moles of electrons transferred and F is the Faraday constant (96485 C/mol). ΔE^{θ} is the standard potential of the electrochemical cell. It should be emphasized that the oxidation half-reaction involves four separate electron transfer steps for each O_2 molecule that is produced and is one of the main bottlenecks for water splitting, while the reduction half-reaction is a much simpler two electron process for each H_2 molecule.

Requirements for the Semiconductor

The primary component of a PEC cell is the semiconductor where critical processes take place including light absorption, charge carrier generation, minority carrier migration towards the semiconductor-electrolyte interface, and majority carrier transportation towards the external circuit connected to the counter electrode. Therefore, the basic physical and photophysical properties of the semiconductor are important for the PEC performance.

Quantum Physics and Semiconductor Basics

“I think it is safe to say that no one understands quantum mechanics”

—Richard P. Feynman

The development of semiconductor devices is regarded as one of the greatest revolutions in technology, but

behind it stands an even greater revolution in general science: quantum physics—a theory based on the principle that matter and energy behave both as particles and as waves.²⁶ When separate atoms are brought in close proximity to form a solid, their electronic structure will be redistributed by the bonding interaction. Two primary constraints need to be satisfied for a given structure: first of all, the Pauli's Exclusion Principle which says that no two electrons in an atom can share the exact same set of quantum numbers. Therefore, discrete atomic levels broaden into a band of levels. Since a typical solid contains a large number of atoms (on the order of $\sim 10^{22} \text{ cm}^{-3}$), a nearly continuous distribution of energies results. Secondly, the shape of the bands of electron states are confined by the finite size of the solid and the periodic array of potentials contained therein. Due to the bonding and anti-bonding energy levels, two energy bands will be formed. The valence band is filled with electrons, while the conduction band is mostly empty. The electrons in the valence band are immobile unless they are excited to the conduction band. The difference between the valence band and conduction band is defined as the bandgap (E_g), where the density of states is zero.

Depending on the bandgap size and electrical properties, materials can be classified into three different classes: (1) metal, (2) semiconductor, and (3) insulator. As illustrated in **Figure 2.2**, a bandgap does not exist in metals because the valence bands overlap with the conduction bands. As a result, electrons can easily pass into the conduction band and the density of free charge carriers is very high. This is why metals have high electrical conductivity. On the other hand, a material with a fully occupied valence band and empty conduction band is an insulator. This is the case when the bandgap exceeds 8 eV and the room temperature thermal energy is insufficient to excite electrons from the valence band to the conduction band. Therefore, insulators have very poor electrical conductivity. Semiconductors stand in between metals and insulators and usually have moderate bandgaps (1-3 eV). While this is not small enough for thermal excitation to take place at room temperature, the typical bandgaps of semiconductors are in the energy range of the photons in sunlight, as shown in **Figure 2.3**.

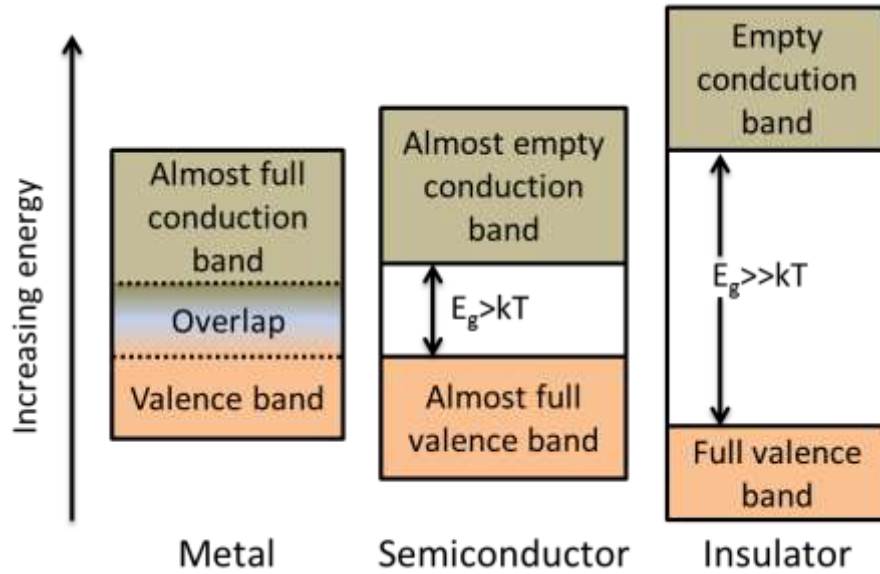


Figure 2.2. Energy diagram of metal, semiconductor and insulator.

Electrons can be excited from the valence band to the conduction band upon illumination. This special property of semiconductors makes them suitable for solar energy conversion, e.g., PV and PEC water splitting applications.

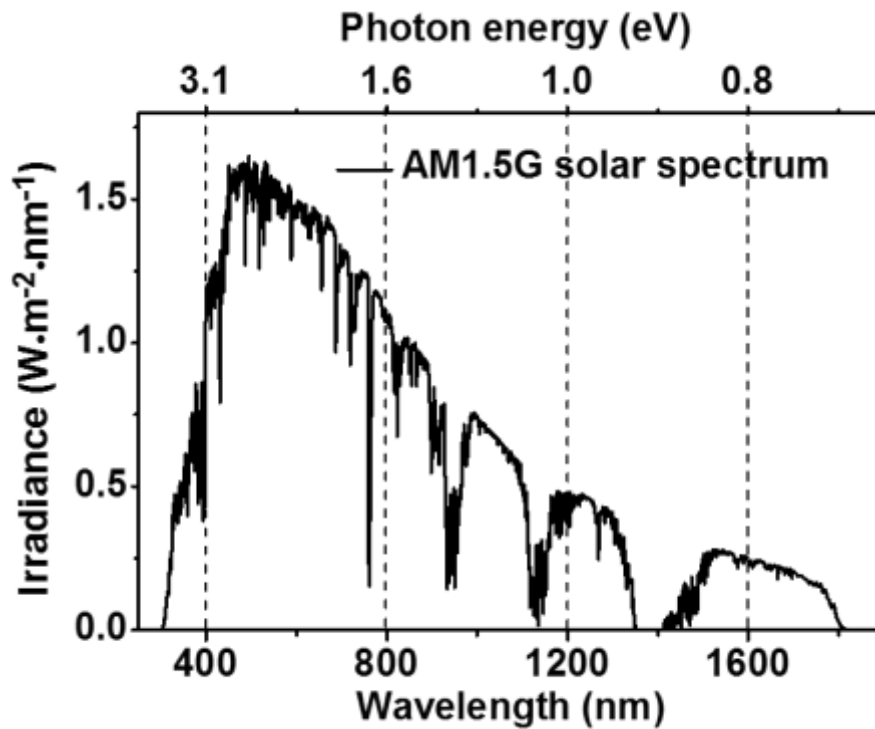


Figure 2.3. AM 1.5G solar spectrum with corresponding photon energy at each wavelength is shown on top. Data source from ²⁷.

In order to discuss the semiconductor requirements for PEC water splitting in detail, several key concepts of semiconductors have to be clearly defined. As depicted in **Figure 2.4**, a semiconductor consists of a valence band (VB) and a conduction band (CB). The band gap (E_g) is defined as the energy difference between the top of the VB (E_v) and the bottom of the CB (E_c). The vacuum level (E_{vac}) is the energy level where an electron has zero kinetic energy with respect to the sample surface. The Fermi level (E_F) is an energy level with 50% chance of being occupied by an electron. In this example the semiconductor is p-type and the E_F is closer to E_v than it is to E_c . In n-type semiconductors, E_F is closer to E_c . The work function (WF) is defined as the energy required to move an electron from the E_F in the semiconductor to a point in free space outside the surface, i.e. at E_{vac} .²⁸

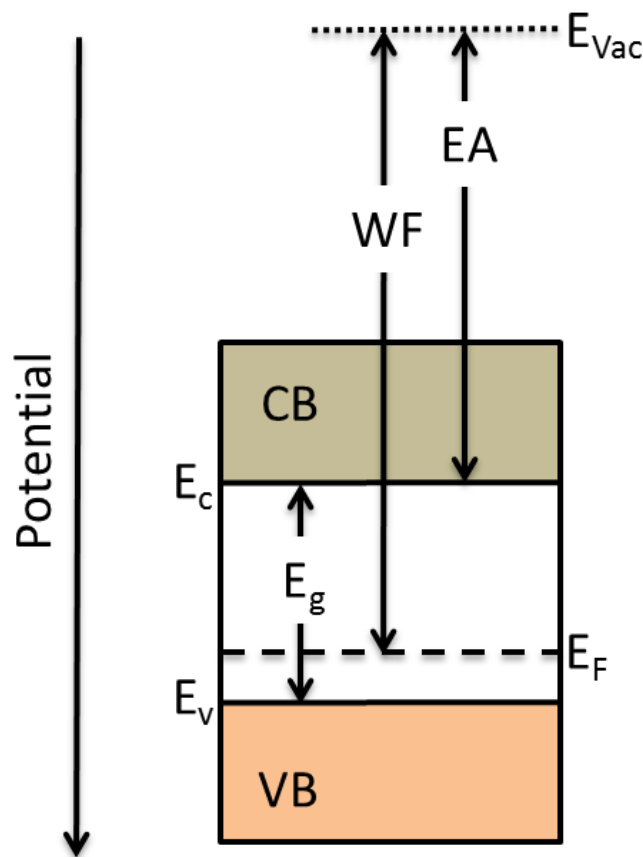


Figure 2.4. Energy diagram of a p-type semiconductor. Valence band (VB), conduction band (CB), band gap (E_g), ionization energy (IE), work function (WF), electron affinity (EA), and vacuum level (E_{vac}).

The distribution of electrons can be described by the Fermi-Dirac distribution and the density of states in the conduction and valence band. The probability that a state of energy E is occupied by an electron is described by the Fermi-Dirac equation,

$$f(E) = \frac{1}{\exp\left(\frac{E-E_F}{kT}\right)+1} \quad (2.9)$$

where E_F is the Fermi level, k is the Boltzmann constant, and T is the temperature (K). The number of available energy states at a certain energy level E , also called density of states ($\rho(E)$), is given by:

$$\rho_C(E) = \frac{m_e^* \sqrt{2m_e^*(E-E_C)}}{\pi^2 \hbar^3} \quad (2.10)$$

$$\rho_V(E) = \frac{m_h^* \sqrt{2m_h^*(E_V-E)}}{\pi^2 \hbar^3} \quad (2.11)$$

Here m_e^* and m_h^* are the effective masses of electrons and holes, respectively. $\hbar = h/2\pi$, h is the Planck's constant. E_C and E_V are the conduction band minimum the valence band maximum energy levels, respectively. The number of free electrons in the energy range between E and $E+dE$ is the number of occupied states:

$$N_{occ}(E) = f(E)\rho(E) \quad (2.12)$$

and the number of free holes states as

$$N_{unocc}(E) = [1 - f(E)]\rho(E) \quad (2.13)$$

More specifically, the number of free electrons (n) and holes (p) in the conduction and valence band can be expressed as:

$$n = \int_{E_C}^{E_{top}} N_{occ}(E) dE = \int_{E_C}^{E_{top}} f(E) \rho_C(E) dE \quad (2.14)$$

$$p = \int_{E_{bottom}}^{E_V} N_{unocc}(E) dE = \int_{E_{bottom}}^{E_V} [1 - f(E)] \rho_V(E) dE \quad (2.15)$$

When the difference between the Fermi level and valence of a p-type semiconductor is more than $3kT$, these two equations can be simplified to:

$$n = N_C \exp\left(\frac{E_F - E_C}{kT}\right) \text{ with } N_C = 2\left(\frac{2\pi m_e^* kT}{h^2}\right)^{3/2} \quad (2.16)$$

$$p = N_V \exp\left(\frac{E_V - E_F}{kT}\right) \text{ with } N_V = 2\left(\frac{2\pi m_h^* kT}{h^2}\right)^{3/2} \quad (2.17)$$

Here N_C and N_V are the effective density of states in the conduction and valence band, respectively.

For practical applications, intrinsic semiconductors are usually not favorable for use because of their poor conductivity. This can be addressed by adding a definite quantity of impurities to introduce additional free

electrons (e^-) or holes (h^+). The impurities (or dopants) are either donors or acceptors. In donor-doped semiconductors, a dopant with higher valency than the host atom is introduced. For example, silicon, which has 4 valence electrons, can be doped with phosphorus, which has 5 valence electrons (see **Figure 2.6b**). This results in extra valence electrons that can be easily excited to the conduction band and thus improve the conductivity of the semiconductor. Since the electron concentration is higher than hole concentration, donor-doped semiconductors are also called n-type semiconductors. The term n-type comes from the negative charge of the electrons. In contrast, acceptor-doped semiconductors have impurities with lower valency than the host atom, e. g., boron (3 valence electrons) in silicon (see **Figure 2.6c**). In this case, electrons can be easily excited from the valence band of the semiconductor to the acceptors, resulting free holes in the valence band of the semiconductor. This also increases the conductivity of the semiconductor. The acceptor-doped semiconductors are defined as p-type semiconductors, here p refers to the positive charges of holes.

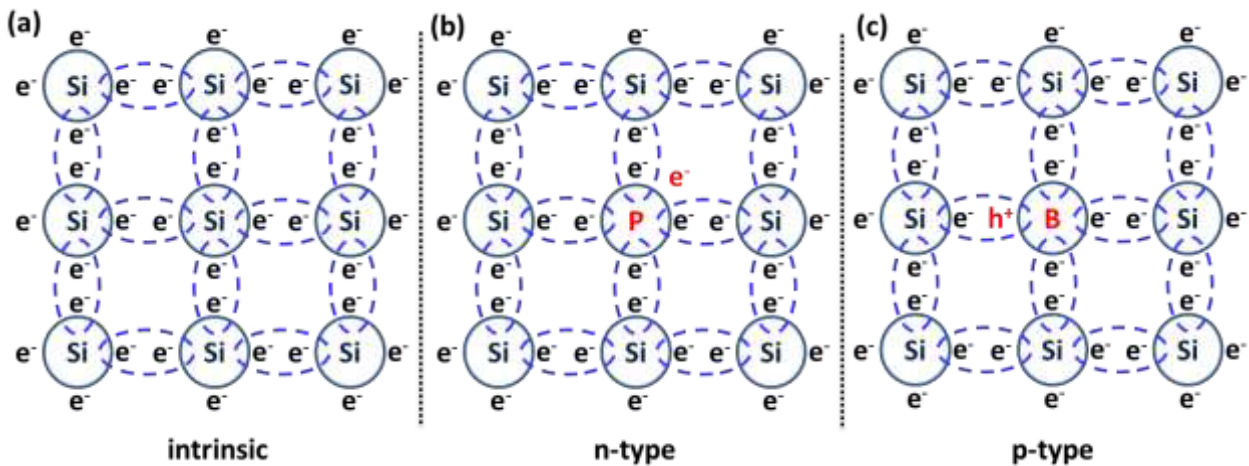


Figure 2.5. Schematic bond for (a) intrinsic silicon; (b) phosphorus doped n-type silicon; (c) boron doped p-type silicon.

As suggested earlier the impurities also affect the location of the Fermi level, as shown in **Figure 2.6**. The Fermi levels of intrinsic semiconductors lay in the middle of the bandgap. However, due to the presence of large number of free electrons in the conduction band, the Fermi level in the n-type semiconductor lies close to the conduction band. In contrast, the Fermi level in a p-type semiconductor is placed close to the valence band because of the high existence of holes.

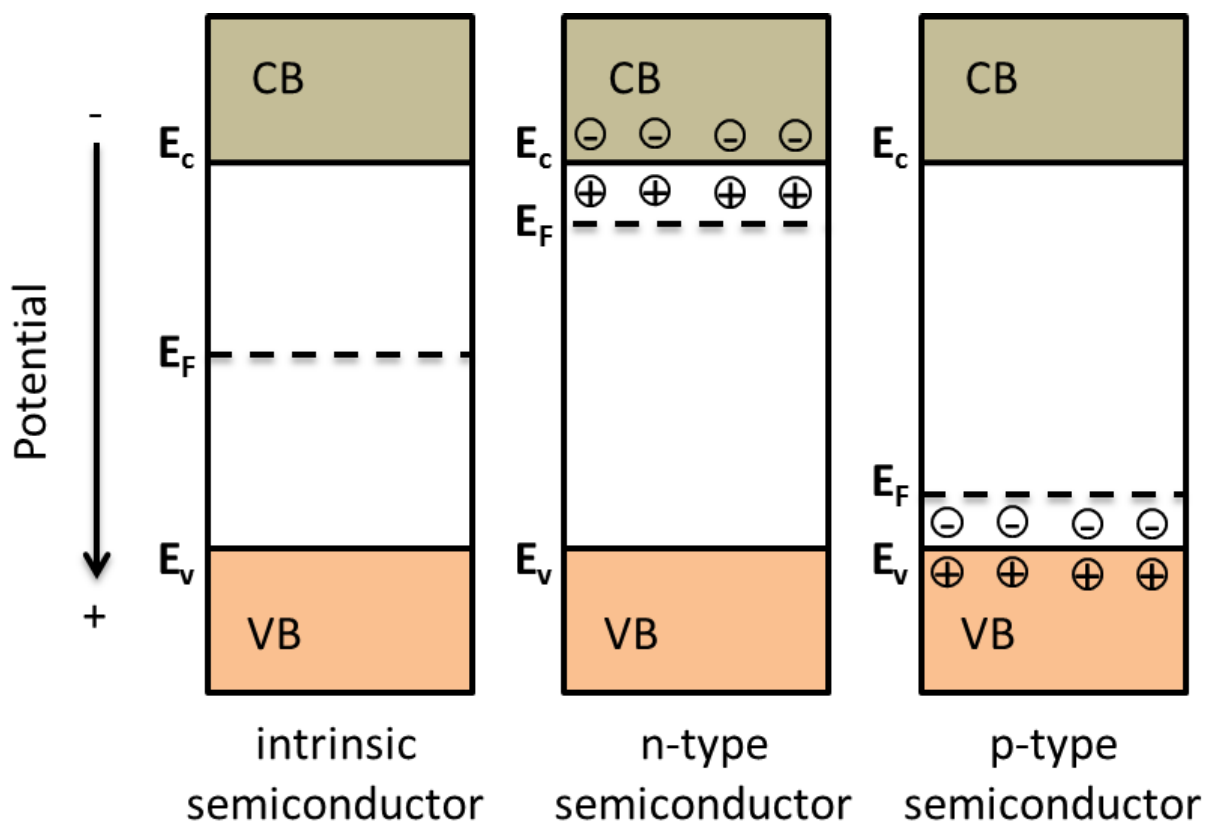


Figure 2.6. Energy diagram of intrinsic semiconductor, n-type semiconductor and p-type semiconductor.

Band Gap and Band Edges Positions

As discussed previously, the overall water splitting reaction is thermodynamically uphill and a minimum energy of 1.229 eV must be supplied by the semiconductor to split water. For a semiconductor, only photons with energy larger than the band gap are absorbed so the band gap is the upper limit of the maximum photovoltage. In order for a single semiconductor to provide enough energy required to drive the water splitting reaction, a minimum band gap of 1.229 eV is required. In addition, the inherent energy losses imposed by thermodynamics (0.3-0.4 eV)²⁹ as well as overpotentials that are required to ensure sufficiently fast reaction kinetics (0.4-0.6 eV)³⁰⁻³¹ should be taken into account when quantifying the optimal band gap for a PEC semiconductor.³² As a result, the bandgap should be at least 1.9 eV if a single semiconductor is used. On the other hand, with respect to light harvesting, the band gap should be as small as possible to absorb a major portion of the solar spectrum. As illustrated in **Figure 2.7**, CdS (2.42 eV),³³ Cu₂O (2 eV),³⁴ and CuGaSe₂ (1.7 eV)³⁵ have the theoretical upper limits in solar-to-hydrogen (STH) efficiency of 9 %, 18 % and 28 %, respectively.

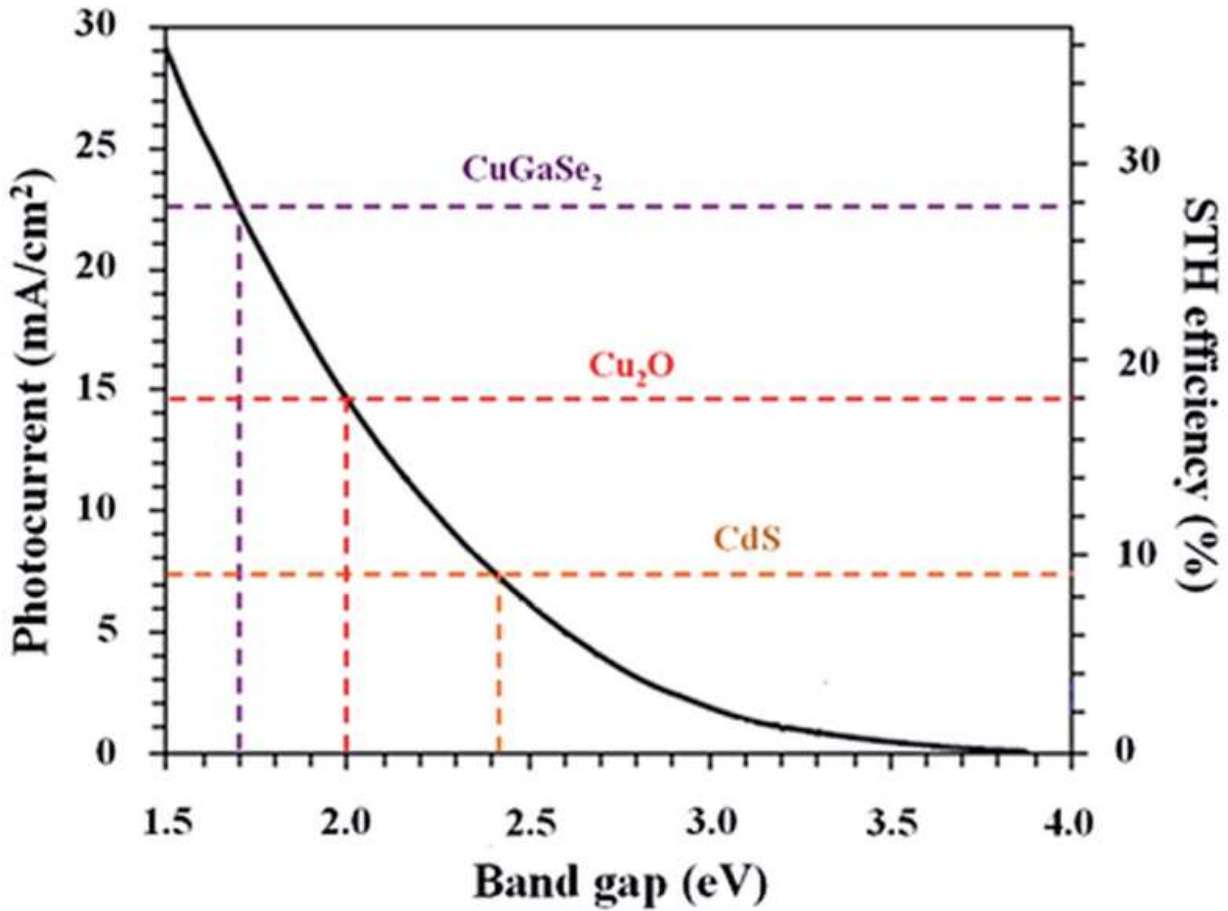


Figure 2.7. The upper limit of the theoretical solar to hydrogen efficiency and photocurrent as a function of bandgap. Figure adapted from ³⁶.

Therefore, for a PEC semiconductor, there is a trade-off between light harvesting (requires small bandgap) and thermodynamic driving force (requires large bandgap). It is suggested that the optimal bandgap of a PEC semiconductor should be ~ 2.03 eV, which corresponds to a STH conversion efficiency of $\sim 16.8\%$.³⁰ Additionally two different semiconductors can be combined in a tandem configuration to reach a higher STH conversion efficiency. For example, a tandem configuration consisting of a top absorber with a larger bandgap of 1.84 eV and a bottom absorber with a smaller bandgap of 1.23 eV can reach a theoretical STH efficiency of 22.8%, as illustrated in **Figure 2.8**.³⁷

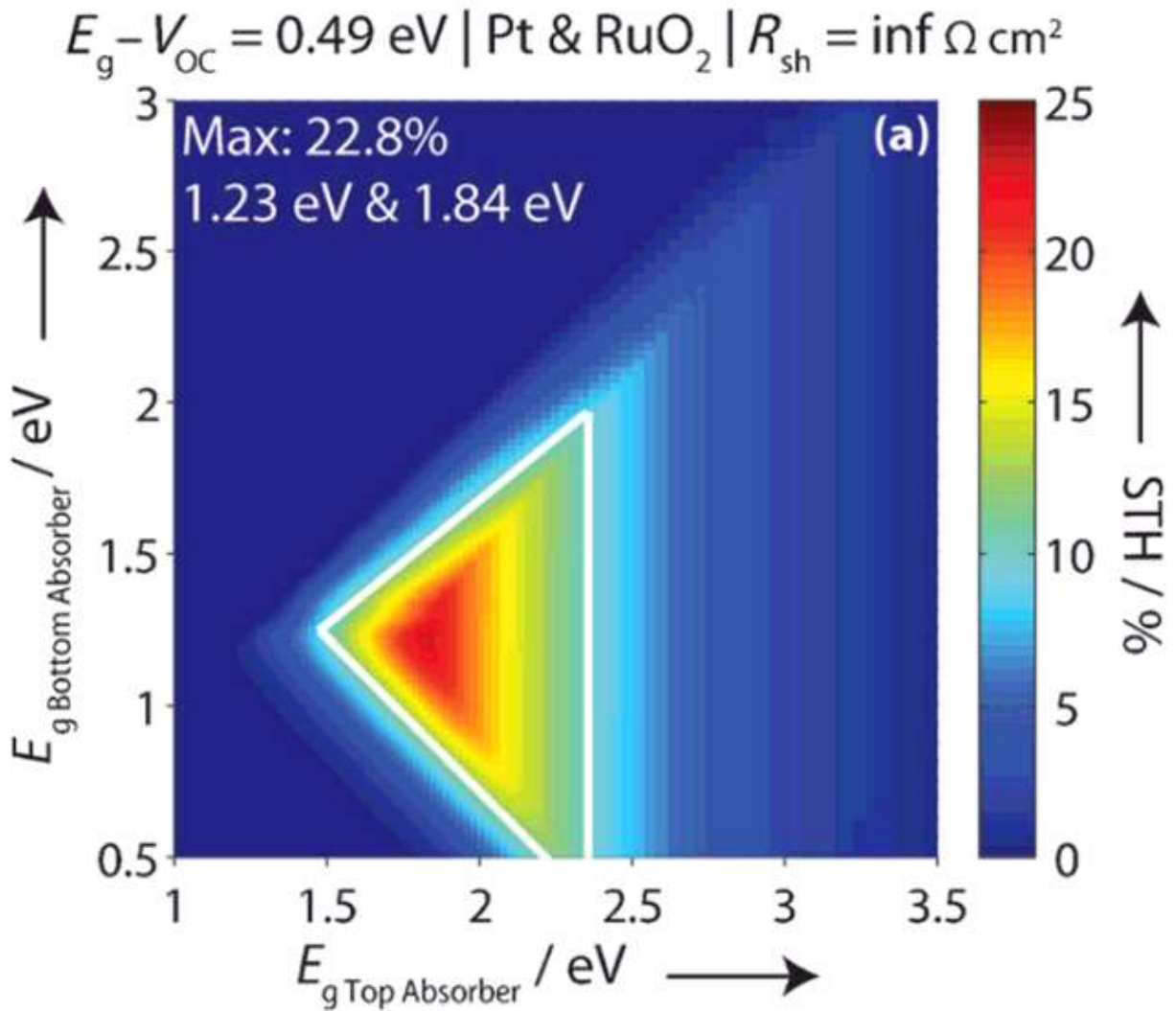


Figure 2.8. STH efficiency contour plots for a dual stacked tandem configuration as a function of bandgaps of the top and bottom absorbers. Figure adapted from reference ³⁷.

In addition to having an optimal band gap energy, semiconductors must also have optimally located band edges to split water. The band edge positions of the semiconductor determine the thermodynamic driving force, i.e. the maximum oxidation and reduction potentials of the photogenerated holes and electrons, respectively. For the PEC water splitting to take place, holes should be able to move from the photoelectrode to the electrolyte for water oxidation. Therefore, the valence band edge should be more positive than the oxidation potential of $\text{H}_2\text{O}/\text{O}_2$. Likewise, the conduction band edge needs to be more negative than the reduction potential of H^+/H_2 , as shown in **Figure 2.9**.

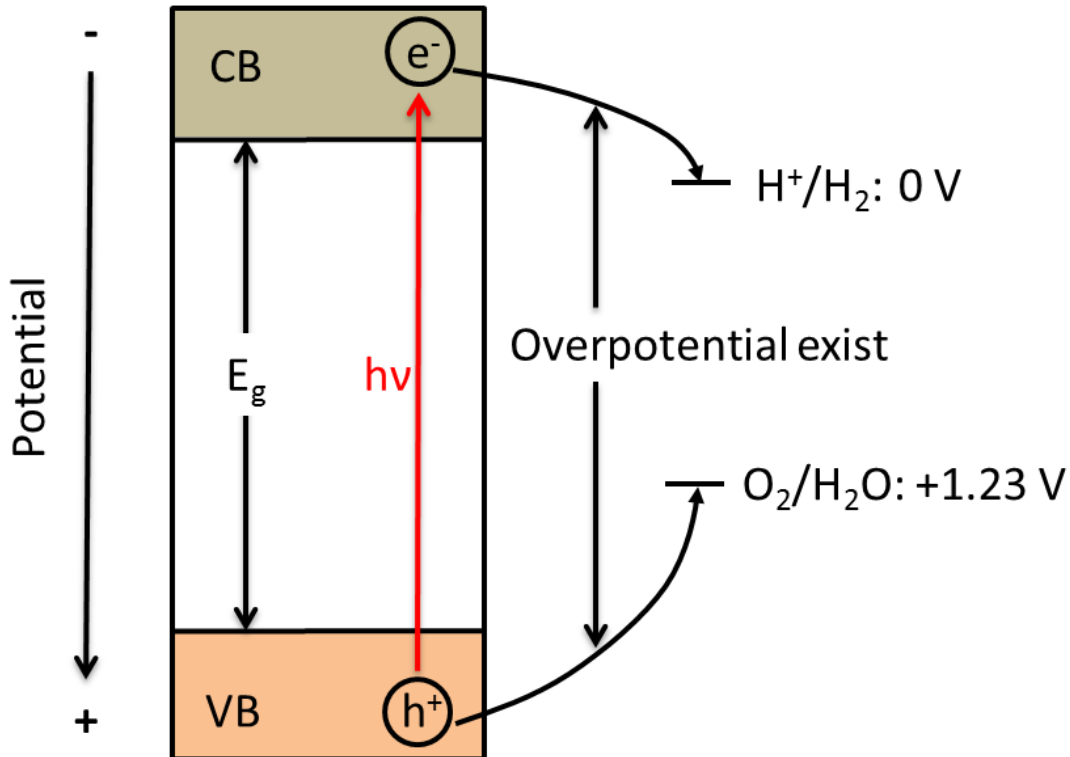


Figure 2.9. Illustration of the required band edge positions for driving the reduction and oxidation reactions.

It is worth noting that actual oxidative (reduction) power of the holes (electrons) in a photocathode (photoanode) is always less than that suggested by the valence band edge (conduction band edge). This is due to the energy loss $e\phi_{SC}$ of the photogenerated carriers while traversing the space charge region (SCR). Additional energy is lost when the majority carriers leave the semiconductor and enter the counter electrode at its Fermi level. For a p-type semiconductor, the total energy loss is

$$E_{loss} = e\phi_{SC} + (E_V - E_F) \quad (2.18)$$

Figure 2.10 shows the band edge energies for some selected metal oxides semiconductors. Wide bandgap materials ($E_g > 3.0$ eV), such as TiO_2 , can offer enough driving force for the overall water splitting reaction because their band edges straddle the potential of water reduction and oxidation potentials. However, their band gaps are so wide that only a small portion of the solar spectrum can be absorbed ($< 4\%$). Narrow band gap materials (e.g., CuWO_4), on the other hand, are able to absorb a larger portion of the solar spectrum, but their band edges are not suitable for driving both water reduction and oxidation. Only a handful of materials (e.g. TaON and CuNbO_4) have band positions that might be able to drive the overall water splitting reaction.

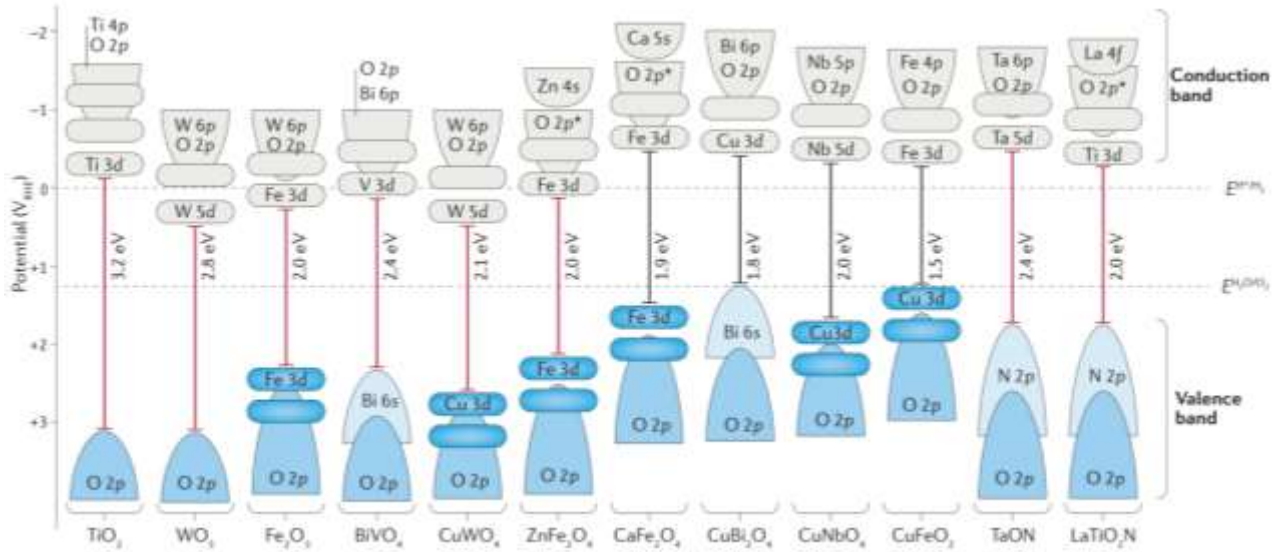


Figure 2.10. Band edge positions for selected metal oxides semiconductors. This figure is adapted from reference ³⁸.

Semiconductor/Electrolyte Interface

“God made the bulk; the surface was invented by the devil”

—Wolfgang Ernst Pauli

In PEC water splitting, the semiconductor will be immersed in aqueous electrolyte. A charge transfer between the semiconductor and the electrolyte will take place until an electrochemical equilibrium is achieved. As shown in **Figure 2.11a**, before a p-type semiconductor is brought into contact with the electrolyte, the number of ionized acceptors equals that of electrons. After contact with the electrolyte, holes will be transferred from the semiconductor to the electrolyte until the Fermi level of the semiconductor reaches the redox potential of the electrolyte, as illustrated in **Figure 2.11b**. A chemical equilibrium will be achieved resulting in a region between the bulk and the surface of the semiconductor where the majorities (holes for p-type) are depleted. This region is defined as the depletion layer or the space charge layer.

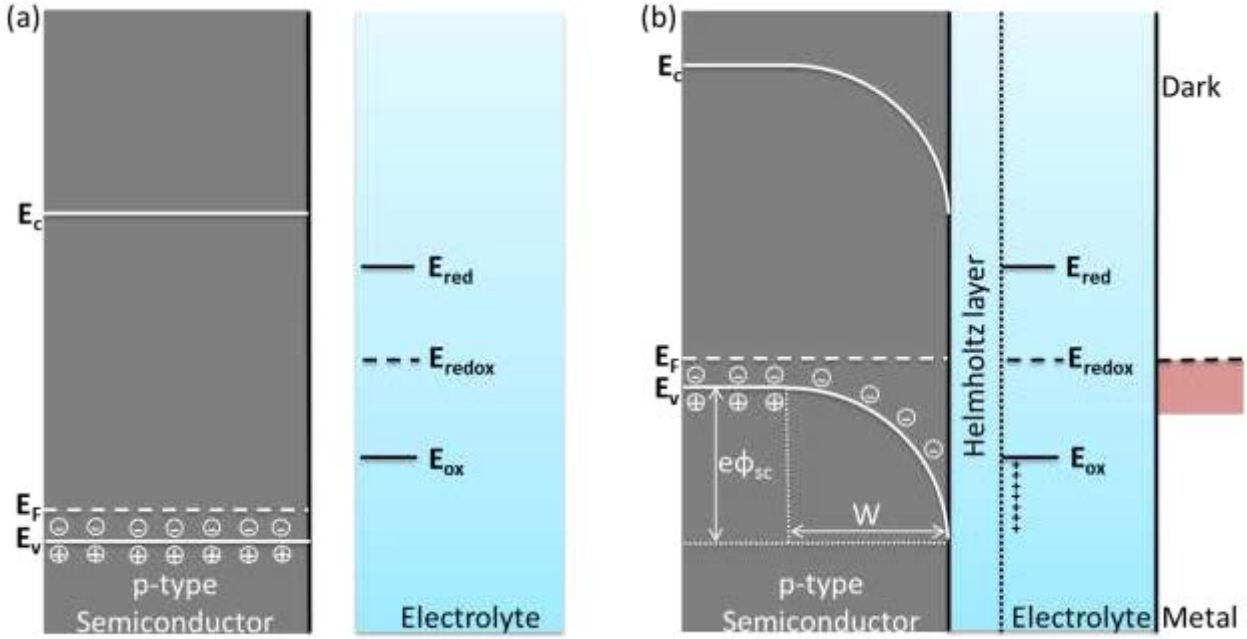


Figure 2.11. Illustration of the formation of electrochemical equilibrium. Band diagrams of the semiconductor and the electrolyte (a) before brought into contact; (b) after brought into contact.

The space charge layer is essential for the separation of the photogenerated charge carriers, since a potential drop (φ_{SC}) is present in this layer. An electric field is formed due to the potential drop, which facilitates the transport of the electrons and holes towards the semiconductor-electrolyte interface and the back contact, respectively. The width of the space charge layer (W) can be expressed as:

$$W = \sqrt{\frac{2 \varepsilon \varepsilon_0}{e N_A} \left(\varphi_{SC} - \frac{kT}{e} \right)} \quad (2.19)$$

where ε is the relative permittivity or dielectric constant, ε_0 is the permittivity of free space, N_A is the concentration of the ionized acceptors, φ_{SC} is the potential drop in the space charge layer, k is the Boltzmann constant, and T is the temperature (K), and e is the electronic charge (C).

A double layer composed of positive and negative charges is also formed at the interface, which is defined as the Helmholtz layer. The width of the Helmholtz layer is usually a few angstroms, and the potential drop (V_H) across the layer is typically in the order of $\sim 0.1-0.5$ V.³⁹ When a bias is applied on the PEC cell, either by an external bias potential or by shining light, the potential difference will be distributed over the space charge layer and the Helmholtz layer. The total capacitance of these layers is given by

$$\frac{1}{C_{tot}} = \frac{1}{C_{SC}} + \frac{1}{C_H} \quad (2.20)$$

Since the layers are connected in series, both layers are associated with the same amount of charge Q

$$Q = \Delta V_{SC} C_{SC} = \Delta V_H C_H \quad (2.21)$$

where ΔV_{SC} and ΔV_H are the potential changes across the space charge layer and the Helmholtz layer, respectively. Since C_H is much larger than C_{SC} , the applied bias will fall mainly across the depletion layer of the semiconductor. Therefore, applying a negative bias on a p-type semiconductor will result in an increase of the band bending. On the contrary, applying a positive bias on a p-type semiconductor or illuminating it will reduce the band bending. The flatband potential (φ_{fb}) is defined as the electrochemical potential that is required to be applied to the semiconductor in the dark to reduce the band bending to zero. The acceptor density (N_A) and the flatband potential (φ_{fb}) can be determined by Mott-Schottky measurements. Mott-Schottky plots are created using the following relationship assuming ideal semiconductor behavior:

$$\frac{1}{C^2} = \frac{2}{e \varepsilon \varepsilon_0 N_A} \left(-\varphi_A + \varphi_{fb} - \frac{kT}{e} \right) \quad (2.22)$$

where C is the capacitance (F/m^2), ε is the relative permittivity or dielectric constant, ε_0 is the permittivity of free space, N_A is the acceptor density (m^{-3}), φ_A is the applied potential, and φ_{fb} is the flat band potential.

PEC Cell under Operating Conditions

The discussions above only concern the properties of the semiconductor and semiconductor/electrolyte interface under equilibrium conditions. The following section will focus how a PEC cell works under illumination with current flow.

Quasi Fermi Level and Photovoltage

Upon illumination, electron-hole pairs are generated and the system is no longer in equilibrium. It is no longer appropriate to use a single Fermi level for the semiconductor, especially in the SCR. In order to interpret the thermodynamic driving force of the semiconductor under illumination, the concept of quasi-Fermi levels is proposed. The quasi-Fermi levels are associated with the concentration of electrons and holes at a certain point in the semiconductor, and are defined as:

$$n = n_0 + \Delta n = N_C e^{-(E_C - E_{F,n}^*)/kT} \quad (2.23)$$

$$p = p_0 + \Delta p = N_V e^{(E_V - E_{F,p}^*)/kT} \quad (2.24)$$

where n_0 and p_0 are the carrier concentrations under equilibrium in the dark, Δn and Δp are the increase in carrier concentrations caused by illumination. For a p-type semiconductor, $n = n_0 + \Delta n \approx \Delta n$ and $p = p_0 + \Delta p \approx p_0$ so that $E_{F,p}^*$ remains horizontal while $E_{F,n}^*$ departs from the Fermi level of the bulk in the active region. The band diagrams for a PEC cell in equilibrium in the dark and under light are illustrated in **Figure 2.12**.

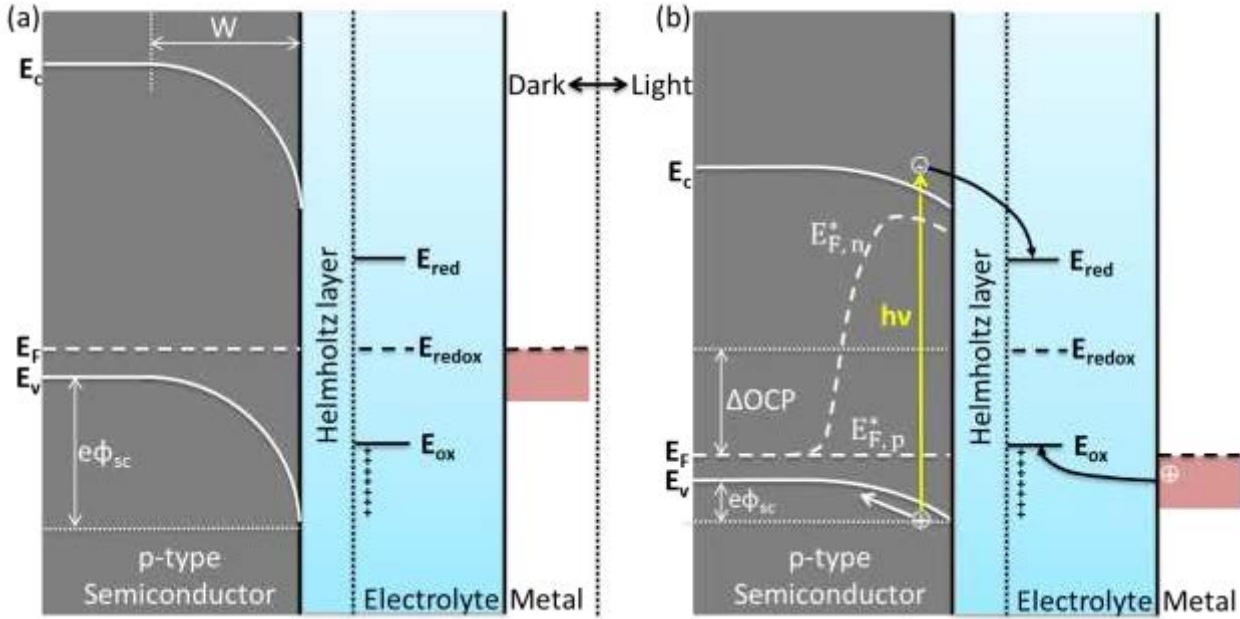
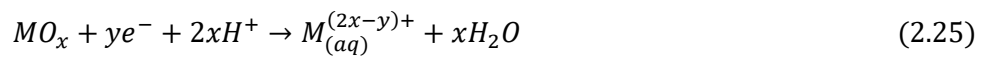


Figure 2.12. Band diagrams for a PEC cell based on a p-type semiconductor photocathode connected to a metal counter electrode (a) under equilibrium in the dark; (b) under illumination.

The energy difference between $E_{F,p}^*$ and $E_{F,n}^*$, the quasi Fermi level splitting, is often used to represent the true thermodynamic driving force of a semiconductor for water splitting.

Photo-corrosion under Illumination

In addition to reacting with the electrolyte species, photogenerated electrons (holes) in semiconductor photoelectrodes can also reduce (oxidize) ions in the semiconductor itself. The name for this decomposition process is photo-corrosion. The corresponding cathodic decomposition reactions can be expressed as:



or



This has been observed for p-type metal oxides such as Cu_2O ⁴⁰⁻⁴¹ and CuBi_2O_4 ⁴²⁻⁴³ when they are directly in contact with aqueous solutions under illumination. For n-type semiconductor, the anodic decomposition reaction can be expressed as:



Bare ZnO, for example, is a well-known n-type metal oxide that suffers from severe photo-corrosion in aqueous environments.⁴⁴⁻⁴⁵ **Figure 2.13** shows the anodic and cathodic decomposition potentials of selected semiconductors. Note that the actual decomposition potentials may vary with pH since they depend on the concentration of the reaction products according to Nernst equation.⁴⁶ Those decomposition potentials combined with the band edge positions of the semiconductor determine whether or not the decomposition reactions can take place.⁴⁷ The cathodic decomposition occurs only when the energy level for cathodic decomposition, $E_{n,d}$, is below the conduction band minimum.

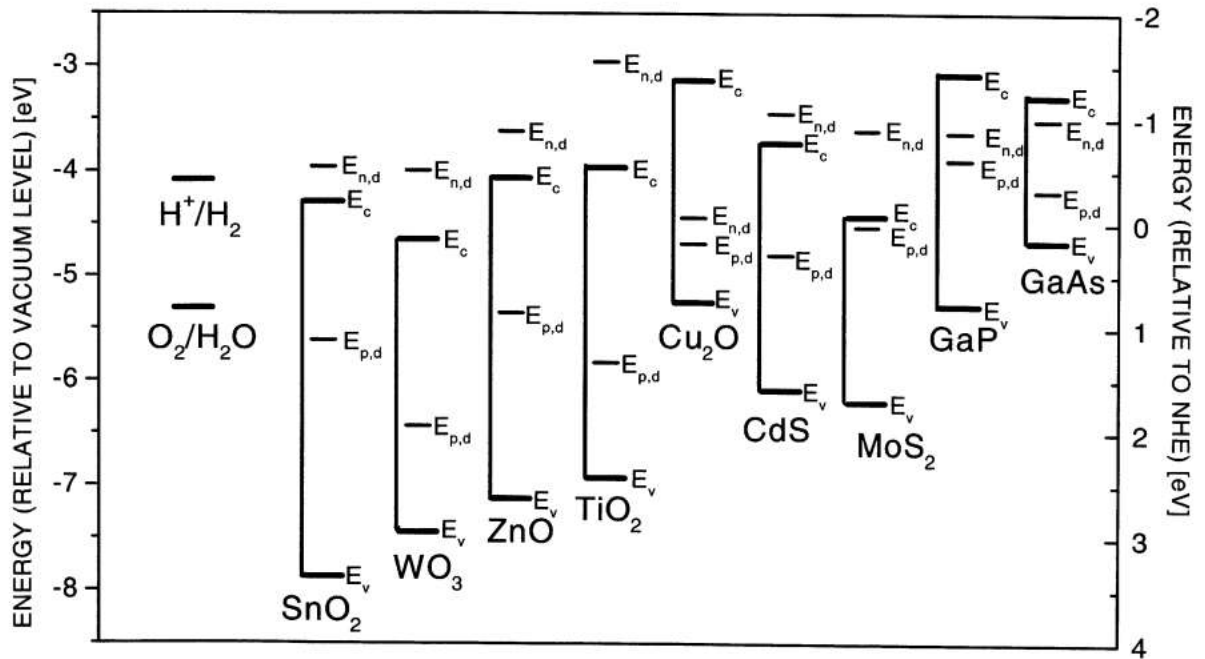


Figure 2.13. Position of decomposition potentials of selected semiconductors. Figure adapted from⁴⁸.

As we can see from **Figure 2.13**, some of the metal oxides have $E_{n,d}$ located above their conduction band minimum (e.g., TiO_2 , WO_3 , SnO_2). Therefore, they are thermodynamically stable against cathodic photo-corrosion. Conversely, the anodic decomposition potential, $E_{p,d}$, position should be above the valence band maximum in

order for the anodic decomposition reactions to take place. Most metal oxides are thermodynamically unstable against anodic photo-corrosion since their $E_{p,d}$ positions are above their valence band maximum.

Many photoanodes based on n-type semiconductors suffer severe photo-corrosion due to self-photo-oxidation by photogenerated holes at the semiconductor/electrolyte interface.⁴⁹ In comparison, photocathodes based on p-type semiconductors are protected from photo-oxidation to some extent, because the photogenerated holes will be transferred towards the back contact before the photo-corrosion due to the band bending at the SCR.³⁶ However, many p-type metal oxide semiconductors such as Cu_2O are susceptible to photo-corrosion by photo-reduction from electrons. The undesired photo-corrosion seriously impedes the application of many materials in PEC water splitting. Protection layers or suitable co-catalysts are usually applied to alleviate the problem. For example, in this thesis, we have adopted the strategy of coating CuBi_2O_4 , a p-type semiconductor with CdS/TiO_2 to protect it from photo-corrosion.⁵⁰ The details will be discussed in Chapter 4.

Energy Conversion Efficiencies

The ultimate goal is to use the PEC cell to convert solar energy into chemical energy in the form of hydrogen. One of the most important indicators of the PEC cell is the energy conversion efficiency. The solar-to-hydrogen (STH) conversion efficiency (η_{STH}) is defined as the ratio of the chemical energy in the generated hydrogen to the solar energy input:

$$\eta_{STH} = \frac{P_{electrical}^{out} - P_{electrical}^{in}}{P_{light}} = \frac{j_{photo} \times (V_{redox} - V_{bias})}{P_{light}} = 1.23 \times j_{photo} \quad (2.28)$$

The total PEC water splitting process is composed of three main steps: (1) light harvesting and absorption to generate charge carriers; (2) charge carrier separation; (3) the injection of the minority charge carriers from the semiconductor to the electrolyte species. First of all, light has to be absorbed by the semiconductor, and the absorption efficiency (η_{abs}) is defined as the number of electron-hole pairs that are generated divided by the amount of incident photons. Secondly, the photo-generated electron-hole pairs have to be separated from each other to avoid recombination. The ratio between the amount of charge carriers reaching their respective interfaces to the number photo-generated charge carriers is defined as the charge separation efficiency (η_{sep}). As illustrated in **Figure 2.14**, only the charge carriers generated in regions ① and ② can be effectively separated and transported to the respective interfaces, whereas in region ③ the electrons recombine with holes. The width of region ① is given by equation 2.19, while the width of region ② is determined by the

diffusion length of the minority charge carriers:

$$L_D = \sqrt{\left(\frac{\mu k T}{e}\right) \tau} \quad (2.29)$$

where μ is mobility ($\text{m}^2 \cdot \text{V}^{-1} \cdot \text{s}^{-1}$), k is the Boltzmann constant, and T is the temperature (K), e is the electronic charge (C), and τ is the charge carrier lifetime (sec). Lastly, the minority charge carriers (electrons for p-type) have to be injected from the semiconductor to the electrolyte and drive the reduction reaction. The ratio between the amount of electrons that undergo the water reduction and the amount that reach the semiconductor/electrolyte interface is called the injection efficiency (η_{inj}).

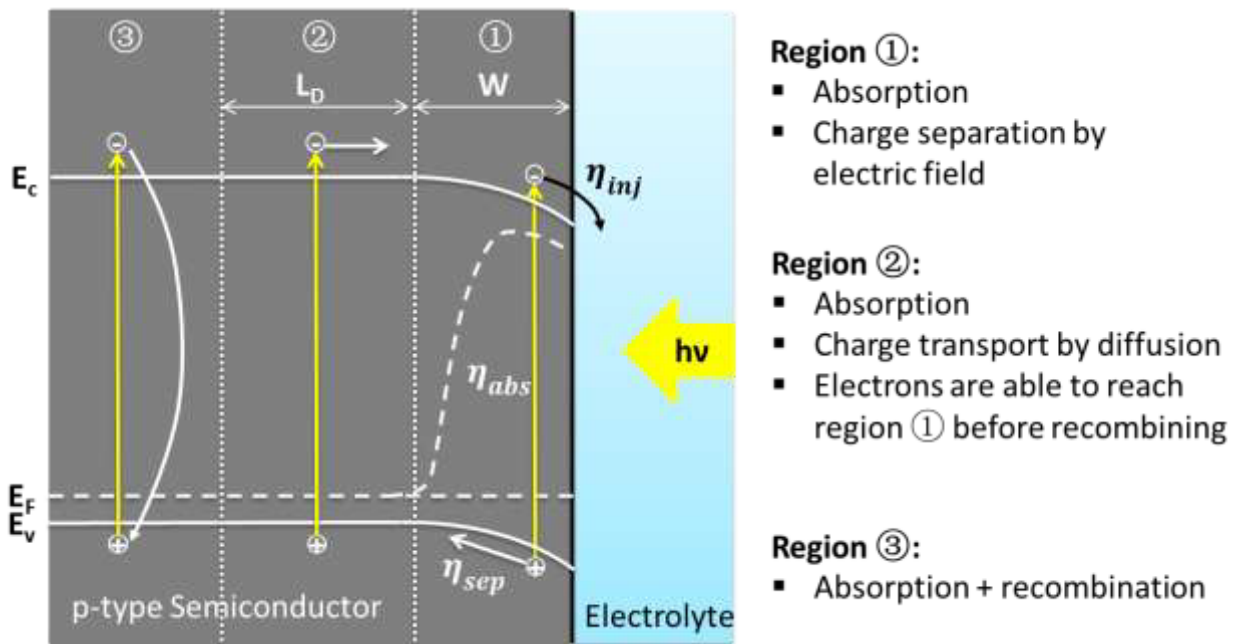


Figure 2.14. Schematic of the processes occurring in a p-type semiconductor under illumination.

Overall, the total efficiency of the PEC water splitting process (η_{STH}) can be alternatively expressed as the product of the three efficiencies described above:

$$\eta_{STH} = \eta_{abs} \times \eta_{sep} \times \eta_{inj} \quad (2.30)$$

Other efficiency expressions such as incident photon-to-current efficiency (IPCE) and absorbed photon-to-current efficiency (APCE) are also used to evaluate the performance of a PEC cell. IPCE is defined as the fraction of the incident photons that is converted to electrons measured by the outer circuit. Sometimes IPCE is also called external quantum efficiency and is given by the following equation:

$$IPCE = \frac{hc}{e} \times \frac{J_{pho}(\lambda)}{\lambda P(W)} = \frac{J_{pho}(\lambda)}{P(W)} \times \frac{1240}{\lambda(nm)} \quad (2.31)$$

where J_{pho} is the photocurrent, P is the power, and λ is the wavelength. APCE is the internal quantum efficiency and is defined as the fraction of the absorbed photons that are converted to photocurrent measured by the outer circuit:

$$APCE \% = \frac{IPCE \%}{A} \quad (2.32)$$

where A is the absorbance.

Photoelectrode Materials

Most of the basic requirements for suitable PEC materials have been described in the previous sections. The main requirements are summarized as follows:⁵¹⁻⁵²

- (1) Suitable bandgap for high light absorption.
- (2) Appropriate band edge positions.
- (3) Efficient charge separation and transport.
- (4) Low overpotential.
- (5) High stability.
- (6) Low cost.

Intensive investigations have been conducted on semiconductor-based water splitting since the pioneering work by J. P. Boddy⁵³ and Fujishima⁵⁴ on TiO₂. This section briefly reviews the current state of the art photocathode and photoanode materials. For more details please refer to the excellent review papers.^{38, 55}

The Hydrogen Evolution Reaction-Photocathode Materials

While numerous n-type semiconductors have been investigated as photoanode materials for water oxidation, very limited work has been conducted on p-type semiconductors as photocathodes for water reduction.^{36, 38, 49} The typical photocathode materials can be divided into several groups: metal oxides, III–V group materials, II–VI group materials, copper-based chalcogenides, and p-Si.⁵⁵

Depending on the type of defects, both n-type and p-type metal oxide semiconductors exist. Metal oxides possessing intrinsic oxygen vacancy as electron donors are generally n-type semiconductors so they are restricted to use as photoanodes (e.g., Fe₂O₃,⁵⁶ WO₃,⁵⁷ and BiVO₄⁵⁸). Distinctively, few metal oxides, such as

Cu_2O ,⁵⁹ CuFeO_2 ,⁶⁰ LaFeO_3 ,⁶¹ CaFe_2O_4 ,⁶² and CuNb_3O_8 ⁶³ are dominated by metal vacancy as acceptors. Therefore, they show p-type behavior and are investigated as photocathode materials. Compared to other non-oxide semiconductors, metal oxide semiconductors often meet the criteria with respect to the chemical stability and low cost. However, they usually have modest optical absorption coefficients, poor charge carrier mobility and short carrier lifetime, and thus low solar to hydrogen conversion efficiency.^{36, 55}

III–V group materials, show potential to be used in PEC water splitting due to their relatively narrow bandgaps, and extraordinary charge carrier mobility.⁵⁵ For example, GaAs has a bandgap of 1.42 eV and exhibits high charge carrier mobility.⁶⁴ The initial work by Khaselev demonstrated an impressive STH efficiency of 9.3 % by using a tandem cell consisting of a p/n GaAs bottom cell connected to a GaInP_2 top cell via a tunnel diode interconnect.⁶⁵ Binary compounds such as InP ⁶⁶ and GaP ⁶⁷ and ternary compounds including GaInP ,⁶⁸ GaInN ,⁶⁹ and AlGaAs ,⁷⁰ were also investigated as photocathode materials. Recently, GaP and InP were used for water splitting with the assistance of external bias.^{66, 71}

Many of the II–VI group materials have high absorption coefficients and are potential materials for PEC water splitting. CdS, a typical II–VI group material, has a direct bandgap of 2.4 eV and owns appropriate valence/conduction band edges for water oxidation/reduction. It is one of the most promising candidates which can potentially split water without external bias.^{33, 72-73} However, CdS is intrinsically n-type due to the formation of sulfur vacancies and it suffers significant photo-corrosion. To address this, p-type Cu doped CdS with a direct bandgap of 2.37 eV was prepared. The CdS:Cu/Pt photocathode produced a photocurrent of 0.6 mA/cm^2 and demonstrated the feasibility of using p-type CdS-based photocathode for hydrogen production.⁷⁴ Another example of II–VI group material is CdTe, which is one of the leading materials for thin film solar cells due to its suitable bandgap and the variety of synthesis methods. CdTe is usually p-type as a result of the existence of Te vacancies and can be used as photocathode for PEC hydrogen reduction.⁷⁵

The copper-based chalcogenides, such as $\text{Cu}_2\text{ZnSnS}_4$, $\text{CuIn}_x\text{Ga}_{1-x}\text{Se}_2$, and CuInS_2 are promising candidates for photovoltaic solar cells.⁷⁶⁻⁷⁸ They are usually p-type because of the intrinsic Cu vacancies. In addition to photovoltaics, the copper-based chalcogenides have also been investigated as photocathode materials for PEC hydrogen production due to their tunable direct bandgap, high absorption coefficient and high photostability.⁷⁹⁻⁸¹

Silicon, an earth abundant and industrial prevalent material, is by far the most widely used semiconductor for solar energy utilization.⁸² Besides its application in solar cells, p-Si is also applied as a photocathode because of its appropriate conduction band edge for hydrogen reduction.⁸³ With a small bandgap of 1.1 eV, the valence band edge of p-type silicon located at a lower level than the oxygen oxidation potential. Therefore, it has to be

combined with an n-type photoanode to achieve overall water splitting.⁸⁴⁻⁸⁵ However, p-type silicon lacks an effective co-catalyst and can suffer from severe etching and oxidation in aqueous electrolytes.^{84, 86}

Among the various photocathode materials, CuBi_2O_4 has recently attracted our attention due to its promising characteristics for PEC water splitting.⁴²⁻⁴³ It has a suitable band gap of 1.5 - 1.8 eV along with a positively positioned valence band and an appropriately positioned conduction band edge for the hydrogen reduction reaction. Therefore, it can absorb a significant portion of the solar spectrum and it also shows an exceptionally positive onset potential in comparison to other p-type materials like p-Si.

The Oxygen Evolution Reaction-Photoanode Materials

Numerous photoanode materials for PEC oxygen evolution reaction have been investigated over the past decades, including n-type metal oxides, and group III–V compounds, and II–VI group materials. As mentioned previously, n-type metal oxides such as TiO_2 , $\alpha\text{-Fe}_2\text{O}_3$, BiVO_4 can be used as photoanode materials. Of which TiO_2 has been extensively investigated as a photoanode material since 1972 due to its high stability, ease of preparation, low cost etc. However, it has a very wide bandgap (over 3 eV) so it can only absorb a very small portion of the solar spectrum, resulting in a very low maximum theoretical STH efficiency.⁸⁷ Efforts have been paid to modify the bandgap either by introducing non-metal species, such as nitrogen, to lift up the valence band position⁸⁸ or by doping with 3d transition metal ions to tailor the conduction band position.⁸⁹ $\alpha\text{-Fe}_2\text{O}_3$, an earth abundant material, has a suitable bandgap (1.9 to 2.32 eV) for visible light absorption.⁵⁶ However, the conduction band of $\alpha\text{-Fe}_2\text{O}_3$ is located at a much more positive position than the hydrogen reduction potential and thus can only be used with the assistance of external bias. Other limitations of $\alpha\text{-Fe}_2\text{O}_3$ are a short-lived charge carrier lifetime, short minority charge carrier diffusion length, low absorption coefficient, and poor water oxidation kinetics.⁹⁰⁻⁹³ Even so, an impressive photocurrent density of 4 mA/cm^2 was achieved with $\alpha\text{-Fe}_2\text{O}_3$.⁹⁴

While some p-type III–V compounds can be used as photocathode materials as described in the previous section, their n-type counterparts are considered as photoanode materials (e.g., n-type GaAs ,⁹⁵ n-type InP ,⁹⁶). Likewise, some II–VI group materials, such as CdS , are investigated not only as photocathode materials but also photoanode materials.^{74, 97} In theory, both hydrogen and oxygen evolution can be achieved over pure CdS due to its moderate bandgap and suitable band edge positions. However, its poor water oxidation kinetics leads to the accumulation of photogenerated holes near the semiconductor/electrolyte interface, resulting in significant photo-corrosion. Hole scavengers are commonly employed to alleviate the photo-corrosion of the II–VI semiconductors (e.g. CdS , CdTe , CdSe , ZnTe).

Among the numerous photoanode materials investigated in the past decades, only few of them can be identified as promising. One of the most successful metal oxide photoanode materials is BiVO_4 . As an n-type semiconductor, BiVO_4 has suitable bandgap (2.4 eV) and appropriate band edge positions for water oxidation.^{58, 98-99} Moreover, it composes of earth abundant elements and has the potential to be applied for large scale water splitting at relative low cost.¹⁰⁰ In this thesis, efforts have been paid on investigating the basic properties of BiVO_4 prepared by magnetron sputtering, as shown in Chapter 5.

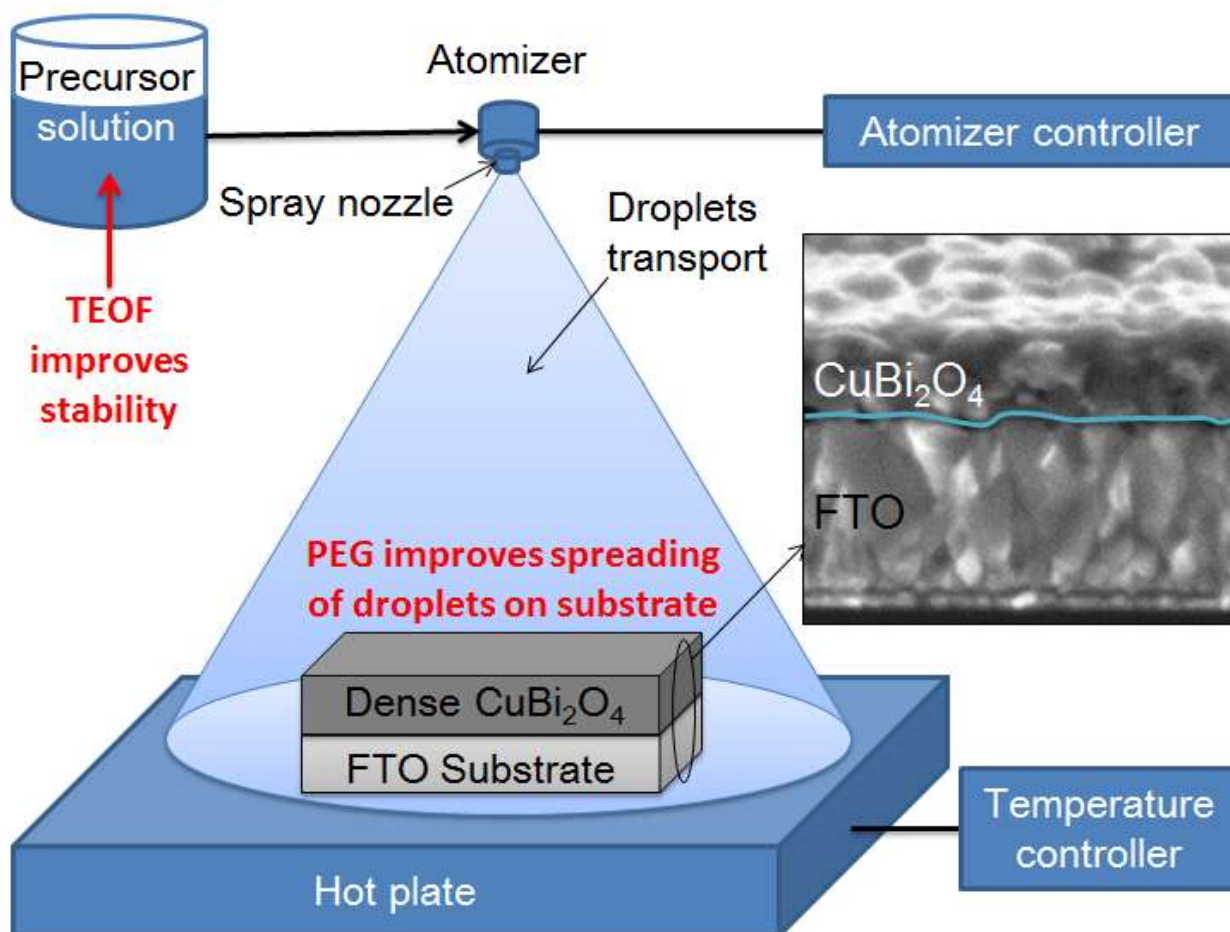
This thesis

Despite the intensive investigations that have been carried out to develop photoelectrode materials, to date no single material has been identified, which meets all of the critical thermodynamic and kinetic requirements for efficient and cost-effective PEC water splitting. Moreover, PEC water splitting has never been implemented on a large scale for practical applications. Therefore, in this thesis, we aim at exploring new materials and modifying the properties of the existing materials to make them more efficient and stable for PEC water splitting. We also investigate economic deposition techniques that can promote PEC water splitting on a large scale for practical applications.

In Chapters 3 and 4, we focus on a new p-type metal oxide material, CuBi_2O_4 , which has been reported to have a moderate bandgap in the range of 1.5 - 1.8 eV.¹⁰¹ Recall from **Figure 2.8** that a top absorber material with a bandgap of 1.84 eV has the potential to reach a theoretical STH efficiency as high as 22.8 % when coupled with a bottom absorber material having a smaller bandgap of 1.23 eV.³⁷ In Chapter 3 we develop and demonstrate a new spray recipe for depositing dense, homogeneous CuBi_2O_4 thin films that can be used for comprehensive evaluation of its optical and electrical properties. Our results demonstrate its potential to be used as an effective photocathode material if the major limitations of poor charge carrier separation and photo-corrosion can be overcome. In Chapter 4 we propose strategies to address these limitations including using gradient self-doping to improve the charge separation efficiency and applying CdS/TiO_2 protection layers and Pt as a catalyst to prevent photo-corrosion and produce hydrogen with a high Faraday efficiency.

Lastly, in Chapter 5, we choose a well-established material, BiVO_4 , to demonstrate the potential of using direct current magnetron sputtering as a scaling up technique for the deposition multinary oxides photoelectrodes. The structure-stoichiometry-electronic property relationships of the sputtered BiVO_4 are thoroughly investigated.

Chapter 3. Spray Pyrolysis of CuBi_2O_4 Photocathodes: Improved Solution Chemistry for Highly Homogeneous Thin Films



The main part of this Chapter was published: Wang, F.; Chemseddine, A.; Abdi, F. F.; van de Krol, R.; Berglund, S. P. *J. Mater. Chem. A*. **2017**, *5*, 12838-12847.

In this Chapter, we develop a spray pyrolysis recipe for the preparation of dense, homogeneous CuBi_2O_4 thin films as photocathodes. The high quality thin films are well-suited for fundamental research of the photophysical and photoelectrochemical properties of CuBi_2O_4 . Several challenges in the spray pyrolysis process are revealed and addressed, which may be applicable to the synthesis of dense, homogenous metal oxide thin films in general. First, the presence of water in the precursor solution causes rapid hydrolysis of Bi^{3+} resulting in non-homogenous spray onto substrates. To overcome this issue, triethyl orthoformate (TEOF) is added as a water scavenger, which significantly improves the stability of the precursor solution (slows precipitation) and improves the homogeneity of thin films (< 70 nm). Second, the poor spreading behavior of the droplets over the substrates during spray results in agglomeration of particles and powder formation and thus prohibits the growth of thicker films with the same level of homogeneity. This challenge is conquered by using polyethylene glycol (PEG) as an additive, which markedly improves the spreading behavior of droplets allowing for the growth of thicker (> 420 nm) dense, homogenous CuBi_2O_4 thin films. The constantly changing chemical composition of the precursor solutions is analyzed using attenuated total reflection infrared (ATR-IR) spectroscopy and the CuBi_2O_4 films are thoroughly characterized using a variety of analytical techniques. The high quality, dense CuBi_2O_4 films produce record photocurrent densities up to $\sim 2.0 \text{ mA/cm}^2$ under AM 1.5 solar simulation along with incident photon-to-current efficiency (IPCE) and absorbed photon-to-current efficiency (APCE) values of 14.0 % and 23.1 %, respectively (for 550 nm light at 0.6 V vs. RHE with H_2O_2 as an electron scavenger).

Introduction

CuBi_2O_4 emerged as a photocathode material for water splitting in 2007, when it was first identified as a photocathode material by Arai.¹⁰² It has a tetragonal structure with lattice parameters $a = b = 8.500\text{--}8.511 \text{ \AA}$, $c = 5.814\text{--}5.823 \text{ \AA}$, $Z = 4$, and space group $P4/ncc$.¹⁰³⁻¹⁰⁴ As shown in **Figure 3.1**, each Bi ion is coordinated with six O atoms, and each Cu ion is connected to four O atoms. The CuO_4 planes are stacked along the c -axis. The unique structure of CuBi_2O_4 plays an important role in establishing its electronic and optical properties. According to DFT calculations,¹⁰⁵ the electronic structure of CuBi_2O_4 consists of a conduction band (CB) and valence band (VB) arising primarily from the Cu 3d and O 2p orbitals, respectively. Copper vacancies are the energetically most probable defects in CuBi_2O_4 . These intrinsic defects are presumably charge-compensated by free holes, which shifts the Fermi level closer to the valence band and causes the p-type behavior of CuBi_2O_4 .

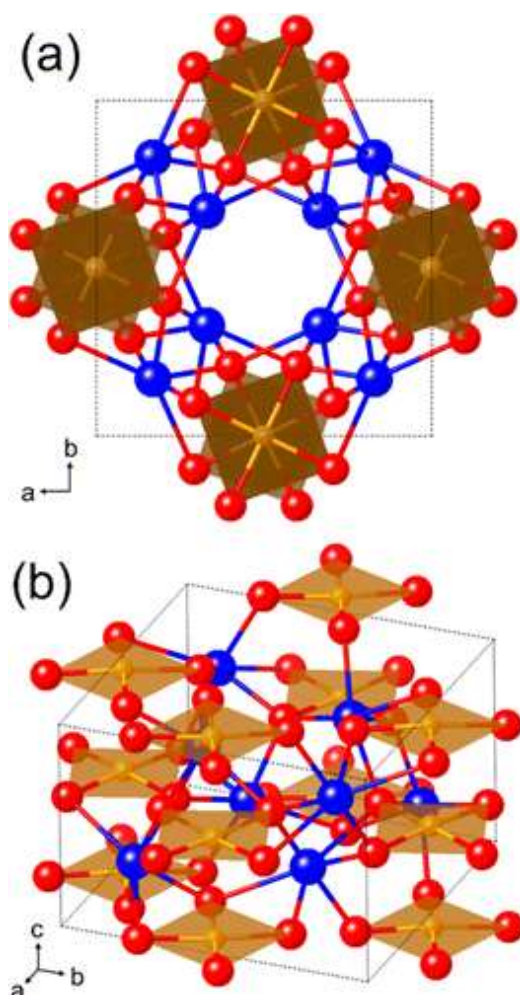


Figure 3.1. CuBi_2O_4 crystal structure as viewed (a) along the c -axis and (b) at an arbitrary angle. Blue, orange, and red spheres represent Bi, Cu, and O atoms, respectively. Figure adapted from ⁴².

CuBi_2O_4 has attracted attention as a promising photocathode material for solar water splitting due to its ideal features. First of all, it has a suitable bandgap of 1.8–1.5 eV so it can absorb a significant portion of the solar spectrum.¹⁰¹ Secondly, the conduction band of CuBi_2O_4 lies above the reduction potential of proton reduction, allowing for solar H_2 production. Moreover, its valence band is located at more positive potentials than that of other photocathode materials (e.g., Cu_2O , p-type Si, p-type GaP) and it shows an exceptionally positive onset potential near +1 V vs. RHE. This implies that the material is able to provide a relatively high internal photovoltage.⁴² Theoretically, CuBi_2O_4 can produce a maximum AM 1.5 photocurrent of 19.7–29.0 mA/cm^2 , assuming all photons with energies higher than the bandgap are absorbed and utilized with 100 % efficiency.¹⁰¹ However, thus far the reported photocurrent densities for CuBi_2O_4 have been well below this theoretical limit.^{102, 106-108} Moreover, fundamental research has been made difficult by the nanoporous surface structure¹⁰⁷⁻¹⁰⁸ and incomplete substrate coverage of the prepared CuBi_2O_4 films.¹⁰⁶ Therefore, new deposition techniques that produce dense, homogeneous CuBi_2O_4 thin films are needed for fundamental studies of the basic material properties so as to thoroughly quantify the factors that limit the photo-conversion efficiency. We report, for the first time, the synthesis of high quality, dense CuBi_2O_4 thin films by spray pyrolysis. To accomplish this, the spray pyrolysis precursor solution had to be modified and controlled with additives. We discuss the chemistry of the precursor solution in detail, which may be applicable to the development of spray pyrolysis recipes for other metal oxide thin films. In addition, the essential optical and photoelectrochemical (PEC) properties of the resulting synthesized CuBi_2O_4 thin films are reported.

Experimental

Material Synthesis

CuBi_2O_4 films were prepared by spray pyrolysis, as illustrated in the schematic (**Figure 3.2**). A CuBi_2O_4 precursor solution was prepared by dissolving $\text{Bi}(\text{NO}_3)_3 \cdot 5\text{H}_2\text{O}$ (98 %, Alfa Aesar) in acetic acid (≥ 99.8 %, Sigma Aldrich) and $\text{Cu}(\text{NO}_3)_2 \cdot 3\text{H}_2\text{O}$ (99 -104 %, Sigma - Aldrich) in absolute ethanol (≥ 99.8 %, Sigma Aldrich). The Bi solution was then added to the Cu solution, and the mixture was diluted to the desired concentration with additional ethanol. For the preparation of solutions with additives, certain amounts of TEOF and PEG (average $M_n = 300$) were added to ethanol before adding the precursors. The substrates were fluorine-doped tin oxide (FTO) coated glasses (7 Ω/sq , Nippon Sheet Glass Co. Ltd.). Prior to deposition, the FTO coated glasses were cleaned by three successive 15 min ultrasonic rinsing steps in 1 vol % Triton in water, acetone, ethanol and dried

under a stream of compressed nitrogen. The substrates were placed on the hot plate and heated to the preset temperature before the deposition was started. The spray nozzle (Quickmist Air Atomizing Spray) was driven by an overpressure of 0.6 bar of nitrogen gas and placed 20 cm above the heating plate. A pulsed deposition mode was used, with one spray cycle consisting of 5 s spray time followed by a delay of 55 s to allow solvent evaporation.

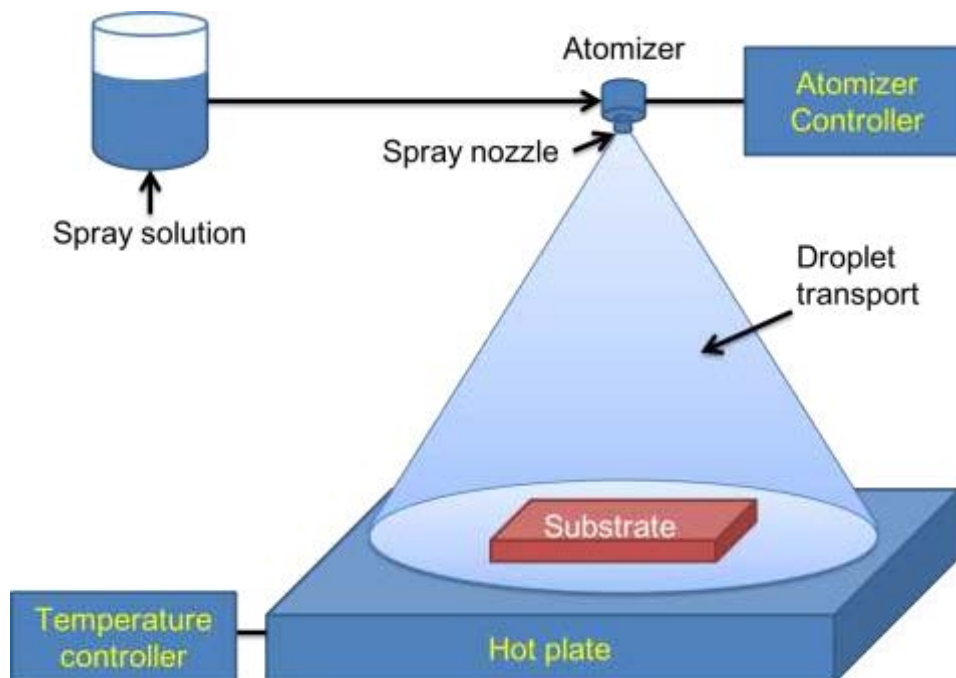


Figure 3.2. Illustration of the spray system.

Material Characterization

Glancing incidence X-ray diffraction (GIXRD) measurements were carried out to investigate the structure and the phase composition of the CuBi_2O_4 films deposited on FTO coated glasses. We used a Bruker AXS D8-Advance X-ray diffractometer with a Cu K_α radiation ($\lambda = 0.154$ nm). The angle of incidence was fixed at 0.3° . The detection angle 2θ was varied from 15° to 60° . The crystallite size was estimated from the calibrated Scherrer Equation as follows,

$$L = \frac{K * \lambda}{\cos \theta * \sqrt{k_{measured}^2 - k_{instrumental}^2}} \quad (3.1)$$

where L is the crystallite size, K is the shape factor constant taken as 0.89, λ is the wavelength of the Cu K_α radiation ($\lambda = 0.154$ nm). The measured broadening $k_{measured}$, and instrumental broadening, $k_{instrumental}$,

were calculated from the following relationship,

$$k_{\text{measured}} = \beta_{\text{measured}} \times \frac{\pi}{180^\circ} \quad (3.2)$$

$$k_{\text{instrumental}} = \beta_{\text{instrumental}} \times \frac{\pi}{180^\circ} \quad (3.3)$$

Here β_{measured} is the FWHM of the diffraction peaks extracted from the XRD pattern of CuBi_2O_4 . $\beta_{\text{instrumental}}$ is determined by measuring the LaB_6 reference material from which the instrumental broadening $k_{\text{instrumental}}$ is estimated to be 0.0031.

The morphology and the elemental composition of the films were analyzed using a LEO GEMINI 1530 field emission scanning electron microscope (FESEM), operated at an acceleration voltage of 5 kV. The surface structure was investigated by atomic force microscope (AFM, Park System, XE-100) operated in tapping mode using an etched Si tip with a tip radius of 10 nm with force constant of 40 N/m. All scans were performed on a scale of $3 \mu\text{m} \times 3 \mu\text{m}$ with the lateral resolved height information on a square array of 256×256 pixels.

The transmittance (T + R) and reflectance (R) spectra of the CuBi_2O_4 films were measured by a UV/Vis spectrometer (Perkin-Elmer Lambda 950) with an integrating sphere, as illustrated in **Figure 3.3**.

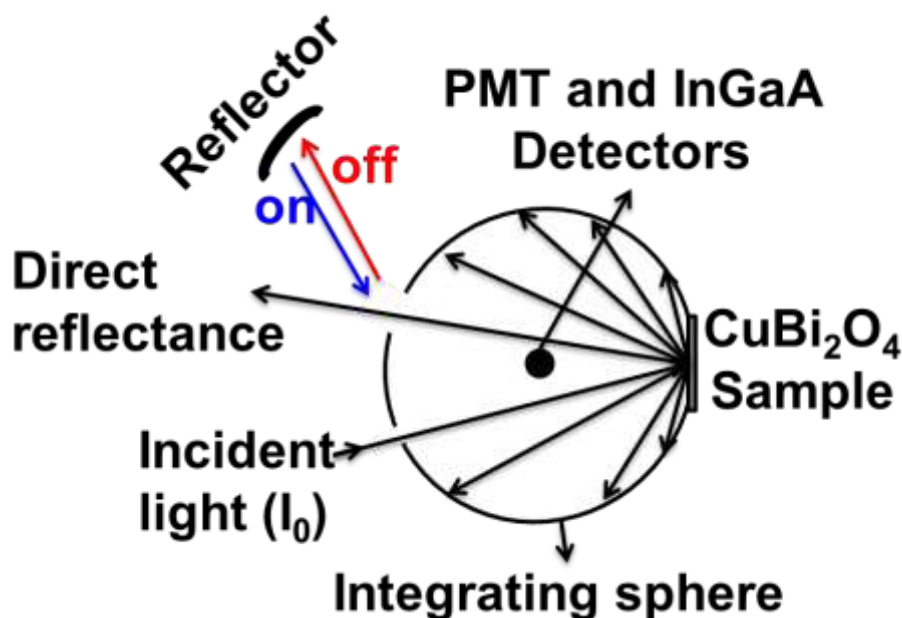


Figure 3.3. Illustration of the measurements of diffuse reflectance (R_{diffuse}) with the reflector off, and direct reflectance + diffuse ($R_{\text{direct+diffuse}}$) with the reflector on.

The diffuse reflectance (R_{diffuse}) was measured with the reflector off while the direct reflectance + diffuse reflectance ($R_{\text{direct+diffuse}}$) was measured with the reflector on. The direct reflectance (R_{direct}) was calculated with the following formula,

$$R_{\text{direct}} = R_{\text{direct+diffuse}} - R_{\text{diffuse}} \quad (3.4)$$

The absorption coefficient was calculated using the following formula,

$$\alpha = \frac{-\ln(\text{transflectance})}{d} \quad (3.5)$$

where d is the film thickness.

Precursor Solution Characterization

The solution chemistry and reaction mechanism were investigated using an IR spectrometer (EQUINOX 55, Bruker). A self-designed capturing technique combined with attenuated total reflection (ATR) was used to prevent the evaporation of the solvents during the measurements, as shown in **Figure 3.4**.

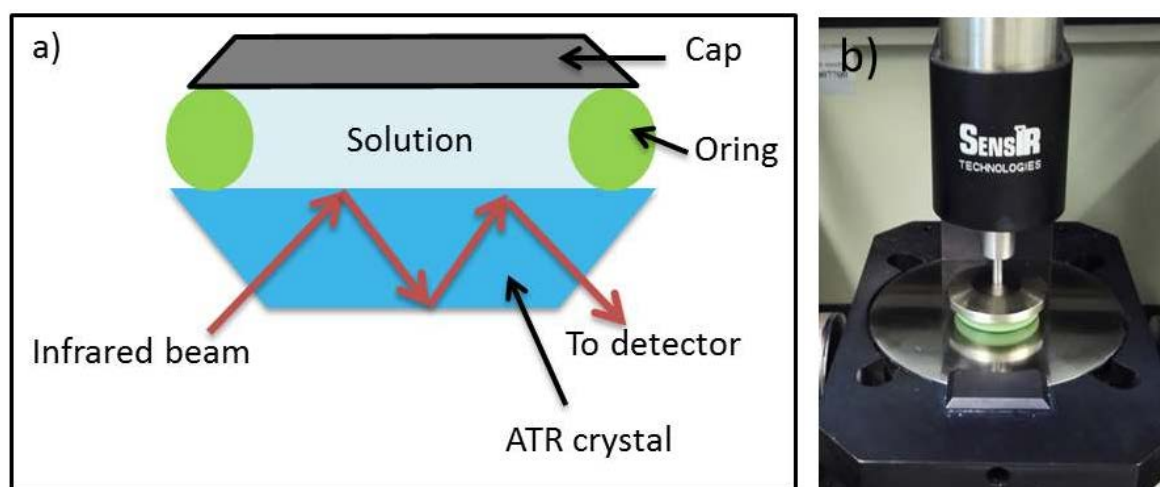


Figure 3.4. Illustration of the self-designed capturing technique combined with attenuated total reflection (ATR); (b) photo of the instrument.

A background measurement was taken before each measurement. For the stability test, each solution was measured every hour for up to 23 h. The measured transmission spectra were divided by the reference spectrum (measured at 0 h) to obtain the relative changes in the optical transmittance (ΔT) as a function of time and the wavenumber.

Electrochemical and Photoelectrochemical Measurements

The PEC measurements were performed using an EG & G Princeton Applied Research 273 A potentiostat in a three-electrode configuration with the CuBi_2O_4 films as the working electrode, an Ag/AgCl reference electrode (saturated KCl), and a platinum wire counter electrode in a quartz-windowed cell, as illustrated in **Figure 3.5**. A Voss Class AAA solar simulator (WXS-50S-5H) was used as an illumination source ($\text{AM } 1.5 = 100 \text{ mW/cm}^2$).

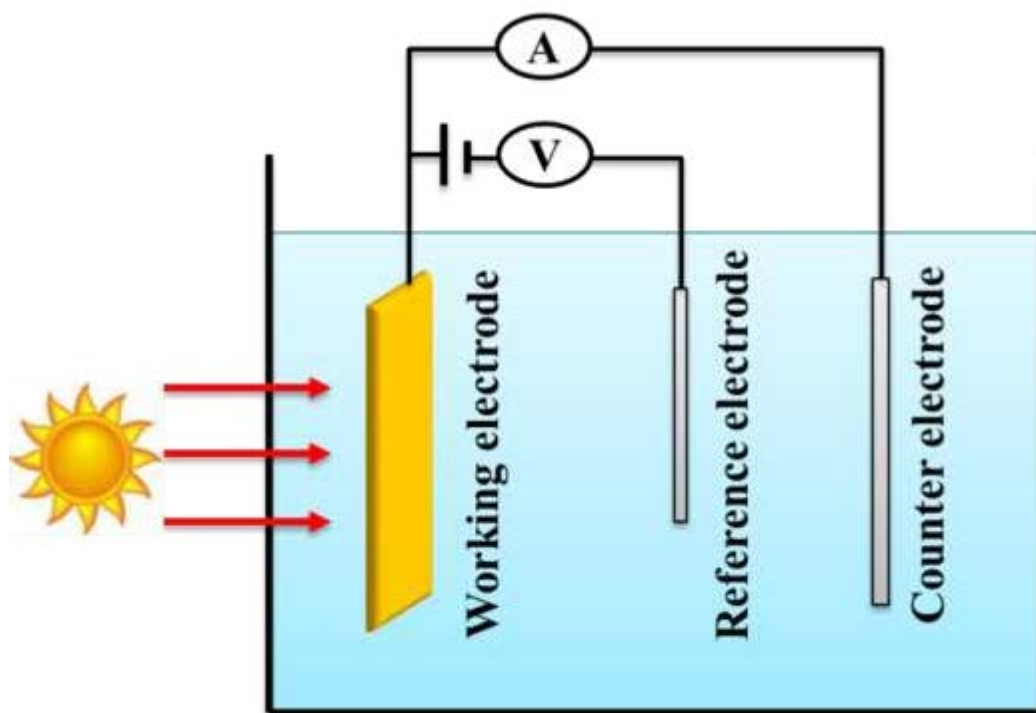


Figure 3.5. Schematic of the three-electrode configuration.

The electrolyte used for all measurements was 0.3 M K_2SO_4 and 0.2 M phosphate buffer (pH 6.65) with Ar bubbling or with H_2O_2 added as an electron scavenger. The pH value of each solution was checked with a pH meter (OAKTON). All potentials were converted to the reversible hydrogen electrode (RHE) scale using the Nernstian relation:

$$V_{RHE} = V_{Ag/AgCl} + 0.0591 \times pH + 0.197(V) \quad (3.6)$$

For incident photon-to-current efficiency (IPCE) and absorbed photon-to-current efficiency (APCE) measurements monochromatic photocurrents were measured with a 300 W quartz tungsten-halogen lamp coupled into a grating monochromator (Acton SpectraPro 150 i). An electronic shutter (Uniblitz LS6) was used, and a long-pass colored glass filter (Schott, 3 mm thick) was placed between the monochromator and the sample to remove second-order diffracted light. The shutter was actuated every 10 s, and the currents were determined

first waiting for 8 s, following by averaging the measured values for 2 s before the shutter was actuated again. A dark and light measurement was taken for each data point, with 1.5 nm wavelength steps between each point. IPCE and APCE were calculated from the following formulas:

$$IPCE \% = \frac{J_{pho}(\lambda)}{P(W)} \times \frac{1240}{\lambda(nm)} \times 100 \quad (3.7)$$

$$APCE \% = \frac{IPCE \%}{A} \quad (3.8)$$

where, J_{pho} is the average photocurrent, P is the power, λ is the wavelength, and A is the absorptance. The IPCE of the CuBi₂O₄ photocathodes were measured at 0.6 V vs. RHE with H₂O₂ added as an electron scavenger.

Figure 3.6 shows the power spectra measured by a spectrometer (Ocean Optics SO # 1218601).

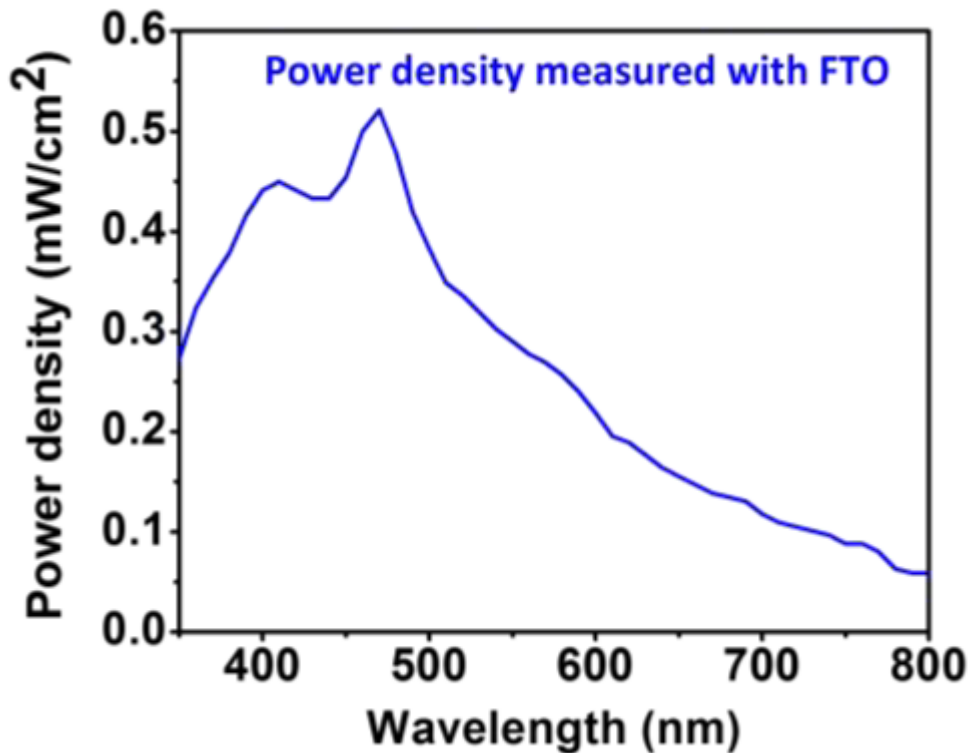


Figure 3.6. Power spectra for back illumination IPCE measurements measured with and without an FTO substrate.

Electrochemical impedance spectroscopy (EIS) and Mott–Schottky measurements were performed using a VersaSTAT 3 Potentiostat (AMETEK Co., Ltd.). Mott–Schottky plots were created based on the following formula,¹⁰⁹

$$\frac{1}{C^2} = \frac{2}{e \epsilon \epsilon_0 N_A} \left(-\varphi + \varphi_{fb} - \frac{kT}{e} \right) \quad (3.9)$$

where C is the capacitance, ϵ is the relative permittivity, ϵ_0 is the permittivity of free space, N_A is the acceptor density, φ_{fb} is the flat band potential. The AFM measurements described above, were used to estimate the real surface area from the geometric surface area of the working electrodes in the PEC cell (i.e., our CuBi_2O_4 photocathode).

Results and Discussion

Development of a Spray Pyrolysis Recipe for CuBi_2O_4

In the following section we explain how the chemistry of the precursor solution must be controlled in order to produce dense, homogenous CuBi_2O_4 thin films synthesized by spray pyrolysis. The precursor solution was always prepared by mixing $\text{Bi}(\text{NO}_3)_3 \cdot 5\text{H}_2\text{O}$ dissolved in acetic acid with $\text{Cu}(\text{NO}_3)_2 \cdot 3\text{H}_2\text{O}$ in ethanol with $\text{Bi}^{3+} : \text{Cu}^{2+}$ ratio of 2 : 1. This mixture resulted in two main challenges. First, the presence of water in the precursor solution caused rapid precipitation of Bi^{3+} resulting in non-homogenous spray onto substrates. Second, poor spreading behavior of the droplets over the substrates during spray resulted in agglomeration and powder formation and thus prohibited the growth of thicker dense films. These challenges were overcome by adding TEOF and PEG to the precursor solution as additives. To understand the solution chemistry we have performed detailed analysis of the precursor solutions and the resulting CuBi_2O_4 films under the following conditions: (1) without additives, (2) with TEOF, and (3) with TEOF and PEG. The changing chemical composition of the precursor solutions was analyzed using attenuated total reflection infrared (ATR-IR) spectroscopy and the CuBi_2O_4 films were thoroughly characterized using x-ray diffraction (XRD), UV-Vis spectroscopy, scanning electron microscopy (SEM), and atomic force microscopy (AFM).

Spray Pyrolysis of CuBi_2O_4 without Additives

We first tried to prepare the precursor solution by mixing $\text{Bi}(\text{NO}_3)_3 \cdot 5\text{H}_2\text{O}$ dissolved in acetic acid with $\text{Cu}(\text{NO}_3)_2 \cdot 3\text{H}_2\text{O}$ in ethanol without any additives. For this condition, precursor solution concentrations of 2, 10, and 20 mM (20 mM Cu^{2+} and 40 mM Bi^{3+}) were tested with an acetic acid to ethanol ratio of 1 : 9. Of these concentrations 20 mM produced the most homogenous CuBi_2O_4 thin films. See **Figure S A1** for SEM images comparing CuBi_2O_4 thin films (~50 nm) synthesized with these precursor solution concentrations without additives. The XRD pattern of the CuBi_2O_4 prepared without additives matches well with the reference pattern of kusachite (PDF# 00-042-0334), as shown in **Figure S A2a**.

As shown in **Figure 3.7a**, the very thin CuBi_2O_4 film (~50 nm) produced using a precursor solution

concentration of 20 mM without additives was fairly homogenous in the center of the FTO substrate. However, at the edges of the substrate the film surface was covered with large particulate agglomerations on the order of 1-3 μm in diameter as illustrated by **Figure 3.7b**. To the bare eye these particulate agglomerations looked like powder. Attempts to spray CuBi_2O_4 films thicker than 50 nm without additives were hampered by powder formation over the entire surface of the substrate accompanied by cracking and flaking of the top layer.

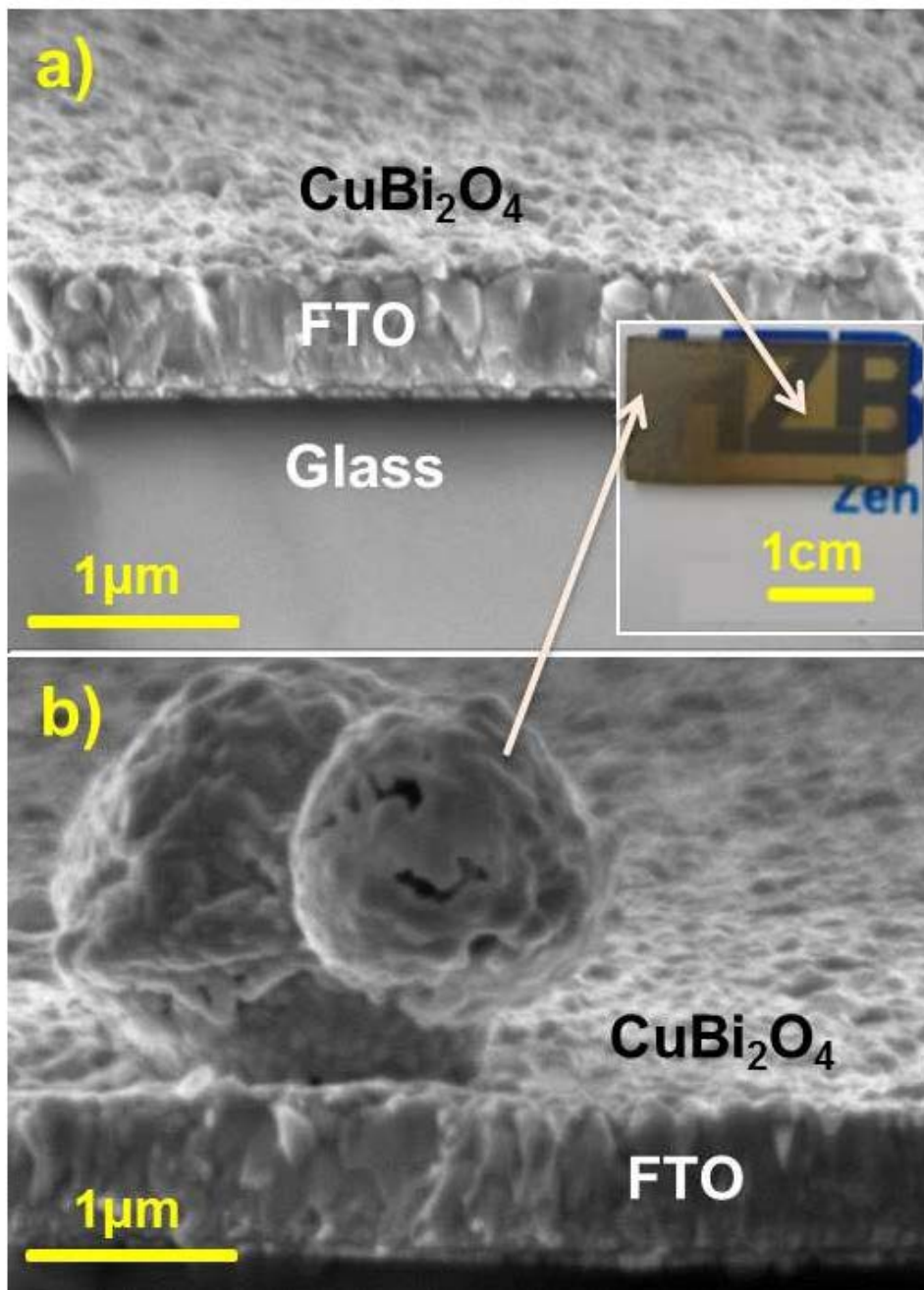


Figure 3.7. Photograph and cross section SEM images of a ~ 50 nm CuBi_2O_4 thin film synthesized on an FTO substrate by spraying 28 mL of 20 mM precursor solution without additives (a) in the center of the substrate and (b) at the edge of the substrate. The substrate temperature was 450 $^\circ\text{C}$.

The powder formation appears to be caused by rapid precipitation of the precursor solution. Freshly prepared precursor solution without additives was highly transparent but within 3.5 h it became cloudy with precipitate as shown in **Figure S A3**. To analyze the precipitate it was collected by filtration and dried in an oven at $75\text{ }^\circ\text{C}$ for 1 h, resulting in a white powder. Some of the white powder was annealed at $500\text{ }^\circ\text{C}$ for 2 h, which turned it to a yellowish color. To determine the chemical composition of the powders they were measured by XRD as shown in **Figure 3.8**.

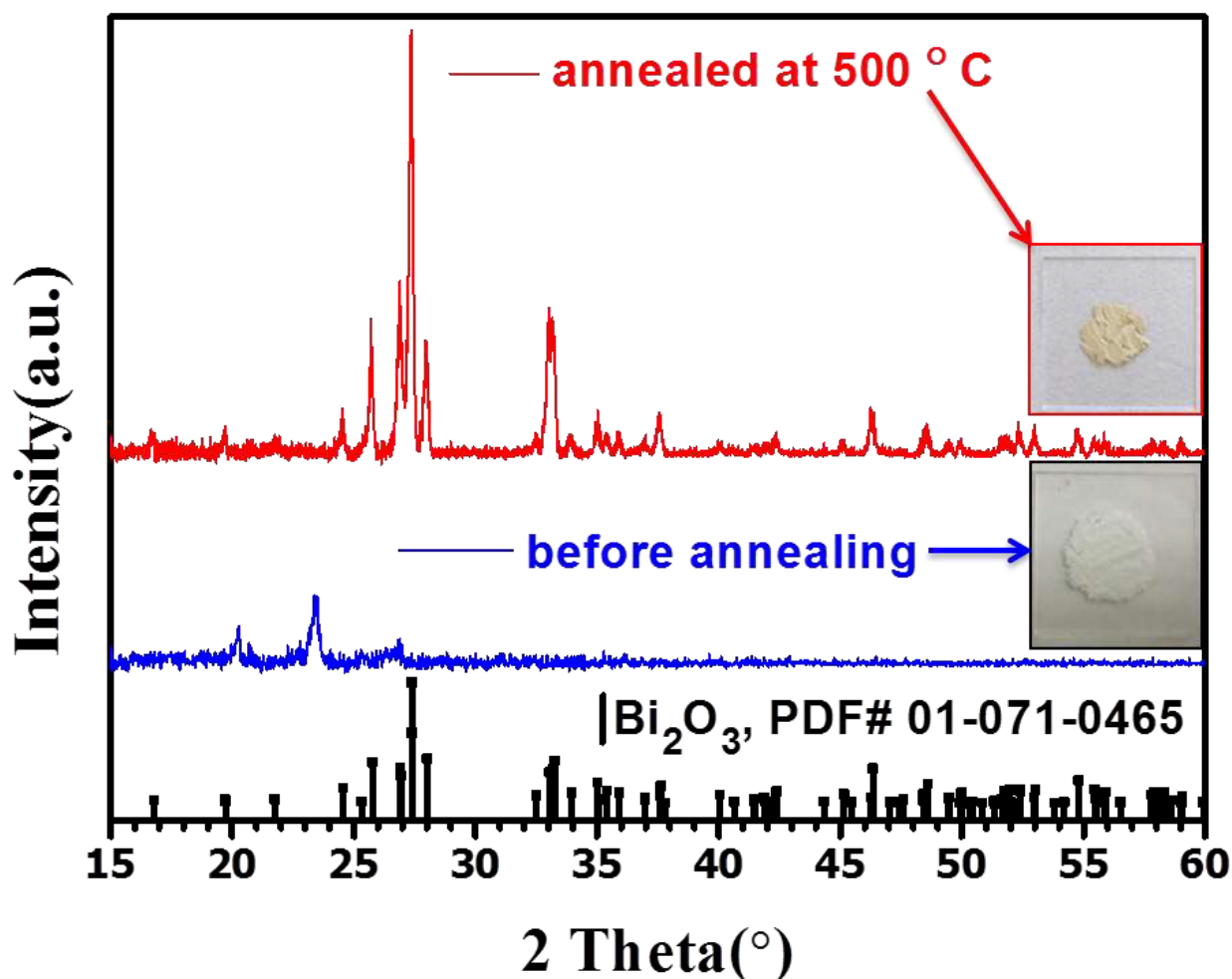
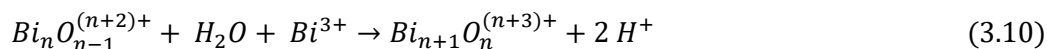


Figure 3.8. XRD diffractogram for the precipitate (a) filtered and dried, before annealing and (b) after annealing at $500\text{ }^\circ\text{C}$ for 2 h. Black vertical lines represent the reference patterns for Bi_2O_3 (PDF # 01-071-0465).

Before annealing the white precipitate was mostly amorphous as it produced a weak XRD signal that could hardly be matched to any reference pattern. The powder that was annealed to $500\text{ }^\circ\text{C}$ produced an XRD pattern that matched very well to the reference pattern for Bi_2O_3 (PDF # 01-071-0465). Since Bi^{3+} and Cu^{2+} were the only metallic cations in the precursor solution, we arrived at the conclusion that the precipitation is due to the

hydrolysis of Bi³⁺. It is well known that the Bi³⁺ can be easily hydrolyzed in the presence of water according to the following reaction,¹¹⁰



In addition acetic acid reacts with ethanol to form ethyl acetate and additional water according to the reaction below,



This can prolong the hydrolysis of Bi³⁺ after the initial water in the solution is used up by hydrolysis. A detailed in situ ATR-IR study was carried out on the precursor solution to investigate the chemical reactions that took place. First we measured the various solvents and additives individually (water, acetic acid, ethanol, TEO, PEG) along with the reaction product of ethanol and acetic acid (ethyl acetate) and the precipitate (hydrolyzed Bi³⁺). The ATR-IR spectra for these chemicals are included in **Figure S A4** and **Figure S A5**.

Since our goal was to observe the changes in the solution, we are interested in the vibration modes of the new products: ethyl acetate and precipitate. As confirmed by **Figure S A4**, a drop in transmittance at 1745 cm⁻¹ (C=O vibration) and 1240 cm⁻¹ (C-O vibration) indicates the presence of ethyl acetate.¹¹¹ The precipitate showed a strong IR band at 1301 cm⁻¹, as shown in **Figure S A5**. This can be assigned to the nitrate vibration of bismuth oxynitrate.¹¹² A decrease in transmittance around 1301 cm⁻¹ was therefore used as an indication of precursor instability.

Figure 3.9 shows the ATR-IR spectra for the precursor solution without additives over a period of 11 h. Without additives, the solution was relatively stable for the first 3 h. Then between 3 h and 4 h, there was an abrupt decrease in transmittance at 1301 cm⁻¹, suggesting that bismuth oxynitrate began to settle near the ATR-IR window.

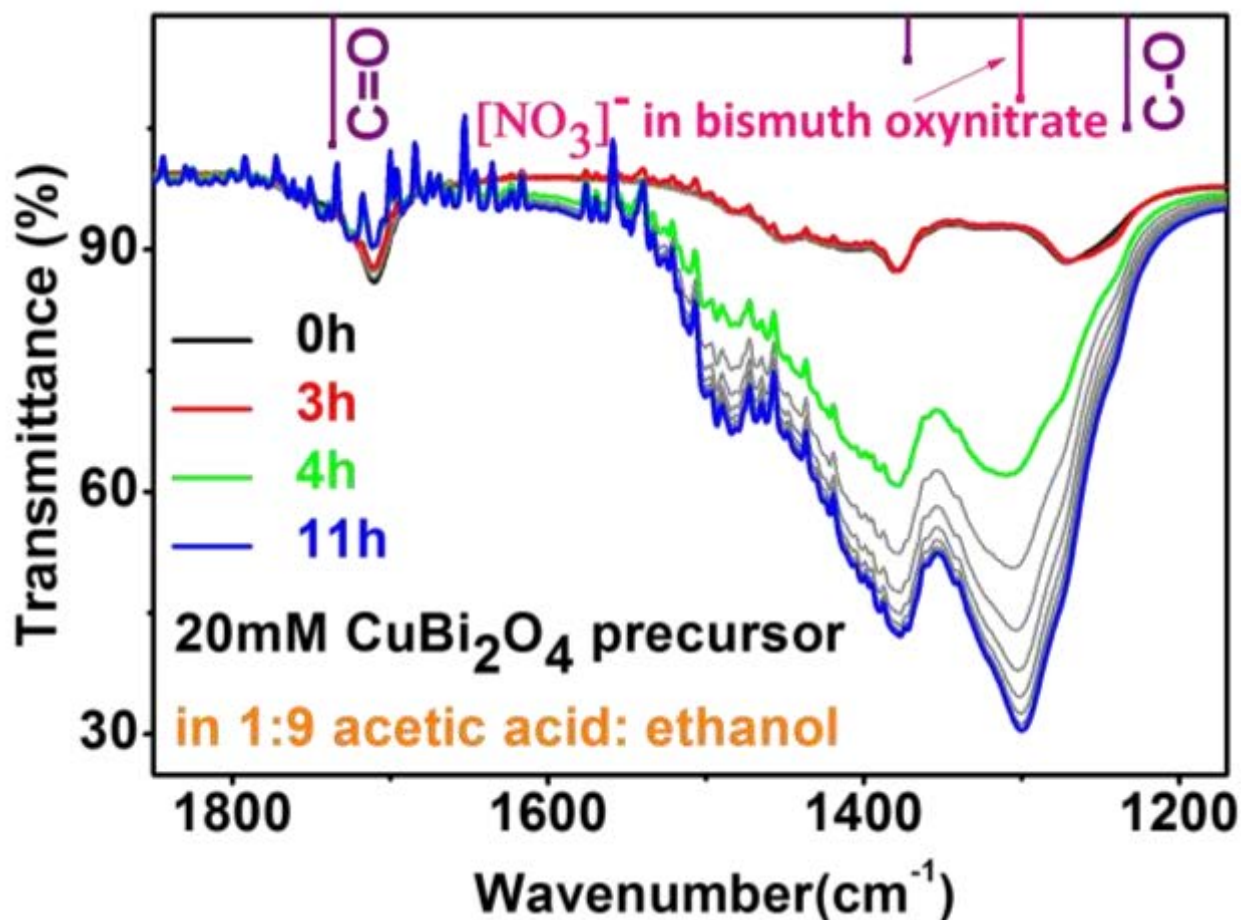


Figure 3.9. ATR-IR spectra of 20 mM CuBi_2O_4 precursor salts dissolved in 1 : 9 acetic acid : ethanol without additives. Purple (|) and pink (|) drop lines represent the peak locations from reference spectrums for ethyl acetate¹¹¹ and bismuth oxynitrate¹¹², respectively. Thin gray curves show the measurements carried out every 1 h between 4 h and 11 h.

The solution stability was probably significantly less than 3 h but during initial precipitation the particle size was likely too small to be detected.¹¹³ The intensity of Bi-O vibration at 1301 cm^{-1} can be very weak if the particle size is small, due to the long wavelength and short penetration depth of the IR light into the solution. In addition we did not observe an ethyl acetate signal at 1745 cm^{-1} (C=O) or 1240 cm^{-1} (C-O). This is because the esterification reaction between acetic acid and ethanol has very slow kinetics without catalyst.¹¹⁴ This was confirmed by a ATR-IR test of solution containing only 1 : 9 acetic acid : ethanol, as shown in **Figure 3.10**. No ethyl acetate peak appeared within 24 h.

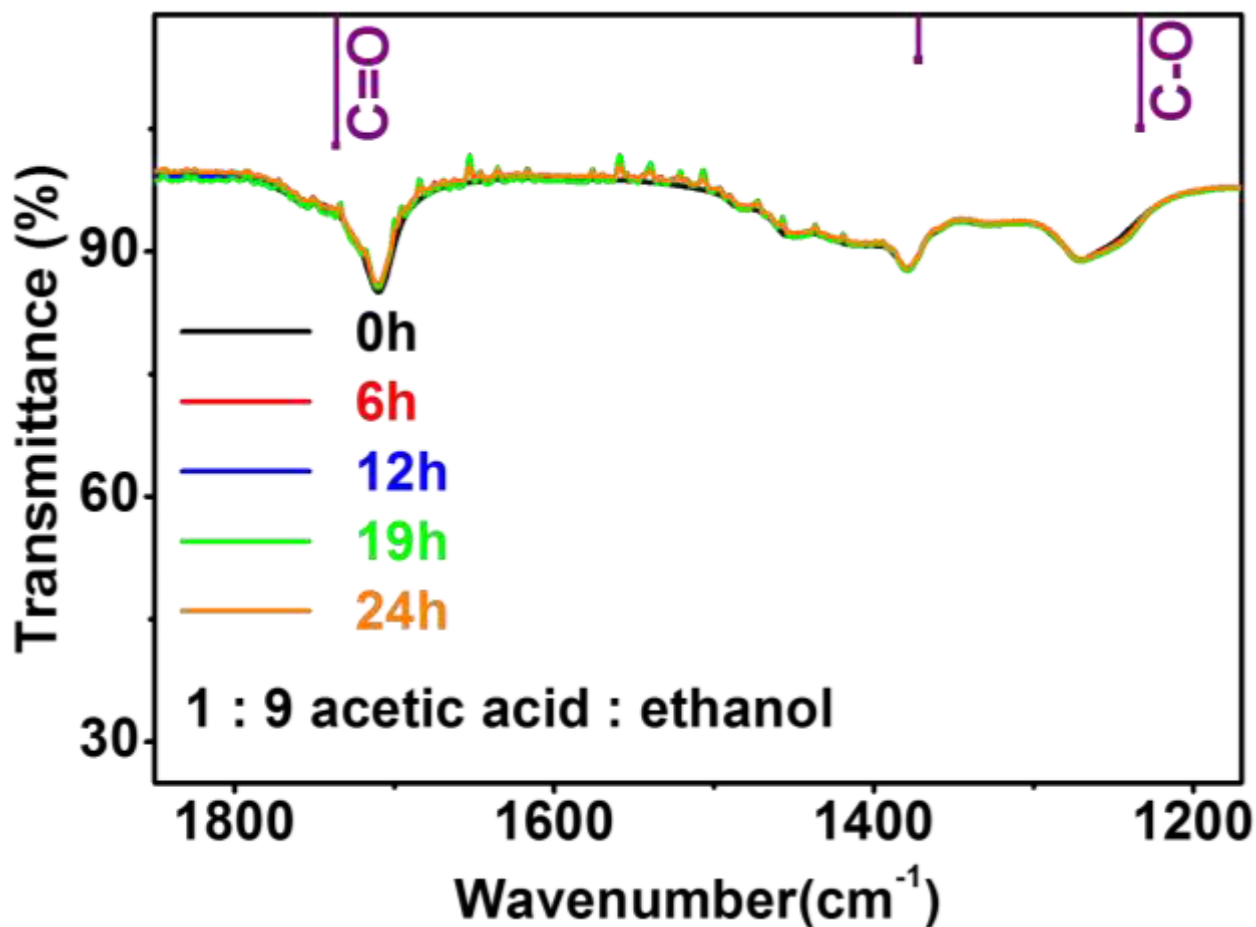
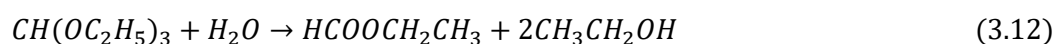


Figure 3.10. ATR-IR spectroscopies of 1 : 9 acetic acid : ethanol.

With XRD analysis of the precipitate and the detailed the ATR-IR analysis of the precursor solution without additives, we have confirmed that rapid precipitation of the solution is due to the hydrolysis of Bi^{3+} . One possible solution to slow down the hydrolysis of Bi^{3+} is to remove water from the solution. Note that it may not be possible to stop hydrolysis indefinitely due to the formation of water from the esterification reaction, although it will be slow without a catalyst. Therefore, we tried adding TEOF, a well-known efficient water scavenger,¹¹⁵ to precursor solution to remove the initial water and slow the hydrolysis of Bi^{3+} as described in the next section.

Spray Pyrolysis of CuBi_2O_4 with TEOF

Here we describe spray pyrolysis of precursor solution containing 20 mM $\text{Cu}(\text{NO}_3)_2 \cdot 3\text{H}_2\text{O}$ and 40 mM $\text{Bi}(\text{NO}_3)_3 \cdot 5\text{H}_2\text{O}$ in 1 : 9 acetic acid : ethanol with the addition of TEOF as a water scavenger. TEOF reacts with water according to the following reaction,



According to the stoichiometry of this reaction between TEOF and water, 4.9 % (by volume) TEOF is required to consume all the water from the initial bismuth and copper nitrate hydrate precursors, acetic acid, and ethanol. Therefore we compared CuBi_2O_4 thin films synthesized using precursor solutions containing 0, 1, 5, and 10 % (by volume) TEOF.

The surface morphologies of the resulting films were investigated using atomic force microscopy (AFM) and the results are shown in **Figure 3.11**. Among these CuBi_2O_4 thin films, the one sprayed with 5 % TEOF clearly shows the lowest Root Mean Squared (RMS) roughness at 34.8 nm. In other words, the smoothest film was obtained with 5 % TEOF added to the precursor solution.

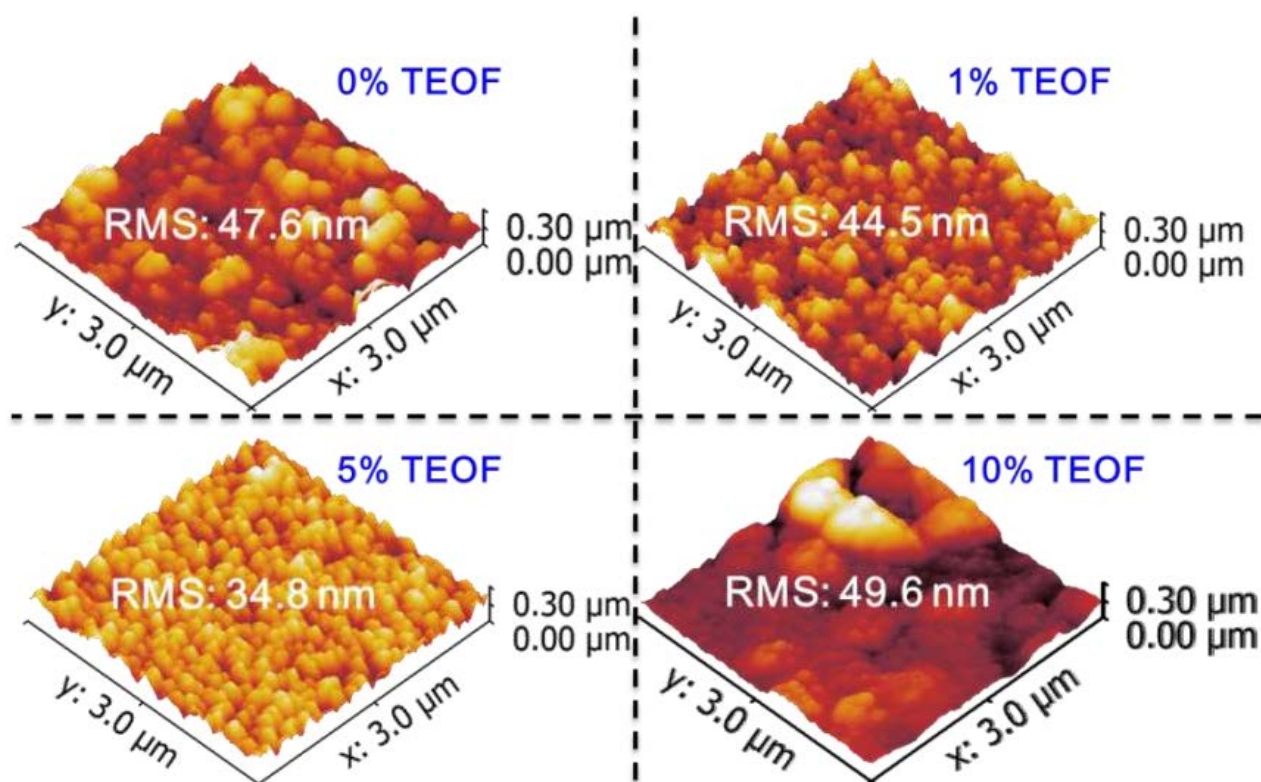


Figure 3.11. AFM images of ~ 50 nm CuBi_2O_4 thin films on FTO deposited using 20 mM precursor solution with 0, 1, 5 and 10 % TEOF.

Direct reflectance measurements were used to further compare the roughness of the films and the results are shown in **Figure 3.12**. The film with the lowest RMS roughness, 5 % TEOF, also shows the highest direct reflectance, which is further evidence that it has the most uniform surface.

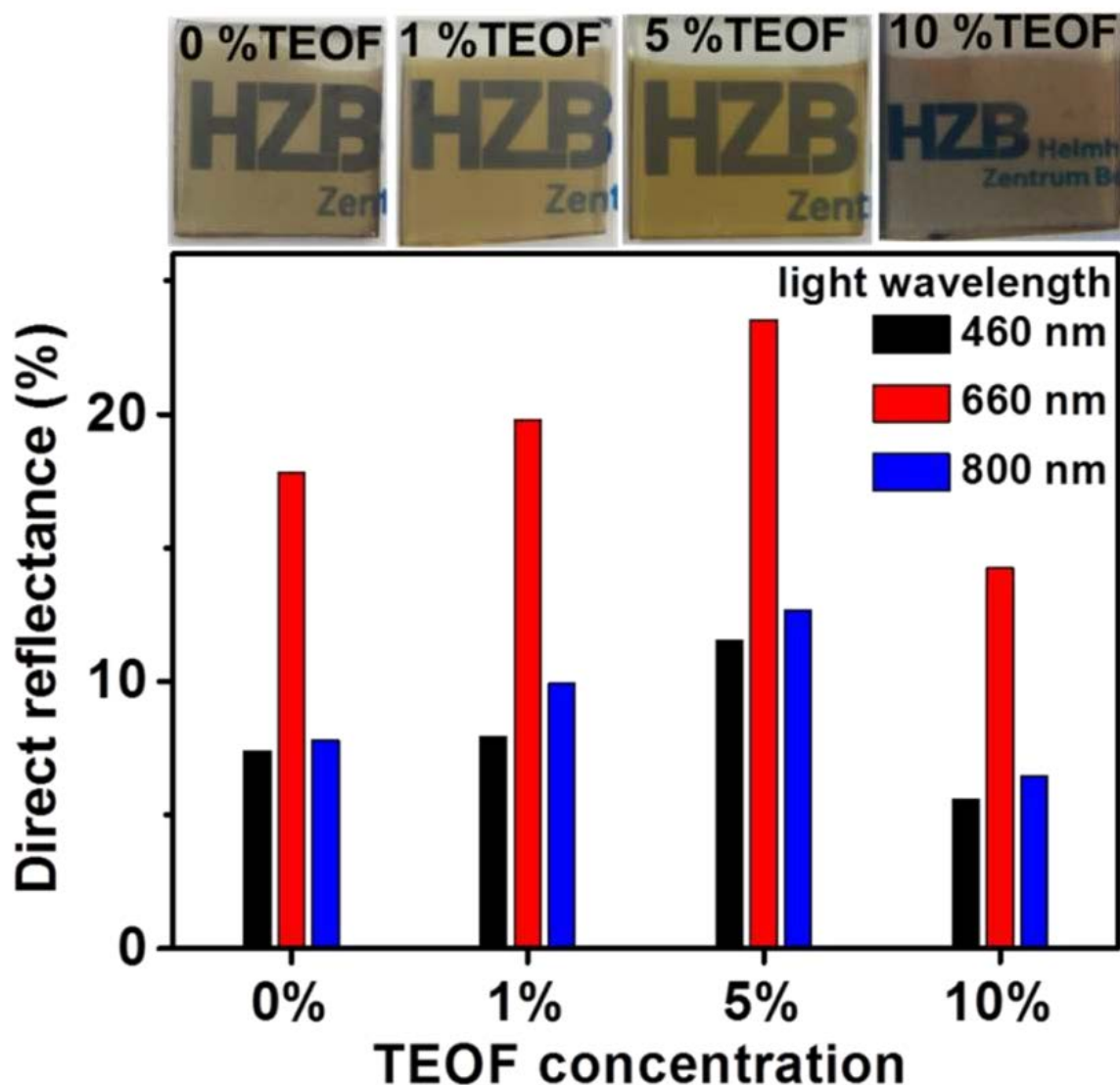


Figure 3.12. Direct reflectance of ~ 50 nm CuBi_2O_4 thin films on FTO deposited using 20 mM precursor solution with 0, 1, 5 and 10 % TEOF. Direct reflectance derived from Figure S A6, Figure S A7, and Figure S A8.

The experimental results demonstrating that the most uniform CuBi_2O_4 film results from the addition of 5 % TEOF matches surprisingly well with the prediction from stoichiometry that 4.9 % TEOF is required to remove all of the water. With less than 5 % TEOF, rapid hydrolysis of Bi would remain a problem since not all of the water would be removed. The addition of more 5 % results in excess TEOF with two possible side effects. First, TEOF has higher boiling point compared to ethanol, which might extinguish the pyrolysis process. Second, excess TEOF would continuously consume water and potentially shift the balance of the esterification reaction to the right. Acetic acid is required to keep the pH of the solution low to ensure that Bi^{3+} remains dissolved. The shift in balance of the esterification reaction with the addition of TEOF is described later in this section.

Another critical parameter in spray pyrolysis is the deposition temperature. It is suggested that only one kind of chemical vapor deposition at certain deposition temperature gives high quality films by spray pyrolysis.¹¹⁶ At low temperature, the droplets simply splash onto the substrate and usually form rough or non-adherent films. At high temperature, the solvents in the droplets evaporate completely before they could reach the hot surface and only solid particles are left. The solid particles directly land on the substrate surface, which usually causes powder formation. The effect of deposition temperature is illustrated in **Figure 3.13**.

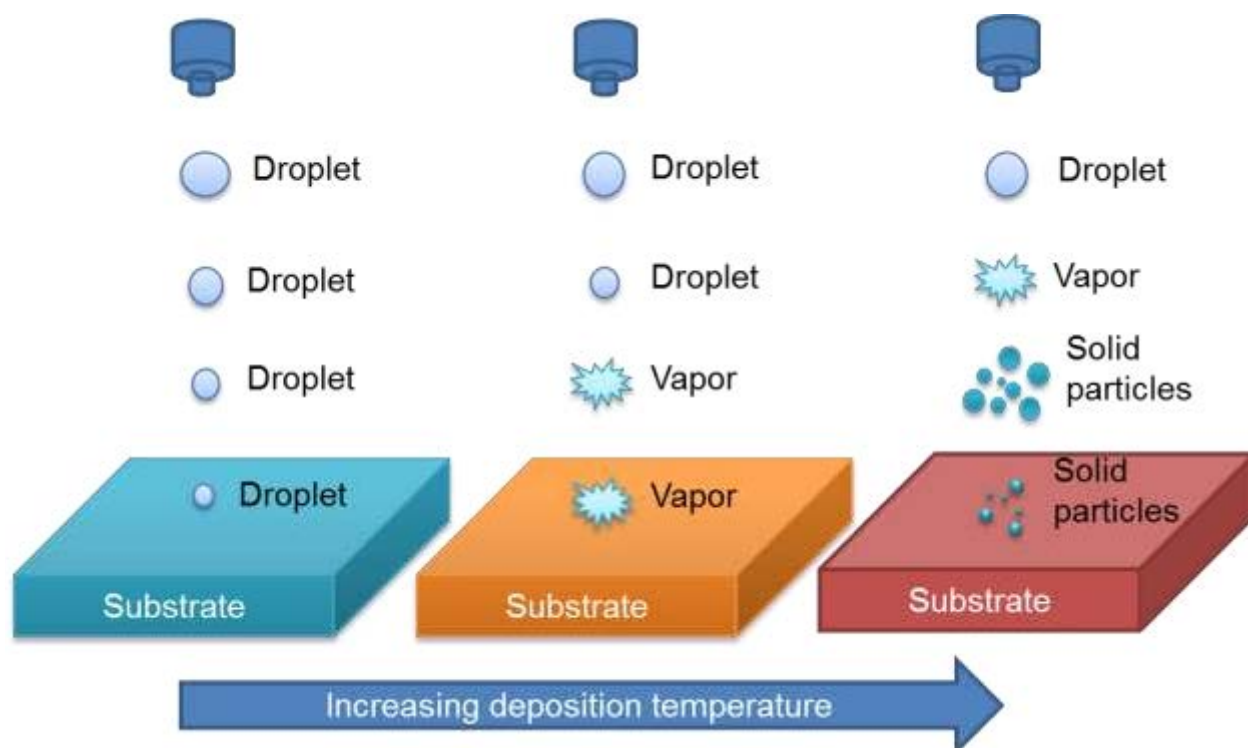


Figure 3.13. Illustration of the effect of deposition temperature on the film formation during the spray pyrolysis.

To determine the optimal substrate temperature for our spray pyrolysis process we performed spray pyrolysis of CuBi_2O_4 from precursor solutions containing 5 % TEOF at 350, 400, 450, and 500 °C. Photographs of the CuBi_2O_4 thin films sprayed at these temperatures are shown in **Figure 3.14**. In our experiments, homogeneous films were obtained only at deposition temperatures of 450 °C and above. XRD confirms that 450 °C is adequate to fully crystallize CuBi_2O_4 as the diffraction pattern of the film synthesized at 450 °C matches very well with the CuBi_2O_4 (kusachitte) reference pattern (see **Figure S A2**). Below 450 °C, powder formation was observed and the films showed poor adhesion to the substrate. At 500 °C, the glass in the FTO substrate melted and deformed slightly.

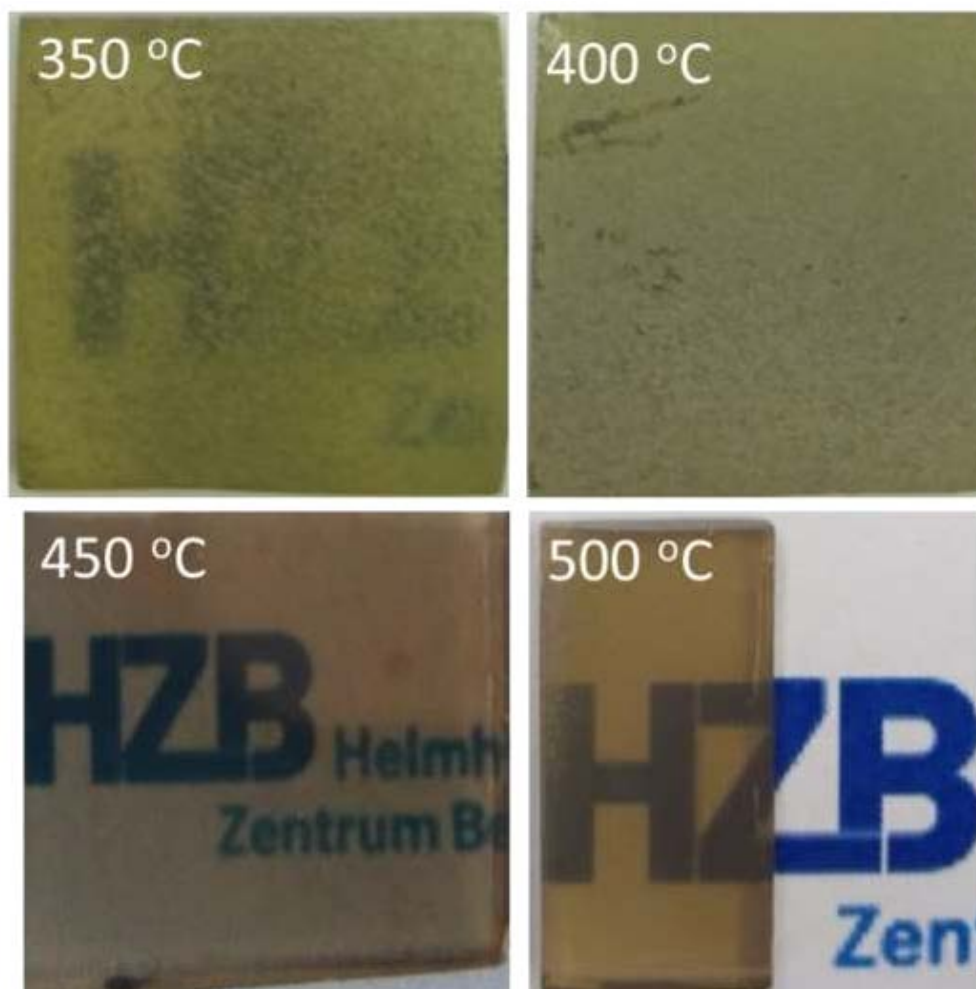


Figure 3.14. Photographs of the CuBi_2O_4 thin films deposited on FTO substrates at different temperatures using 20 mM precursor solution with 5 % TEOF.

Figure 3.15 shows the morphologies of the films with different thickness sprayed with 5 % TEOF and a substrate temperature of 450 °C. The addition of 5 % TEOF allowed the deposition of 50 nm CuBi_2O_4 thin films that were homogenous and dense over the entire substrate as shown in **Figure 3.15a**. However, when the thickness was 70 nm and higher agglomeration of particles and powder formation occurred once again on the edge of the substrates, as shown in **Figure 3.15c**. So even with the addition of TEOF to stabilize the solution (slow the hydrolysis of Bi^{3+}) there remained a hindrance to producing uniform films over 70 nm.

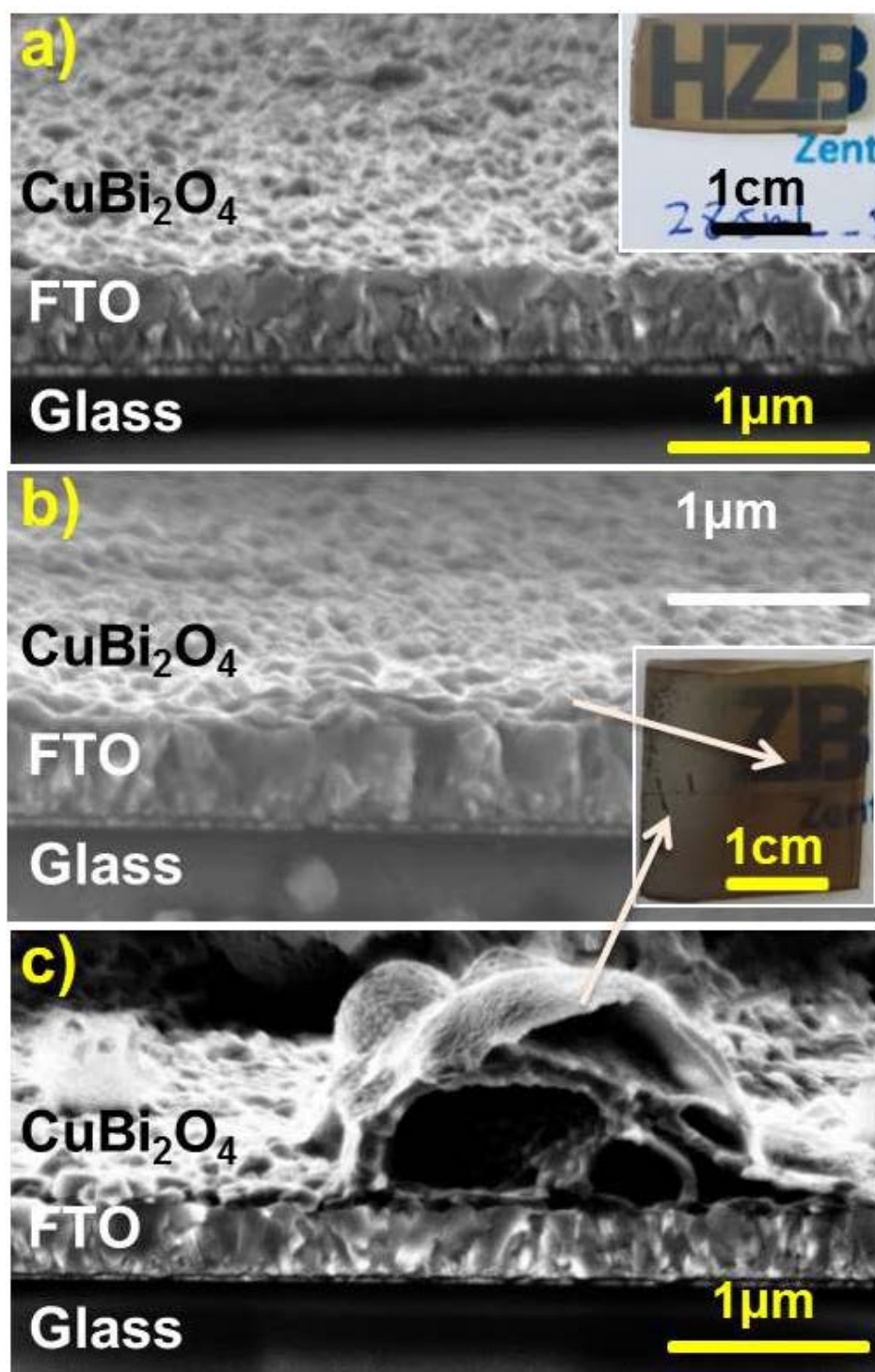


Figure 3.15. Photographs and cross section SEM images of CuBi_2O_4 films synthesized on FTO by spraying 20 mM precursor solution with 5 % TEOF (a) ~50 nm thick homogeneous film, (b) ~70 nm thick film in the center of the substrate, and (c) ~70 nm thick film at the edge of the substrate. The 50 and 70 nm films were produced by spraying 28 and 40 mL of precursor solution, respectively. The substrate temperature of 450 °C was chosen because it resulted in the most homogeneous CuBi_2O_4 thin films without deforming the FTO substrate.

Figure 3.16 shows the ATR-IR spectra for the 20 mM precursor solution with 5 % TEOF over a period of 23 h. Adding 5 % TEOF significantly improved the stability of the solution. The solution was relatively stable within the first 9 h followed by an abrupt decrease in transmittance at 1301 cm^{-1} between 9 h and 10 h, suggesting that the bismuth oxynitrate began to settle near the ATR-IR window. The stable duration of the 20 mM CuBi_2O_4 precursor solution was significantly increased from 3 h to 9 h after adding 5 % TEOF. This is because 5 % TEOF consumed all the water from the initial bismuth and copper nitrate hydrate precursors and solvents and therefore prevented the rapid hydrolysis of Bi^{3+} .

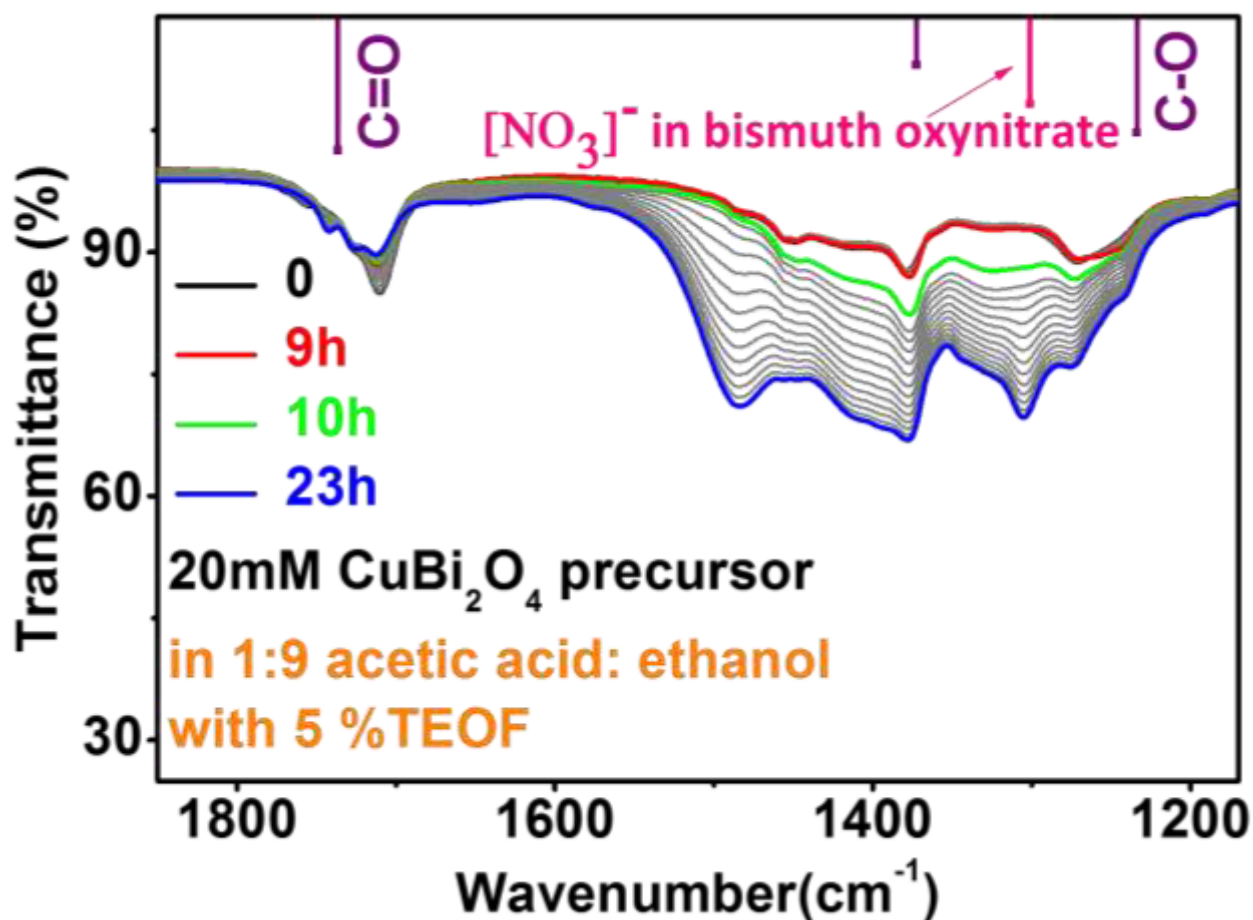
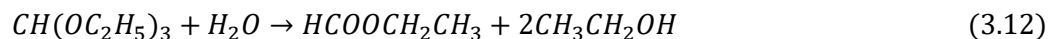


Figure 3.16. ATR-IR spectra of 20 mM CuBi_2O_4 precursor salts dissolved in 1 : 9 acetic acid : ethanol with 5 % TEOF. Purple (|) and pink (|) drop lines represent the reference spectrums for ethyl acetate and bismuth oxynitrate, respectively. Thin gray curves show the measurements carried out every 1 h between 10 h and 23 h.

Another observation is that the esterification reaction was actually accelerated with TEOF. The appearance of the peak at 1745 cm^{-1} (C=O vibration) and the emergence of the small shoulder at 1240 cm^{-1} (C-O vibration) indicate the formation of ethyl acetate from the esterification reaction. This is because the equilibrium of the

esterification reaction was shifted to the right by removing water via:



Spray Pyrolysis of CuBi₂O₄ with TEOF and PEG

Since the addition of 5 % TEOF dramatically increased the stability of the 20 mM precursor solution (from approximately 3 h to 9 h), the formation of powder on the edge of the substrates was no longer fully attributed to precipitate in the precursor solution. Other factors were causing agglomeration of particles on the surface of the CuBi₂O₄ film. We tentatively attribute it to poor spreading behavior of the droplets across the surface of the thicker CuBi₂O₄ films. Powder formation has been observed during the spray pyrolysis of other materials and one solution to address this issue was the addition of PEG.¹¹⁷⁻¹¹⁸ Therefore, we also tried adding PEG in addition to TEOF to improve the spreading behavior of the droplets and prevent powder formation.

Figure 3.17 shows the morphologies of the films sprayed using 20 mM precursor solution with 5 % TEOF and 1 % PEG (by volume) at thickness of 50, 70, and 270 nm. All three films showed high homogeneity across the entire substrate. Clearly, the addition of 1 % PEG allows the deposition of dense, homogenous for a wide range of thickness. With 5 % TEOF and 1 % PEG, homogeneous CuBi₂O₄ thin films with thicknesses over 420 nm were also synthesized without powder formation, as shown in **Figure S A9**. XRD shows tetragonal structure for the ~270 nm CuBi₂O₄ sprayed using 20 mM precursor solution with 5 % TEOF and 1 % PEG on FTO at 450 °C, and the crystallite size was estimated to be ~37 nm (see **Figure S A2b**). The presence of PEG in the precursor solution significantly improved the spreading behavior of the droplets on the substrate surface and powder formation was completely prevented. This has been explained by the binding properties of polymers. PEG can entwine throughout the spray-out drops and lead to formation of a dense network of PEG chains, which can help forming dense and compact film¹¹⁷⁻¹¹⁸. Adding small percentages of ethylene glycol or PEG to ethanol has been reported to increase the solution density, viscosity, and boiling point, while decreasing the surface tension.¹¹⁹⁻¹²⁰ This may allow the sprayed droplets to spread more uniformly across the surface of the CuBi₂O₄ films during the pyrolysis process.

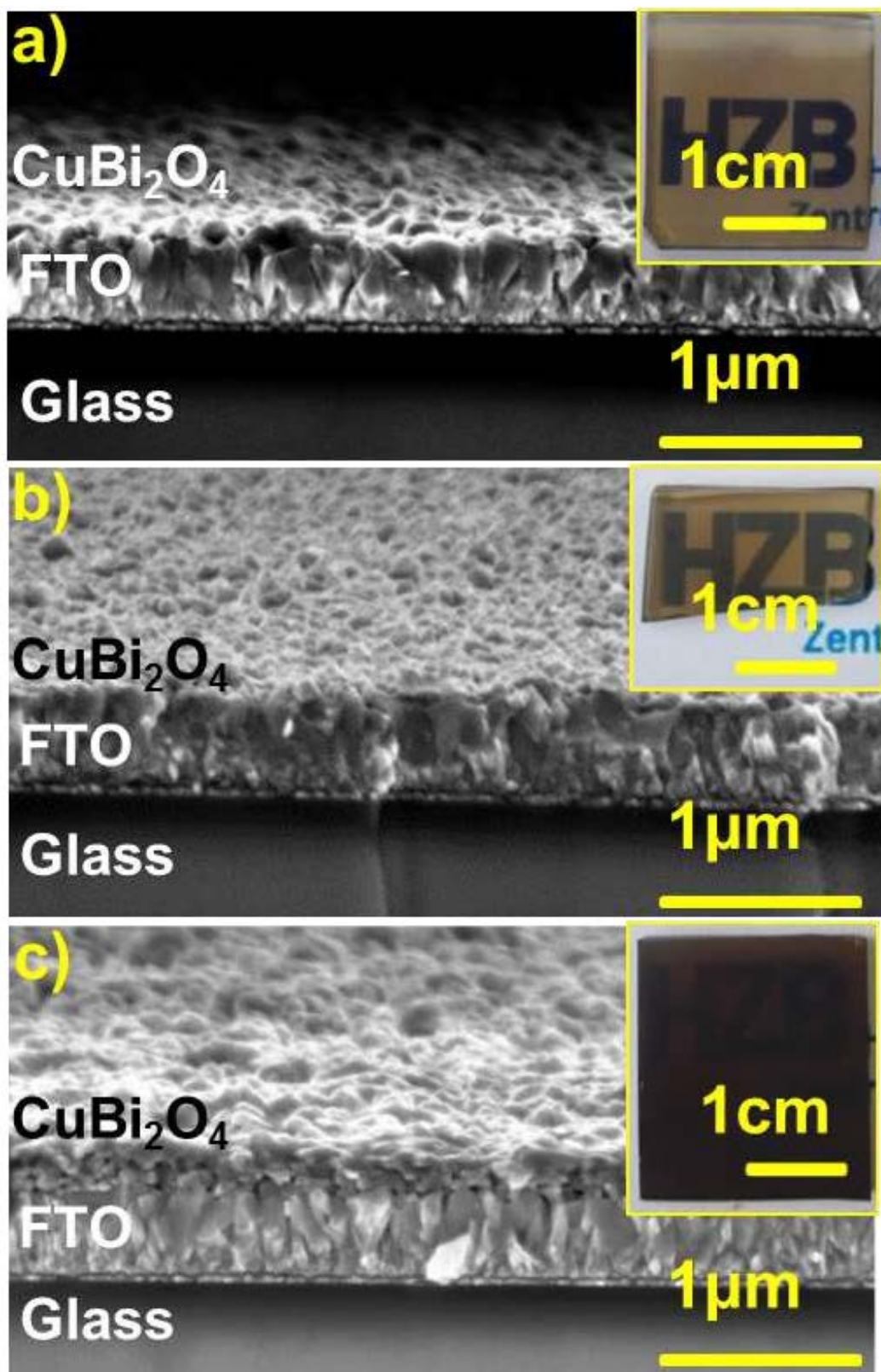


Figure 3.17. Photographs and cross section SEM images of CuBi_2O_4 films on FTO deposited at 450°C using 20 mM precursor solution with 5 % TEOF and 1 % PEG. (a) ~ 50 nm, (b) ~ 70 nm, and (c) ~ 270 nm homogeneous films. The films were produced by spraying 100, 130, and 400 mL of precursor solution, respectively.

Figure 3.18 shows the ATR-IR spectra for the 20mM precursor solution with 5 % TEOF and 1 % PEG over a period of 23 h. With 5 % TEOF and 1 % PEG, the precursor solution was relative stable for 12 h. Then an abrupt decrease in transmittance at 1301 cm^{-1} was observed between 12 h and 13 h, indicating the beginning of rapid precipitation of bismuth oxynitrate.

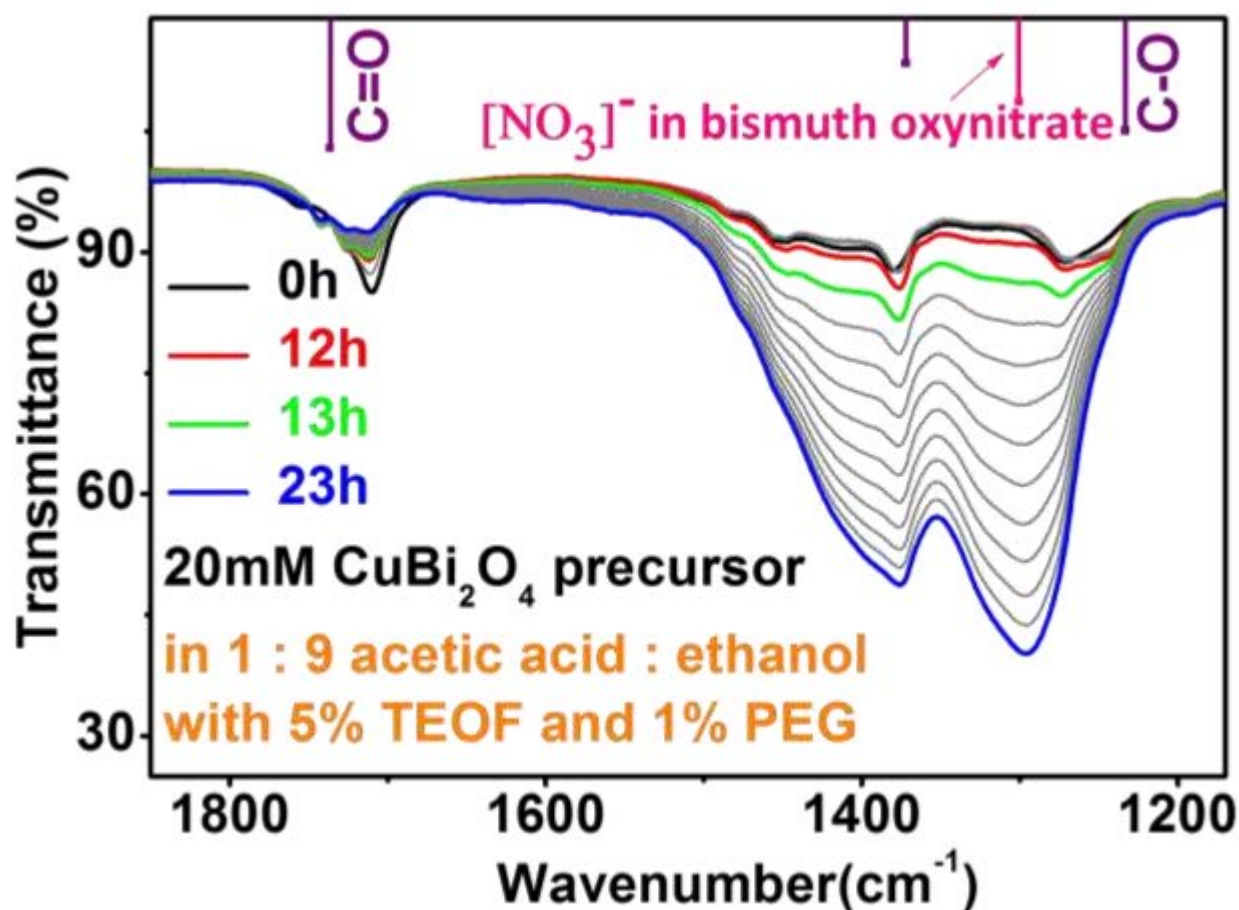


Figure 3.18. ATR-IR spectra of 20 mM CuBi_2O_4 precursor salts dissolved in 1 : 9 acetic acid : ethanol with 5 % TEOF and 1 % PEG. Purple (|) and pink (|) drop lines represent the reference spectrums for ethyl acetate and bismuth oxynitrate, respectively. Thin gray curves show the measurements carried out every 1 h between 13 h and 23 h.

Summary of the Optimized Recipe

Figure 3.19 summarizes the relative change in transmittance (ΔT) for the 20 mM CuBi_2O_4 precursor in 1 : 9 acetic acid : ethanol (a) without additives; (b) with 5 % TEOF; (c) with 5 % TEOF and 1 % PEG. It clearly shows how the additives help improving the stability of the precursor solution.

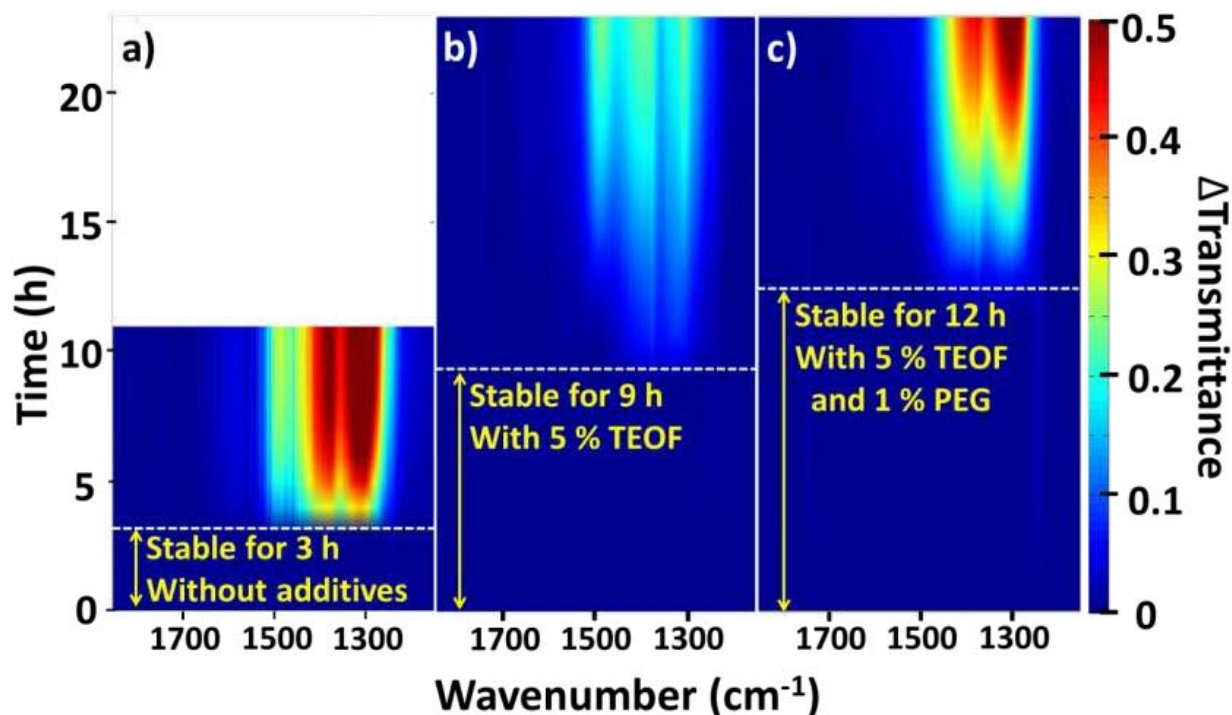


Figure 3.19. Relative change in transmittance (ΔT) for the 20 mM CuBi_2O_4 precursor in 1 : 9 acetic acid : ethanol (a) without additives; (b) with 5 % TEOF; (c) with 5 % TEOF and 1 % PEG. Transmittance was extracted from **Figure 3.9**, **Figure 3.16**, **Figure 3.18** and divided by the reference spectrum (measured at 0 h) to obtain the relative changes in the optical transmittance (ΔT) as a function of time and the wavenumber.

Now the dense and homogenous CuBi_2O_4 thin films can be deposited and the parameters of the optimized recipe are summarized in **Table 3.1**.

Table 3.1. Summary of the optimized spray pyrolysis recipe parameters.

Parameter	Detail
Precursor salts	20 mM $\text{Cu}(\text{NO}_3)_2 \cdot 3\text{H}_2\text{O}$ 40 mM $\text{Bi}(\text{NO}_3)_3 \cdot 5\text{H}_2\text{O}$
Solvent	1 : 9 acetic acid : ethanol
Substrate temperature	450 °C
Additives	5 % TEOF and 1 % PEG (vol %)
Carrier gas pressure (N_2)	0.6 bar
Distance between nozzle and substrate	20 cm
Spray cycle	5 s spray + 55 s delay

In the next section, we use the optimized spray recipe to deposit a series of films for the investigation of the optical and PEC properties of CuBi_2O_4 .

PEC Performance and Optical Properties

Optical Absorption Properties

The absorbance of the CuBi₂O₄ thin films was determined by performing UV-Vis measurements. **Figure 3.20a** shows the absorbance of CuBi₂O₄ photocathodes synthesized at several different thicknesses (111, 270, and 421 nm) on quartz substrates. The 270 and 421 nm CuBi₂O₄ films each show a slight onset in absorbance at around 825 nm, which corresponds to an absorption onset of ~1.51 eV. **Figure 3.20b** shows the absorption coefficient (α) calculated from the absorbance and the film thicknesses estimated from cross-section SEM images. The close overlapping of the spectra for different film thicknesses suggests that the calculated absorption coefficient, an intrinsic property of the material itself, is indeed accurate. The high quality CuBi₂O₄ film exhibits an average absorption coefficient of $3.57 \times 10^4 \text{ cm}^{-1}$ for 550 nm light, which leads to a penetration depth of $\alpha^{-1} = 280 \text{ nm}$. This value is very close to the previously reported value for nanoporous CuBi₂O₄ photoelectrodes in which α was calculated from the absorbance and the effective thickness (the theoretical thickness of a dense film).¹⁰⁸ This is a strong indication that the CuBi₂O₄ films synthesized by spray pyrolysis are extremely dense and compact.

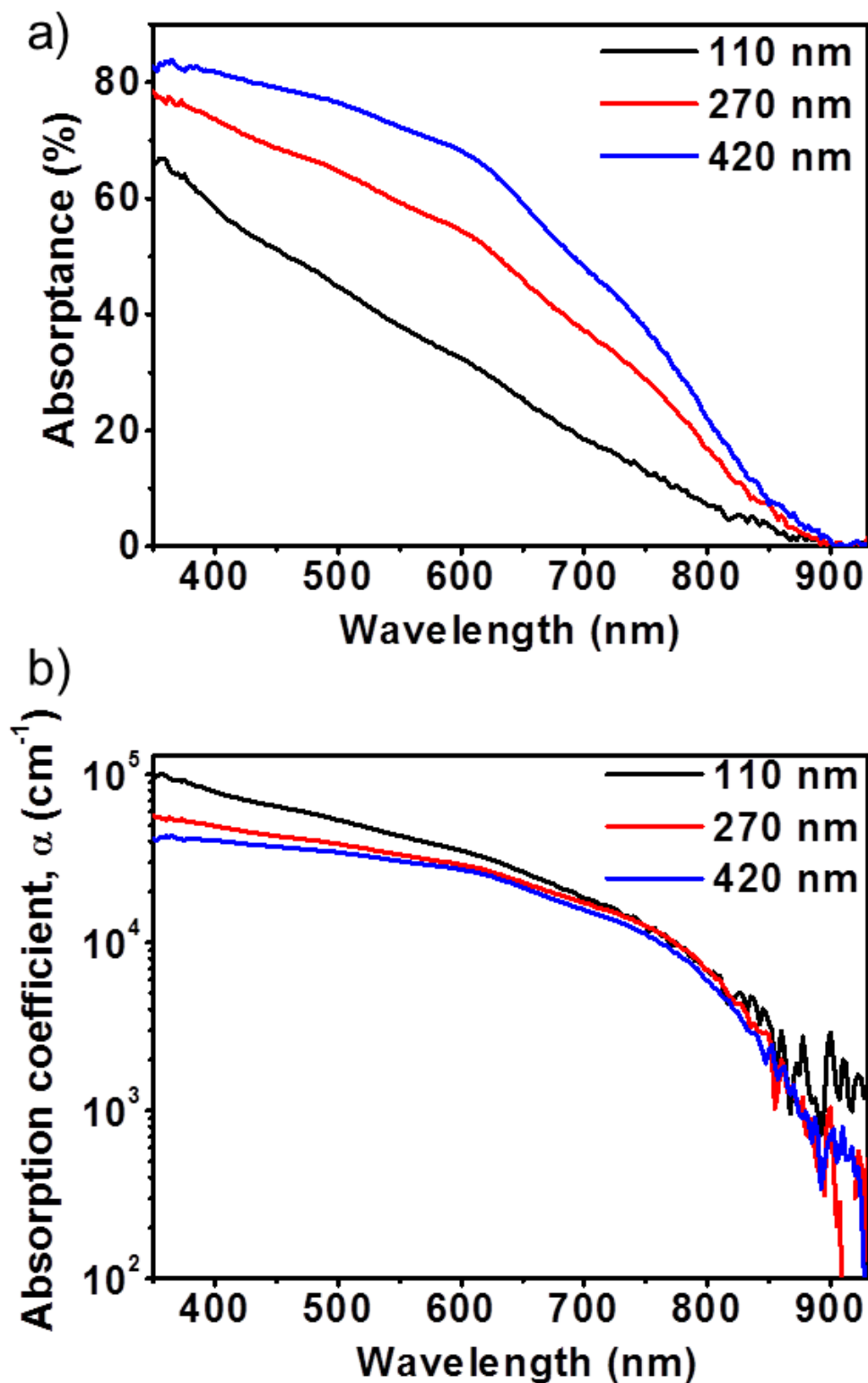


Figure 3.20. (a) Absorbance spectra for CuBi_2O_4 films deposited on quartz substrates with various spray volumes resulting in thicknesses of 111, 270, and 421 nm (b) Absorption coefficient for CuBi_2O_4 films with different thicknesses. Both plots were derived from transmittance measurements. Film thicknesses were estimated from cross section SEM images (see Figure S A9).

We derived Tauc plots, as shown in **Figure 3.21**, in an attempt to extract the bandgap. However neither the direct nor indirect Tauc plot shows a steep, linear section that would allow for accurate identification of a bandgap value. Similar difficulty in deriving the bandgap by applying Tauc plots has been demonstrated for other metal oxide semiconductors.¹²¹⁻¹²² Nevertheless, the direct bandgap Tauc plot approaches $(\alpha h\nu)^2 = 0$ near $h\nu \approx 1.50$ eV and the indirect Tauc plot shows an inflection in $(\alpha h\nu)^{1/2}$ around $h\nu \approx 1.41$ eV. Therefore, the bandgap of CuBi_2O_4 by spray pyrolysis is determined to be in the range of 1.41-1.50 eV, which is at the low end of previously reported values (1.5-1.8 eV).^{42, 102, 123-125} Such early absorption onset may correspond to the defects in the structure,¹²⁶ surface states,¹²⁷ and/or tailing of the valence band states.¹²⁸

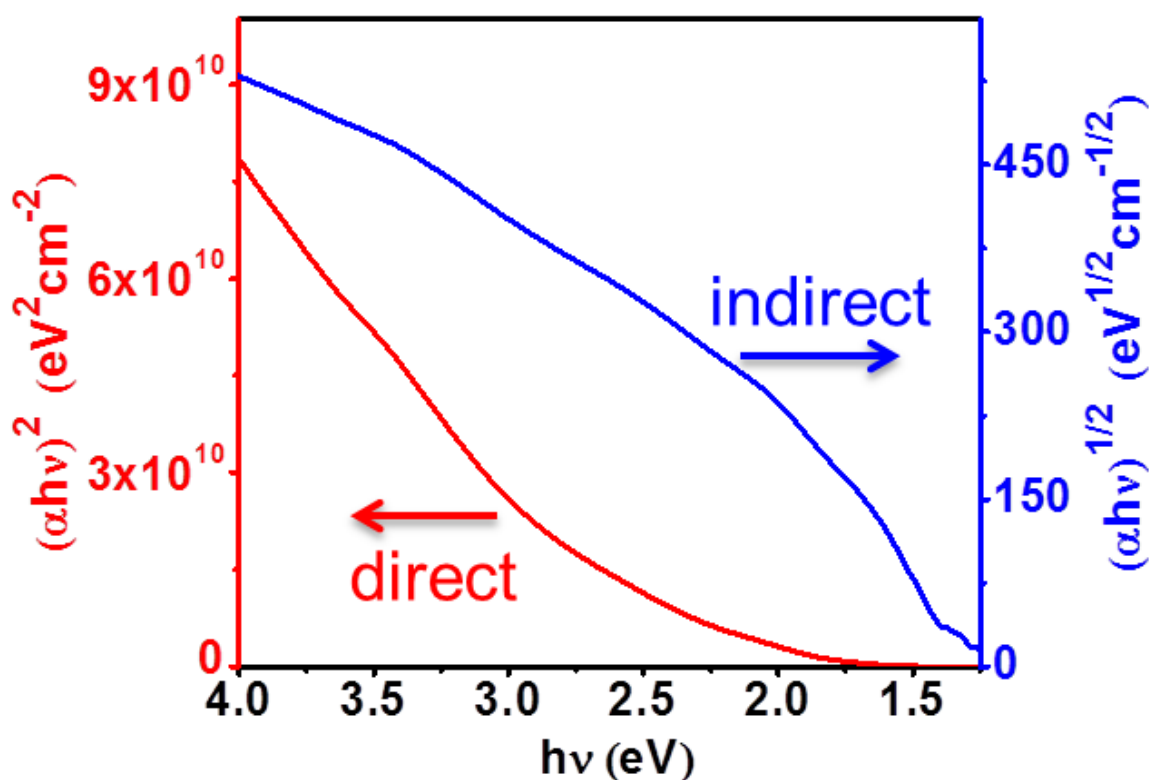


Figure 3.21. Direct and indirect bandgap Tauc plots for CuBi_2O_4 films deposited with 20 mM precursor solution with 5 % TEOF and 1 % PEG on quartz substrates.

In order to have a whole picture of the band diagram of CuBi_2O_4 , electrical impedance spectroscopy (EIS) and Mott-Schottky measurements were carried out to determine the flat band potential (φ_{fb}) and acceptor density (N_A). As shown in **Figure 3.22a**, above 1 kHz, the real part of the impedance is constant, while the imaginary part has a slope of nearly -1. This suggests that the system behaves as a resistance in series with a pure capacitance. Therefore, the Mott-Schottky measurements were performed at frequencies higher than 1 kHz.

Figure 3.22b shows that at all three different frequencies the system behaves as a simple RC series circuit. This implies that the Mott-Schottky conditions are indeed fulfilled and the changes in capacitance can be attributed to the changes in the width of the SCR as a function of the applied potential.

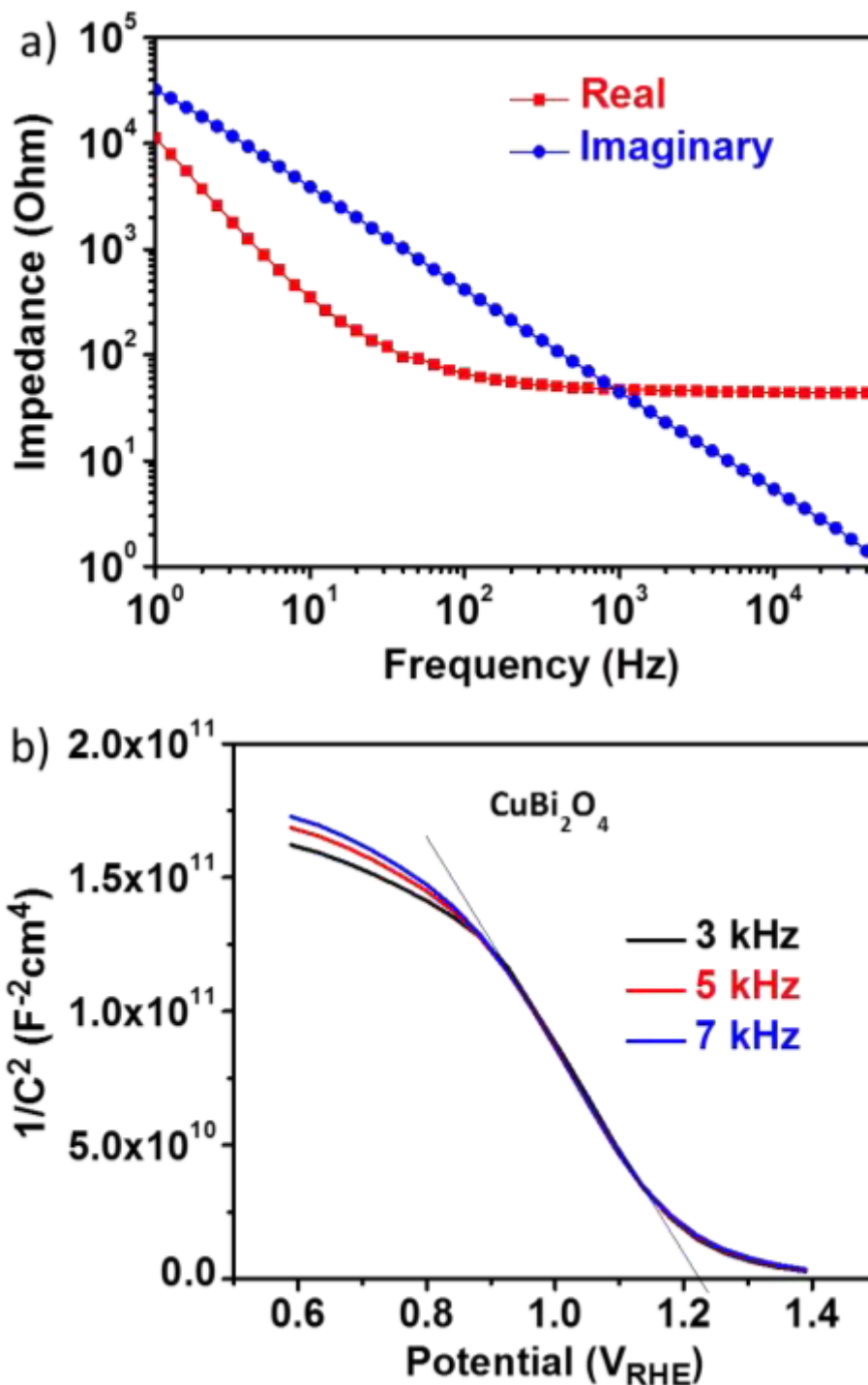


Figure 3.22. (a) Electrochemical impedance spectroscopy at 1.0 V vs. RHE; (b) Mott-Schottky plot for a ~ 270 nm CuBi_2O_4 film (sprayed using 20 mM precursor solution with 5 % TEOF and 1 % PEG on FTO at 450°C) performed in 0.3 M K_2SO_4 and 0.2 M phosphate buffer (pH 6.65). The surface area was corrected by AFM, see Figure S A10.

From the extrapolated x-axis intercept, the flat band potential (ϕ_{fb}) of the sprayed CuBi_2O_4 films is estimated to be at about 1.21 V vs RHE and the acceptor density (N_A) was calculated to be about $3.7 \times 10^{18} \text{ cm}^{-3}$ from the slope. Assuming that CuBi_2O_4 has an effective density of states of $5 \times 10^{19} \text{ cm}^{-3}$, this places the Fermi level less than 0.077 V away from the valence band edge.¹² Combined with bandgap determined from the Tauc plots, the conduction band and valence band edges are estimated to be located at -0.17 and 1.29 V vs. RHE, respectively. Since the conduction band is more negative than 0.0 V vs. RHE, the CuBi_2O_4 thin films have the potential to drive the proton reduction reaction photoelectrochemically.

Photocurrent and Quantum Efficiency

To assess the photoactivity of the dense, homogenous CuBi_2O_4 photocathodes we used various PEC techniques including linear sweep voltammetry (LSV) scans under chopped (light/dark) light. **Figure 3.23** shows various chopped LSV scans for the ~ 270 nm thick CuBi_2O_4 photocathode.

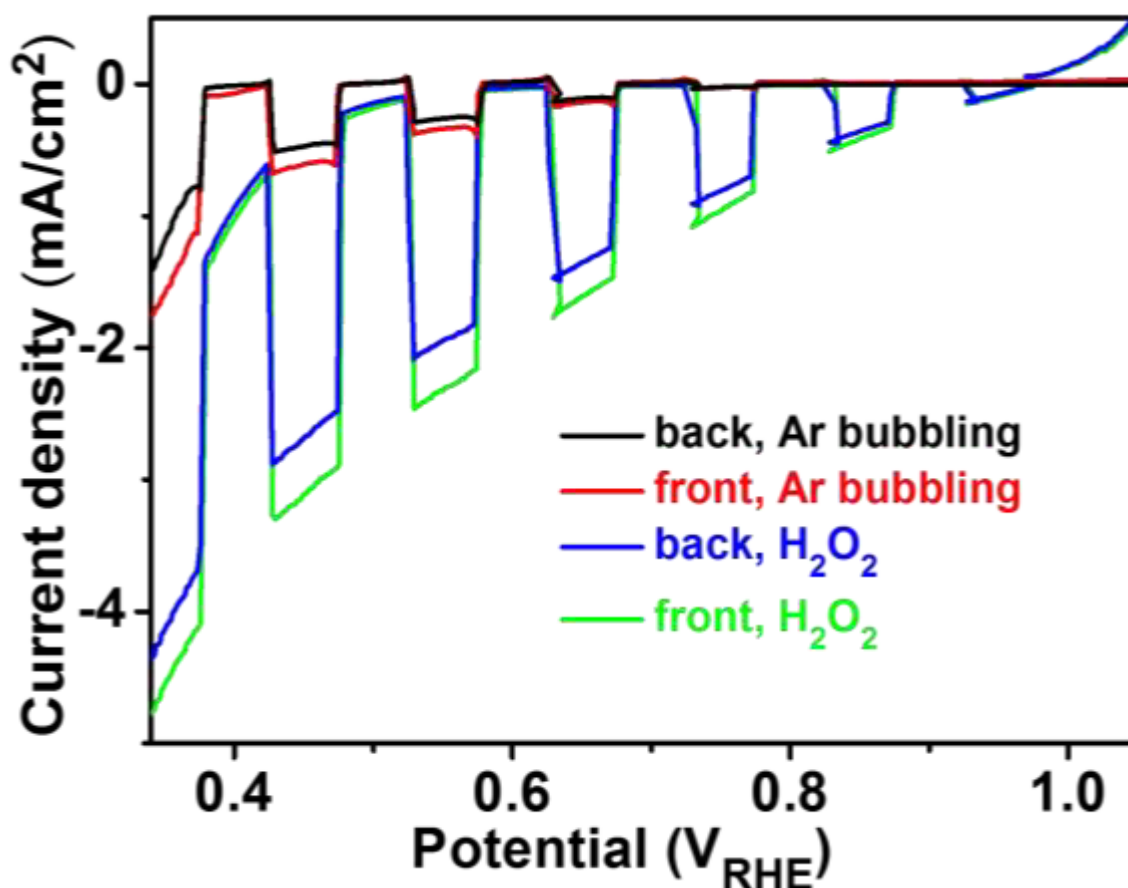


Figure 3.23. Chopped (light/dark) linear sweep voltammetry scans for ~ 270 nm CuBi_2O_4 (sprayed using 20 mM precursor solution with 5 % TEOF and 1 % PEG, 450 °C) performed in 0.3 M K_2SO_4 and 0.2 M phosphate buffer (pH 6.65) with Ar bubbling and with H_2O_2 under front and back illumination.

The LSV scans were performed with illumination from the front (electrolyte- CuBi_2O_4 side) and back (FTO substrate side) with Ar bubbling or with H_2O_2 added as an electron scavenger. Ar gas was bubbled into electrolyte to purge dissolved oxygen so that the photocathodes could be tested for activity towards proton reduction rather than oxygen reduction.^{107-108, 129-130} With Ar bubbling the photocurrent density is relatively low ($< 0.3 \text{ mA/cm}^2$ at 0.6 V vs. RHE for both front and back illumination). This is most likely due to poor reaction kinetics towards the proton reduction reaction. H_2O_2 is much easier to reduce than protons, both kinetically and thermodynamically (reduction potential is 0.815 V vs. RHE for H_2O_2 compared to 0.0 V vs. RHE for H^+), so H_2O_2 can be used as an electron scavenger to probe the performance of the CuBi_2O_4 photocathodes without limitations in the reaction kinetics. With H_2O_2 added to the electrolyte the CuBi_2O_4 photocathodes show a clear photocurrent onset at ~ 1.0 V vs. RHE and reach a significantly higher maximum photocurrent density (2.0 mA/cm^2 at 0.6 V vs. RHE for back illumination). This dramatic increase in photocurrent density in the presence of H_2O_2 provides evidence that bare CuBi_2O_4 are limited by poor kinetics towards the proton reduction reaction. It should be noted that the addition of H_2O_2 into the electrolyte may be accompanied by current-doubling at low light intensities but in this case the increase in photocurrent density is nearly 8-fold so even if current-doubling occurs the increase due to overcoming reaction kinetics is at least 4-fold.¹³¹ In addition, the photocurrent density of 2.0 mA/cm^2 (with H_2O_2) establishes a new record for un-doped CuBi_2O_4 .^{105, 107-108, 132} The limiting photocurrent density is likely even higher but it could not be reached at potentials more negative than ~ 0.5 V vs. RHE as there was significant dark current most likely due to Cu^{2+} corrosion with Ar bubbling. It has been reported that Cu^{2+} can be reduced to Cu^+ at potentials negative than 0.6 V vs. RHE in neutral solution.⁵⁰ This is confirmed by the LSV tests on sprayed CuO and CuBi_2O_4 films, as shown in **Figure 3.24**. At potentials negative than 0.22 and 0.42 V vs. RHE, the cathodic dark current increases significantly for CuBi_2O_4 and CuO, respectively.

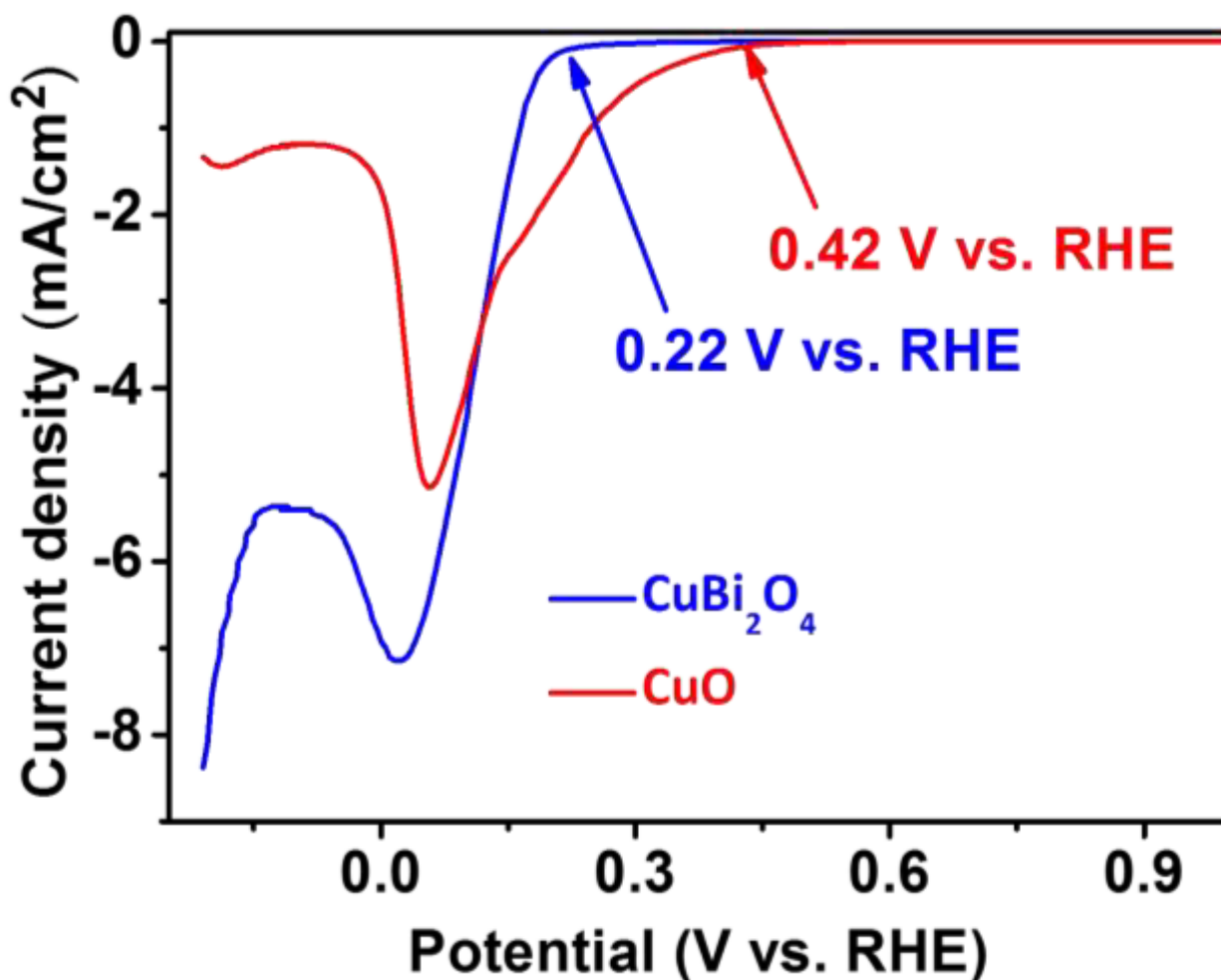


Figure 3.24. Linear sweep voltammetry scans in the dark for ~ 270 nm CuBi_2O_4 (sprayed using 20 mM precursor solution with 5 % TEOF and 1 % PEG on FTO at 450°C) and ~ 100 nm CuO (sprayed using 20 mM $\text{Cu}(\text{NO}_3)_2 \cdot 3\text{H}_2\text{O}$ in ethanol on FTO at 450°C) performed in 0.3 M K_2SO_4 and 0.2 M phosphate buffer (pH 6.65) with Ar bubbling in the dark.

To make a fair comparison with previous reports on CuBi_2O_4 photoelectrodes, we also performed the PEC measurements in 0.1 M KOH with O_2 bubbling, as shown in. At 0.6 V vs. RHE, our dense and compact CuBi_2O_4 photocathode produces a photocurrent density of ~ 1.6 mA/cm^2 under AM 1.5 solar simulation, which is twice as much as the reported value (~ 0.8 mA/cm^2) of a highly porous CuBi_2O_4 photocathode tested under similar conditions.¹⁰⁷

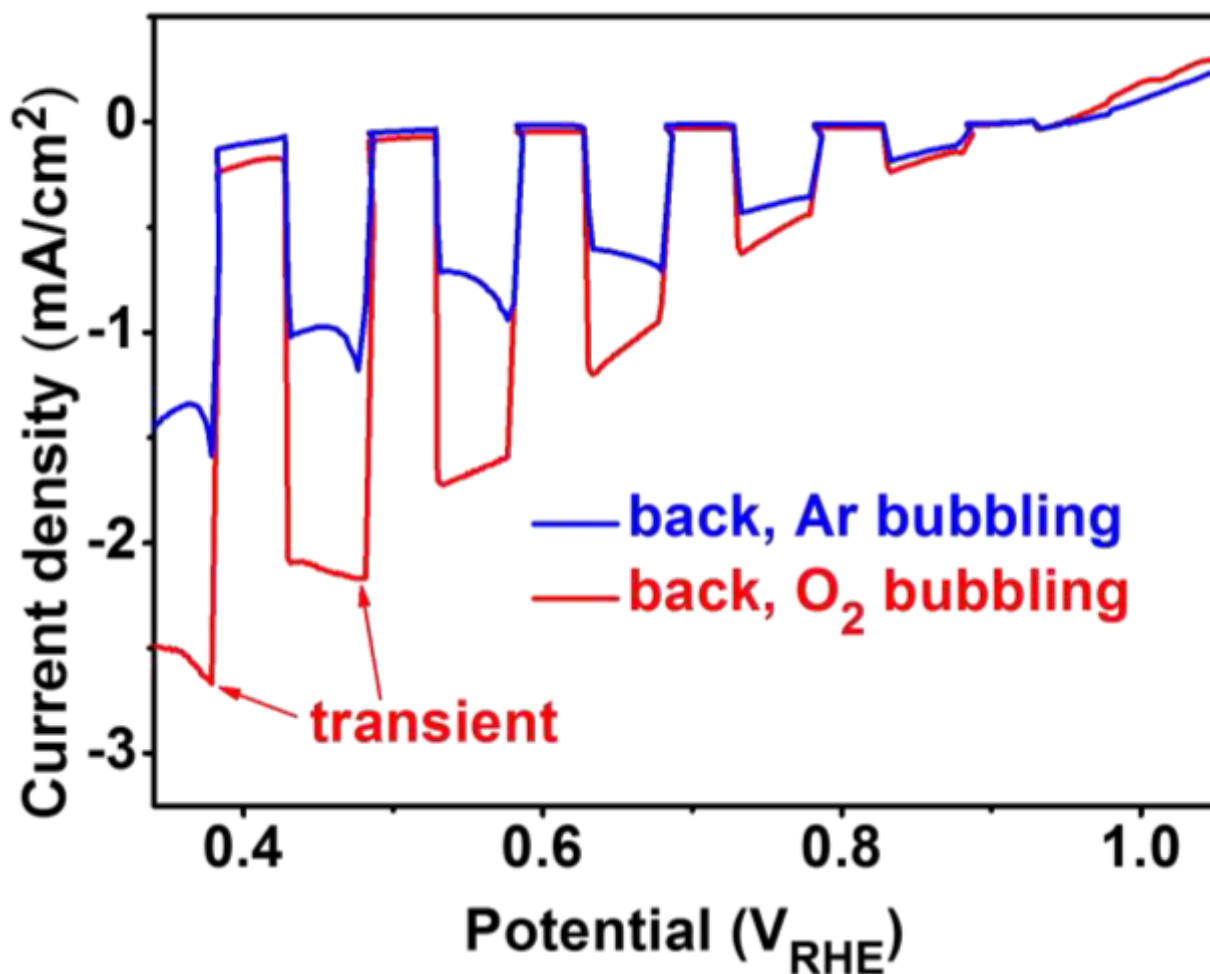


Figure 3.25. Chopped (light/dark) linear sweep voltammetry scans for a ~ 270 nm CuBi_2O_4 photocathode (sprayed using 20 mM precursor solution with 5 % TEOF and 1 % PEG on FTO at 450°C). The measurement was performed in 0.1 M KOH (pH 12.8) with Ar bubbling and with O_2 bubbling under back illumination.

Unlike the chopped LSV scans with H_2O_2 , the chopped LSV scans with O_2 bubbling show gradual transient spikes in cathodic photocurrent when the light is turned on. This is attributed to the low concentration of dissolved O_2 , which cannot sustain current densities higher than ~ 2.8 mA/cm^2 . We confirmed this by performing pure electrochemical measurements with Pt wires as electrodes in the same electrolyte. **Figure 3.26a** shows that at 1.15 V vs. RHE, there is nearly no current, while a photocurrent of ~ 2.8 mA/cm^2 is reached on the Pt wire. A square wave voltammetry of a Pt wire was conducted with a potential step (2 s at 1.15 V vs. RHE and 2 s at 0.15 V vs. RHE) in 0.1 M KOH with O_2 bubbling. The transient peak in **Figure 3.26b** reveals that the low concentration of dissolved O_2 cannot sustain current densities higher than ~ 2.8 mA/cm^2 .

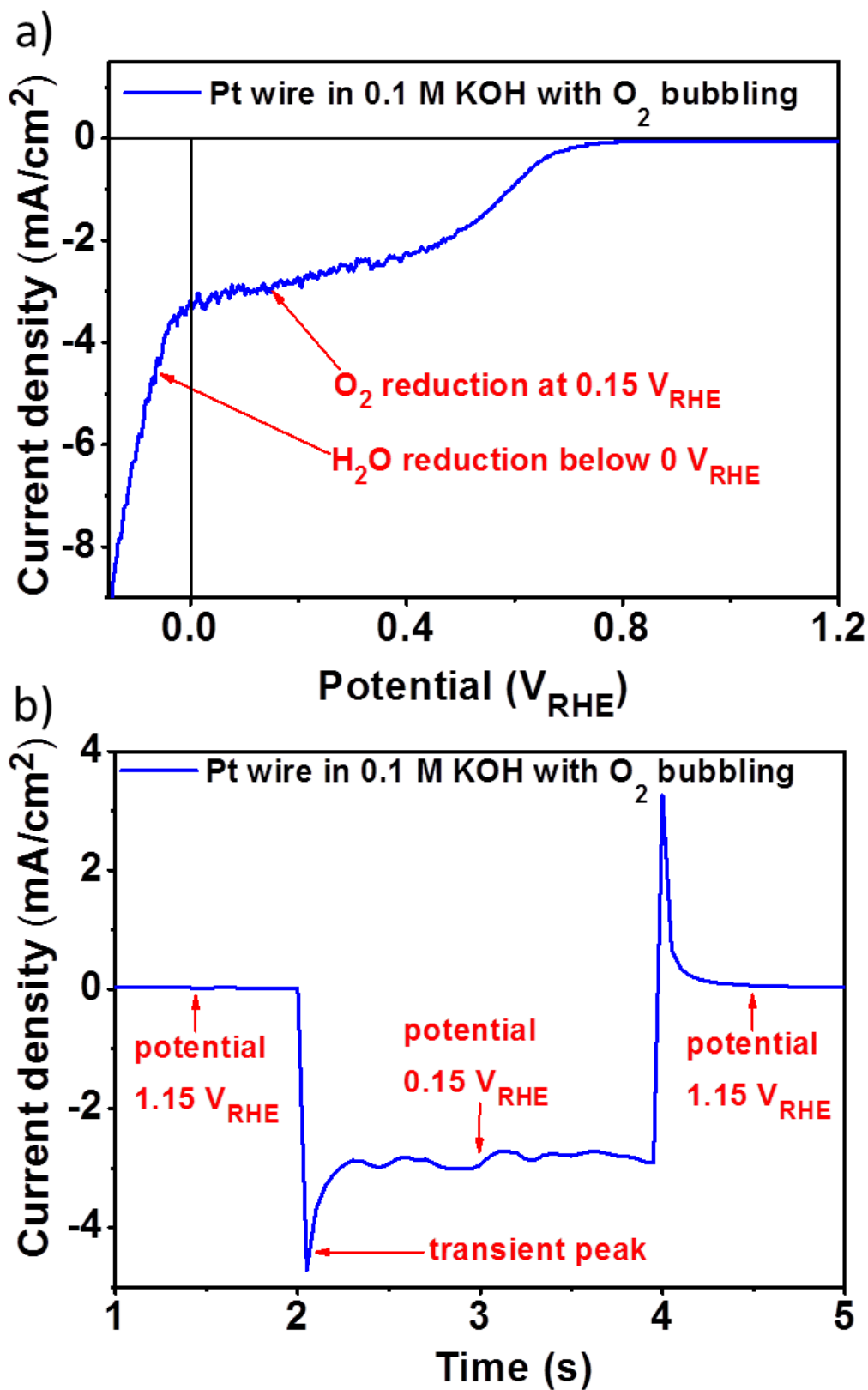


Figure 3.26. (a) Linear sweep voltammetry scan for a Pt wire performed in 0.1 M KOH with O_2 bubbling (pH 12.8); (b) Square wave voltammetry of a Pt wire measured with a potential step (2 s at 1.15 V vs. RHE and 2 s at 0.15 V vs. RHE) in 0.1 M KOH with O_2 bubbling (pH 12.8).

The quantum efficiency of the CuBi_2O_4 photocathode was determined using IPCE and APCE measurements. **Figure 3.27** shows the IPCE and APCE spectra under back illumination along with the upper limit for IPCE based on the absorbance of the CuBi_2O_4 film (see **Figure 3.20**).

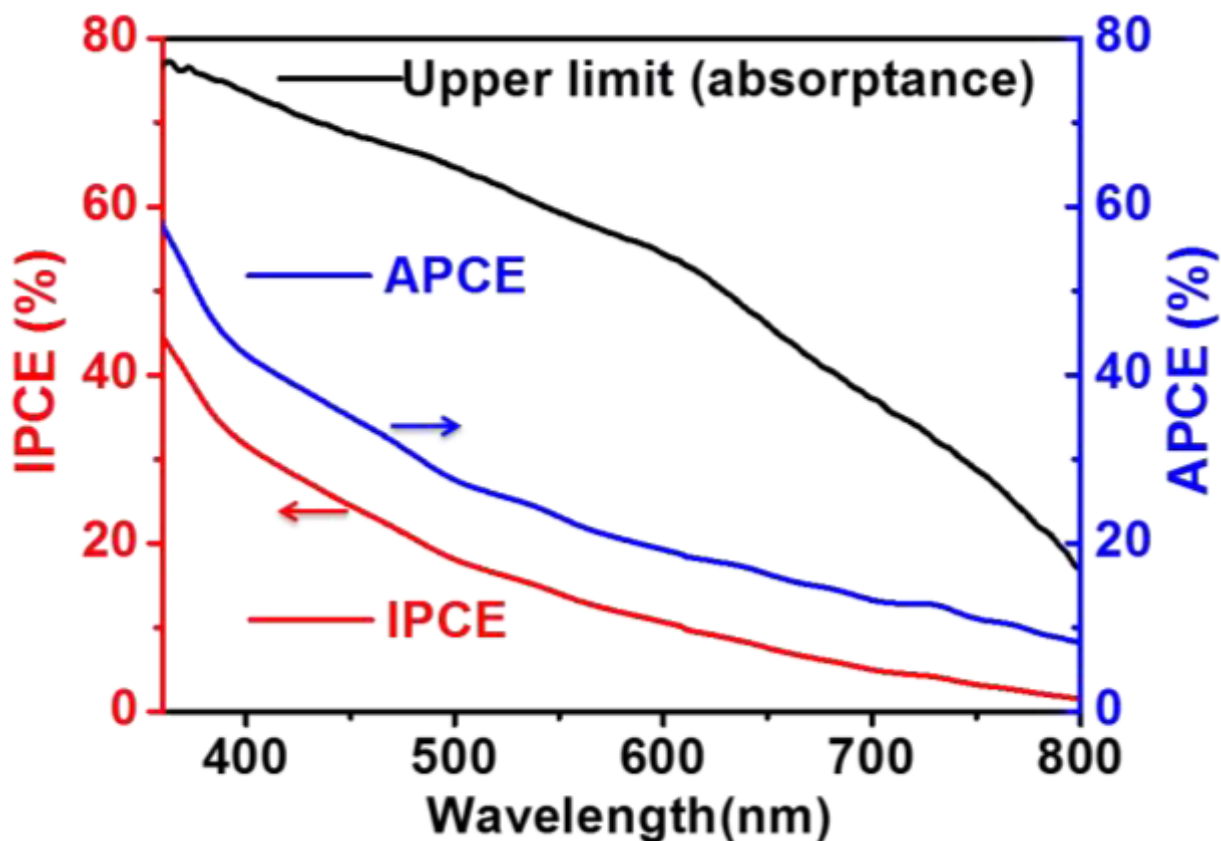


Figure 3.27. IPCE and APCE spectra for ~ 270 nm CuBi_2O_4 films (sprayed using 20 mM precursor solution with 5 % TEOF and 1 % PEG, 450 °C). The measurements were performed at 0.6 V vs RHE in 0.3 M K_2SO_4 and 0.2 M phosphate buffer (pH 6.65) with H_2O_2 under back illumination. The black line represents the maximum obtainable IPCE values for these photocathodes based on the absorption spectra. Raw data for IPCE can be found in **Figure S A11**.

These IPCE and APCE values were calculated using the light that passed through the FTO and directly irradiated the CuBi_2O_4 thin film ($E_{\text{CuBi}_2\text{O}_4}(\lambda) = E_{\text{lamp}}(\lambda) \times T_{\text{FTO}}$) so these are quantum efficiency values for the CuBi_2O_4 thin film rather than the entire photocathode. In general the IPCE values are well below the upper absorptance limit for CuBi_2O_4 and the APCE values are below 60 % for all wavelengths, even with the addition of H_2O_2 as an electron scavenger. Assuming that with H_2O_2 added the injection efficiency is 100 % at the CuBi_2O_4 -electrolyte interface, then the low IPCE and APCE values indicate that the photo-conversion efficiency of CuBi_2O_4 is largely limited by bulk recombination and that the majority of photo-generated electrons do not even reach the CuBi_2O_4 -electrolyte interface. In the visible light region (wavelengths between 400 and 700 nm) these

CuBi₂O₄ thin films synthesized by spray pyrolysis show considerably higher IPCE values than were previously reported for CuBi₂O₄ photocathodes synthesized by drop-casting.¹⁰⁸ This improvement may be due to the densely packed, high quality CuBi₂O₄ crystallites obtained by combustion of the precursors during spray pyrolysis as opposed to the sparse, elongated particles obtained by other methods.^{106, 108} For 550 nm light at 0.6 V vs. RHE, the 270 nm CuBi₂O₄ film produces IPCE and APCE values of 14.0 % and 23.1 %, respectively. The entire CuBi₂O₄ photocathode (glass/FTO/CuBi₂O₄) yields IPCE and APCE values of 12.7 % and 19.7 %, respectively, which is a new record for CuBi₂O₄ at such a positive potential.^{106-108, 132}

The predicted AM 1.5 photocurrent density ($J_{AM1.5}$) of the photocathodes can be estimated by multiplying the IPCE values by the transmittance of the FTO substrate and the AM 1.5 solar photon flux and subsequently integrating this for wavelengths below 800 nm according to the following relationship.

$$J_{AM1.5} = \int_{280}^{800} (IPCE(\lambda) \times T_{FTO} \times \Phi_{AM1.5}(\lambda) \times e) d\lambda \quad (3.13)$$

where, $J_{AM1.5}$ is the total solar photocurrent in A/m², $\Phi_{AM1.5}(\lambda)$ is the photon flux of sunlight in photons/m²/s, λ is the wavelength in m, and e is the electronic charge. This results in an expected photocurrent density of 2.2 mA/cm² at 0.6 V vs. RHE, which is very close to the 2.0 mA/cm² obtained for the chopped LSV measurements under AM 1.5 solar simulation.

The photocurrent density of 2.0 mA/cm² is a new benchmark for this material. Moreover, integration of the absorbance spectrum (for the 270 nm CuBi₂O₄ film) over the AM 1.5 solar spectrum for all wavelengths below 800 nm results in an estimated maximum photocurrent density ($J_{abs,max}$) of 15.1 mA/cm². This corresponds to a maximum solar-to-hydrogen conversion efficiency of 18.6 % using the following formula,

$$\eta_{STH,max} = \frac{J_{abs,max} \times (V_{redox} - V_{bias})}{P_{light}} \times \eta_F \approx \frac{1.23 \text{ V} \times J_{abs,max}}{100 \text{ mW/cm}^2} \quad (3.14)$$

(for unbiased water splitting at 100 % faradaic efficiency under AM 1.5 illumination)

where V_{redox} is 1.23 V at room temperature based on the lower heating value of 237 kJ/mol, V_{bias} is the applied bias, and η_F is the faradaic efficiency.

Stability Test

To test the stability of the CuBi₂O₄ photocathodes, the PEC measurements were carried out in a solution of 0.3 M K₂SO₄ and 0.2 M phosphate buffer both with Ar bubbling and with H₂O₂ at a constant potential of 0.6 V vs RHE for several hours under chopped illumination, as shown in **Figure 3.28**.

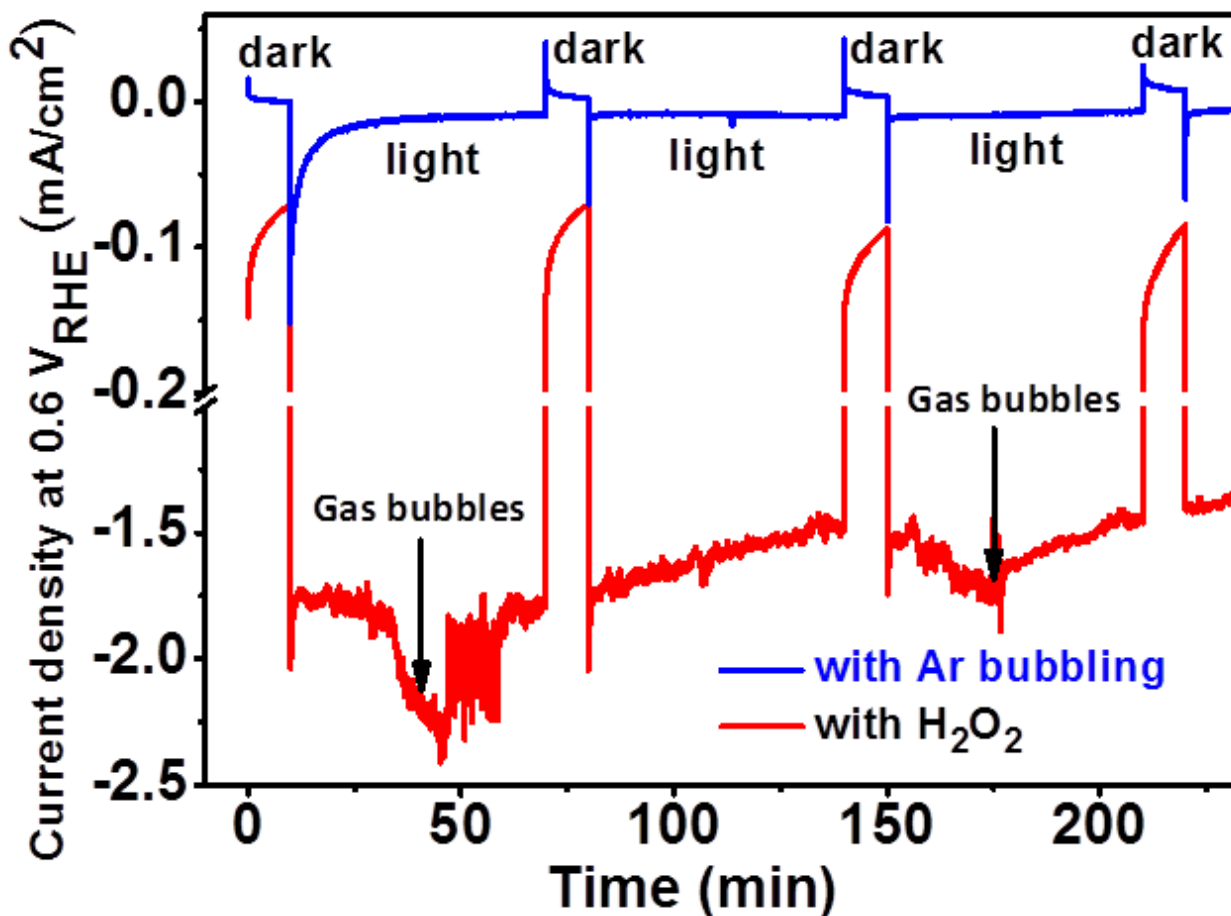


Figure 3.28. Constant potential measurement at 0.6 V vs RHE for a ~ 270 nm CuBi_2O_4 photocathode (sprayed using 20 mM precursor solution with 5 % TEOF and 1 % PEG on FTO at 450 °C) in the dark and light (AM 1.5 irradiation). Measurements were done in 0.3 M K_2SO_4 and 0.2 M phosphate buffer (pH 6.65) with Ar bubbling and with H_2O_2 .

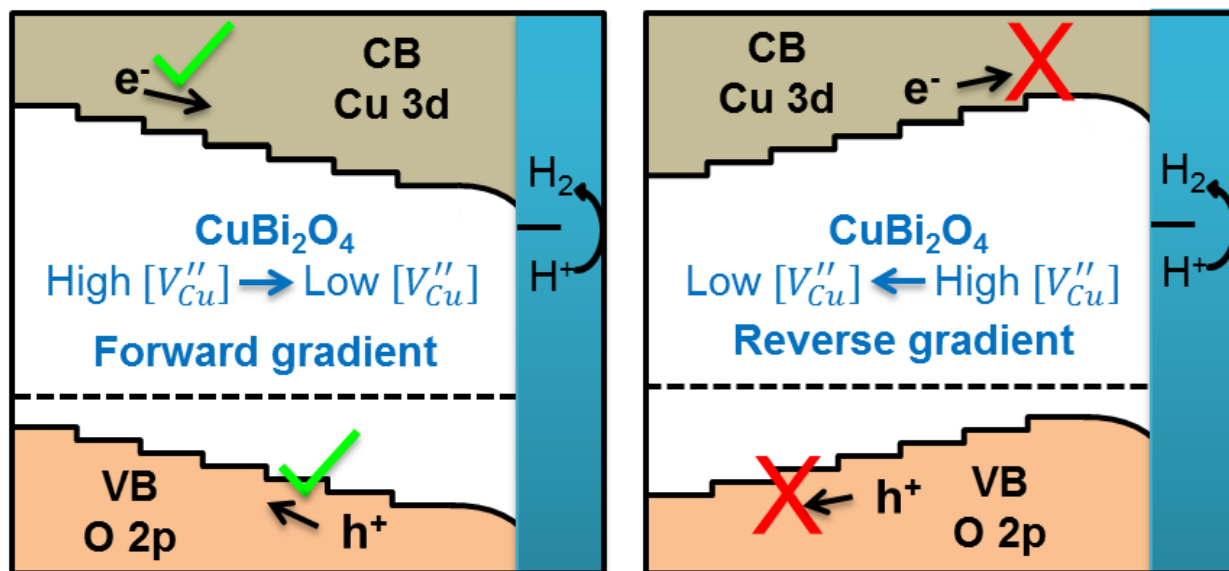
With Ar bubbling, the photocurrent density decreases by 80 % within 15 min due to photo-corrosion and poor kinetics towards the proton reduction reaction. In contrast, with the presence of H_2O_2 , the photocathodes' stability is improved, and photocurrent decreases by only 24 within 180 min. This is attributed to the increased injection efficiency of photo-generated electrons into the electrolyte, which implies that the instability of CuBi_2O_4 can be solved by applying appropriate surface modification (e.g., co-catalyst deposition) that allows fast electron transfer towards proton reduction.

Conclusions

For the first time, a spray pyrolysis recipe has been developed to prepare dense and homogeneous CuBi_2O_4 photocathodes which are well-suited for fundamental research of photophysical and photoelectrochemical

properties. Initial optical and photoelectrochemical tests were performed. The optical behavior is consistent with previous reports on this material. The photoelectrochemical performance sets a new benchmark with photocurrent densities as high as 2 mA/cm^2 along with IPCE and APCE values of 14.0 % and 23.1 %, respectively for 550 nm light (at 0.6 V vs. RHE with H_2O_2 as an electron scavenger).

Several challenges in the spray pyrolysis process were identified and addressed using strategies that may be applicable to the synthesis of dense, homogenous metal oxide thin films in general. The challenge of rapid precipitation in the precursor solution was confirmed to be caused by the hydrolysis of Bi^{3+} in the presence of water. Adding 5 % TEOF effectively prevents the rapid hydrolysis of Bi^{3+} by scavenging the initial water and thus significantly increases the stability of the precursor solution. The addition of 1 % PEG in the precursor solution remarkably improves the spreading behavior of the droplets on the substrate surface and therefore prevents the powder formation completely. Our approaches to improve the stability of the precursor solution and the homogeneity of the film could easily be applied to the spray pyrolysis of other metal oxides.



The main part of this Chapter was **accepted by JACS**: Wang, F.; Septina, W; Chemseddine, A; Abdi, F. F; Friedrich, D; Bogdanoff, P; van de Krol, R; Tilley, S. D.; Berglund, S. P. *J. Am. Chem. Soc.* **2017**, **accepted**.

It was demonstrated in Chapter 3 that the PEC performance of CuBi₂O₄ is largely limited by low charge separation efficiency. To address this limitation, this Chapter describes a new strategy of using forward gradient self-doping to improve the charge separation efficiency of CuBi₂O₄. Gradient self-doped CuBi₂O₄ photocathodes are prepared with forward and reverse gradients in copper vacancies using a two-step-diffusion-assisted spray pyrolysis process. Decreasing the Cu : Bi atomic ratio is shown to shift the flat-band of the CuBi₂O₄ photocathodes to more positive potentials. Thus, the formation of a gradient in the Cu : Bi atomic ratio leads to a gradient in Cu vacancies within the CuBi₂O₄ photocathodes, as well as an internal electric-field that facilitates the charge separation. Compared to homogeneous CuBi₂O₄ photocathodes, CuBi₂O₄ photocathodes with a forward gradient show highly improved charge separation efficiency and enhanced PEC performance for photoreduction reactions, while CuBi₂O₄ photocathodes with a reverse gradient show significantly decreased charge separation efficiency and reduced PEC performance. At 0.6 V vs. RHE, an AM 1.5 photocurrent of -2.5 mA/cm² (with H₂O₂) and a charge separation efficiency of 34.0 % (550nm) are achieved for the CuBi₂O₄ photocathodes with a forward gradient, establishing a new benchmark for this material. The gradient self-doping does not require the introduction of external dopants and therefore the intrinsic tetragonal crystal structure and carrier mobility of CuBi₂O₄ are maintained. To improve the stability, the forward gradient self-doped CuBi₂O₄ photocathodes are protected with a CdS/TiO₂ heterojunction and coated with Pt as an electrocatalyst. The CuBi₂O₄/CdS/TiO₂/Pt photocathodes show highly improved stability and a photocurrent density of -0.9 mA/cm² is obtained at 0.0 V vs. RHE with a faraday efficiency of ~91 %.

Introduction

The attractive characteristics of CuBi_2O_4 as a photocathode material for water splitting are introduced in Chapter 3 despite the relatively low photocurrent densities that have been reported so far.^{101-102, 106-108} Our work in Chapter 3 reveals that the PEC performance of CuBi_2O_4 is limited mainly by two factors. First, poor charge separation prevents photo-generated carriers from reaching the CuBi_2O_4 -electrolyte interface resulting in low photoconversion efficiency. Second, CuBi_2O_4 suffers from serious photo-corrosion under the operating conditions for proton reduction.⁴³ Therefore, in Chapter we aim at strategies to improve the charge separation efficiency of CuBi_2O_4 and ways of stabilizing it from photo-corrosion.

One approach to improve the charge separation of a semiconductor material is to create a built-in electric field. Creating a heterojunction by combining it with another semiconductor is a commonly used approach to enhance band bending. However, this requires two semiconductors with suitable aligned energy levels¹³³⁻¹³⁵ and proper synthesis of the heterojunction. The high presence of defects at the interface often causes high level of recombination.¹³⁶ Another way to create an internal electric field is by forming a homojunction, in which the same semiconductors with equal bandgaps but different doping levels are brought into contact. A solar cell composed of p-n silicon is a good example for a homojunction device. Similarly, photoelectrodes can also be prepared as homojunctions. For instance, it has been demonstrated that the formation of an internal electric field in gradient doped $\text{W}:\text{BiVO}_4$ photoanodes can significantly enhance the charge separation efficiency.⁵⁸ Compared to heterojunctions, homojunctions are usually easier to prepare since only one semiconductor material is required. However, there are undesired drawbacks of such homojunctions. For example, the addition of an external dopant can cause distortion of the intrinsic structure, create recombination centers, and/or decrease the charge carrier mobility, as has been reported for W doped BiVO_4 .¹³⁷¹³⁸ What's more, the external dopant may cause complexity in the material synthesis process.

In this Chapter, we develop a new strategy for creating effective homojunctions within multinary metal oxides like CuBi_2O_4 without inducing external dopants. Recall from Chapter 3 that DFT calculation¹⁰⁵ suggests that the conduction band (CB) and valence band (VB) consist mainly of Cu 3d and O 2p orbitals, respectively. Copper vacancies (denoted as V''_{Cu}) are the most probable defects in CuBi_2O_4 and they lead to empty states within the valence band, which shifts the Fermi level down to the valence band and causes the p-type behavior of CuBi_2O_4 . In principle, the Fermi level energy of CuBi_2O_4 can be tailored by varying the concentration of V''_{Cu} . In this Chapter we have taken advantage of this principle and develop a synthesis procedure that results in a V''_{Cu}

gradient within CuBi₂O₄. Such a V''_{Cu} gradient leads to a gradient in the flatband potential and therefore a built-in electric field is created without the introduction of an external dopant. CuBi₂O₄ photocathodes synthesized with a forward gradient in V''_{Cu} show significantly enhanced charge separation efficiency compared to photocathodes without a gradient. To the best of my knowledge, this concept of using gradient self-doping to create an internal electric field in a multinary metal oxide photoelectrode has never been reported before. The results in this Chapter should promote this concept for other multinary metal oxides.

To address the second problem of photo-corrosion, protection layers can be applied to photoelectrodes, which prevent direct contact with the aqueous electrolyte. In this work, a CdS/TiO₂ protection layer is applied to the surface of the forward gradient CuBi₂O₄ photocathodes followed by Pt coating as an electrocatalyst. This dramatically improves the stability of the CuBi₂O₄ photocathodes, allowing for long term (several hours) hydrogen evolution at high faraday efficiency.

Experimental

Material Synthesis

Homogenous CuBi₂O₄ films were prepared using the optimized spray pyrolysis recipe as described in Chapter 3 with Triethyl orthoformate (TEOF) and polyethylene glycol (GEP) as additives.⁴³ CuBi₂O₄ films with a forward gradient were prepared through two-step diffusion-assisted spray pyrolysis as illustrated in **Figure 4.1**. First a 40 mM Bi³⁺ precursor was prepared by dissolving Bi(NO₃)₃ · 5H₂O (98 %, Alfa Aesar) in 1 : 9 acetic acid (≥ 99.8%, Sigma Aldrich) : ethanol (≥ 99.8 %, Sigma Aldrich) and sprayed onto FTO substrate at a deposition temperature of 450 °C resulting a yellow Bi₂O₃ film as confirmed by XRD. Next a 20 mM Cu²⁺ precursor was prepared by dissolving Cu(NO₃)₂ · 3H₂O (99-104 %, Sigma - Aldrich) in ethanol (≥ 99.8 %, Sigma Aldrich) and sprayed successively on top of the Bi₂O₃ film at 450 °C, during which Cu impregnated the Bi₂O₃ at high temperature. The high mobility and small size of Cu allow the intercalation between Bi₂O₃ and the incoming Cu²⁺ and facilitate the impregnation of Cu into the frame of Bi₂O₃. Post annealing was not required. Reverse gradient CuBi₂O₄ films were prepared with the alternative spray of Cu²⁺ precursor first followed by Bi³⁺ precursor. The two-step process allows the spray of Bi³⁺ precursor and Cu²⁺ precursor separately without additives, avoids rapid hydrolysis of Bi³⁺, and results in a growth rate of 2.7 nm/min, which is 3.3 times higher than that of our previous reported recipe.⁴³

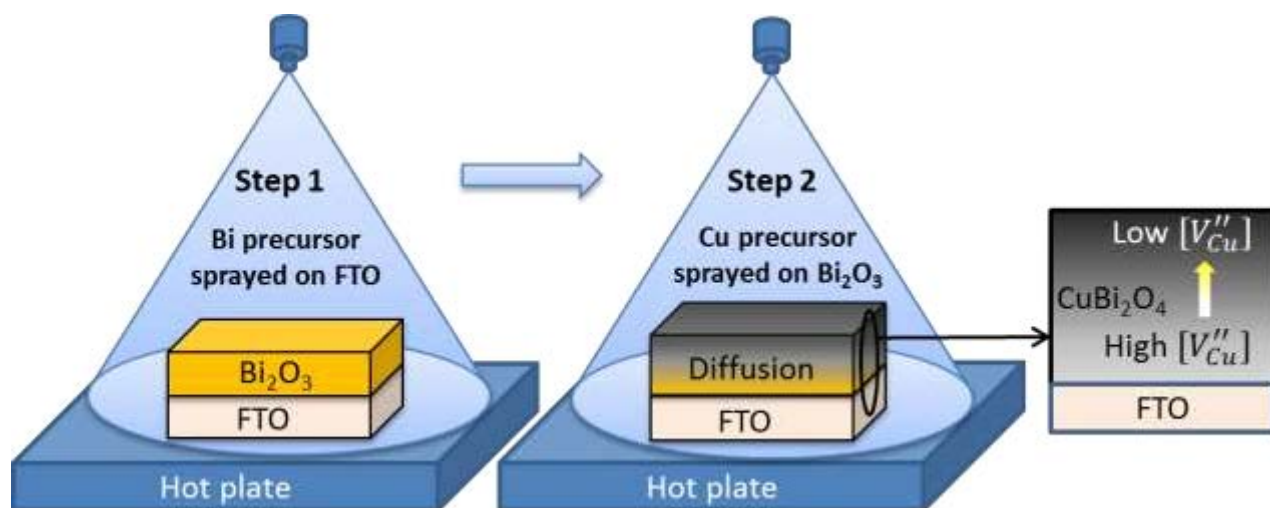


Figure 4.1. Sketch of the two-step-diffusion-assisted spray pyrolysis of CuBi_2O_4 with a forward gradient.

CdS/TiO_2 overlayers were deposited onto the forward gradient CuBi_2O_4 films using chemical bath deposition (CBD) of CdS followed by atomic layer deposition (ALD) of TiO_2 as previously reported for CuO photocathodes.⁵⁰ The platinum electrocatalyst was photoelectrodeposited onto the $\text{CuBi}_2\text{O}_4/\text{CdS}/\text{TiO}_2$ from a solution containing 1 mM H_2PtCl_6 in 0.1 M Na_2SO_4 , using a constant cathodic current of $25 \mu\text{A}/\text{cm}^2$ for 10 min with constant illumination from a AM 1.5 solar simulator (LOT-QuantumDesign GmbH). The photoelectrodeposition was performed in a two-electrode configuration with Pt mesh as a counter electrode.

Material Characterization

The morphology and the elemental distribution of the films were analyzed using a LEO GEMINI 1530 field emission scanning electron microscope (FESEM) with an energy dispersive X-ray fluorescence (EDX) spectrometer, operated at an acceleration voltage of 5 kV and 20 kV for SEM and EDX, respectively. The cross section elemental distribution of the CuBi_2O_4 films was determined by EDX mapping, where the Cu (K_α) and the Bi (M) peaks were used to calculate the Cu and Bi content, respectively. The structure of the films were investigated with a Bruker AXS D8-Advance X-ray diffractometer with a Cu K_α radiation ($\lambda = 0.154 \text{ nm}$) using Glancing incidence X-ray diffraction (GIXRD) measurements. Scherrer analysis was performed as described in our previous paper.¹³⁹ The short-range structure and vibration modes were analyzed by Raman spectroscopy (Dilor micro LabRam, Horiba) with a laser excitation wavelength of 635 nm and a power of 0.6 mW at the objective (spot size: $\sim 1 \mu\text{m}$ in diameter). The surface morphology was investigated by atomic force microscopy (AFM, Park System, XE-100) operated in tapping mode using an etched Si tip with a tip radius of 10 nm and a force constant of 40 N/m. All

scans were performed on a scale of 5 $\mu\text{m} \times 5 \mu\text{m}$ with the lateral resolved height information on a square array of 256 \times 256 pixels.

The charge carrier mobility and lifetime were investigated by time resolved microwave conductivity (TRMC) measurements. TRMC is a non-contact technique based on the measurement of the change of the microwave power reflected by a sample induced by a pulsed laser, as illustrated in **Figure 4.2**.¹⁴⁰⁻¹⁴³

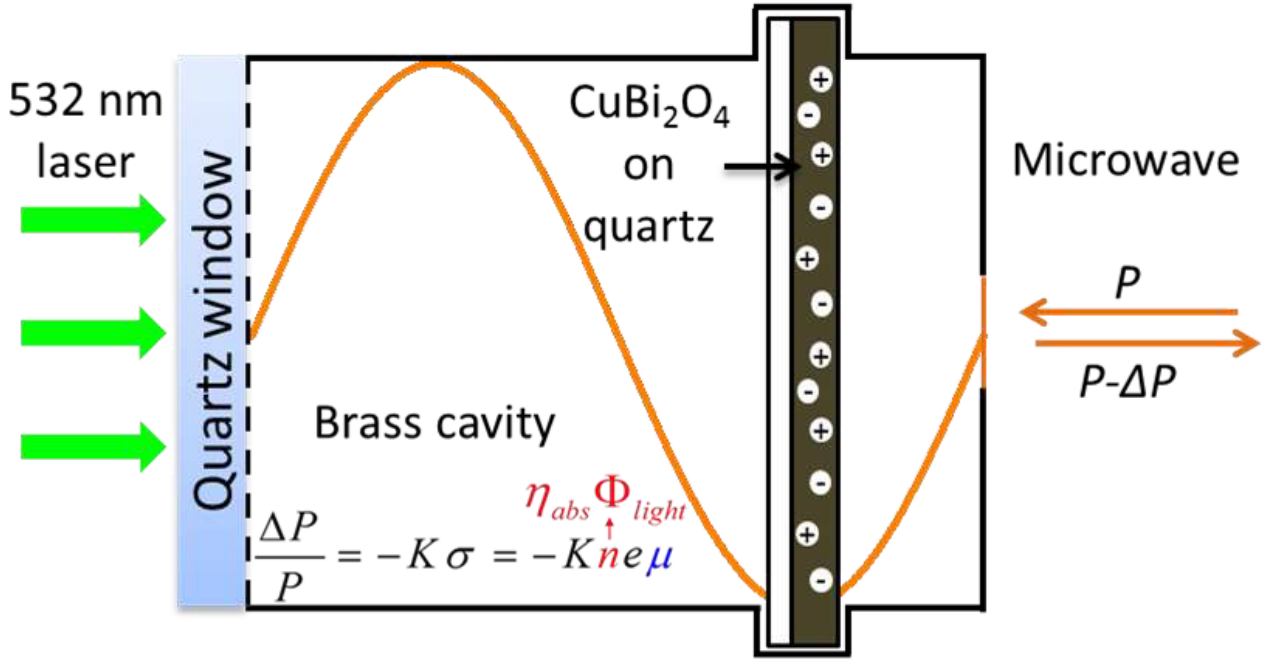


Figure 4.2. Illustration of the time resolved microwave conductivity (TRMC) measurements.

The X-band (8.2-12.4 GHz) microwaves are generated using a voltage controlled oscillator (SiversIMA VO3262X). The resonance frequency of the cavity, loaded with the sample, was determined by measuring the reflected power as a function of the microwave frequency and normalized with respect to the power measured for a fully reflecting copper plate. From the resulting resonance curve the resonance frequency f_0 , corresponding to minimum reflected power and maximum electric field strength within the cavity, was found to be 8521 MHz for our CuBi₂O₄ films. During the measurements, a change in the microwave power reflected by the cavity upon sample excitation by 6 ns (full-width at half-maximum) pulses of a frequency-trippled Q-switched Nd:YAG laser at a wavelength of 532 nm (10 Hz repetition rate), $\Delta P/P$, was monitored and correlated to the photoinduced change in the conductance of the sample, ΔG , according to

$$\frac{\Delta P}{P}(t) = -K\Delta G(t) \quad (4.1)$$

where K is the sensitivity factor derived from the resonance characteristics of the cavity and the dielectric properties of the medium. From the measured change in the photoconductance, the product of the charge carrier generation yield (Φ) and the sum of electron and hole mobilities ($\Sigma\mu$) can be obtained according to

$$\Phi \Sigma \mu = \frac{\Delta G}{I_0 \beta e F_A} \quad (4.2)$$

where I_0 is the incident intensity per pulse, e is the elementary charge, β is the ratio of the inner dimensions of the cavity (width and height), and F_A is the fraction of incident photons absorbed within the sample. The F_A values ranged from 0.56 to 0.61 at a wavelength of 532 nm, determined from transmittance measurements with a double-beam spectrometer Lambda 950 (Perkin-Elmer). The laser pulse intensity was 4.9×10^{14} photons cm^{-2} for all measurements. The maximum sum of charge carrier mobilities ($\Phi \Sigma \mu_{\text{max}}$) was obtained from the peak signal and the carrier lifetime constants were deduced from the decay of the curve. The charge carrier diffusion lengths (L_D) were calculated from the following formula,

$$L_D = \sqrt{\left(\frac{\mu k T}{e}\right) \tau} \quad (4.3)$$

where μ is mobility ($\text{m}^2 \cdot \text{V}^{-1} \cdot \text{s}^{-1}$), k is the Boltzmann constant, T is the temperature (K), e is the electronic charge (C), and τ is the charge carrier lifetime (s).

Electrochemical and PEC Measurements

Details about the PEC, IPCE, APCE measurements can be found in the experimental section of Chapter 3. Electrical impedance spectroscopy (EIS) and Mott–Schottky measurements were performed using a VersaSTAT 3 Potentiostat (AMETEK Co., Ltd.). Mott–Schottky plots were created based on the following formula,¹⁰⁹

$$\frac{1}{C^2} = \frac{2}{e \varepsilon \varepsilon_0 N_A} \left(-\varphi + \varphi_{fb} - \frac{k T}{e} \right) \quad (4.4)$$

where C is the capacitance per unit area (F/m^2), ε is the relative permittivity (dielectric constant), ε_0 is the permittivity of free space, N_A is the acceptor density, and φ_{fb} is the flat-band potential. AFM was used to estimate the real surface area from the geometric surface area of the working electrode in the PEC cell (i.e., our CuBi₂O₄ photocathode).

The ε value for CuBi₂O₄ is expected to vary with Cu/Bi ratio and frequency; however, there are limited reports on this value in the literature. For bismuth cuprate glasses, it was demonstrated that ε depends on the

Cu : Bi ratio and frequency, which can be modeled using the Cole-Cole equation.¹⁴⁴⁻¹⁴⁵ We therefore adopted this technique to calculate ε for various CuBi₂O₄ films and frequencies. **Table 4.1** shows the ε_0 , ε_∞ , τ_0 , and α values interpolated/extrapolated from the reference.¹⁴⁴

Table 4.1. Parameters (ε_0 , ε_∞ , τ_0 , α) at 298K.

Cu : Bi ratio	ε_0	ε_∞	τ_0 (s)	α
1 : 3	58	33	5.1×10^{-4}	0.47
1 : 2	98	34	3.1×10^{-4}	0.53
1 : 1	205	34	5.3×10^{-4}	0.49

The dielectric constant ε (real part of the complex dielectric value) was calculated using the Cole-Cole equation,¹⁴⁵

$$\varepsilon = \varepsilon_\infty + \frac{(\varepsilon_0 - \varepsilon_\infty)[1 + (w\tau_0)^{1-\alpha} \sin(\frac{1}{2}\pi\alpha)]}{1 + 2(w\tau_0)^{1-\alpha} \sin(\frac{1}{2}\pi\alpha) + (w\tau_0)^{2(1-\alpha)}} \quad (4.5)$$

where ε_0 and ε_∞ are the “static” and “infinite frequency” dielectric constants, $w = 2\pi \times$ frequency, τ_0 is the generalized relaxation time, and α is the Cole-Cole distribution parameter. The results are shown in **Figure 4.3**.

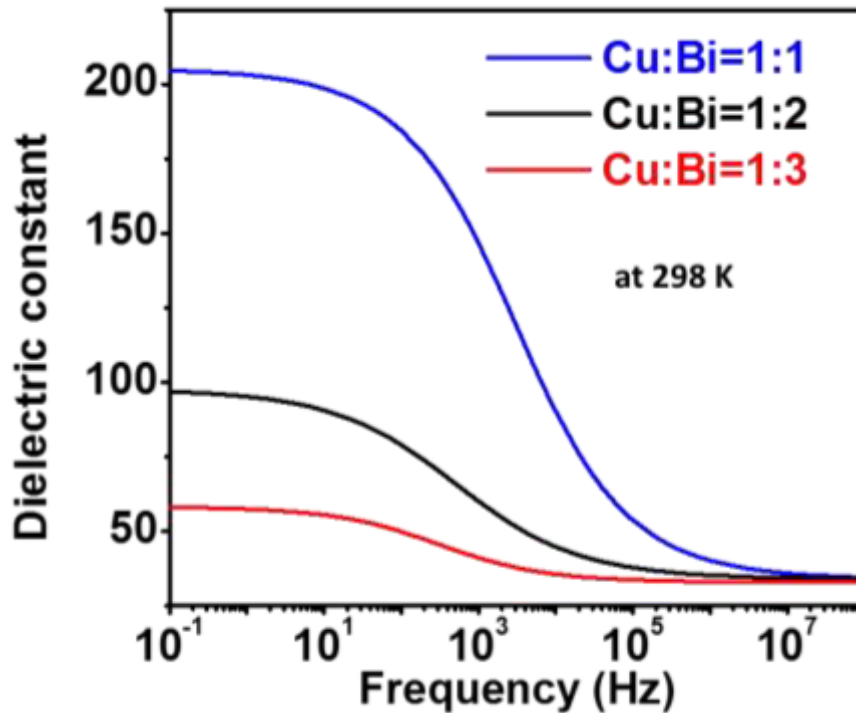


Figure 4.3. Dielectric constant of bismuth cuprate as function of Cu : Bi ratio and frequency.

The PEC stabilities of the CuBi_2O_4 and $\text{CuBi}_2\text{O}_4/\text{CdS}/\text{TiO}_2/\text{Pt}$ photocathodes were tested in a three-electrode configuration using a BioLogic SP-200 potentiostat with illumination from a AM 1.5 solar simulator (LOT-QuantumDesign GmbH). The reference electrode was Ag/AgCl (saturated KCl) and a Pt mesh was used as the counter electrode. The sample was placed in a quartz-windowed PEC cell equipped with an O-ring to fix the area to 0.28 cm^2 . A solution of $0.3 \text{ M K}_2\text{SO}_4$ with 0.2 M phosphate buffer (pH 6.65) was used as an electrolyte with N_2 bubbling during the measurement.

For hydrogen detection, differential electrochemical mass spectrometry (DEMS) measurements were carried in a PEC cell with a thin electrolyte layer ($\sim 100 \mu\text{m}$) between the $\text{CuBi}_2\text{O}_4/\text{CdS}/\text{TiO}_2/\text{Pt}$ photocathode and a gas permeable membrane (ethylene-tetrafluoroethylene copolymer, Scimat) as shown in **Figure 4.4**.

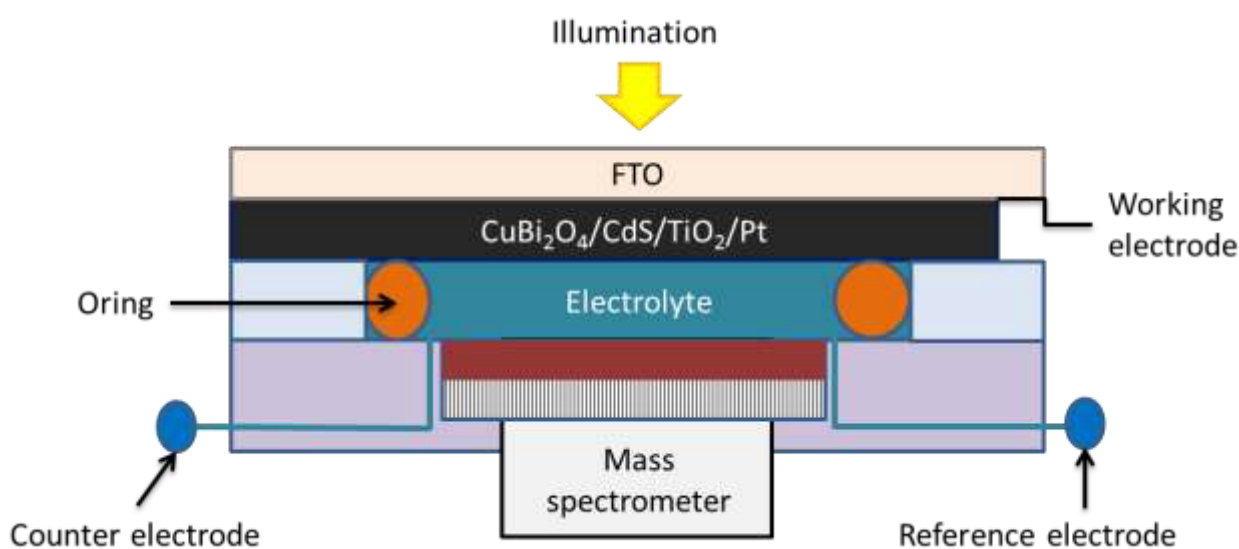


Figure 4.4. Sketch of the PEC cell used for the differential electrochemical mass spectrometry (DEMS) measurements.

The photocathode was illuminated from the backside using a 150 W Xe lamp with an AM 1.5 G filter. The light power was adjusted to approximately $650 \text{ mW}/\text{cm}^2$ for light wavelengths between 400 and 900 nm . The gas permeable membrane acted as an inlet to the first vacuum chamber of a dually pumped vacuum system. A variable leak valve connected the first chamber to the second high vacuum chamber, which housed the quadrupole mass spectrometer (Pfeiffer Vacuum, QMG 220 M1). The DEMS cell design was closed with stagnant electrolyte so all gaseous or volatile compounds formed by the photocathode were collected through the permeable membrane and detected by the mass spectrometer. Two small holes in the electrolyte channel allowed for filling of the cell and insertion of the Ag/AgCl reference electrode and Pt wire counter electrode. To calibrate the PEC cell the hydrogen signal was measured vs. current for a Pt sheet. Then the Faradaic efficiency

for the photocathode could be calculate using the following equation, under the assumption that the Pt sheet has 100 % Faradaic efficiency for the hydrogen evolution reaction,

$$\eta_{faradaic} = \frac{H_2 \text{ signal from photocathode}}{H_2 \text{ signal from Pt sheet}} \quad (4.6)$$

After each DEMS measurement the electrolyte was exchanged to avoid undesired shifts in the pH.

Results and Discussion

Crystal Structure, Morphology and Composition

To check the crystal structure and phase composition of the different CuBi₂O₄ films, X-ray diffraction (XRD) and Raman analysis were performed. **Figure 4.5** shows the XRD diffractograms of the forward gradient, homogeneous, and reverse gradient CuBi₂O₄ films on FTO (F : SnO₂) substrates. The JCPDS reference pattern for SnO₂ (PDF#00-046-1088) and tetragonal CuBi₂O₄ (PDF# 42-0334) are indicated with green and pink bars, respectively. All CuBi₂O₄ films show strong peaks at 20.88°, 28.01°, and 46.7°, which can be assigned to the (200), (211), and (411) lattice planes of tetragonal CuBi₂O₄, respectively. Scherrer analysis of the XRD patterns reveals that the CuBi₂O₄ films with forward and reverse gradients have similar crystallite sizes both in the range of 35-40 nm (see **Figure S B1**). For the homogenous and forward gradient CuBi₂O₄ films, two additional peaks at 35.44° and 38.68° appear. These two peaks can be attributed to the (002) and (111) reflexes of monoclinic CuO (PDF# 48-1548). This is probably due to premature thermal decomposition of Cu(NO₃)₂ · 3H₂O in the precursor solution to CuO which can occur at temperatures as low as 310 °C.¹⁴⁶ In addition, the two-step-diffusion-assisted spray pyrolysis process for the forward gradient involves spraying Cu(NO₃)₂ · 3H₂O as the top layer, which receive a higher flux of incident x-rays during the XRD measurement.

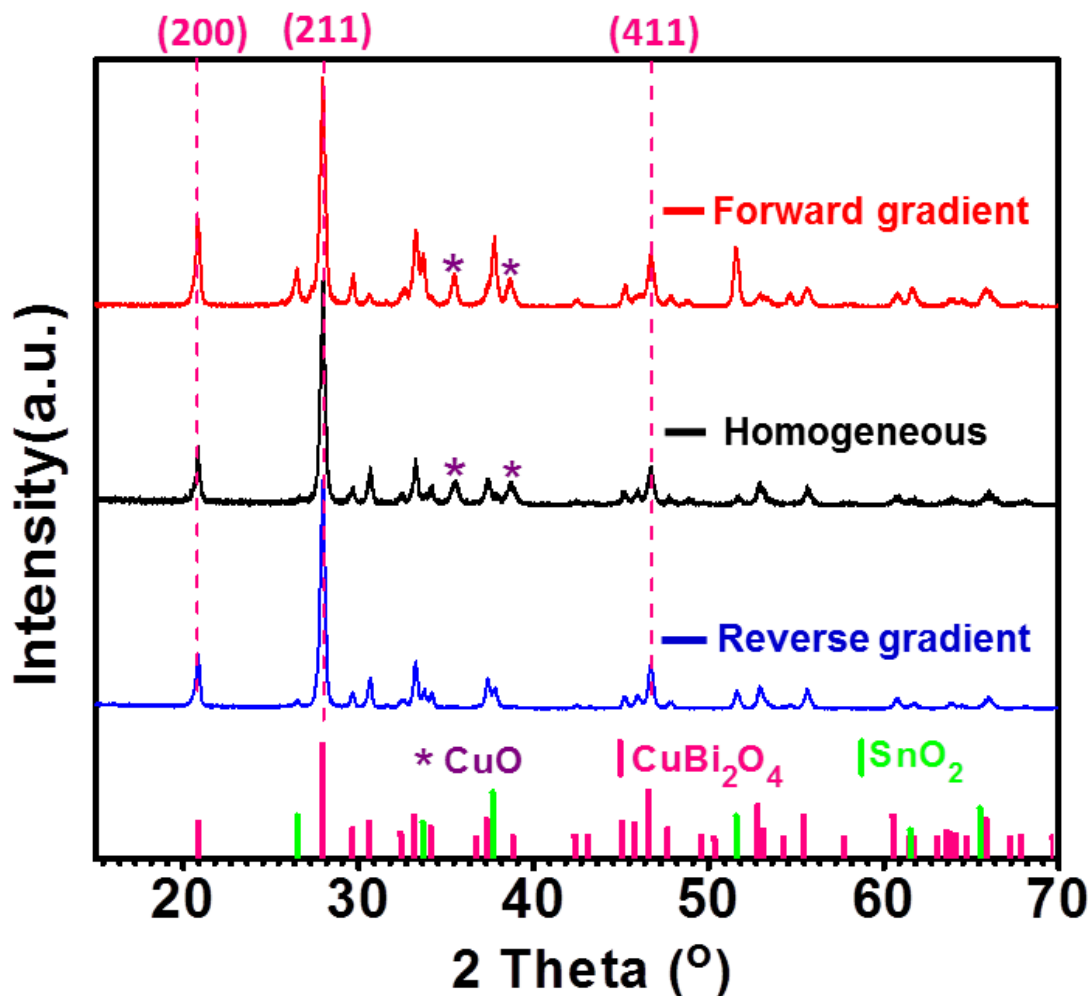


Figure 4.5. XRD diffractograms of ~ 270 nm CuBi_2O_4 films with forward gradient, without gradient, and with reverse gradient. All films were deposited on FTO substrates.

Figure 4.6 shows the Raman spectrums of the different CuBi_2O_4 samples. The main Raman bands for CuBi_2O_4 centered at 126, 261, 405, and 577 cm^{-1} were observed for all the films.¹⁴⁷⁻¹⁴⁸ The band at 126 cm^{-1} represents the A_{1g} mode and can be assigned to the translational vibration of the CuO_4 plane. The strong band at 261 cm^{-1} corresponds to the rotation of two stacked CuO_4 squares in opposite directions.¹⁴⁷⁻¹⁴⁹ The peak at 296 cm^{-1} can be attributed to either E_g or B_{2g} mode and may correspond to the CuO_4 deformation. The band observed at 405 cm^{-1} is attributed to the A_{1g} mode of the Bi-O stretching vibration, whereas the broad peak at 577 cm^{-1} can be ascribed to the A_{1g} mode of the in-plane breathing of CuO_4 squares.¹⁴⁷⁻¹⁴⁹ Apart from the CuBi_2O_4 peaks, the two additional peaks at ~ 296 and 344 cm^{-1} can be assigned to the A_g and B_g vibration of CuO , suggesting the existence of CuO .¹⁵⁰ Raman peaks for Bi_2O_3 are not observed. In general, the Raman results are well in accordance with the XRD results.

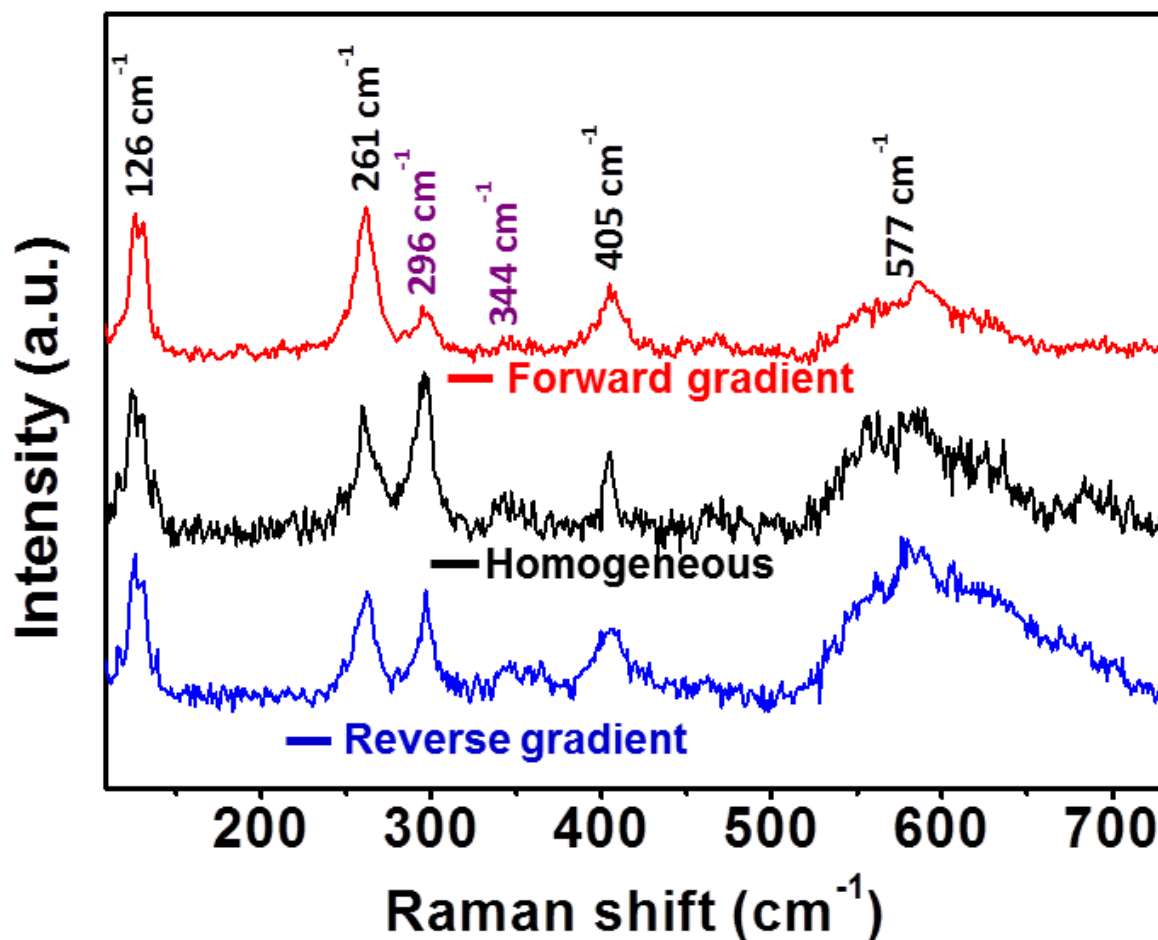


Figure 4.6. Raman spectrums for ~ 270 nm CuBi_2O_4 photocathodes with forward gradient, without gradient and with reverse gradient.

The morphologies of the CuBi_2O_4 films were characterized by scanning electron microscopy (SEM). **Figure 4.7** show cross-sectional SEM images of the different CuBi_2O_4 photocathodes, all films have a thickness of ~ 270 nm. The homogenous CuBi_2O_4 film is dense and compact as depicted previously in Chapter 3.¹³⁹ The forward gradient film approaches a cauliflower-type structure due to Bi-rich stem-shaped particles being coated with smaller Cu-rich nanoparticles. The reverse gradient shows the opposite with a thin Cu-rich layer coated with larger Bi-rich clusters. This is also confirmed by EDX mapping of the cross-sections. It is worth noting that the reverse gradient film shows a relatively high surface roughness compared to the other films as confirmed by atomic force microscopy (see **Figure S B2**). However, it produces substantially lower PEC performance (shown in the following section), so the specific surface area of the film can be ruled out as the main determinant in photoactivity. This is as expected, since we added H_2O_2 as an electron scavenger and therefore there should not be any kinetic limitations in the electrochemical reaction.

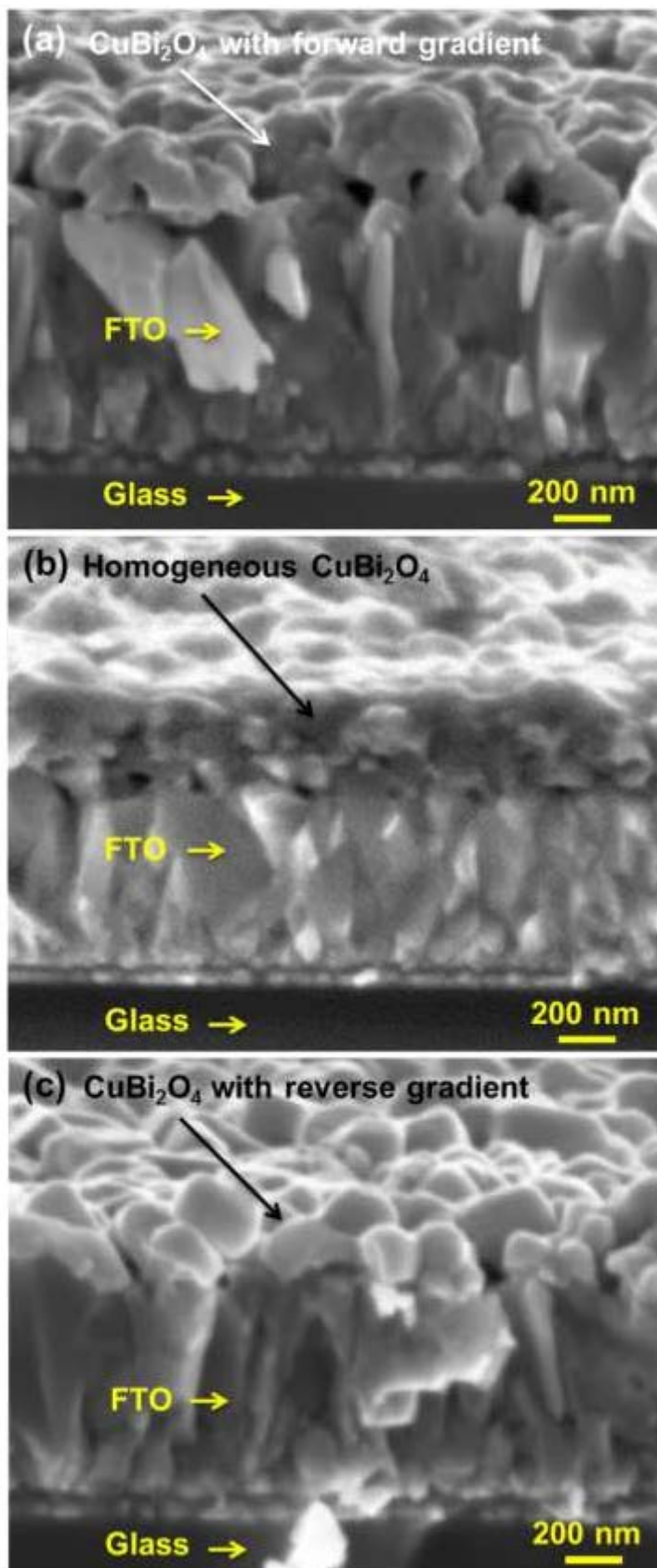


Figure 4.7. SEM images of ~ 270 nm CuBi_2O_4 thin films (a) with forward gradient, (b) without gradient and (c) with reverse gradient.

The elemental composition and distribution were investigated by energy dispersive X-ray (EDX) spectroscopy. **Figure 4.8a** shows a cross-section SEM image of a forward gradient CuBi_2O_4 photocathode with an EDX mapping overlaid. It is clear that the Cu content decreases from the top to the bottom while the Bi content increases from the bottom to the top. A linear scan of the EDX mapping was performed in the direction indicated by the green arrow in **Figure 4.8a** and the element count is plotted in **Figure 4.8e**. This confirms that a gradient in the Cu:Bi ratio is indeed created within the forward gradient CuBi_2O_4 photocathode. In contrast, a gradient in the opposite direction was confirmed for the CuBi_2O_4 photocathodes with reverse gradient, as shown in **Figure S B3**. Although the Cu : Bi gradient in the reverse gradient film is not nearly as obvious as in the forward gradient film, the Cu : Bi ratio at the surface of the reverse gradient film is clearly lower than the Cu : Bi ratio deeper in the film. This is probably due to the different film formation mechanisms. For the forward gradient film, copper is deposited on top of Bi_2O_3 , which can be seen as a host structure for the small copper ions. In this case the film does not go through dramatic structural and morphological changes as the copper ions diffuse in. For the reverse gradient film, the CuO bottom layer must undergo significant structural changes to incorporate the relatively large bismuth ions and form CuBi_2O_4 .

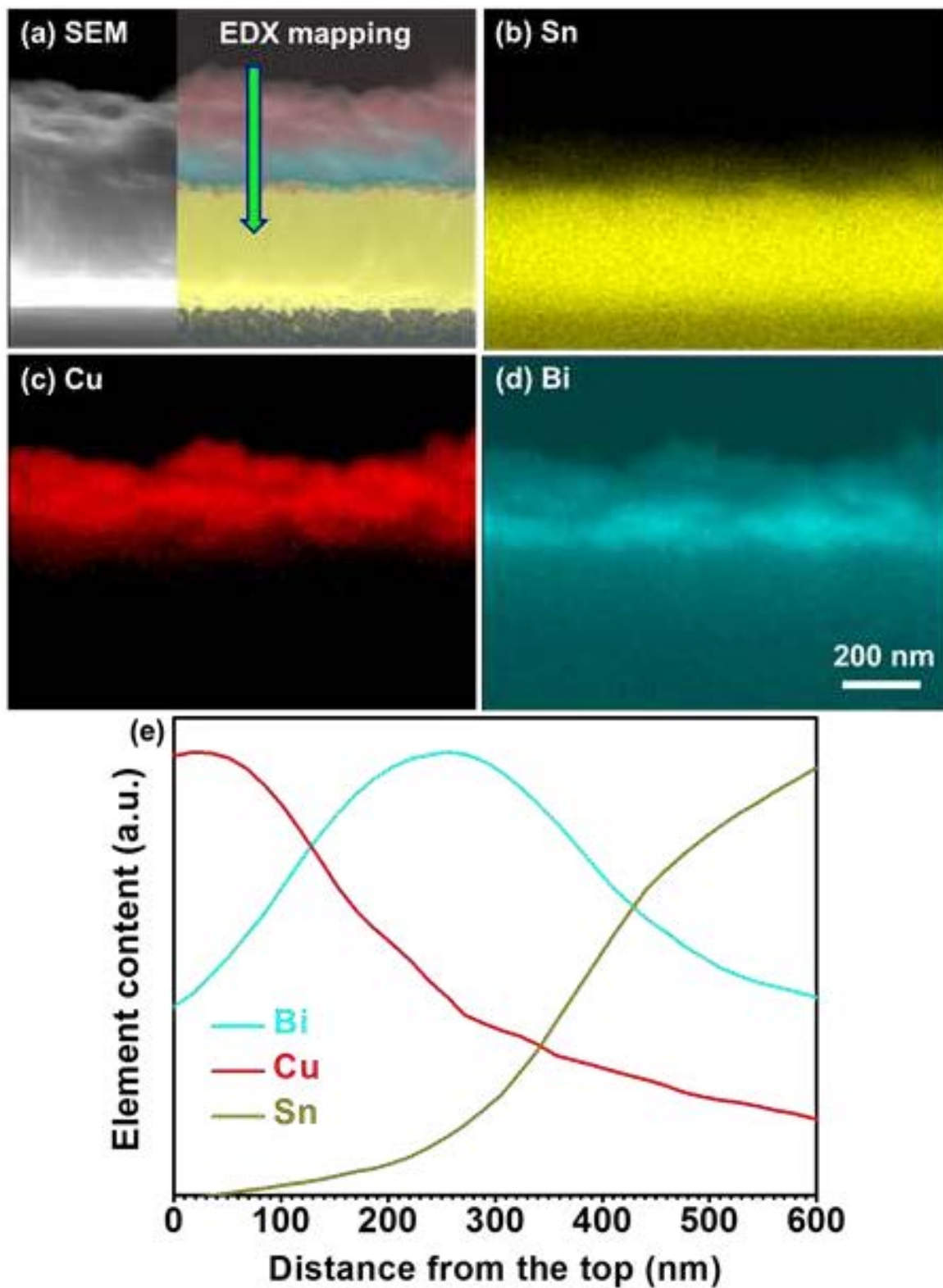


Figure 4.8. (a) SEM image with EDX mapping overlaid, (b) Sn distribution, (c) Cu distribution, (d) Bi distribution, and (e) linear scan of each elemental distribution in the direction of the blue arrow for a forward gradient CuBi_2O_4 photocathode.

PEC Performance and Optical Properties

Figure 4.9a shows a chopped linear sweep voltammetry (LSV) scan for three different CuBi_2O_4 photocathodes synthesized with a uniform CuBi_2O_4 composition (homogenous) or with gradient self-doping (forward and reverse). The homogeneous CuBi_2O_4 photocathodes were prepared by the optimized recipe as described in Chapter 3,¹³⁹ while the gradient self-doped CuBi_2O_4 photocathodes were fabricated using the two-step-diffusion-assisted spray pyrolysis process described in the experimental section. All three photocathodes were synthesized on FTO substrates to a CuBi_2O_4 thickness of ~ 270 nm.

All the measurements were performed with back illumination (FTO substrate side), which shows slightly higher photocurrent density than with front illumination, as shown in **Figure S B4**. To probe the bulk properties of CuBi_2O_4 , H_2O_2 was added to the electrolyte as an electron scavenger to avoid kinetic limitations. The CuBi_2O_4 photocathode with the forward gradient shows higher PEC performance than the homogeneous photocathode for a wide range of film thicknesses, as demonstrated in **Figure 4.9b** in which the photocurrent densities at 0.6 V vs. RHE were extracted from LSV measurements and plotted as a function of the CuBi_2O_4 film thickness. CuBi_2O_4 photocathodes with a reverse gradient were only tested at one thickness but produced substantially lower photocurrent than the homogeneous film. At 0.6 V vs. RHE, the ~ 270 nm CuBi_2O_4 photocathodes with a forward gradient produce a record photocurrent density of -2.5 mA/cm.^{242, 107, 132, 139}

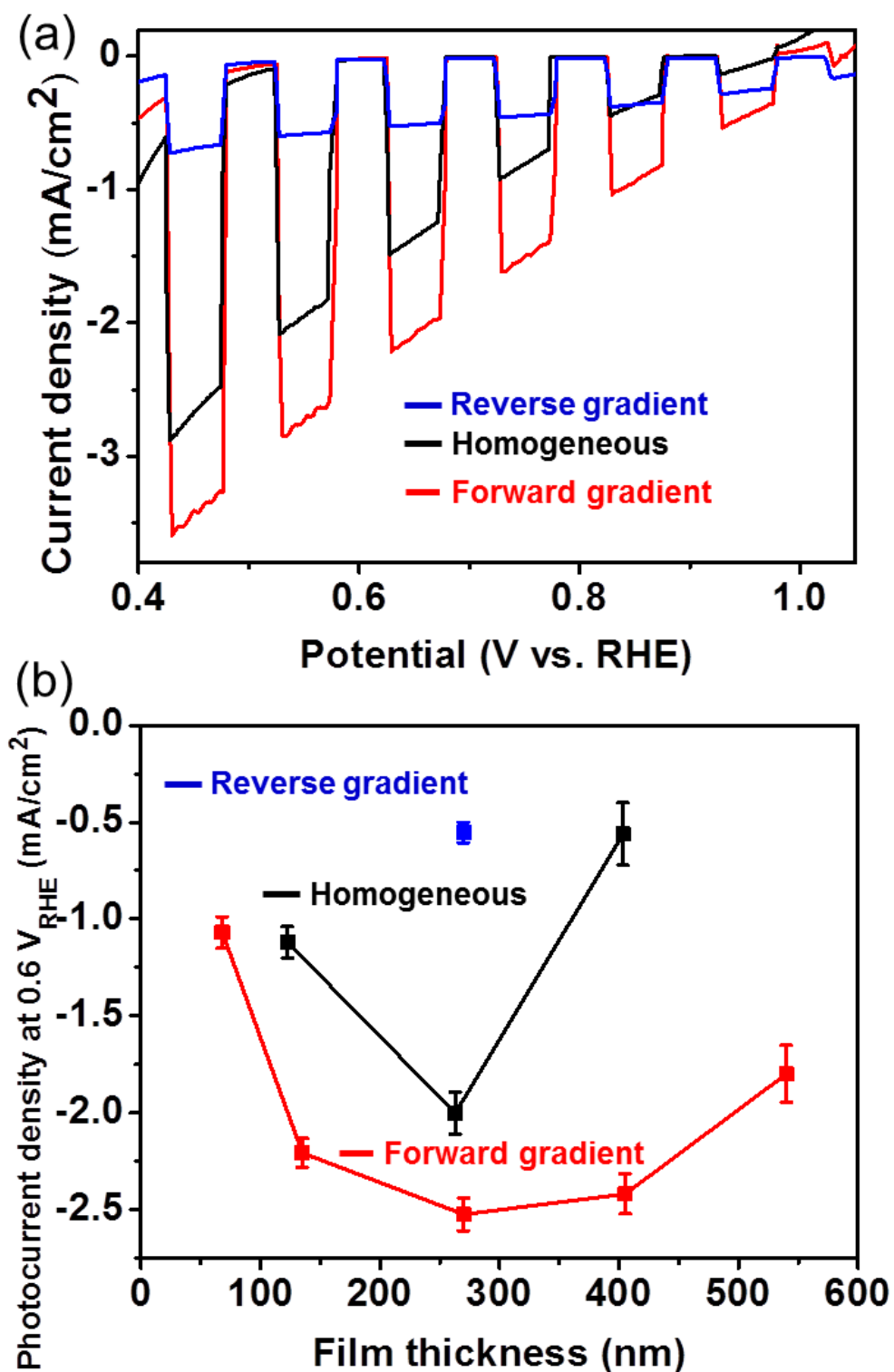


Figure 4.9. (a) Chopped LSV scans for CuBi_2O_4 photocathodes synthesized to a thickness of ~ 270 nm with uniform composition (homogeneous) or with gradient self-doping (forward and reverse); (b) Average photocurrent densities at 0.6 V vs. RHE as a function of film thickness extracted from LSV scans (see **Figure S B5** for LSV scans). The measurements were performed in $0.3 \text{ M K}_2\text{SO}_4$ and 0.2 M phosphate buffer ($\text{pH } 6.65$) with H_2O_2 under back illumination.

IPCE and APCE were carried out to quantify the quantum efficiency of the different CuBi₂O₄ photocathodes. **Figure 4.10a** shows the APCE spectra for each photocathode measured at 0.6 V vs. RHE under back illumination. The APCE values were calculated using the IPCE (see **Figure S B6**, **Figure S B7**, and **Figure S B8**) and the absorbance spectra shown in **Figure 4.10b**. For the most intense region of the AM 1.5 solar spectrum (420 to 800 nm), the CuBi₂O₄ photocathode with a forward gradient shows significantly higher APCE than the homogeneous CuBi₂O₄ photocathode, which is consistent with its improved PEC performance. Conversely, the CuBi₂O₄ photocathode with a reverse gradient exhibits remarkably lower APCE than the homogeneous CuBi₂O₄ photocathode for wavelengths above 420 nm. No significant difference in absorbance was observed among the different CuBi₂O₄ films. Here, the APCE was measured with H₂O₂ added to the electrolyte as an electron scavenger so the injection efficiency can be assumed to be 100 % and therefore the APCE can really represent the charge separation efficiency. At 550 nm, the forward gradient, homogeneous, and reverse gradient CuBi₂O₄ photocathodes show APCE (charge separation efficiency) of 34 %, 22 % and 9 %, respectively. This means the forward gradient indeed facilitates the charge separation efficiency whereas the reverse gradient hinders it.

For short wavelengths (≤ 420 nm), the APCE values of homogeneous and reverse gradient films are actually higher than that of the forward gradient films. One possible explanation for this is that the higher energy, shorter wavelength photons generate more electron-hole pairs near the FTO/CuBi₂O₄ interface (due to the high absorption coefficient). For the forward gradient films, this region has a higher concentration of Cu vacancies (vide infra) and consequently a higher re-combination rate. Whereas electron-hole pairs generated further into the CuBi₂O₄ film by lower energy light are more efficiently separated by the internal electric-field.

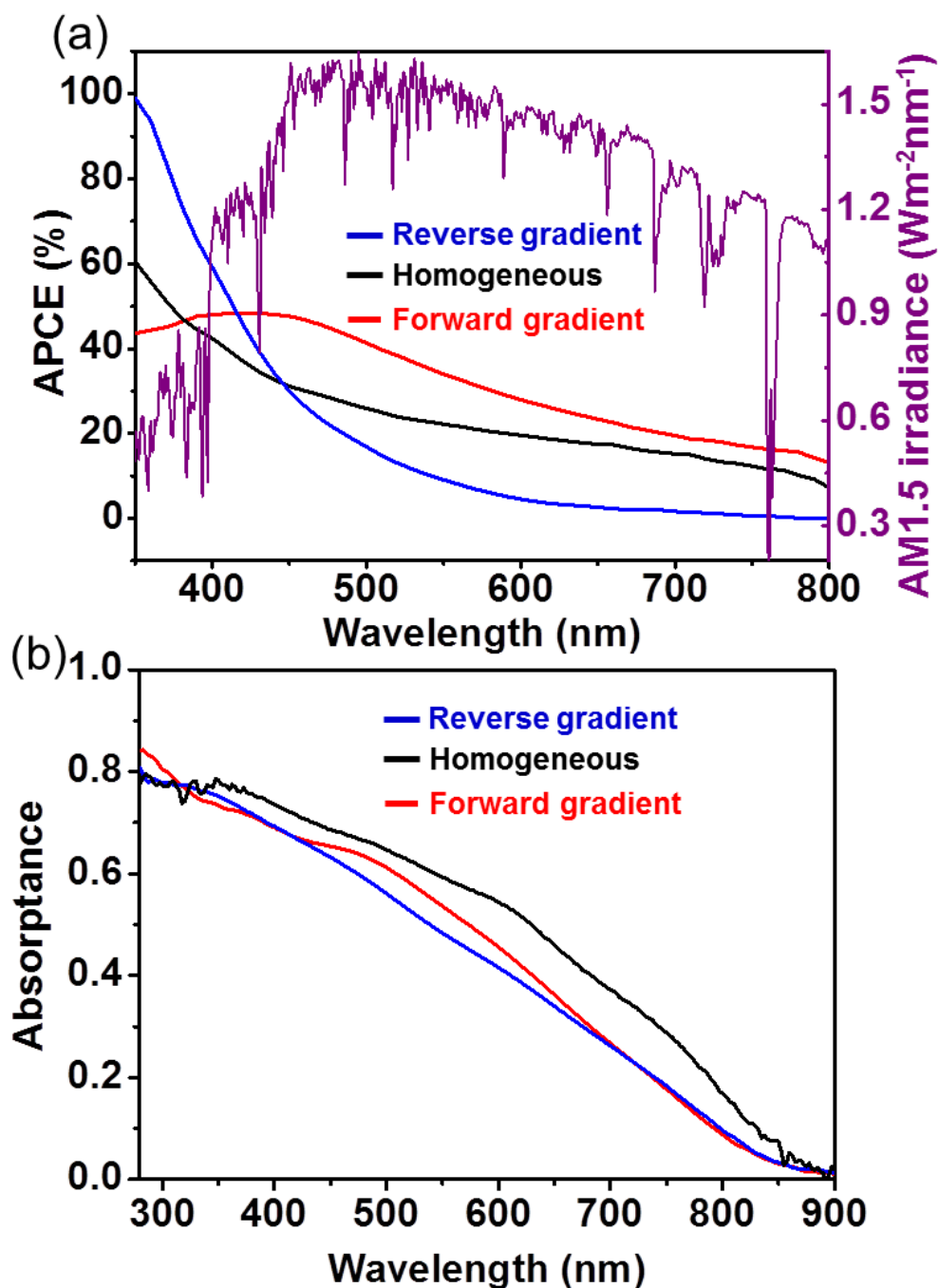


Figure 4.10. (a) APCE spectra along with the AM 1.5 irradiance spectrum; and (b) Absorption spectra for different CuBi₂O₄ photocathodes. All films have thickness of ~270 nm.

We note that when H₂O₂ is used as an electron scavenger for photoelectrochemical tests, current doubling is possible. To try to exclude the possibility of current doubling we tested the CuBi₂O₄ photocathodes in other kinetically facile redox couples as well, including FeCl₂/FeCl₃ (Fe²⁺/Fe³⁺) and NaI/I₂ (3I⁻/I₃⁻) in acetonitrile. Unfortunately, FeCl₂/FeCl₃ resulted in extremely high dark currents at potentials more negative than 0.6 V vs. NHE (**Figure S B9**) and NaI/I₂ produced large transient spikes in the photocurrent (**Figure S B10**), presumably due

to recombination or back reactions at the photocathode surface.¹⁵¹⁻¹⁵² We therefore conclude that FeCl₂/FeCl₃ and NaI/I₂ are not effective electron scavengers for our CuBi₂O₄ Films. In our previous study we tested homogeneous CuBi₂O₄ photocathodes in KOH with O₂ bubbling as an electron scavenger; however, O₂ also has the possibility of current doubling at low light intensities and transient spikes in photocurrent were observed.^{43, 130} Of all the electron scavengers that we tested, H₂O₂ was the only one that completely eliminated the transient spikes in photocurrent and prevented high dark current thereby allowing us to probe the charge separation efficiency within the CuBi₂O₄ films.

Improving Charge Separation by Gradient Self-doping

In order to understand how the forward and reverse gradients affect the charge separation efficiency and the PEC performance, we looked into the bulk properties of different films. The carrier mobility, lifetime, and diffusion length of the different CuBi₂O₄ films were investigated using time resolved microwave conductivity (TRMC) measurements. **Figure 4.11** shows the TRMC signal as a function of time for ~270 nm CuBi₂O₄ films with forward gradient, without gradient, and with reverse gradient.

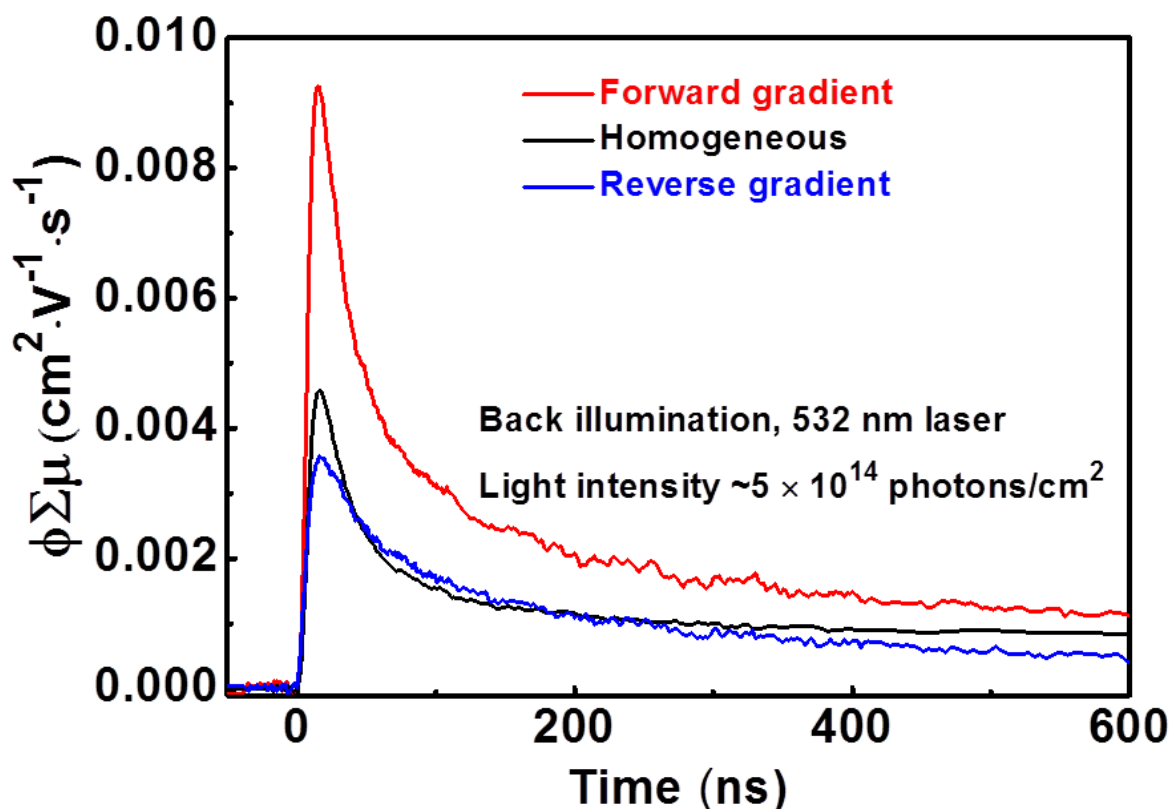


Figure 4.11. TRMC signal for ~270 nm CuBi₂O₄ films deposited on quartz substrates (a) with forward gradient; (b) without gradient; and (c) with reverse gradient.

The charge carrier mobilities (μ) were extracted from the peak TRMC signals ($\phi\Sigma\mu_{\max}$), while the charge carrier lifetimes were deduced from the decay of the curve. The fitting can be found in **Figure S B11**. The corresponding diffusion lengths were calculated from the charge carrier mobilities and lifetimes. The TRMC results are summarized in **Table 4.2**.

Table 4.2. Summary of the charge carrier mobility ($\phi\Sigma\mu_{\max}$), time constants (τ_1 and τ_2), and the corresponding diffusion lengths (L_{D1} and L_{D2}). The error estimates reflect the spread in the measured values for different samples.

CuBi ₂ O ₄ film	$\phi\Sigma\mu_{\max}$ ($10^{-3} \text{ cm}^2 \text{ V}^{-1} \text{ s}^{-1}$)	τ_1 (ns)	τ_2 (ns)	L_{D1} (nm)	L_{D2} (nm)
Forward gradient	9.3 ± 2.2	20.2 ± 3.6	142.6 ± 5.5	20.6 ± 3.5	60.0 ± 9.9
Homogeneous	4.6 ± 0.7	22.7 ± 0.7	153.0 ± 10.4	16.3 ± 0.3	42.4 ± 1.5
Reverse gradient	3.6 ± 0.8	35.0 ± 1.3	237.2 ± 6.3	16.9 ± 1.5	43.9 ± 3.5

The forward gradient, homogeneous, and reverse gradient films shown μ values of 0.0093, 0.0046, and $0.0036 \text{ cm}^2 \text{ V}^{-1} \text{ s}^{-1}$, respectively. The self-doped films show mobilities on the same order of magnitude as the un-doped homogeneous film, which is in sharp contrast to the significant decrease (20 times) in mobility observed when W was incorporated into BiVO₄ as an external dopant.¹³⁷⁻¹³⁸ Two different lifetimes were found for all three films, which is similar to CuBi₂O₄ films synthesized by drop-casting.⁴² The L_{D1}/L_{D2} values for the forward gradient, homogeneous, and reverse gradient films have are 21 nm/60 nm, 16 nm/42 nm, and 17 nm/44 nm, respectively.

The charge carrier diffusion length for the different films was compared since it is an important factor in determining the charge separation of a PEC material. As summarized in **Table 4.2**, all the films show charge carrier diffusion lengths on the same order of magnitude. However, the photocurrent density of the forward gradient film is ~ 5 times higher than that of the reverse gradient film, as shown in **Figure 4.9**. Such a small difference in charge carrier diffusion lengths cannot explain the large difference in photocurrent. Other factors must play a bigger role in affecting the charge separation efficiency and PEC performance.

We continued to investigate how the Cu : Bi ratio affects the Fermi level and valence band edge of CuBi₂O₄. The optimized spray pyrolysis recipe was used to prepare homogeneous CuBi₂O₄ films with different stoichiometries: (a) Cu : Bi = 1 : 3, Cu-deficient CuBi₂O₄, (b) Cu : Bi = 1 : 2, stoichiometric CuBi₂O₄, and (c) Cu : Bi = 1 : 1, Cu-rich CuBi₂O₄.¹³⁹ **Figure 4.12** shows that the non-stoichiometric CuBi₂O₄ films still maintain the intrinsic tetragonal structure, as confirmed by XRD.

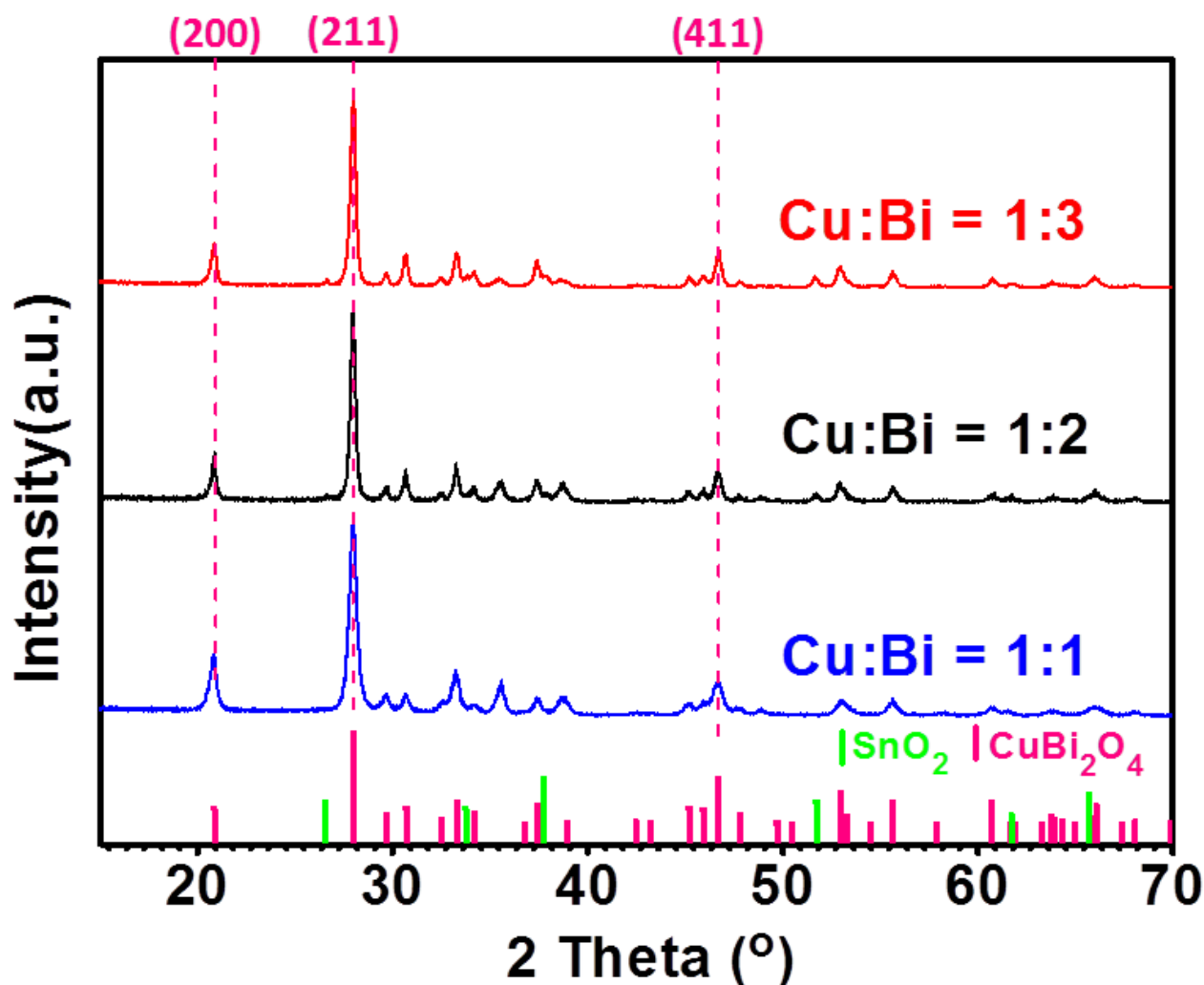


Figure 4.12. XRD diffractograms for homogeneous CuBi_2O_4 films with different stoichiometries: (a) $\text{Cu} : \text{Bi} = 1 : 3$, Cu-deficient CuBi_2O_4 , (b) $\text{Cu} : \text{Bi} = 1 : 2$, stoichiometric CuBi_2O_4 , and (c) $\text{Cu} : \text{Bi} = 1 : 1$, Cu-rich CuBi_2O_4 .

Mott-Schottky measurements were performed as shown in **Figure S B12**, **Figure S B13**, and **Figure S B14**. The surface area of each film was estimated by atomic force microscopy (AFM). The flat-band potential (φ_{fb}) was determined from the extrapolated x-axis intercepts of Mott-Schottky plots and the acceptor density (N_A) was calculated from the slopes. The results summarized in **Table 4.3** show that the φ_{fb} shifts to more positive potentials when the $\text{Cu} : \text{Bi}$ ratio decreases i.e. the relative Cu content decreases. Since a decrease in the $\text{Cu} : \text{Bi}$ ratio is expected to increase the concentration of V_{Cu}'' , this strongly supports our hypothesis that the Fermi level can be tailored simply by controlling the V_{Cu}'' . Furthermore, a gradient in the $\text{Cu} : \text{Bi}$ ratio can lead to a gradient in Fermi level relative to the valence band position resulting in internal band-bending.

Table 4.3. ϕ_{fb} and N_A values for ~270 nm CuBi₂O₄ films with different Cu : Bi ratios.

CuBi ₂ O ₄ film	Cu : Bi ratio	ϕ_{fb} (V vs. RHE)	N_A (cm ⁻³)
Cu-deficient CuBi ₂ O ₄	1 : 3	1.25 ± 0.02	~7.3×10 ¹⁹
Stoichiometric CuBi ₂ O ₄	1 : 2	1.21 ± 0.01	~7.6×10 ¹⁸
Cu-rich CuBi ₂ O ₄	1 : 1	1.09 ± 0.02	~6.9×10 ¹⁸

This concept is illustrated in **Figure 4.13**. CuBi₂O₄ films with different Cu : Bi ratios possess different Fermi levels before contact, as shown in **Figure 4.13a**. After contact, the Fermi level will equilibrate so that the CB and VB bend at each interface as illustrated by **Figure 4.13b**. The band bending in the CuBi₂O₄ photocathode with a forward gradient is shown in **Figure 4.13c**, which would facilitate charge separation by pushing electrons towards the CuBi₂O₄-electrolyte interface while pulling holes towards the back contact.

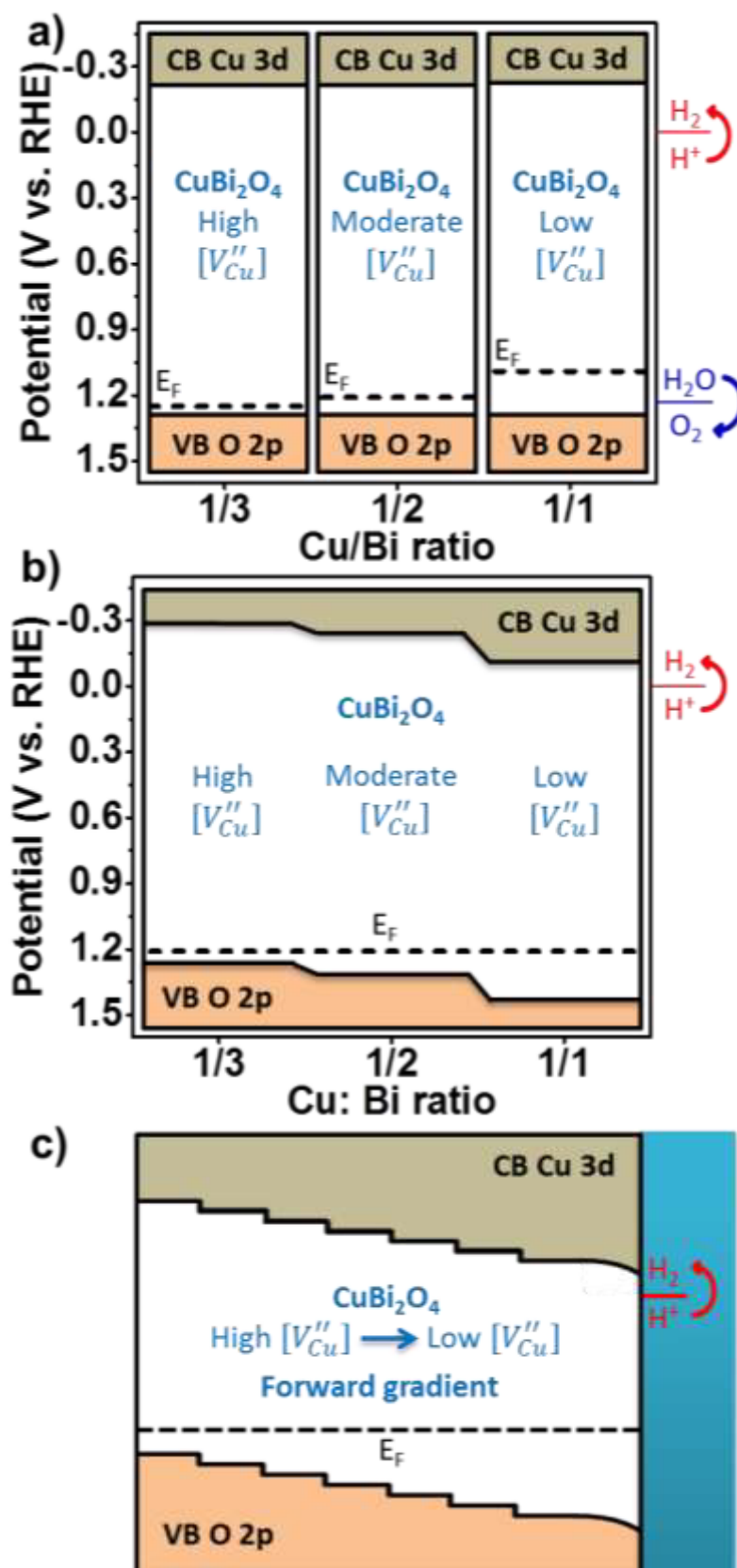


Figure 4.13. (a) Flat-band potential of homogeneous CuBi_2O_4 films with different stoichiometries; (b) The formation of a CuBi_2O_4 homojunction when brought in to contact; (c) The formation of CuBi_2O_4 with a forward gradient.

Now a brief summary of the main results in this Chapter would lead to a reasonable explanation for the improvement in PEC activity for the CuBi_2O_4 with forward gradient. Recall that the morphology and charge carrier diffusion lengths were ruled out as main determinants for PEC activity in section 4.3.1, section 4.3.2, and section 4.3.3. We finally come to the conclusion that the observed improvement in charge separation efficiency and PEC performance is mainly due to the internal electrical field induced by the forward gradient in $[V''_{\text{Cu}}]$.

Hydrogen Production and Stability under Operation

Since the ultimate goal is to utilize CuBi_2O_4 as a material for hydrogen production, we tested the forward gradient CuBi_2O_4 photocathodes under water splitting conditions without electron scavenger. As we know, many Cu-based metal oxides, including CuO and CuBi_2O_4 , are seriously limited in use as photocathodes due to photo-corrosion under the operating conditions of water splitting.¹⁵³ This is also the case for our forward gradient CuBi_2O_4 films, as confirmed by the chopped LSV scan performed in pH neutral electrolyte with Ar bubbling (shown in **Figure 4.14**). At potentials more negative than 0.4 V vs. RHE the CuBi_2O_4 photocathode shows a rapid increase in dark current due to electrochemical corrosion. The Cu^{2+} in CuBi_2O_4 is most likely reduced as reported previously.⁴²

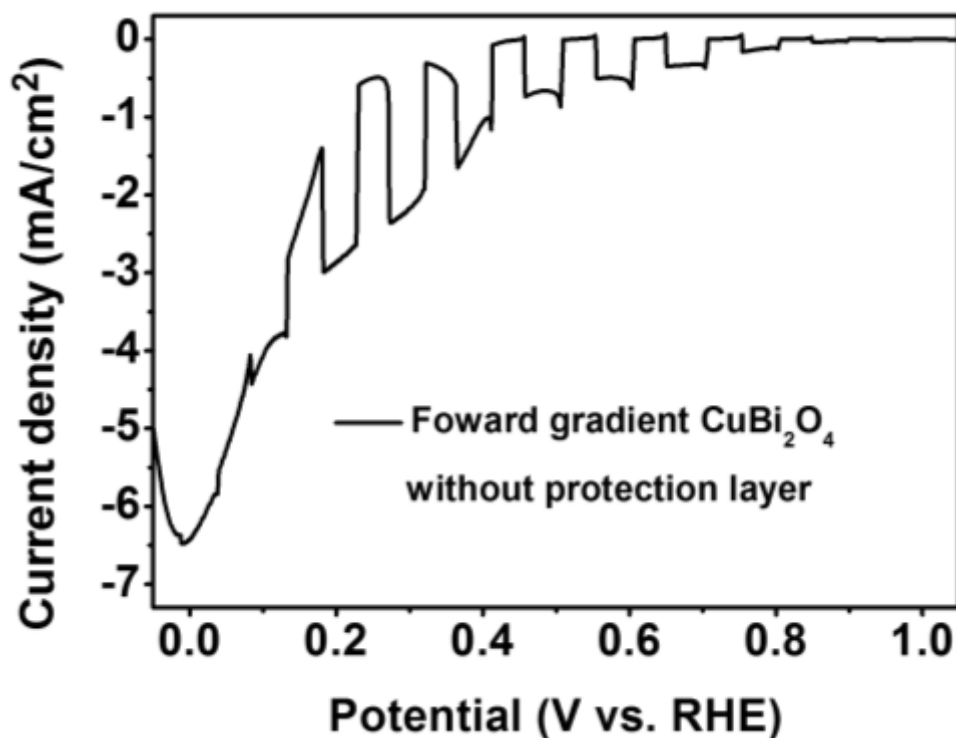


Figure 4.14. Chopped LSV for a forward gradient CuBi_2O_4 photocathode. The measurement was performed in 0.3 M K_2SO_4 and 0.2 M phosphate buffer (pH 6.65) with Ar bubbling under back illumination.

TiO_2 has been shown to be suitable to protect photoelectrodes from photo-corrosion due to its suitable alignment of the conduction band edge with the hydrogen redox potential, high transparency and high stability.¹⁵⁴ For example, a sputtered TiO_2 layer on top of a thin Ti metal layer was shown to protect the Si photocathode for H_2 evolution.¹⁵⁵ TiO_2 deposited on Cu_2O by atomic layer deposition was demonstrated to not only protect the absorber material but also facilitate charge extraction.¹⁵⁵ Recently, CuO photocathodes were successfully protected by CdS/TiO_2 multilayers with Pt as an electrocatalyst for the hydrogen evolution reaction. The protected $\text{CuO}/\text{CdS}/\text{TiO}_2/\text{Pt}$ photocathodes showed photocurrent densities higher than $-1 \text{ mA}/\text{cm}^2$ at 0 V vs. RHE with a Faradiac efficiency of nearly 100 % for hydrogen production.⁵⁰ Here we tried the same protection layer for our CuBi_2O_4 photocathodes with a forward gradient to improve their stability. **Figure 4.15** shows the cross section SEM image of the forward gradient $\text{CuBi}_2\text{O}_4/\text{CdS}/\text{TiO}_2/\text{Pt}$ photocathode.

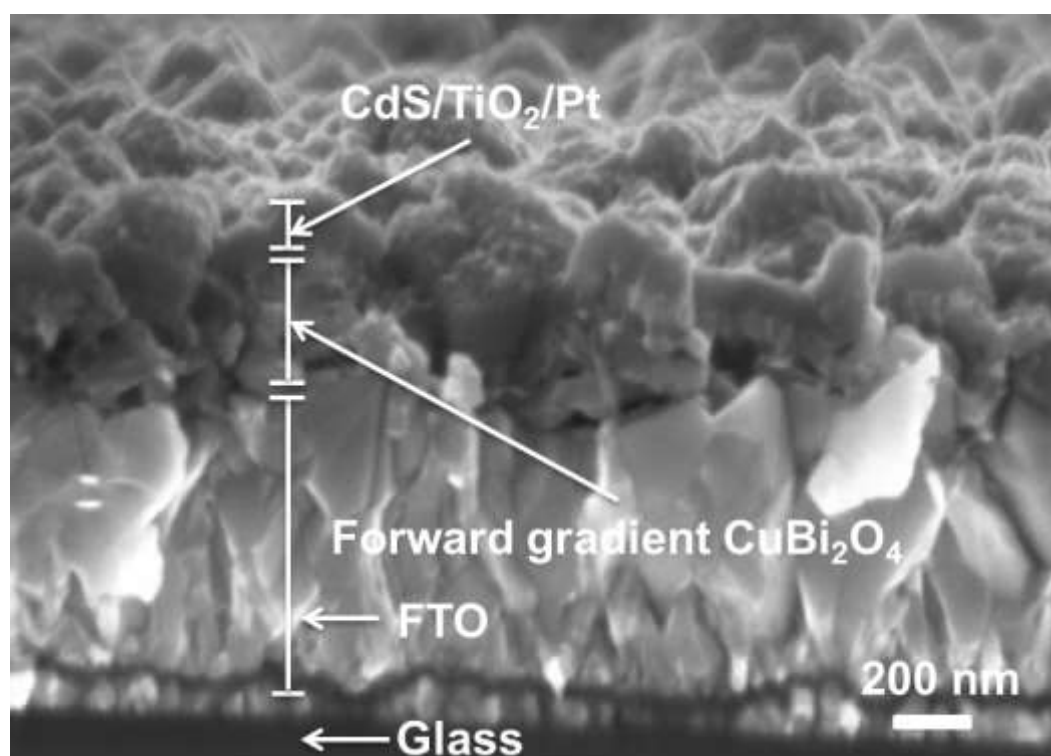


Figure 4.15. Cross section SEM image of a forward gradient $\text{CuBi}_2\text{O}_4/\text{CdS}/\text{TiO}_2/\text{Pt}$ photocathode with the different layers indicated.

The forward gradient $\text{CuBi}_2\text{O}_4/\text{CdS}/\text{TiO}_2/\text{Pt}$ photocathode was PEC tested, as shown by the chopped LSV in **Figure 4.16a**. In contrast to the unprotected CuBi_2O_4 photocathode (**Figure 4.14**), the protected $\text{CuBi}_2\text{O}_4/\text{CdS}/\text{TiO}_2/\text{Pt}$ photocathode (**Figure 4.16a**) shows nearly zero dark current at all the measured potentials. The protected $\text{CuBi}_2\text{O}_4/\text{CdS}/\text{TiO}_2/\text{Pt}$ photocathode produces a photocurrent density of $-0.9 \text{ mA}/\text{cm}^2$ at 0.0 V vs. RHE. Indeed, the $\text{CdS}/\text{TiO}_2/\text{Pt}$ protects the CuBi_2O_4 from fast corrosion.

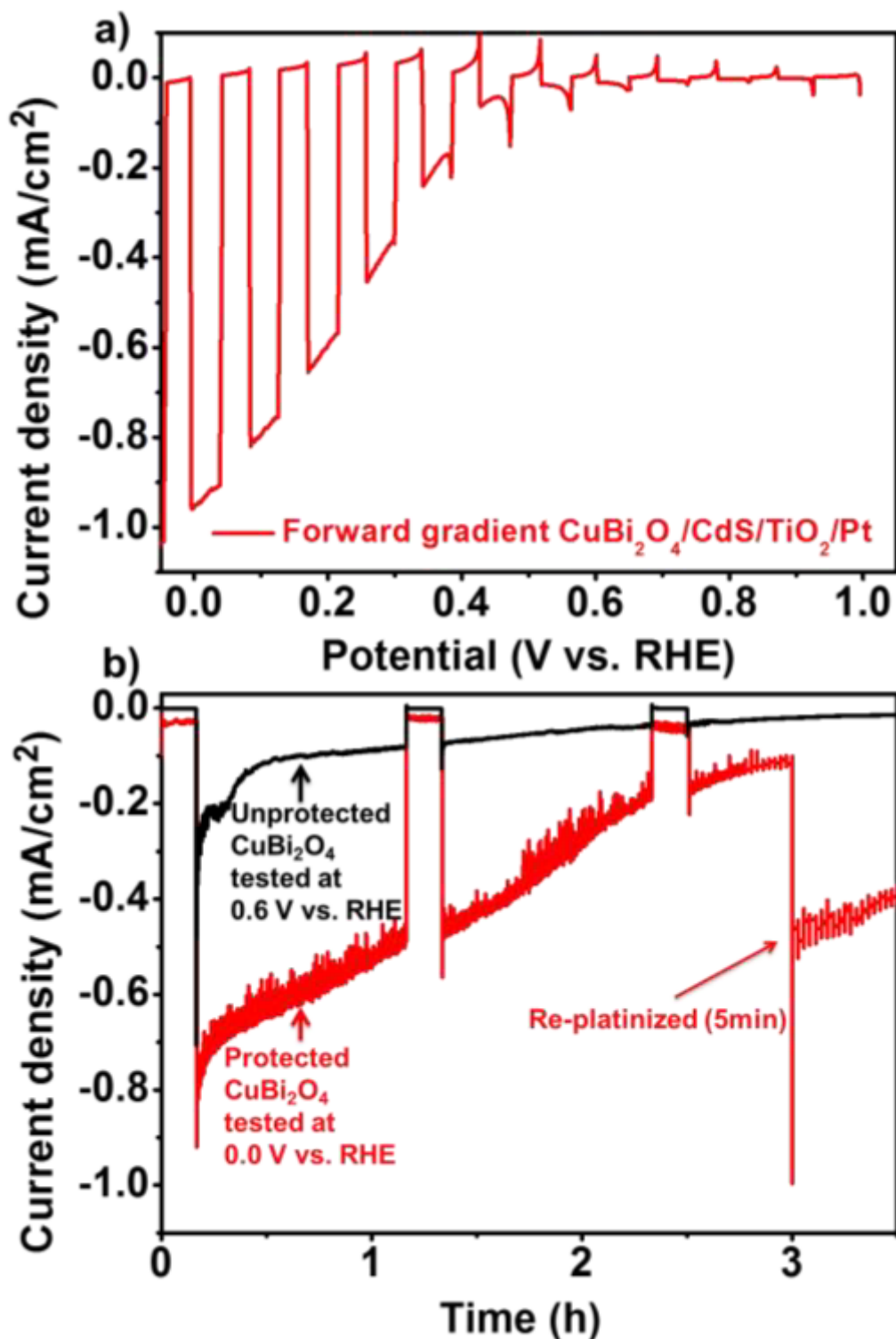


Figure 4.16 (a) Chopped LSV for a forward gradient $\text{CuBi}_2\text{O}_4/\text{CdS}/\text{TiO}_2/\text{Pt}$ photocathode, and (b) Constant potential measurements for an unprotected CuBi_2O_4 photocathode at 0.6 V vs. RHE (black line) and a forward gradient $\text{CuBi}_2\text{O}_4/\text{CdS}/\text{TiO}_2/\text{Pt}$ photocathode at 0.0 V vs. RHE (red line). Measurements were done in 0.3 M K_2SO_4 and 0.2 M phosphate buffer (pH 6.65) with Ar bubbling under front ($\text{CuBi}_2\text{O}_4/\text{CdS}/\text{TiO}_2/\text{Pt}$) and back (CuBi_2O_4) illumination.

To test the long term stability of the bare CuBi₂O₄ as well as the protected CuBi₂O₄/CdS/TiO₂/Pt photocathodes, their photocurrent densities were measured in pH neutral electrolyte with nitrogen bubbling at a constant potential for several hours under periodically chopped illumination, as shown in **Figure 4.16b**. Even at a relatively positive potential of 0.6 V vs. RHE, the unprotected CuBi₂O₄ photocathode corrodes very fast as indicated by the immediate decay of the black line and a decrease in photocurrent density of 89 % within 1 h. In contrast, the CuBi₂O₄/CdS/TiO₂/Pt shows a much more gradual decay in photocurrent density over the course of several hours. A significant portion of this decay is likely due to gradual delamination of the Pt electrocatalyst, as confirmed by the restore of photocurrent density when the photocathode was re-platinized (for 5 min instead of the initial 10 min) after 3 h. This result suggests that the forward gradient CuBi₂O₄ photocathodes can be further stabilized by optimizing the coverage of the protection layer coverage and adhesion of the electrocatalyst.

The total charge that has passed for the red curve in **Figure 4.16b** is estimated to be - 3601 mC/cm² by integrating the photocurrent density of the CuBi₂O₄/CdS/TiO₂/Pt photocathode over the time of the constant potential measurement and surface area. The obtained value is more than 10 times larger than the total charge needed to reduce all of the Cu²⁺ and Bi³⁺ in the CuBi₂O₄ film (- 471 mC/cm²). Therefore at least 87 % of the photocurrent density was used for another photo-reduction reaction, which was most likely proton reduction. In addition, gas bubbles were observed on the photocathode surface during the measurement, as illustrated in **Figure S B15**.

Lastly, we quantitatively confirmed hydrogen evolution and determined the Faradaic efficiency of the protected CuBi₂O₄/CdS/TiO₂/Pt photocathodes. For these, differential electrochemical mass spectrometry (DEMS) measurements were carried out. To quantify the hydrogen evolution, first we measured the hydrogen signal and current on a Pt sheet, as shown in **Figure 4.17**.

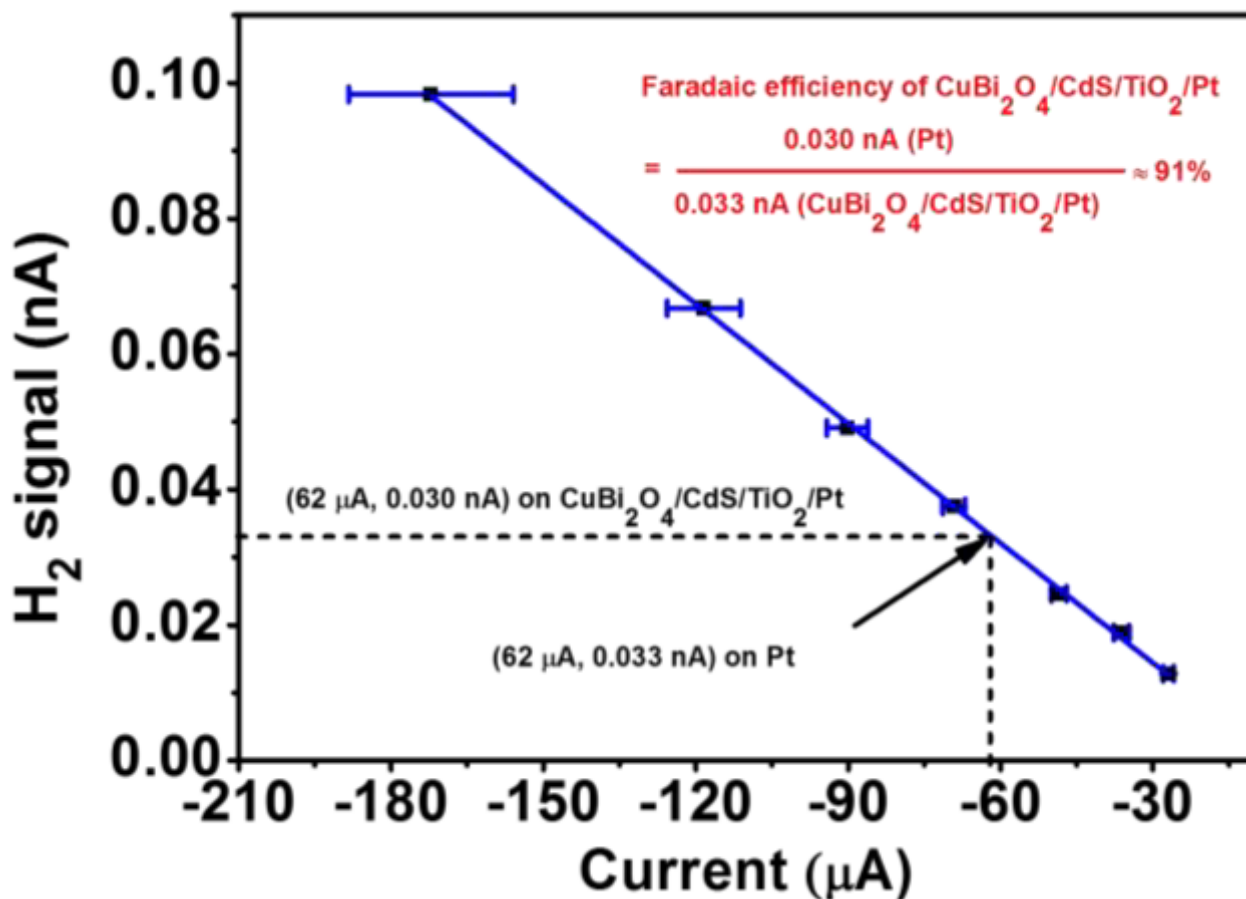


Figure 4.17. Correlation between the hydrogen signal and current on Pt. Measurements were done using a Pt sheet as the working electrode in 0.3 M K₂SO₄ and 0.2 M phosphate buffer (pH 6.65) under back illumination (to match the temperature of the photocathode measurements).

Then we performed the measurements on CuBi₂O₄/CdS/TiO₂/Pt photocathode. **Figure 4.18a** shows the current density (blue) and hydrogen signal (red) as a function of potential. The current density shows an onset potential at around 0.4 V vs. RHE, where the hydrogen signal also starts to rise. After 1 h PEC test at a constant potential of 0.0 V vs. RHE, the CuBi₂O₄/CdS/TiO₂/Pt photocathode maintained a current signal of -62 μA and a hydrogen signal of 0.030 nA, as shown in **Figure 4.18b**. Using the calibration curve in **Figure 4.17**, the Faradaic efficiency (η_{Faradaic}) was calculated to be ~91 % from **equation 4.6**.

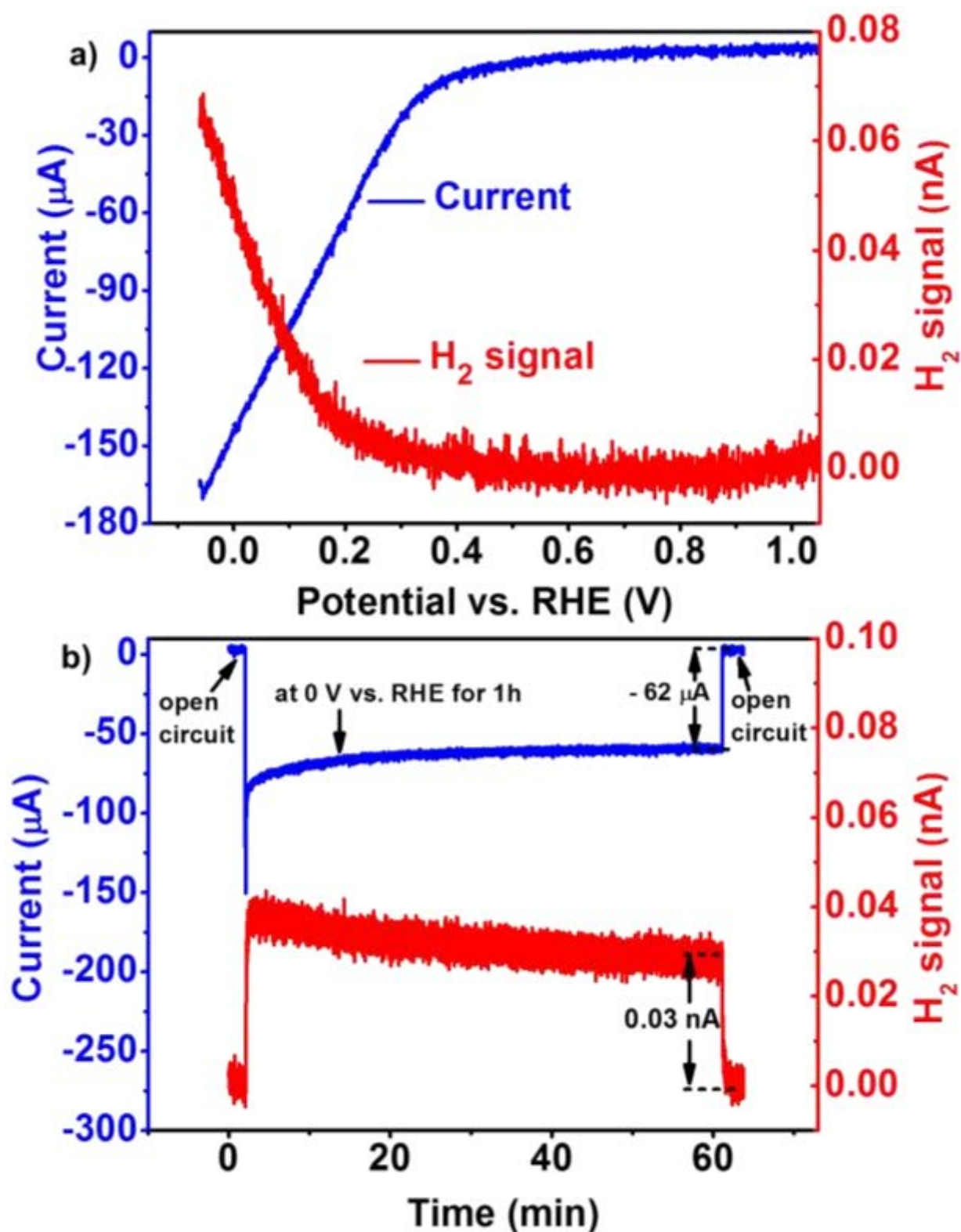
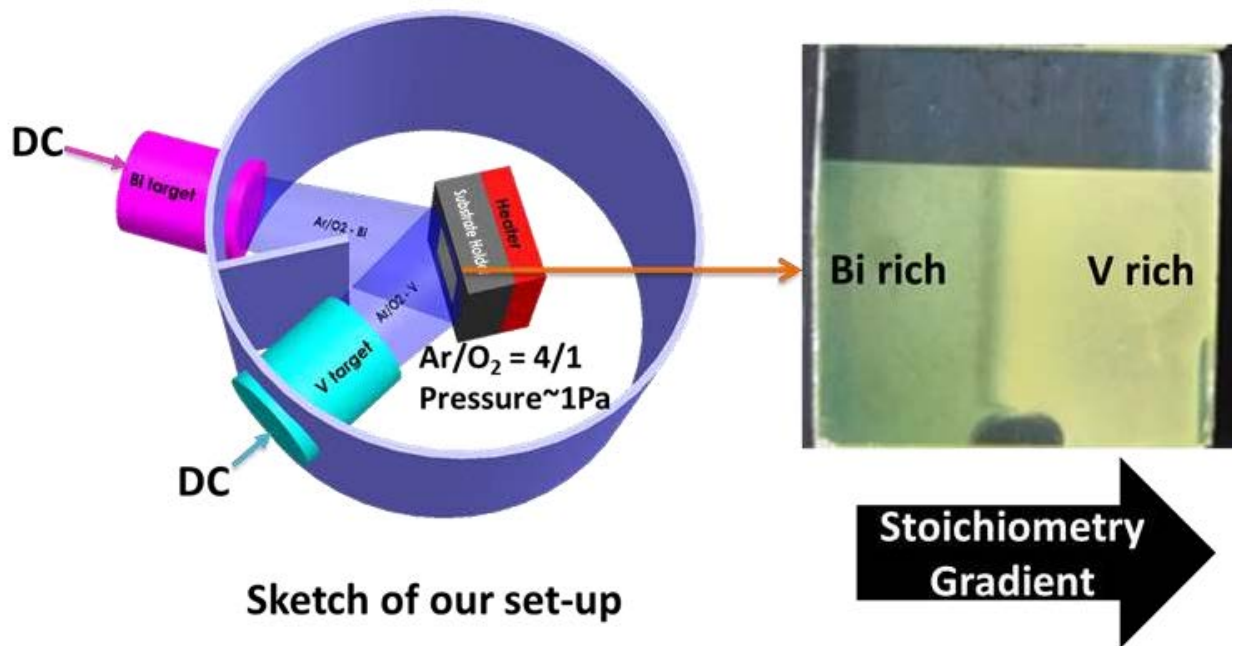


Figure 4.18. (a) DEMS LSV scans for a forward gradient $\text{CuBi}_2\text{O}_4/\text{CdS}/\text{TiO}_2/\text{Pt}$ photocathode with a scan rate of 2 mV/s; and (b) DEMS constant potential measurements for a forward gradient $\text{CuBi}_2\text{O}_4/\text{CdS}/\text{TiO}_2/\text{Pt}$ photocathode at 0.0 V vs. RHE, showing current (blue) and hydrogen signal (red). Measurements were done in 0.3 M K_2SO_4 and 0.2 M phosphate buffer (pH 6.65) under back illumination.

Conclusions

Gradient self-doped CuBi₂O₄ photocathodes were prepared by a simple two-step-diffusion-assisted spray pyrolysis process. Compared to homogeneous CuBi₂O₄ photocathodes, CuBi₂O₄ photocathodes with a forward gradient show highly improved charge separation efficiency and therefore increased PEC performance for reduction reactions, while CuBi₂O₄ photocathodes with a reverse gradient show reduced charge separation efficiency and consequently decreased PEC performance. This is attributed to the internal band bending created by the gradients in V''_{Cu} induced by the forward and reverse gradients in the Cu : Bi ratio. At 0.6 V vs. RHE, the forward gradient CuBi₂O₄ photocathodes produce record photocurrent densities for CuBi₂O₄ up to -2.5 mA/cm² (with H₂O₂ as an electron scavenger) under AM 1.5 simulated sunlight along with a charge separation efficiency of 34.0 % for 550 nm light. The gradient self-doping does not require the addition external dopants and as a result the tetragonal crystal structure and intrinsic charge carrier mobility of CuBi₂O₄ are maintained. The concept of using forward gradient self-doping to improve charge separation can be easily applied to other multinary metal oxides. To measure hydrogen evolution, the forward gradient photocathode was coated with a CdS/TiO₂ layer, followed by Pt deposition on top as an electrocatalyst. The CuBi₂O₄/CdS/TiO₂/Pt photocathode show highly improved stability compared to the bare CuBi₂O₄ and hydrogen was evolved at 0.0 V vs. RHE with a faradaic efficiency of ~91 %.

Chapter 5. Direct Current Magnetron Sputtering of Photoactive BiVO_4 : Role of Stoichiometry on Grain Size, Structure, Carrier Mobility and Lifetime



The main part of this Chapter will be submitted for publication: Wang, F.; Ellmer, K. et al. Reactively magnetron sputtered photoactive BiVO_4 films: structure-stoichiometry-electronic property relationships, 2017, prepared.

As described in Chapter 2, overall water splitting consists of two half reactions: the oxygen evolution reaction (OER) at the anode or photoanode and the hydrogen evolution reaction (HER) at the cathode or photocathode. To date most researchers have focused on n-type metal oxide photoanode materials for the OER rather than p-type metal oxides. Compared to the HER, the OER is actually more complex and challenging because it involves four sequential proton-coupled electron transfer steps as well as oxygen-oxygen bond formation. Nevertheless, significantly more progress has been made on metal oxide photoanode materials such as BiVO₄, a material for which photocurrents near its theoretical maximum efficiency have been reported.¹⁵⁶ In Chapters 3 and 4, we showed our efforts in developing CuBi₂O₄ as a new photocathode material for the HER. In this Chapter, we focus on BiVO₄, a well-established photoanode material for the OER, in an effort to demonstrate direct magnetron sputtering, a highly scalable synthesis technique, as a method for making metal oxide photoelectrodes. Additionally, direct magnetron sputtering using separate Bi and V metallic targets provides the opportunity to vary the V : Bi atomic ratio of the synthesized BiVO₄ thin films. We will show the effect of stoichiometry on grain size, electronic properties, and PEC performance of BiVO₄ thin film photoanodes. Time-resolved microwave conductivity (TRMC) measurements reveal strong dependence of carrier mobility and lifetime on the V : Bi ratio. Moreover, as the V : Bi ratio increases (i.e. excess vanadium is incorporated), the grain size increases and monoclinic BiVO₄ phase becomes more prominent. The improved crystallinity and the increased grain size at higher V : Bi ratios strongly correlates with improved electronic properties and hence increased photocurrent density. However, as the V : Bi ratio is increased from 1.06 to 1.29, V₂O₅ starts to phase segregate from BiVO₄ inducing new boundary defects and distortion of the BiVO₄ crystal structure causing the mobility and lifetime decrease along with the photocurrent density.

Introduction

BiVO₄, a multinary metal oxide, can exist in three different crystal structures: (a) tetragonal scheelite; (b) monoclinic scheelite; and (c) zircon type BiVO₄.¹⁵⁷ Of all the structures, each V is connected with four O atoms forming a tetrahedron, while each Bi is coordinated by eight O atoms forming a dodecahedral structure. In both tetragonal scheelite and monoclinic scheelite, each BiO₈ dodecahedron is surrounded by eight VO₄ tetrahedrons. In zircon type BiVO₄, each BiO₈ dodecahedron is surrounded by six VO₄ tetrahedrons instead of eight. Compared to tetragonal scheelite, the monoclinic scheelite shows more distortion in the Bi-O and V-O bonds. The distortion in the monoclinic scheelite is claimed to enhance the local polarization, improve the charge carrier separation, and consequently the photocatalytic activity.⁹⁸ The electronic structure is also correlated to the photocatalytic activity. The VB and CB of zircon-type BiVO₄ consist of O 2p orbitals and V 3d orbitals, respectively, while the charge transition in scheelite BiVO₄ occurs between Bi 6s or hybrid Bi 6s - O 2p orbitals and V 3d orbitals, respectively, as illustrated in **Figure 5.1**. Therefore, the scheelite BiVO₄ has smaller bandgap than the zircon-type BiVO₄.¹⁵⁸ The reduced bandgap for scheelite BiVO₄ has also been confirmed by DFT calculations.¹⁵⁹⁻¹⁶⁰ Of the three different structures, monoclinic BiVO₄ is found to be the most photocatalytically active and therefore it has attracted more attention as a photoanode material.

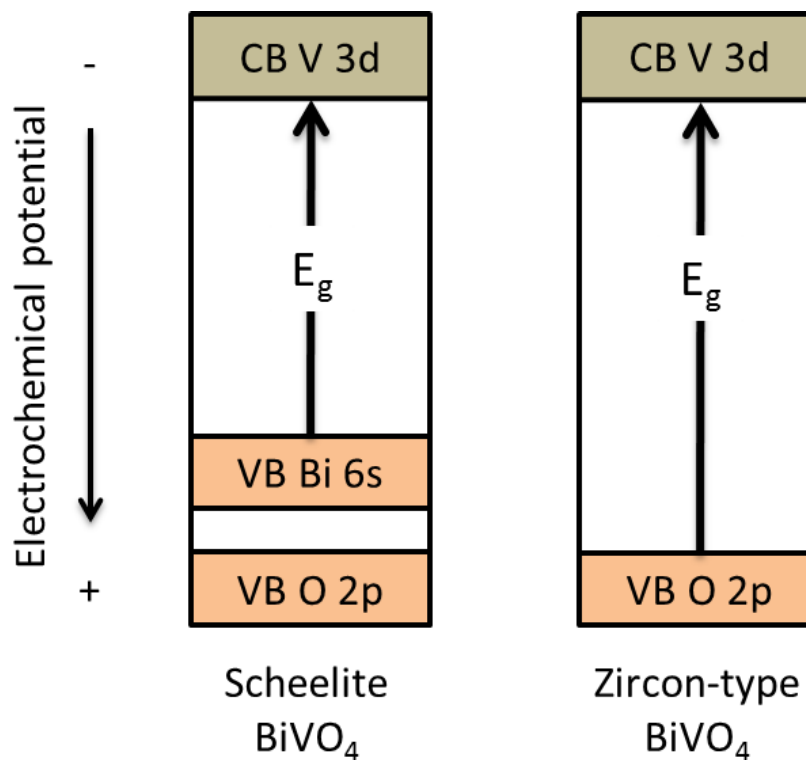


Figure 5.1. Schematic electronic structure of scheelite and zircon-type BiVO₄.

Monoclinic BiVO₄ is currently the highest performing metal oxide photoanode material for solar water splitting. It has a low bandgap of ~2.4 eV so it can absorb UV and visible light up to 520 nm. Theoretically, it can produce a maximum photocurrent density of ~7.5 mA/cm², corresponding to a maximum STH conversion efficiency of ~9.2%.^{58, 98-99} The valence band of monoclinic BiVO₄ lies significantly more positive than the water oxidation potential while its conduction band is close to the H₂/H⁺ redox potential.¹⁶¹⁻¹⁶² Moreover, it is estimated to have low effective masses for both electrons and holes, allowing for effective charge transport.¹⁶³⁻¹⁶⁴ In addition, BiVO₄ is composed of relatively inexpensive elements and it is non-toxic.¹⁰⁰

In recent years monoclinic BiVO₄ has been intensively investigated and as a result remarkable photocurrent densities of up to 6.7 mA/cm² (AM1.5, at 1.23 V vs. RHE) have been achieved.¹⁵⁶ Various synthesis methods such as hydrothermal preparation¹⁶⁵⁻¹⁶⁷, spin-coating¹⁶⁸⁻¹⁷⁰, spray pyrolysis,¹⁷¹⁻¹⁷³ and electrochemical deposition^{156, 174-175} have been applied to prepare small area BiVO₄ photoanodes. However, if such a material is to be used in practical water splitting applications, scale-up is one of the main challenges to be addressed.¹⁷⁶ Specifically, large-scale and cost-effective deposition technologies for the preparation of efficient photoelectrodes are needed.

Reactive magnetron sputtering (RMS) is an excellent technique for the deposition of thin films on large area substrates at relatively low substrate temperatures.¹⁷⁷⁻¹⁷⁸ RMS has been intensively investigated as a deposition technique for thin films because the sputtering of metallic targets in the presence of reactive gases makes it possible to prepare compound films such as nitrides, oxides, carbides.¹⁷⁹⁻¹⁸⁰ It has been widely used to produce various metal oxides (e.g. Bi₂O₃,¹⁸¹ Al₂O₃,¹⁸² and ZnO¹⁸³) on a large industrial scale with high degree of conformality and good control of stoichiometry. Recently, BiVO₄ thin films were successfully prepared by RMS, however, the sputtering rate was only 2.5 nm/min with the combination of a high-power direct current (DC) power supply for the V target and a radio frequency (RF) power supply for the Bi₂O₃ target.¹⁸⁴⁻¹⁸⁵ An initial attempt to sputter BiVO₄ using metallic Bi and V targets with separate direct current power supplies illustrates that sputter deposition of photoactive BiVO₄ is indeed viable, but the efficiencies still need to be improved.¹⁸⁶ One crucial factor for multinary metal oxides is the stoichiometry of the films. It has been demonstrated that stoichiometry affects the photoactivity of the BiVO₄ films and the highest performance is usually observed for V-rich films.^{173, 184} However, the mechanism behind the stoichiometric effect remains unclear up to now.

To investigate this in more detail, monoclinic BiVO₄ thin films with V : Bi atomic ratio ranging from 0.68 to 1.29 (here V : Bi is represented mathematically as V/Bi) were prepared by direct current reactive magnetron sputtering from Bi and V targets. The highest photoactivity occurs under slightly V-rich deposition conditions

($j_{\text{ph,AM1.5}} \geq 1.5 \text{ mA/cm}^2$) while the Bi-rich BiVO₄ films ($V : \text{Bi} < 1$) show relatively low photoactivity ($j_{\text{ph,AM1.5}} \leq 0.5 \text{ mA/cm}^2$). Charge carrier dynamics and recombination processes were investigated by time-resolved microwave conductivity (TRMC) measurements. A strong dependence of carrier mobility and lifetime on the V : Bi ratio is observed. Furthermore, TRMC measurements at different light intensities reveal initial trap filling and recombination effects. Moreover, the monoclinic BiVO₄ phase becomes more prominent with increasing V : Bi ratio. The improved crystallinity and the increased grain size at higher V : Bi ratios correlates to improved electronic properties and hence increased photocurrents of the BiVO₄ films. However at excess V : Bi ratios, Raman spectroscopy and chemical mapping by EDX showed that V₂O₅ starts to segregate from BiVO₄. Lastly, a high sputtering rate of 30 nm/min was achieved for the synthesis, which is significantly higher than that previously reported in literature.¹⁸⁴

Experimental

Film Preparation

BiVO₄ films were prepared by reactive magnetron co-sputtering of Bi (99.9 %) and V (99.99 %) targets at 350 °C, as shown in **Figure 5.2**. The power was fixed at 40 W and 450 W for the Bi and V target, respectively. Due to the much higher sputtering yield of Bi compared to V¹⁸⁷, the distance between the Bi target and the substrate was doubled to obtain the same deposition rate for Bi and V on the substrate. A mixture of Ar and O₂ was used for the reactive co-sputtering with an Ar gas flow of 6.4 sccm and an O₂ flow of 25.5 sccm. The total pressure and the O₂ partial pressure were fixed at 1.0 Pa and 0.20 Pa, respectively. For this O₂ concentration in the sputtering gas, the two target surfaces were completely oxidized, and the Bi and V deposition rates on the substrate were nearly equal. Due to the arrangement of the two targets with respect to the substrate (see **Figure 5.2**), a stoichiometry gradient was established from the left to the right side of the substrate.

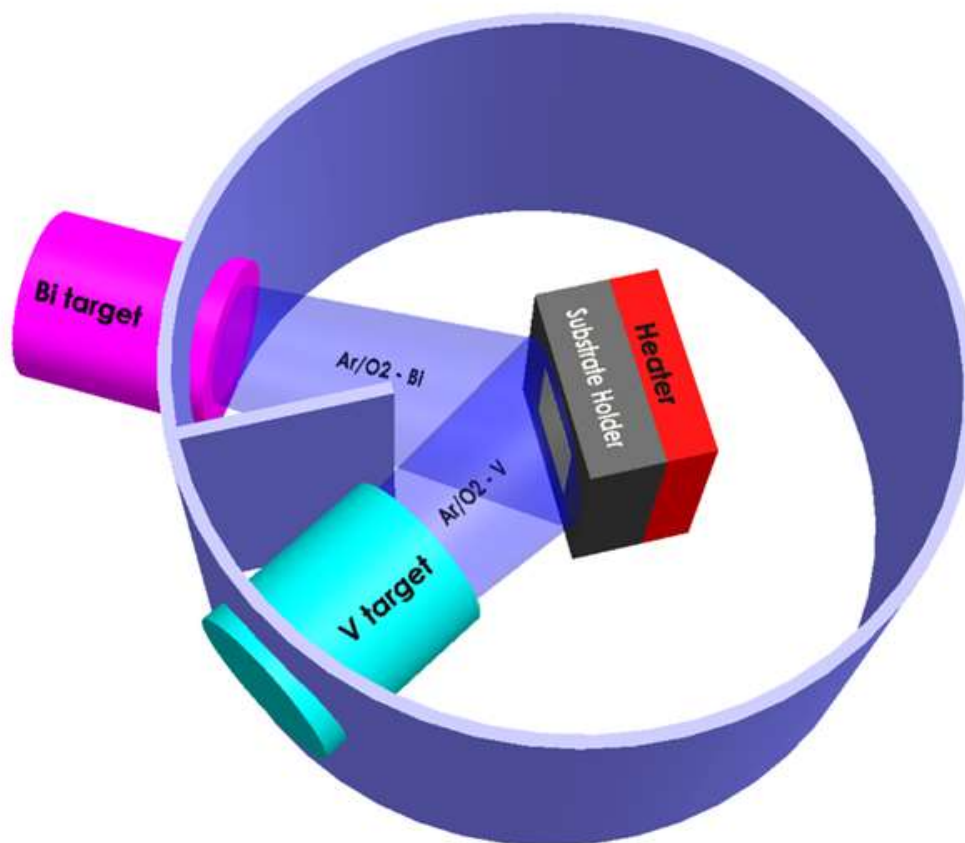


Figure 5.2. Scheme of the process chamber for magnetron sputtering system.

Prior to the deposition, the fluorine-doped tin oxide (FTO) coated glass substrates were ultrasonically cleaned for 15 min in isopropanol (Sigma), rinsed with de-ionized water, and dried with compressed nitrogen. The substrates were heated to the preset temperature before the deposition. The typical deposition duration of 6 min yielded a film thickness of about 180 nm for all samples, which corresponds to a deposition rate of ~ 30 nm/min. After deposition, the heater was switched off and the as-deposited thin films were transferred to the load-lock chamber when the temperature dropped below 200 °C. Then the films were annealed in air at 500 °C for 2 h in a muffle furnace with a temperature ramp of 10 K/min.

We note that while Bi and V have densities in the same order of magnitude, Bi has an atomic mass ~ 4 times higher than V. In order to obtain stoichiometric BiVO₄ (V : Bi atomic ratio 1 : 1), Bi needs to be consumed 2.5 times faster than V by volume. This results in a large difference in targets erosion profiles (**Figure 5.3**), and leads to a time-based variation in stoichiometry (V : Bi atomic ratio) since the shape of the erosion groove has been reported to affect the sputtering rate and element distribution.¹⁸⁸⁻¹⁸⁹

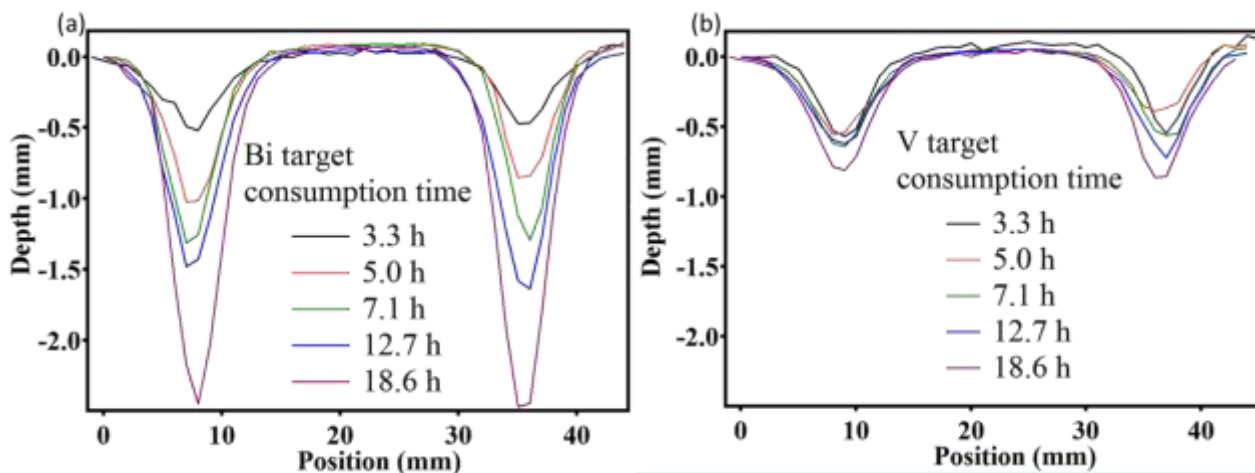


Figure 5.3. Erosion profiles of (a) Bi target, and (b) V target as a function of consumption time. The power was fixed at 40 W and 450 W for the Bi and V target in order to get stoichiometric BiVO₄ (V : Bi atomic ratio 1 : 1).

Film Characterization

The morphology and the elemental composition (V : Bi ratio) of the films were analyzed using a LEO GEMINI 1530 field emission scanning electron microscope (FESEM) with an energy dispersive X-ray fluorescence (EDX) spectrometer, operated at an acceleration voltage of 7 kV and 20 kV for SEM and EDX, respectively. The composition of the BiVO₄ films was determined from EDX mapping (30×25 μm² area), while the V K_α and Bi M peaks were used to calculate the V and Bi content, respectively. Since the EDX analysis depends on electron energy and the substrate parameters, it has to be calibrated. We did this calibration with BiVO₄ films deposited on glassy carbon substrates which were measured by Rutherford backscattering (RBS) with 1.7 MeV He⁺ ions and a backscattering angle of 170°. A correction factor of 0.85 was determined, as shown in **Figure S C1**. RBS is a standard free method for the analysis of the chemical composition of thin films with an accuracy of 1-2 %.¹⁹⁰

The crystal structure and phase composition of the sputtered BiVO₄ films were analyzed with a Bruker AXS D8-Advance X-ray diffractometer. The Cu (K_α) X-ray tube was operated at 40 kV and 40 mA, and the measurements were carried out in the symmetrical Bragg-Brentano θ/2θ diffraction geometry. A 0.1 mm slit was used allowing for the locally resolved analysis. For the sake of clarity, we would like to note that there are two different definitions used for the crystallographic description of the monoclinic crystal structure.¹⁹¹ Definition 1 defines the longest axis of the unit cell as the c direction, whereas definition 2 defines the longest unit cell axis along the b direction.¹⁹² One should be clear about the convention when comparing with other papers because the indices to identify planes depend on the selection of the setting. In this paper, we used definition 1 where

the longest axis in the unit cell is defined as the c axis.¹⁹³ The crystallite sizes of the BiVO₄ films were estimated by the Scherrer equation from the full width at half maximum (FWHM) of the XRD patterns using equation 3.1, i.e., corrected for the instrumental peak width. The phase composition characterization was also carried out by Raman spectroscopy as described in the experimental section of Chapter 4.

Time-resolved microwave conductivity (TRMC) measurements were performed to determine the charge carrier mobility and lifetime of the BiVO₄ films. The details of TRMC experiments can be found in the experimental section of Chapter 4. Specifically, the wavelength of the laser was 355 nm for BiVO₄ instead of 532 nm as it was for CuBi₂O₄. The laser pulse intensities were adjusted by the use of calibrated filters and varied from 6.3×10^{12} to 3.4×10^{14} photons cm⁻².

The film thicknesses were measured using a DEKTAK profilometer and from cross-section SEM images. The optical transmittance (T) and reflectance (R) spectra were measured with a UV/Vis double-beam spectrometer (Perkin-Elmer Lambda 950). The absorption coefficient (α) was determined from

$$\alpha = -\frac{\ln\left(\frac{T}{1-R}\right)}{L} \quad (5.1)$$

where T and R are the optical reflection and transmission, respectively, L is the film thickness.¹² The bandgap was determined from the Tauc plots, as shown in **Figure S C2**.

PEC Measurements

PEC measurements were performed using an EG&G Princeton Applied Research 273A potentiostat, in a three-electrode configuration as described in the experimental section of Chapter 3. The BiVO₄ films were tested as working electrodes with an Ag/AgCl (saturated KCl) reference electrode, and a platinum wire counter electrode. The electrolyte used for all measurements was 0.5 M Na₂SO₄ in 0.1 M potassium phosphate buffer solution (pH=6.7). The pH value of each solution was checked with a pH meter (OAKTON). All potentials were converted to the reversible hydrogen electrode (RHE) scale using **Equation 3.6**.

Results and Discussion

Photocurrent at Different V : Bi ratios

We first checked the PEC performance of the BiVO₄ films with different stoichiometries. As shown in **Figure 5.4a**, Bi-rich BiVO₄ films (V : Bi \leq 1) synthesized at 300 °C exhibit relatively low photocurrents. With increasing

V : Bi ratio (from 0.86 to 1.06), the photocurrent (at 1.23 V vs. RHE) increased significantly from 0.55 to 1.5 mA/cm². Further increasing the V : Bi ratio from 1.06 to 1.29 only resulted in a slight increase in photocurrent from 1.5 to 1.55 mA/cm². A similar trend was found for BiVO₄ films deposited at other temperatures, as shown in **Figure 5.4b**.

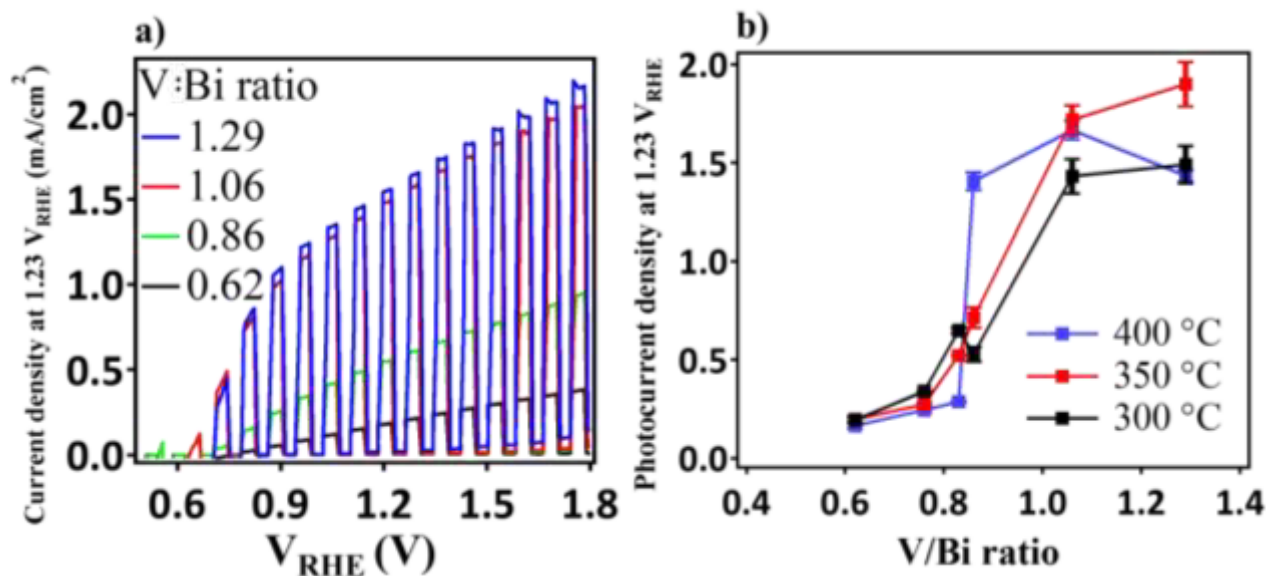


Figure 5.4. (a) Photocurrent density of ~180 nm BiVO₄ films deposited at 300 °C; (b) Photocurrent density at 1.23 V vs. RHE as a function of V : Bi ratio for BiVO₄ films deposited for 6 min at 300 °C (black), 350 °C (red), 400 °C (blue). Back illumination with H₂O₂. Film thickness was estimated from the cross section SEM images, as shown in **Figure S C3**.

Since all the measurements in **Figure 5.4** were performed with H₂O₂ added as an hole scavenger, the injection efficiency can be assumed to be 100 %, therefore the variations in photocurrent are attributed to the bulk properties of the BiVO₄ films, i.e., the photocurrents can be directly related to the electronic properties such as the minority charge carrier diffusion length.

Charge Carrier Mobility, Lifetime, and Diffusion Length

The bulk electronic properties of BiVO₄ were determined using TRMC measurements. The charge carrier mobility was extracted from the peak in the TRMC signal and the carrier lifetime was deduced from the decay of the signal. These results for different stoichiometries are summarized in **Figure S C4**.

Figure 5.5a shows the TRMC signal, with the peak signal representing the charge carrier mobility, for different V : Bi atomic ratios. The two Bi-rich BiVO₄ films (V : Bi ≤ 1) exhibit relatively low mobility and the film

with a slight excess of V (V : Bi = 1.06) clearly shows the highest mobility.

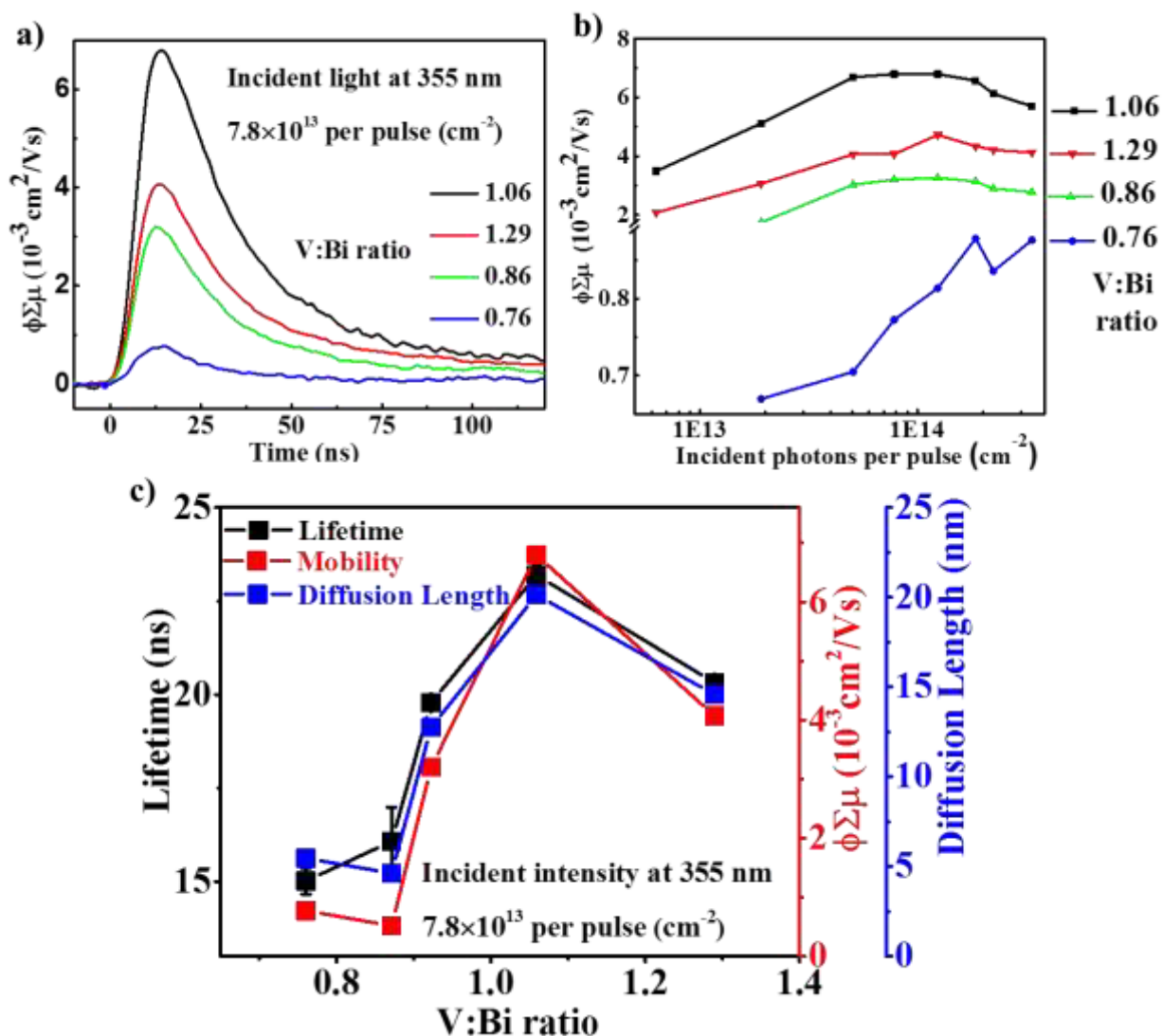


Figure 5.5. (a) TRMC signals measured for BiVO₄ films with for different V : Bi ratios; (b) Maximum observed TRMC signals as a function of light intensity; (c) Carrier mobility, lifetime and diffusion length as a function of V : Bi ratio.

The TRMC measurements were also conducted at different light intensities. **Figure 5.5b** shows an increase in the conductivity as a function of light intensity for all samples, which indicates that carrier trapping occurs.¹³⁸ The V-rich films showed maximum mobility at the light intensity of approximately 1×10^{14} photos/cm²/pulse. The presence of a maximum can be attributed to the competition between electron trap filling and non-geminate recombination, as has been reported for W-doped BiVO₄.¹³⁷ As the light intensity is increased towards this maximum the electron traps are continuously filled, but as the intensity is increased further the increased number of photo-generated electrons and holes results in increased electron-hole recombination. The mobility

of the Bi-rich films increased with light intensity without reaching a maximum, indicating that the trap filling still dominates even at the highest measured light intensity. At a light intensity of 1×10^{13} photons/cm²/pulse, a carrier mobility of 4×10^{-3} cm²V⁻¹s⁻¹ was observed for a BiVO₄ film with V : Bi ratio of 1.06, which is slightly lower than the previous reported value (7.5×10^{-3} cm²/Vs) for BiVO₄ films prepared by spray pyrolysis.¹³⁷ Additionally, the mobility of the BiVO₄ films synthesized by spray pyrolysis showed continuously decreasing mobility with increasing light intensity so electron trap filling was not the dominant path for the loss of photo-generated electrons.

Unlike CuBi₂O₄, for which two time constants were found, only one time constant is needed to fit the TRMC signal decay of the sputtered BiVO₄ films. The lifetime of the sputtered BiVO₄ films is in the order of 15-25 ns, which is shorter than that of sprayed BiVO₄ films (~40 ns).¹³⁷ The diffusion lengths were calculated from the mobility and lifetime values using equation 4.3. The diffusion lengths of the sputtered BiVO₄ films are in the order of 20-30 nm which is smaller than that of the sprayed BiVO₄ films (~70 nm).¹³⁷ **Figure 5.5c** shows the mobility, lifetime and the corresponding diffusion length as a function of V : Bi ratio. Surprisingly, all the mobility, lifetime, and diffusion length values show very similar dependence on the stoichiometry of the BiVO₄ films.

Crystal Structure and Preferential Growth

In general, charge transport in semiconductors is strongly affected by the crystal structure. Previous studies have demonstrated that photogenerated electrons and holes tend to accumulate on different crystal facets. Certain facets favor reduction reaction while others prefer oxidation reaction.¹⁹⁴⁻¹⁹⁸ In order to understand the effect of stoichiometry on different crystal facets we performed detailed XRD analysis of our BiVO₄ films synthesized by DC reactive magnetron sputtering (DCRMS). **Figure 5.6** shows the XRD patterns of the sputtered BiVO₄ films with different V : Bi ratios. The characteristic peaks of FTO substrate are marked by asterisks (*). The reference XRD pattern of monoclinic BiVO₄ was displayed by purple bars (JCPDS 83-1697). The peaks at 19.00 °, 28.97 °, 30.55 °, 34.51 °, 35.24 °, 42.49 °, 46.75 °, 53.32 ° and 54.62 ° were observed for all films, which can be assigned to the (011), (112), (004), (200), (020), (015), (204), (116) and (031) reflections of monoclinic BiVO₄, respectively.¹⁵⁷ As explained previously, the monoclinic BiVO₄ phase is more photoactive compared to the tetragonal phase due to its distortion.^{98, 100} In addition to the FTO and monoclinic BiVO₄ peaks, the Bi-rich films (V : Bi ratio < 1) show peaks at $2\theta = 10.66^\circ$ and 28.20° , which can be assigned to the (110) reflection of Bi_{8.1}V_{0.9}O₁₄¹⁹⁹ and (140) reflection of Bi₂VO_{5.5},²⁰⁰ respectively. They both become weaker with increasing V : Bi ratio and disappear in the V-rich films. However, no V_xO_y peaks are observable in the XRD patterns, even for the

V-rich films. This is probably due to the small crystallite size of V₂O₅. The BiVO₄ (112) and (004) peaks show increasing intensity with increasing V : Bi ratio accompanied by the decrease of intensity of the Bi₂VO_{5.5} (140) peak. The Bi₂VO_{5.5} (140) peak disappears in the more V-rich films while the BiVO₄ (004) peak becomes the most prominent peak at V : Bi ratio 1.29. Moreover, compared with the relative intensities shown in the standard patterns, it can be seen in the V-rich films that the (002) and (004) peaks of monoclinic BiVO₄ exhibit an enhanced intensity, suggesting a preferential growth along the [001] direction. For a perfect flat and dense BiVO₄ film, such preferred orientated growth along the [001] direction would lead to dominant exposure of {001} facets. It has been demonstrated that the {001} facets of BiVO₄ tend to accumulate photogenerated electrons instead of holes, and thus favor reduction reaction instead of oxidation reaction.²⁰¹⁻²⁰² This seems to be in contrast with the improved in PEC performance that we observed for V-rich films (**Figure 5.4**). We note that, in practical, preferred growth along the [001] direction does not necessarily mean dominant exposure of {001} facets due to the presence of surface roughness (vide infra), an example is illustrated in **Figure S C5**. Therefore, for our V-rich films BiVO₄ with certain surface roughness, the prevalent exposure of facets rather than {001} in the V rich BiVO₄ films is possible. Facet-selective photo-deposition of metals (by using AgNO₃ or H₂PtCl₆ as precursors) on the surface of the sputtered BiVO₄ may allow us to quantify the portion of exposed {001} facets.²⁰¹

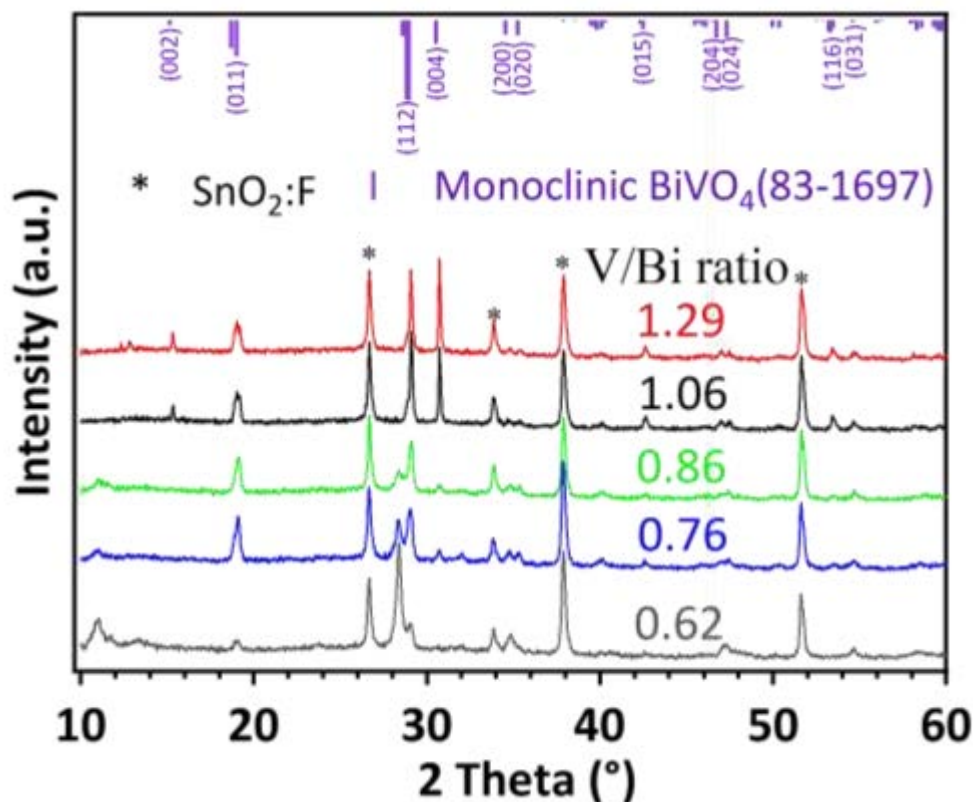


Figure 5.6. XRD patterns of the BiVO₄ thin films at different V : Bi ratio.

The crystallite size of the BiVO₄ films were estimated by the Scherrer formula from the full width at half maximum (FWHM) of the XRD patterns, as shown in **Figure S C6**. The crystallite size is in the order of 20-35 nm, which is much smaller than the lateral grain size estimated from the SEM images (see **Figure 5.7**). This is probably due to the fact that by XRD in Bragg-Brentano geometry only the vertical domain size is probed. Note that it is the vertical domain size that is essential for the separation and transport of the charge carriers from the bulk of the semiconductor to the semiconductor-electrolyte interface.

Morphology and Grain Size

The morphology of the sputtered BiVO₄ films with different stoichiometries was investigated by SEM, as shown in **Figure 5.7a-d**. Clear grain boundaries were observed for all films and the average grain sizes were estimated from the SEM images and plotted as a function of V : Bi ratio, as shown in **Figure 5.7e**. In general, the grain size increases with the V : Bi ratio. The Bi rich films (V : Bi ratio < 1) show relatively small grain sizes on the order of 85-108 nm. A slight excess of V results in a significant increase in grain size for the film with a V : Bi ratio of 1.06 while further increasing in V : Bi ratio from 1.06 to 1.29 only results in a slight increase in grain size. The same trend was also found for the BiVO₄ films deposited at 350 °C and 400 °C, as shown in **Figure S C7**. AFM analysis shows that there is no significant difference in surface roughness among the sputtered BiVO₄ films with different stoichiometries, see **Figure S C8**.

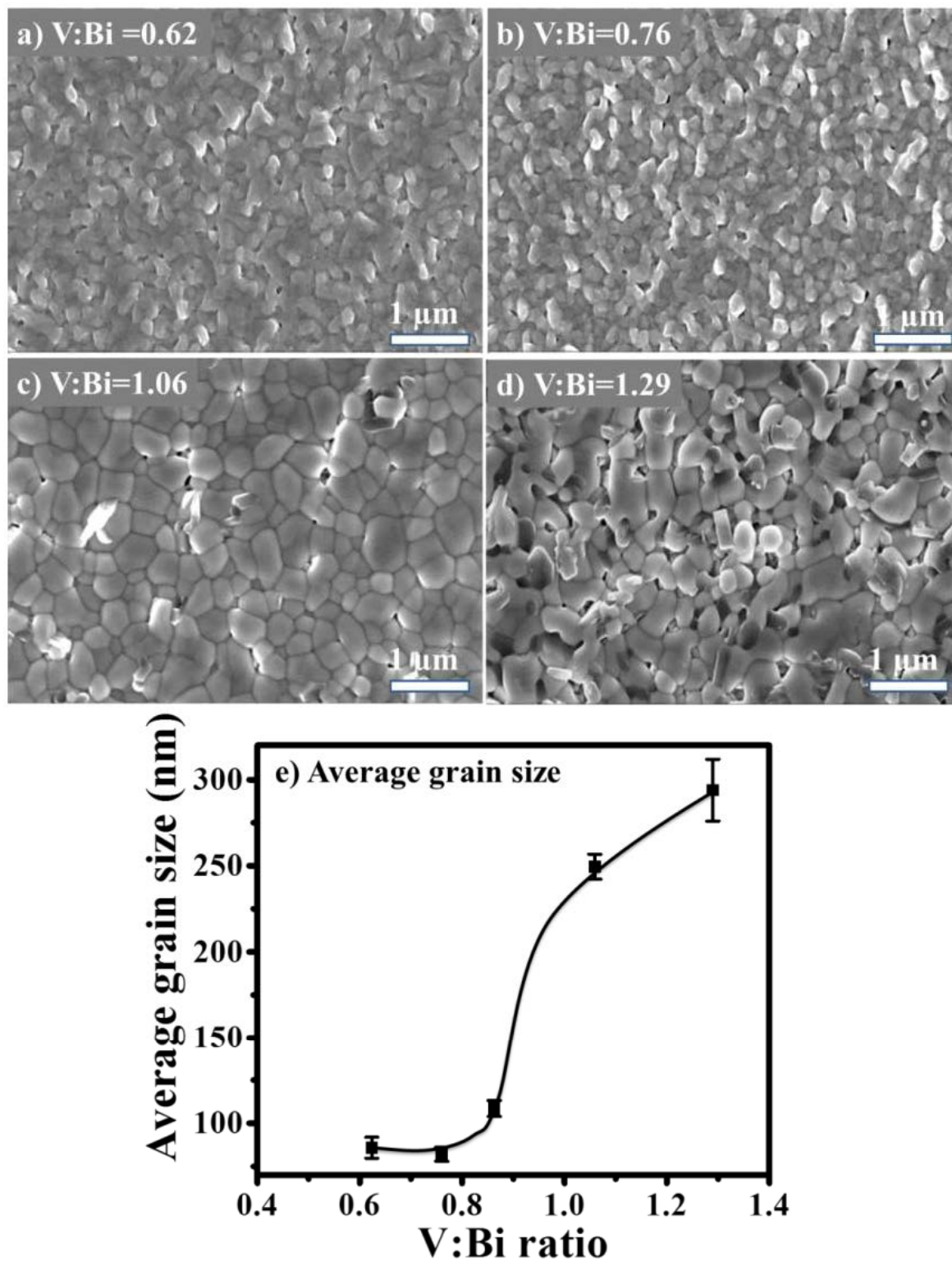


Figure 5.7. SEM images of ~ 180 nm BiVO₄ films deposited at 300 °C with V : Bi ratio of (a) 0.62, (b) 0.76, (c) 1.06, (d) 1.29; and (e) average lateral grain size, derived from the SEM images, as a function of the V : Bi ratio.

Figure 5.8 depicts the dependency of the PEC performance, the diffusion length, and the average grain size on V : Bi ratio. In general, the current density at 1.23 V vs. RHE and the diffusion length show very similar

dependences on the V : Bi ratio, which is reasonable because longer diffusion length is expected to result in higher photocurrent in the BiVO₄ films. Recall that in **Figure 5.5c**, as the average grain size increases from 85 to 249 nm, both the mobility and lifetime increase so that the calculated charge diffusion length also increases, indicating a very strong relationship between the grain size and the electronic properties. One possible explanation is that traps are localized at grain boundaries so that photogenerated charge carriers close to the boundaries are more likely to reach and recombine. The recombination loss at grain boundaries is known as one of the predominant loss mechanisms in polycrystalline semiconductors.²⁰³⁻²⁰⁴ The grain boundaries could act not only as traps but also efficient recombination centers giving rise to a high surface recombination velocity.²⁰⁵ Similar to varistors, the depletion of oxygen vacancies in grain boundaries can result in the formation of back-to-back Schottky barriers, which would result in low grain boundary conductivity relative to the bulk conductivity.²⁰⁶ At lower V : Bi ratio, the average grain size is small and therefore the chance that the photogenerated charge carriers recombine at the boundaries is relatively high. As the V : Bi ratio increases from 0.62 to 1.06, the grain size increases and the number of small grains largely reduces. That is why high mobility and lifetime were observed.

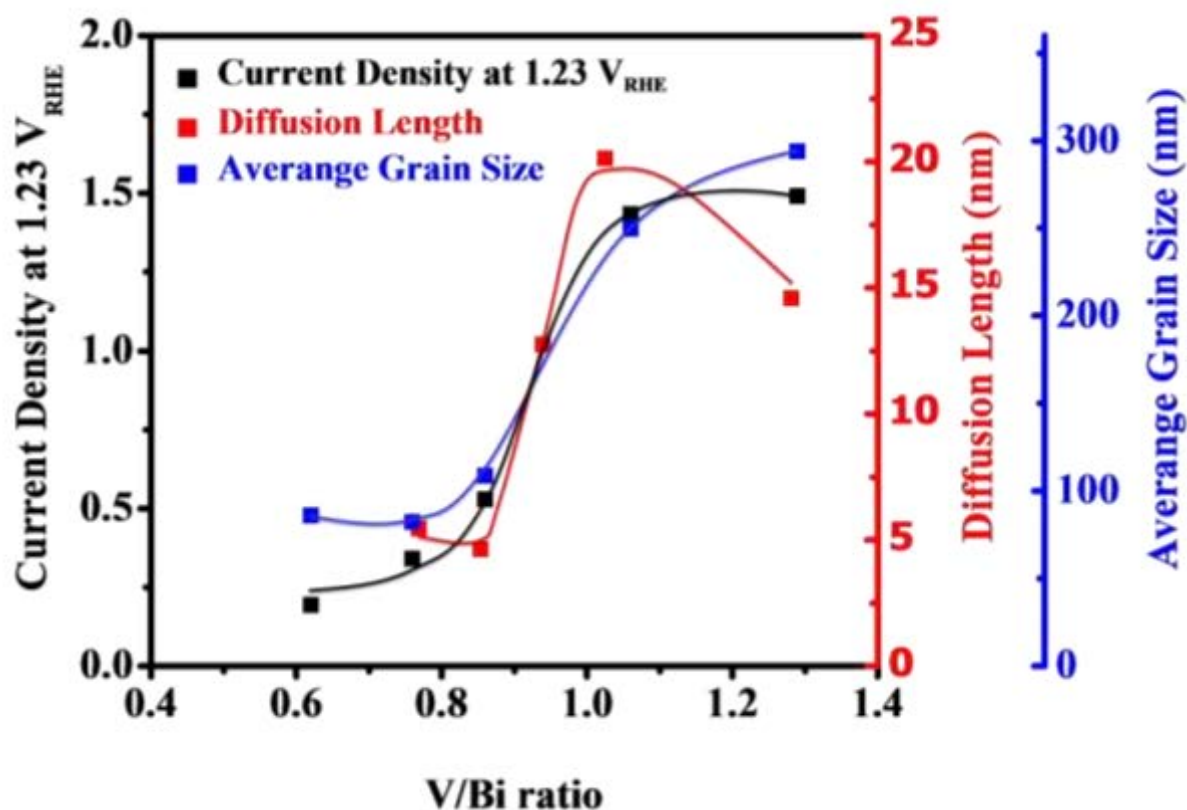


Figure 5.8. Current density at 1.23 V vs. RHE (black); diffusion length (red) and average grain size (blue) of the ~180 nm BiVO₄ thin films deposited at 300 °C as a function of V : Bi ratio.

However, as the V : Bi ratio increased from 1.06 to 1.29, the mobility and lifetime started to decrease while the grain size kept increasing. Since the XRD analysis did not reveal any VO_x phases in **Figure 5.6**, it is necessary to use alternative methods to identify the vanadium excess phase in the V-rich BiVO₄ films. For this reason, Raman spectroscopy and EDX mapping were carried out to determine the structure and distribution of the excess vanadium.

Phase Segregation

Figure 5.9a shows the Raman spectra of the sputtered BiVO₄ films with various V : Bi ratios. The main peaks of monoclinic BiVO₄ centered at 327, 368, and 828 cm⁻¹ were observed for all sputtered BiVO₄ films.^{158, 174, 207-208} Those characteristic monoclinic BiVO₄ Raman peaks became sharper as the V : Bi ratio increases from 0.62 to 1.06 but then become weaker as the V : Bi ratio increases from 1.06 to 1.29. The V-rich films show, apart from the monoclinic BiVO₄ peaks, additional peaks at 284, 400, 705 and 980 cm⁻¹, which can be assigned to the vibrational modes of V₂O₅.¹⁸⁴ This suggests that the excess of V exists in the V-rich films in the form of V₂O₅. These V₂O₅ peaks become even more pronounced in films with higher V : Bi ratio. For the Bi-rich films, the band at ~828 cm⁻¹ which is assigned to V-O stretching slightly shifted to higher wavenumbers, as shown in **Figure S C9**. This shift can be attributed to the presence of Bi₂V₅O_{5.5} phase, as previously reported for Bi rich BiV_xO_y,²⁰⁹ and is consistent with the observation in XRD. In addition, clear broadening of this band was observed, indicating a disorder caused by a change in cation-oxygen coordinations.²¹⁰

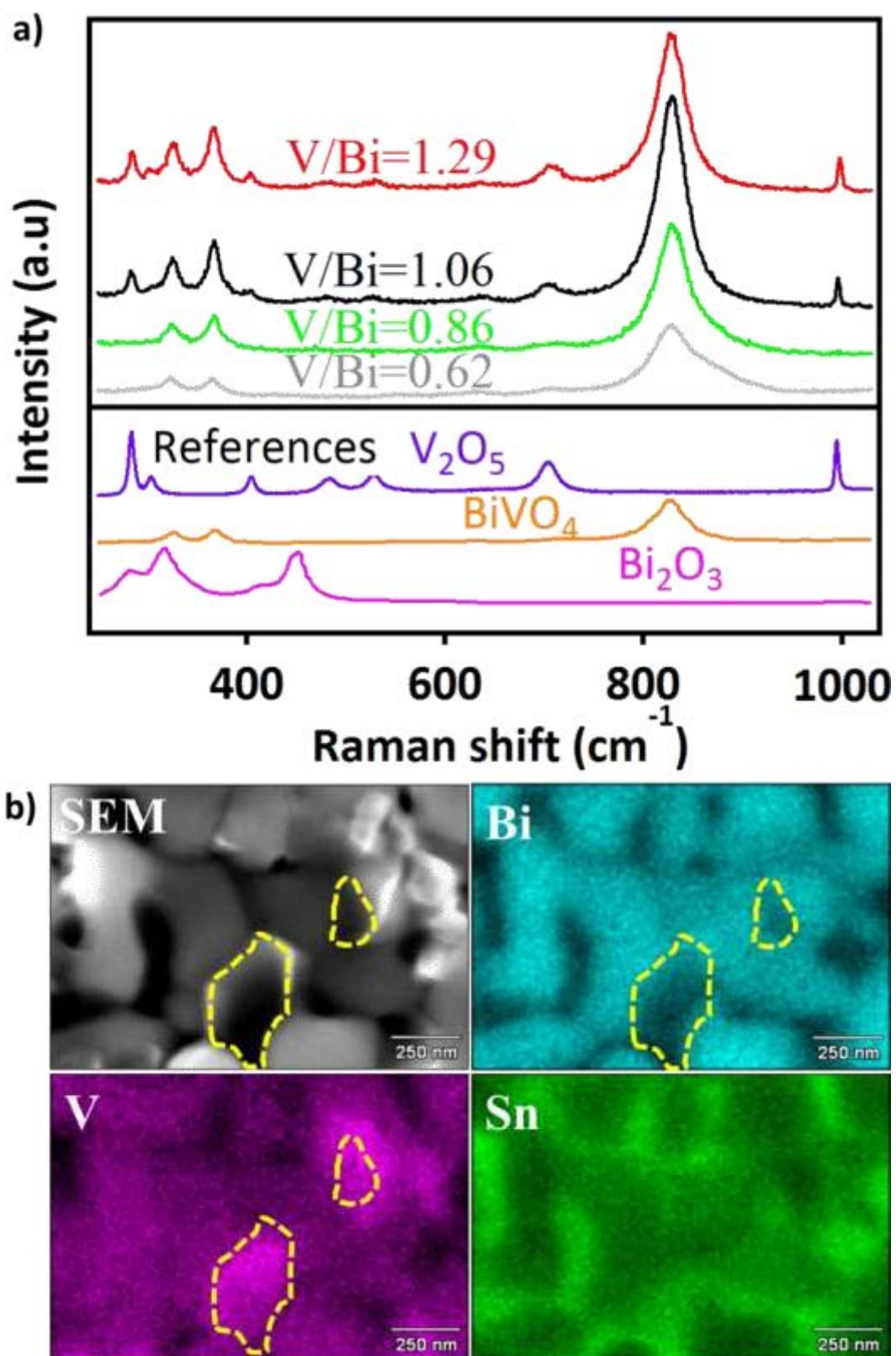


Figure 5.9. (a) Raman spectra of sputtered films with different stoichiometry; (b) EDX mapping of BiVO₄ at V : Bi ratio 1.29.

The location and distribution of the vanadium oxide was illustrated by EDX mapping, as shown in **Figure 5.9b**. The marked region is rich in V while deficient in Bi, suggesting the existence of vanadium oxide as flakes. Those flakes are only observed in BiVO₄ films with a high V : Bi ratio of 1.29. No phase separation was visible in the EDX mappings for BiVO₄ films with V : Bi ratio lower than 1.29, as shown in **Figure S C10**, **Figure S C11**, and **Figure S C12**. The phase segregation of V₂O₅ from BiVO₄ could result in additional grain boundary defects. However, V₂O₅ peaks do not appear in the XRD pattern. Either the V₂O₅ remains amorphous or the crystallite size of V₂O₅ is too small to be detected by XRD.

Conclusions

Monoclinic BiVO₄ films with various V : Bi atomic ratios were prepared by direct current magnetron sputtering (DCMS) using metallic Bi and V targets with a high sputtering rate of 30 nm/min, demonstrating the possibility of multinary metal oxide photoelectrode production by DCMS that can be potentially scaled up. Both the charge carrier mobility and lifetime increase with increasing V : Bi ratio, which is also accompanied by an increase in grain size. This can be explained by the reducing the surface area of grain boundary defects caused by the increasing grain size. Bi-rich films (V : Bi < 1) with small grain size show relatively low charge carrier mobilities, lifetimes, diffusion lengths, and photocurrent densities. A slight excess of V results in significant increase in the mobility, lifetime, diffusion length and consequently photocurrent density. In V-rich films, the monoclinic phase becomes more prominent and preferential growth along [001] direction was observed. However, too much excess V results in the phase segregation of V₂O₅ from BiVO₄, which may create new boundary defects leading to the decrease in mobility and lifetime at excessive V : Bi ratios.

Summary and Outlook

Overview of Completed Work

This thesis developed new recipe for preparing CuBi_2O_4 photocathodes, proposed new strategy to improve the charge separation efficiency in multinary metal-oxide-based photoelectrodes, explored direct current magnetron sputtering as a potential large scale deposition technique for preparation of BiVO_4 , investigated the stoichiometric effect on grain size, electronic properties and PEC performance.

Chapter 1 presents the motivation for the research carried out in this thesis, in which the energy crisis, CO_2 emission, climate change, and possible solutions are briefly introduced. The attractive characteristics of PEC water splitting are depicted. The working principle of PEC cell, semiconductor basics, and requirements for photoelectrode materials are summarized in Chapter 2.

Chapter 3 reveals the main challenges in preparing homogeneous CuBi_2O_4 photocathodes by spray pyrolysis. Prior to the spray, the rapid hydrolysis of Bi^{3+} in the precursor solution with the presence of water causes fast precipitation prohibiting homogeneous spray onto substrates. This is conquered by adding triethyl orthoformate (TEOF) to avoid the premature hydrolysis of the Bi^{3+} in the precursor solution. During the spray, the poor spreading behavior of the droplets over the substrates results in powder formation and therefore prohibit the growth of thicker films with the same level of homogeneity. This is addressed by adding polyethylene glycol (PEG), which significantly improves the spreading behavior of the droplets over the substrates allowing the formation of homogeneous, dense CuBi_2O_4 films. Our self-designed capture technique combined with attenuated total reflection infrared (ATR-IR) spectroscopy is a very useful characterization method for in-situ analysis of the solution chemistry, and the strategies we applied to improve the solution chemistry might be applicable for developing solution-based recipe for the synthesis of other metal oxides. A record photocurrent density of $\sim 2.0 \text{ mA/cm}^2$ was achieved by the dense CuBi_2O_4 films. However, our results suggest that the PEC performance of the sprayed CuBi_2O_4 films is largely limited by the low charge separation and poor stability under operation conditions.

Chapter 4 proposes a new strategy of using forward gradient self-doping to improve the charge separation efficiency in CuBi_2O_4 films. A simple two-step-diffusion-assisted spray pyrolysis process was used to prepare self-doped CuBi_2O_4 photocathodes with forward and reverse gradient in copper vacancy. The charge separation efficiency is shown to be highly improved and impeded in the forward gradient film and reverse gradient film, respectively. The forward gradient CuBi_2O_4 photocathodes produce an AM 1.5 photocurrent of -2.5 mA/cm^2 (with

H₂O₂) and a charge separation efficiency of 34.0 % (550nm), establishing a new benchmark for this material. To improve the stability of the forward gradient CuBi₂O₄ photocathodes, a CdS/TiO₂ protection layer together with a Pt catalytic layer were applied, which tremendously improve the stability of the forward gradient CuBi₂O₄ photocathodes. At 0.0 V vs. RHE faraday efficiency of ~91 % is achieved by the CuBi₂O₄/CdS/TiO₂/Pt, and it generates a photocurrent density of -0.9 mA/cm². The strategy we applied to improve the charge separation efficiency in CuBi₂O₄ can be easily applied to other multinary metal oxide photoelectrodes.

Chapter 5 shows our efforts on developing direct magnetron sputtering (DCMS) as a potential large scale deposition technique to prepare photoelectrodes. Monoclinic BiVO₄ thin films with various V : Bi ratios were prepared from independent Bi and V metallic targets with a high sputtering rate of 30 nm/min, demonstrating that DCMS of photoactive multinary oxides is indeed viable. The role of stoichiometry on grain size, structure, carrier mobility and lifetime is thoroughly investigated. Our results show that the mobility, lifetime and diffusion length increase with the V : Bi ratio, which might be caused by the increasing grains size at higher V : Bi ratio that leads to less grain boundary defects. The Bi-rich BiVO₄ films (V : Bi < 1) showed relatively small grain size, low mobility, short lifetime and thus low photoactivity. A slight excess of V significantly increases the grain size, and results in a significant increase in mobility, lifetime and consequently PEC performance. Preferential growth along {001} facet was observed for V-rich films. At high V : Bi ratio, V₂O₅ starts to segregate from BiVO₄, which might create new grain boundary defects and leads to decreasing mobility and lifetime.

Outlook

Despite great efforts in the search for suitable materials for PEC water splitting, thus far an ideal candidate has not been identified that can meet all the crucial requirements for practical large scale H₂ production. In general, further developments may focus on exploring new materials with good visible light response, suitable band edges, good electronic properties, rapid charge transfer, and high stability or efforts can focus on optimizing the electronic and optical properties of already established materials. Theoretically, DFT calculations are helpful in predicting and understanding the material properties that are relevant to PEC and therefore point towards a rational design of PEC materials.^{105, 160} However, it is not always trivial and more theoretical and computational models need to be developed. Experimentally, new deposition techniques (e.g. pulsed laser deposition) combined with high throughput screening have emerged as a useful tool to build up material libraries and accelerate the discovery and optimization of new PEC materials.^{102, 124} The material studied in this thesis, CuBi₂O₄, was in fact 'discovered' to be a promising photocathode material during one of the earlier combinatorial studies in photoelectrochemical water splitting.¹⁰²

Despite the progress made on CuBi_2O_4 through the work described in this thesis and by other researchers, there are still several remaining challenges to be addressed. Specifically: (1) Further quantification of charge carrier dynamics and recombination in dense CuBi_2O_4 films. The author has observed a strong wavelength dependency of charge carrier mobility for CuBi_2O_4 , but additional TRMC measurements under various wavelengths of light with different light intensities are required along with modeling to draw solid conclusions. In addition, DFT calculations of the effective mass of electrons and holes in CuBi_2O_4 may allow us to separately estimate electron and hole mobilities from the TRMC signal. (2) Identification of an optimal back contact material for CuBi_2O_4 . As described in Chapter 3, CuBi_2O_4 has a very positive flat-band potential of ~ 1.21 V. vs RHE which corresponds to a work function at ~ 5.7 eV below the vacuum level. The most commonly used FTO has work function of ~ 5.0 eV and is suitable for many n-type photoanode materials.²¹¹ However, it is not positive enough for most p-type photocathode materials. Therefore, developing back contact materials with higher work function (e.g. NiO) is needed for p-type photocathode materials like CuBi_2O_4 to avoid the formation of Schotky barrier. (3) Development of protection layers for CuBi_2O_4 photocathodes. Chapter 4 demonstrates that the $\text{CdS}/\text{TiO}_2/\text{Pt}$ layers can significantly improve the stability of sprayed CuBi_2O_4 photocathodes under the operating conditions for hydrogen production. However, the onset potential was shifted to less positive potentials, which may be due to the misalignment of the band edges of the semiconductors causing a loss in photovoltage. Other protection layers like $\text{Ga}_2\text{O}_3/\text{TiO}_2/\text{Pt}$ will be tested in an attempt to protect CuBi_2O_4 while maintaining the photovoltage. (4) Fabrication of a CuBi_2O_4 tandem PEC device. As stated in Chapter 1, CuBi_2O_4 has the potential to reach a high theoretical STH efficiency over ~ 22 % when coupled with a bottom absorber material having a smaller bandgap.³⁷ Specifically, a tandem cell composed of CuBi_2O_4 as a top absorber and Si as a bottom absorber is worth testing.

In the end of this thesis, the author would like to re-emphasize that one of the main motivations for this work is to reduce CO_2 emissions by replacing fossil fuels with solar fuels. However, the PEC water splitting process terminates at H_2 production and does not involve any carbon fixation. An alternative way to reach the goal is to return CO_2 to a useful state by CO_2 photoreduction, which has attracted growing attention in the last few decades.²¹² Although it is beyond the scope of this thesis, the knowledge accumulated in PEC water splitting can be easily shared and applied to CO_2 photoreduction. Moreover, it has been demonstrated that PEC water splitting can even be combined with CO_2 photoreduction to build a biosynthetic system.²¹³ In the future, PEC water splitting and CO_2 photoreduction can be developed in parallel or combined to reach the goal of reducing CO_2 emissions and moving to a system of renewable energy production.

Appendix A: Supplemental Information for Spray Pyrolysis of CuBi_2O_4 Photocathodes: Improved Solution Chemistry for Highly Homogeneous Thin Films

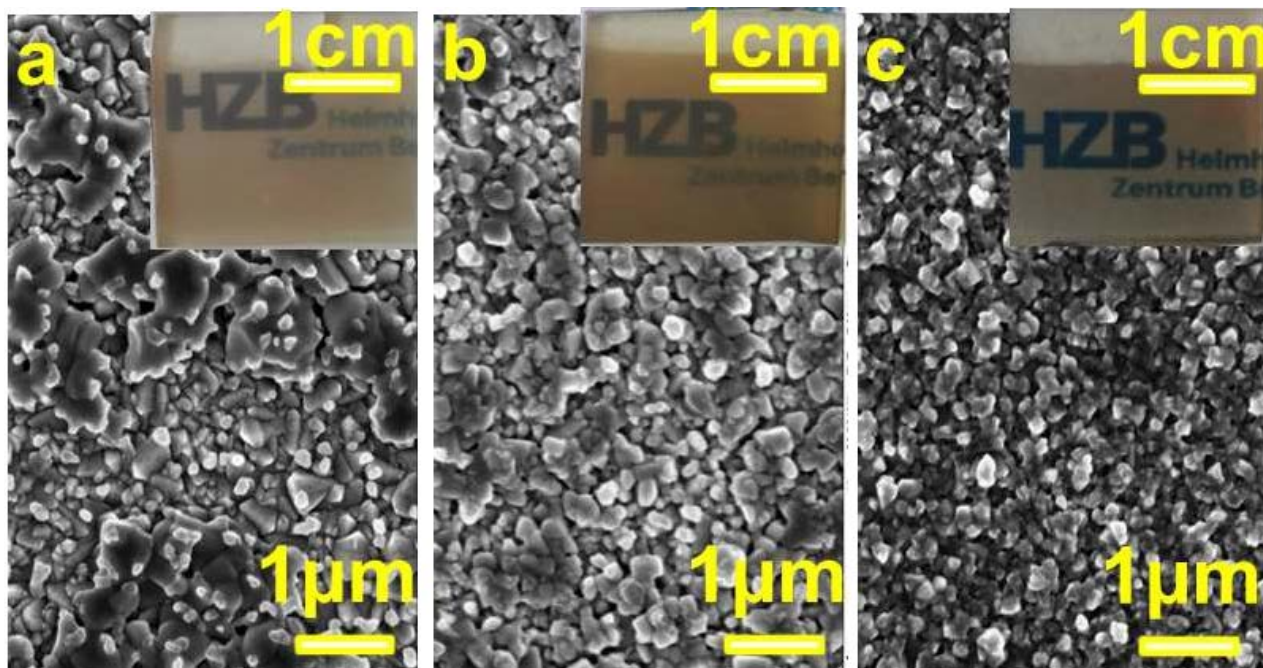


Figure S A1. SEM images of CuBi_2O_4 films with the same amount of precursors (a) 2 mM 285 mL (b) 10 mM 57 mL (c) 20 mM 28.5 mL.

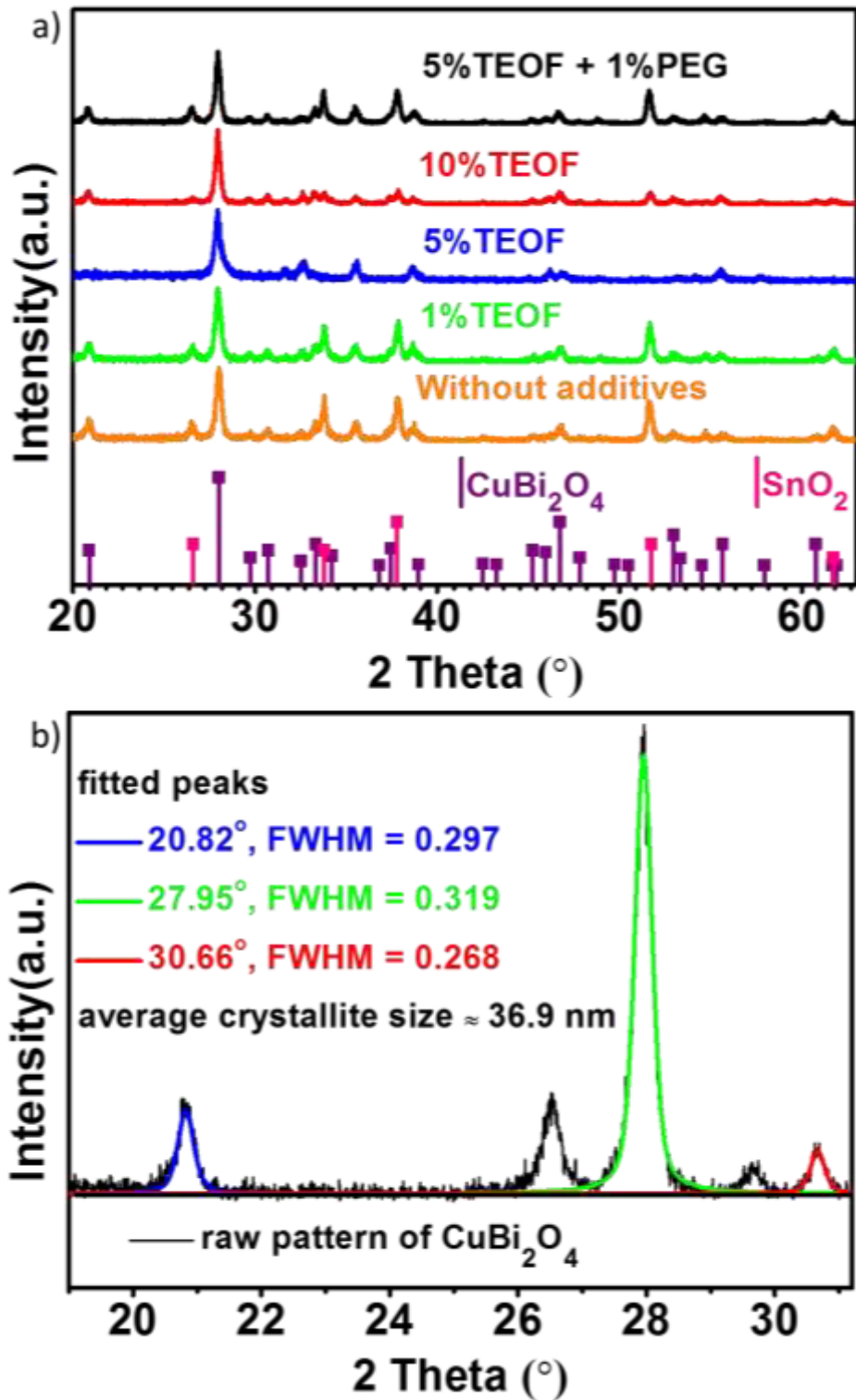


Figure S A2. (a) XRD diffractogram for CuBi_2O_4 photocathodes synthesized by spray pyrolysis (450 °C) on FTO substrates. Purple and cyan drop lines represent the reference patterns for CuBi_2O_4 and SnO_2 , respectively; (b) Scherrer analysis of a ~ 270 nm CuBi_2O_4 film sprayed using 20 mM precursor solution with 5 % TEOF and 1 % PEG on FTO at 450 °C.



Figure S A3. Photos of different spray pyrolysis precursor solutions over time.

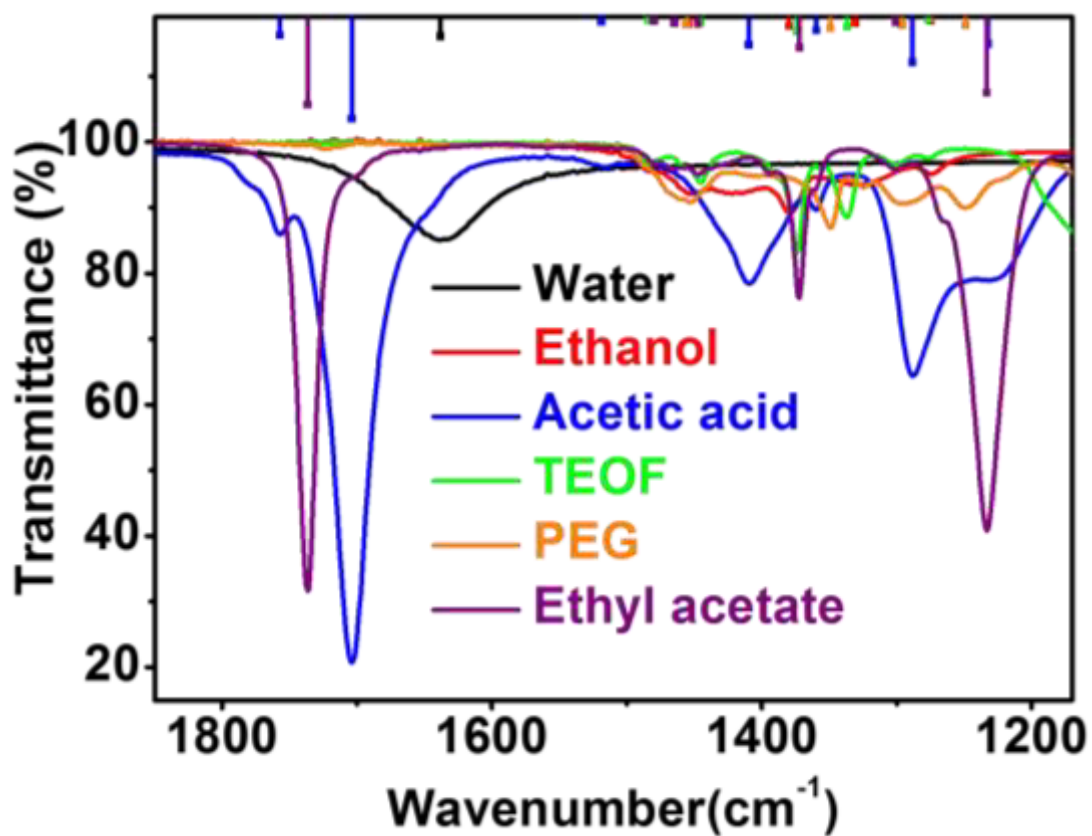


Figure S A4. ATR-IR references of the solvents.

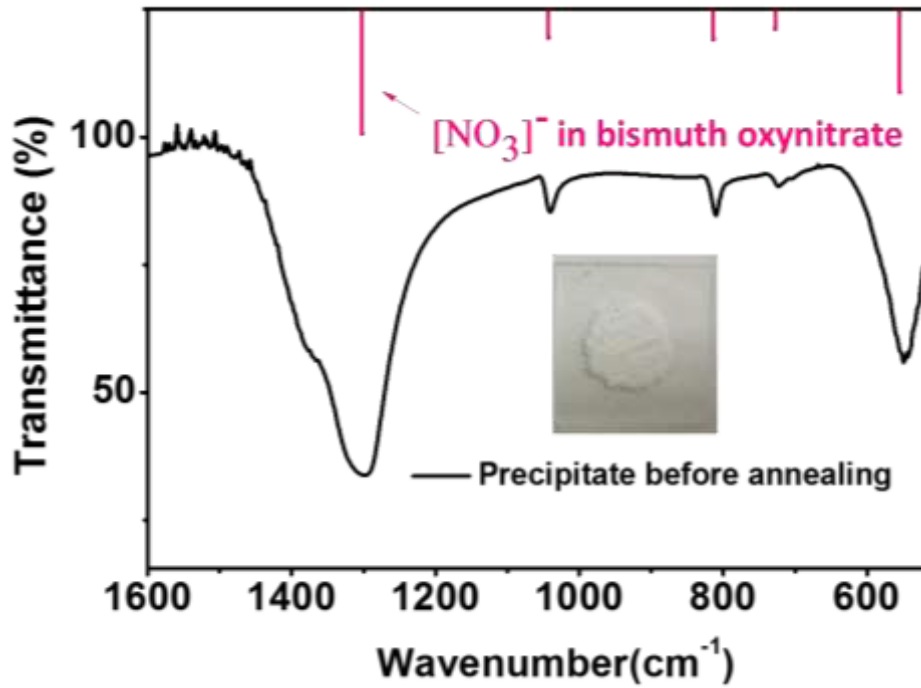


Figure S A5. ATR-IR reference of the precipitate filtered from the 20 mM precursor solution without additives after 24 h.

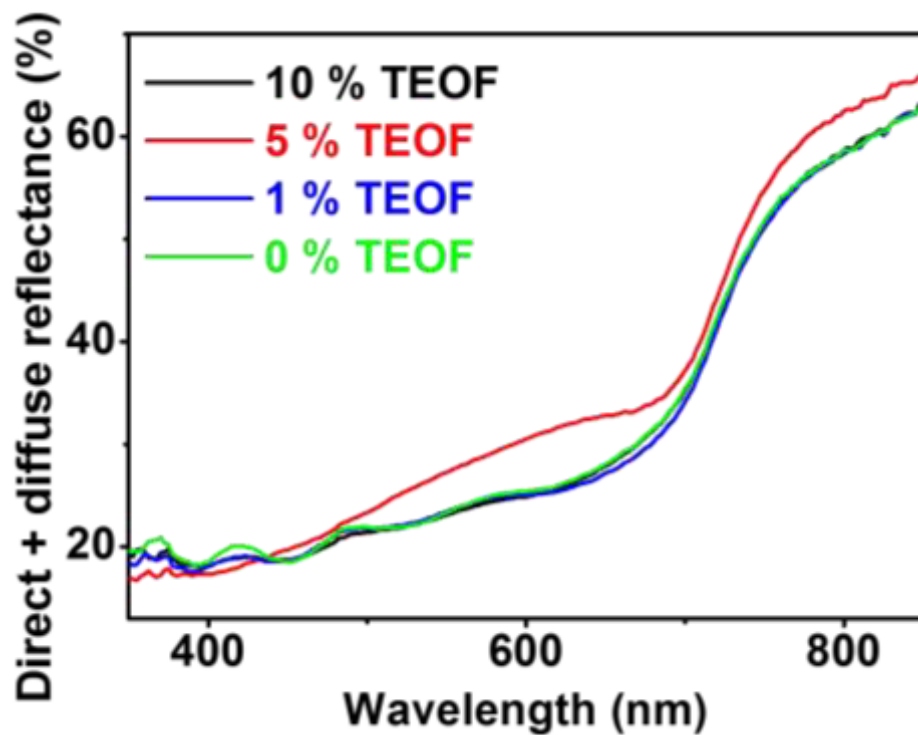


Figure S A6. Reflectance spectra (direct reflectance + diffuse) for CuBi₂O₄ photocathodes sprayed with 0, 1, 5 and 10 % TEOF. Film thickness is ~50 nm for all.

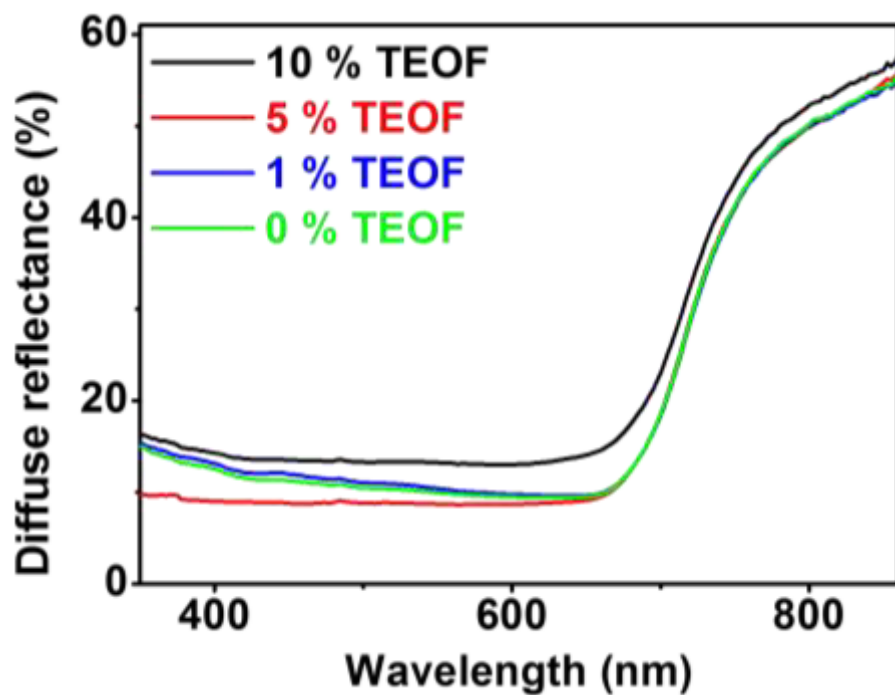


Figure S A7. Diffuse spectra for CuBi_2O_4 photocathodes sprayed with 0, 1, 5 and 10 % TEOF. Film thickness is ~ 50 nm for all.

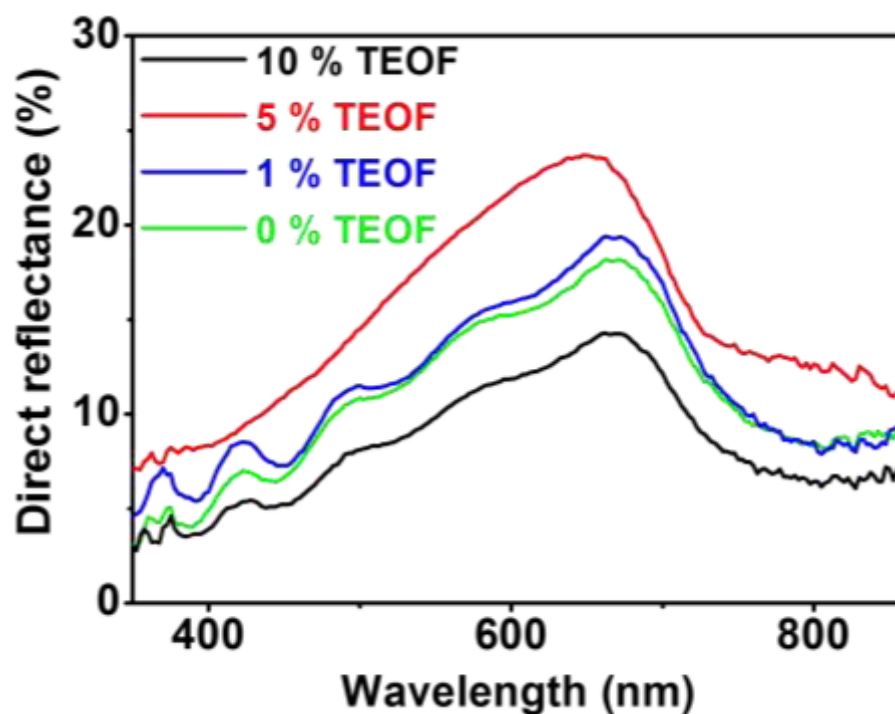


Figure S A8. Direct reflectance spectra for CuBi_2O_4 photocathodes sprayed with 0, 1, 5 and 10 % TEOF. Film thickness is ~ 50 nm for all.

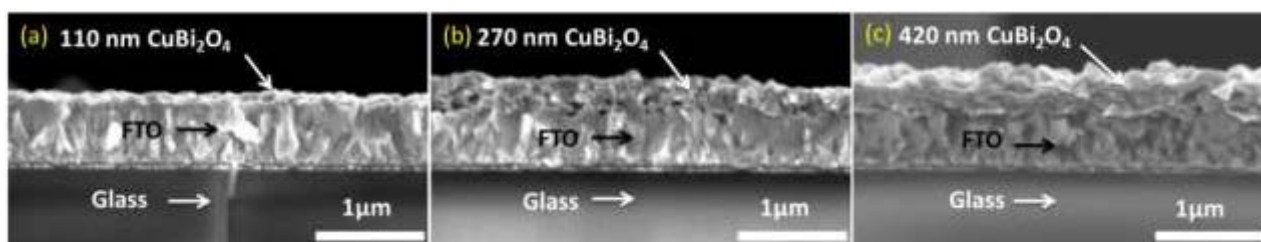


Figure S A9. Cross section SEM images of CuBi_2O_4 films on FTO deposited with 20 mM precursor solution with 5 % TEOF and 1 % PEG (a) ~ 110 nm (b) ~ 270 nm (c) ~ 420 nm.

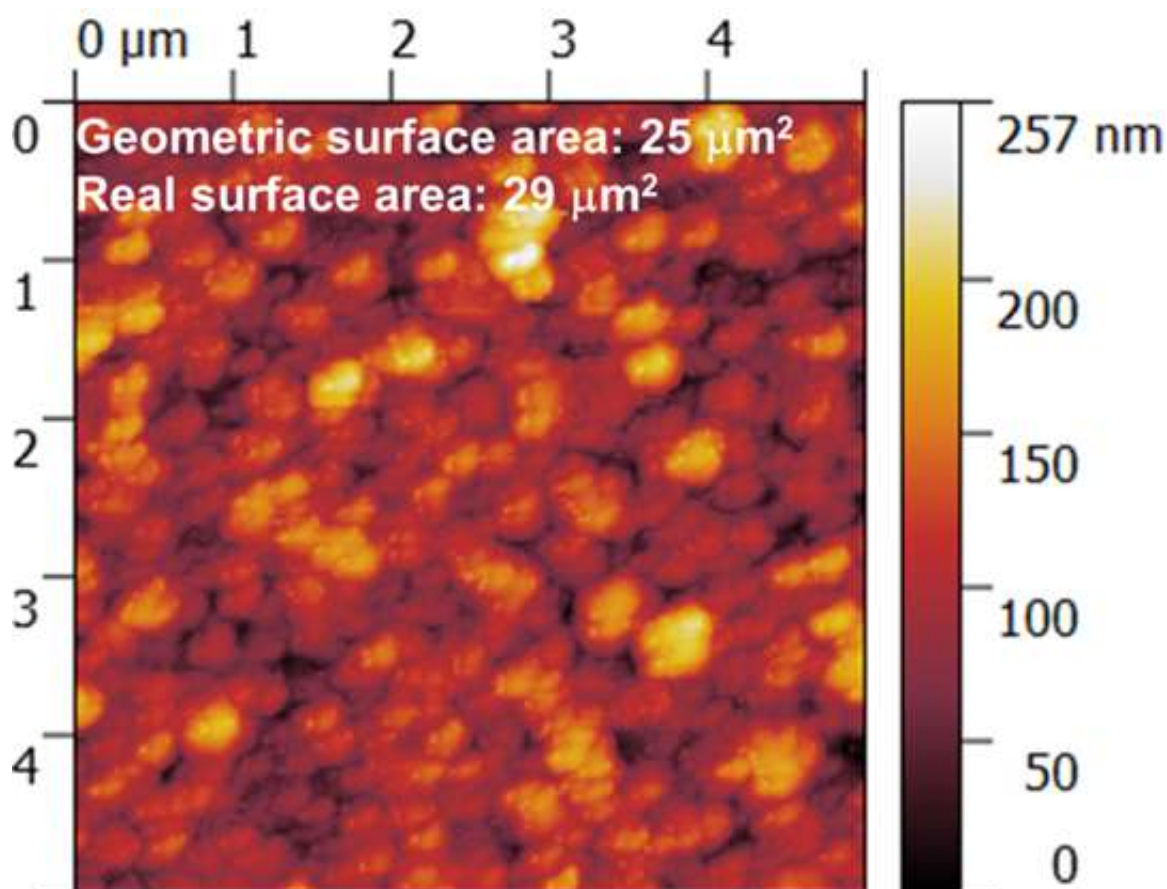


Figure S A10. Atomic force microscopy (AFM) image of ~ 270 nm CuBi_2O_4 (sprayed using 20 mM precursor solution with 5 % TEOF and 1 % PEG on FTO at 450°C). The ratio of real surface area to geometric surface area is estimated to be $29/25 = 1.2$ based on the surface roughness.

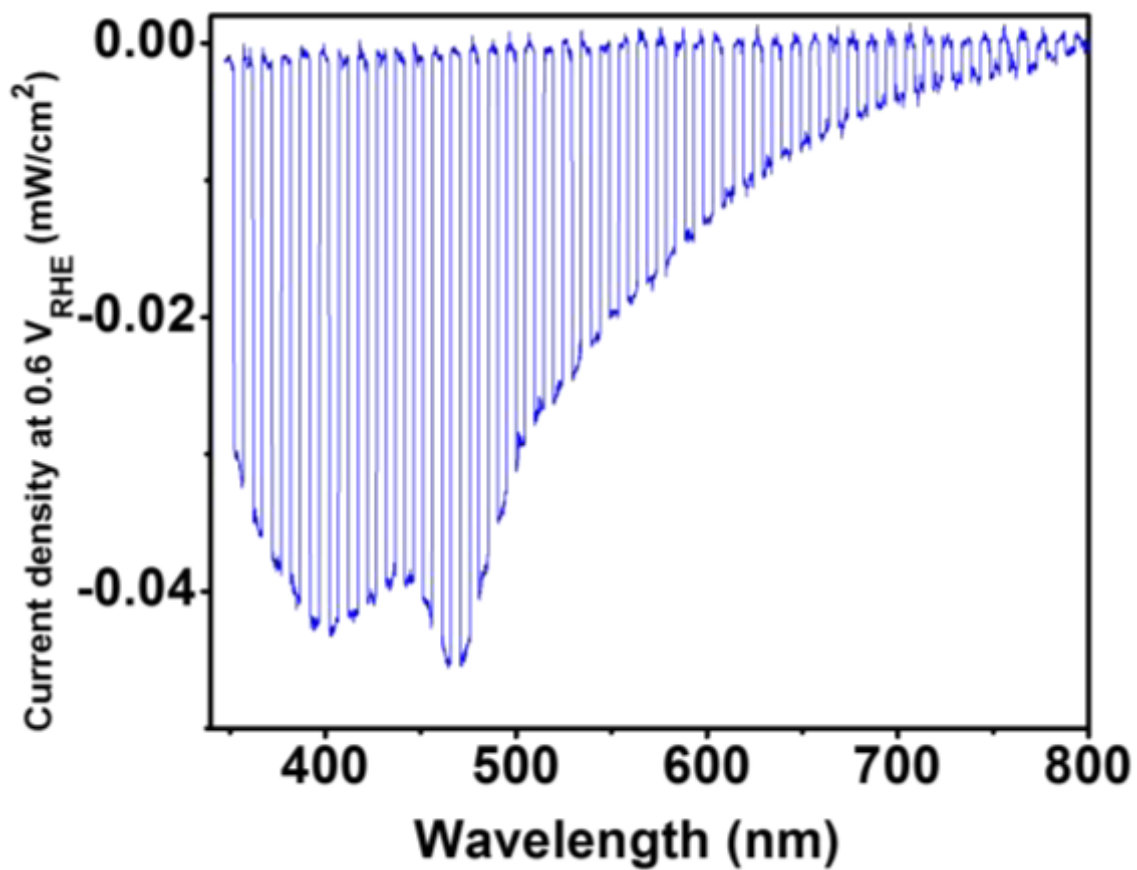


Figure S A11. Dark and light current density for back illumination IPCE measurement of a ~ 270 nm CuBi_2O_4 film on deposited on FTO at 450°C using 20 mM precursor solution with 5 % TEOF and 1 % PEG. The difference between light and dark current density was used to calculate the average photocurrent (J_{ph}) for each wavelength.

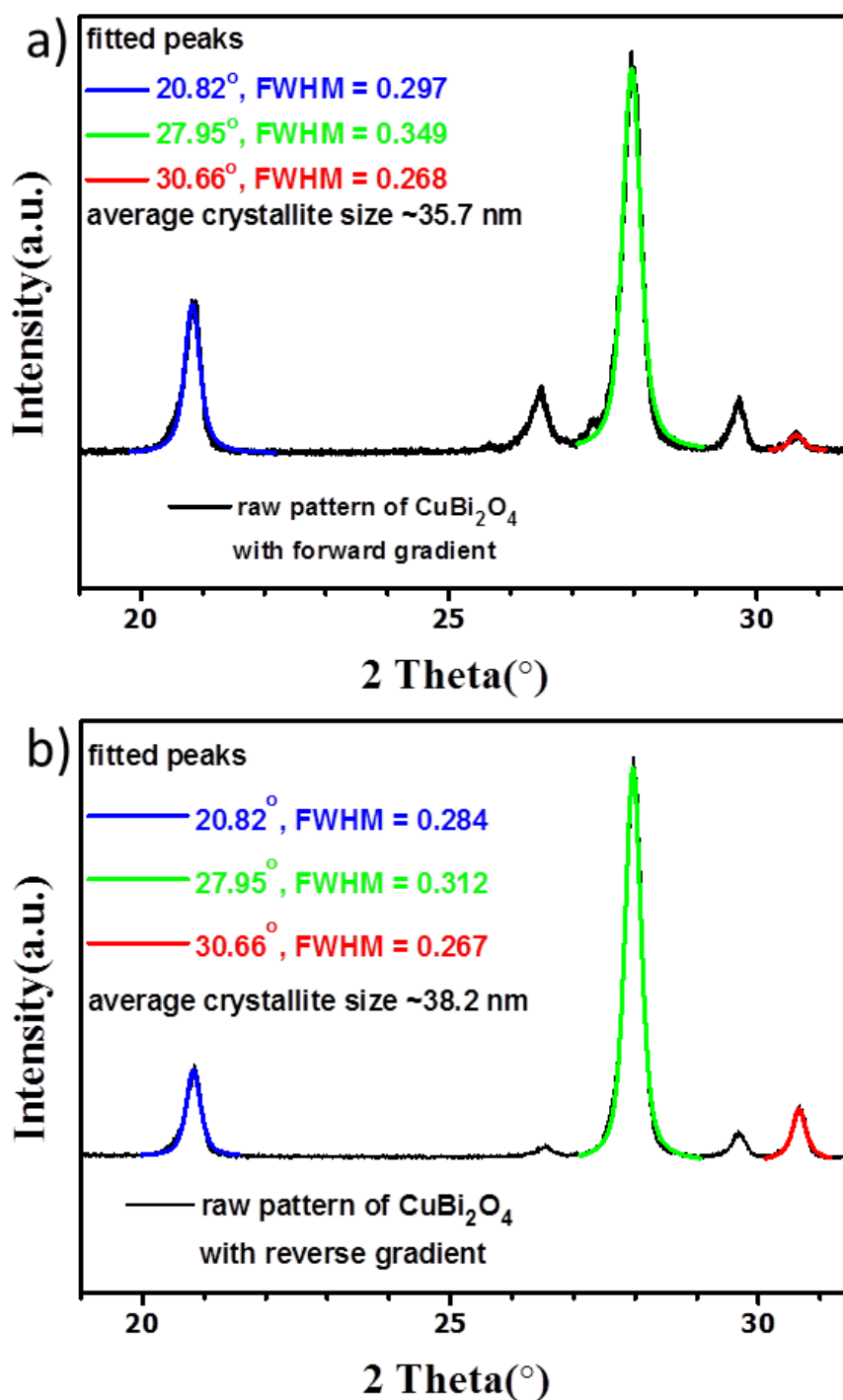
Appendix B: Supplemental Information for Gradient Self-doped CuBi_2O_4 with Highly Improved Charge Separation Efficiency

Figure S B1. Scherrer analysis of a ~ 270 nm CuBi_2O_4 film (a) with a forward gradient; (b) with a reverse gradient. The average crystallite size was calculated from the three peaks for CuBi_2O_4 at 2θ values of 20.82° , 27.95° and 30.66° . Instrumental broadening was corrected using a standard LaB_6 reference material.

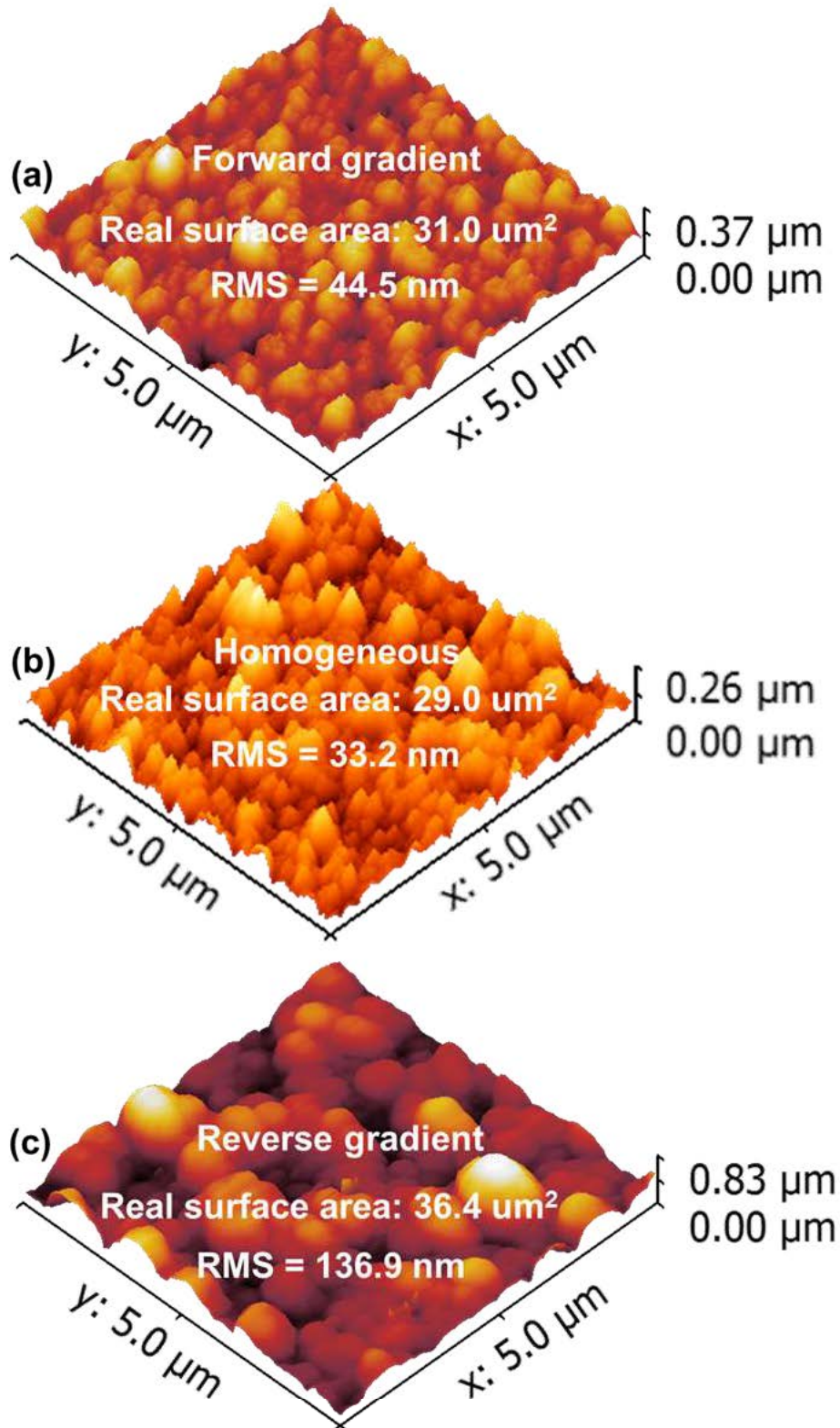


Figure S B2. AFM images of a ~ 270 nm CuBi_2O_4 film (a) with a forward gradient, (b) without a gradient (homogeneous), and (c) with a reverse gradient.

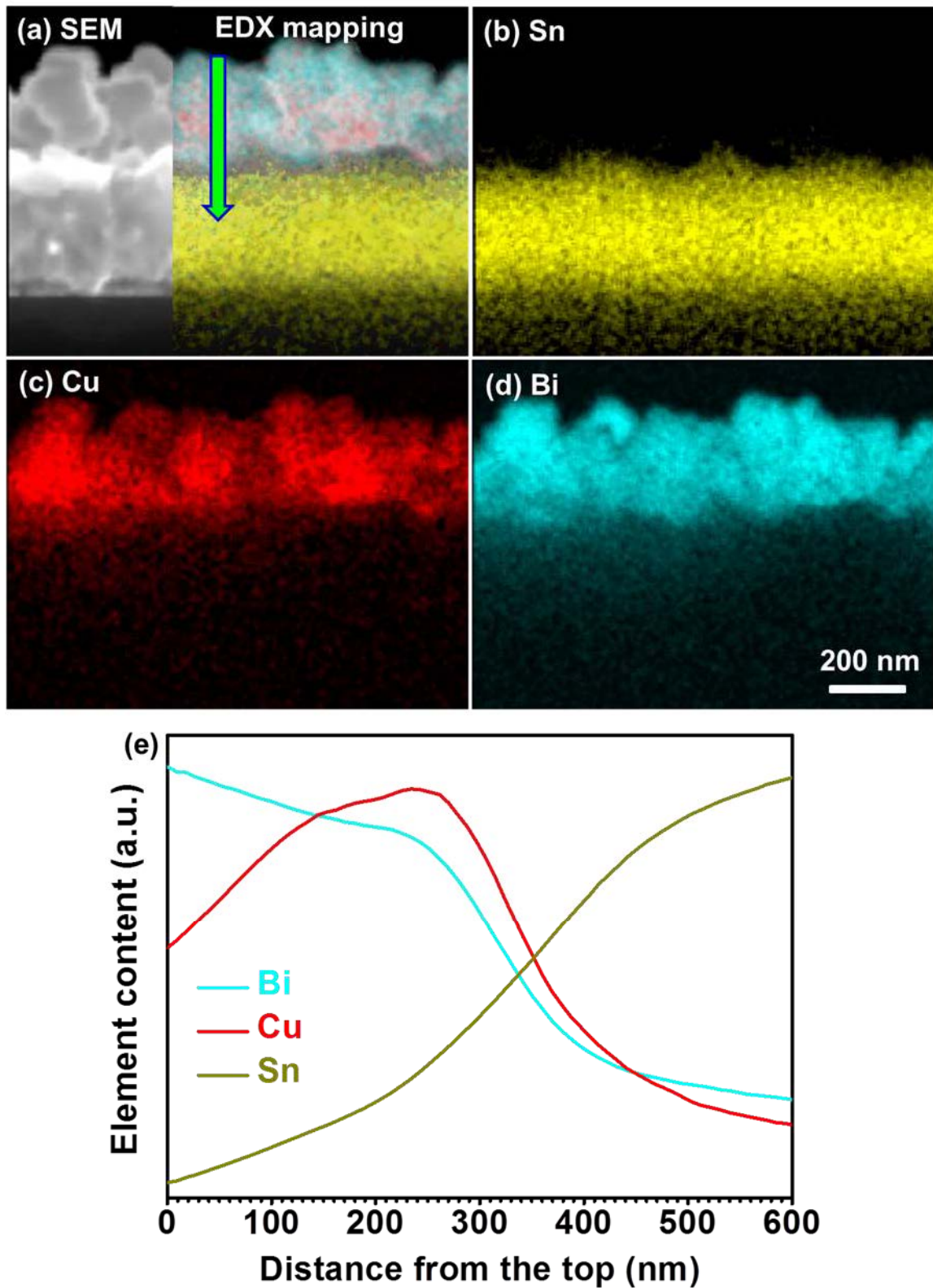


Figure S B3. (a) SEM image with EDX mapping overlaid, (b) Sn distribution, (c) Cu distribution, (d) Bi distribution, and (e) linear scan of each elemental distribution in the direction of the blue arrow for a reverse gradient CuBi_2O_4 photocathode.

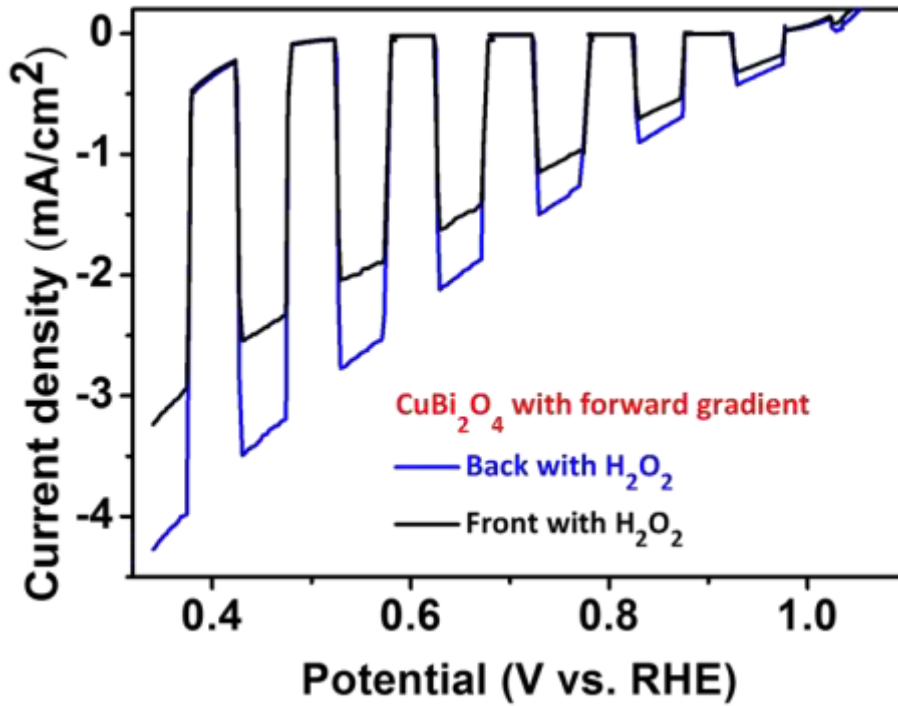


Figure S B4. LSV scans for a ~ 270 nm CuBi_2O_4 film with a forward gradient measured in 0.3 M K_2SO_4 and 0.2 M phosphate buffer (pH 6.65) with H_2O_2 added as an electron scavenger under back illumination.

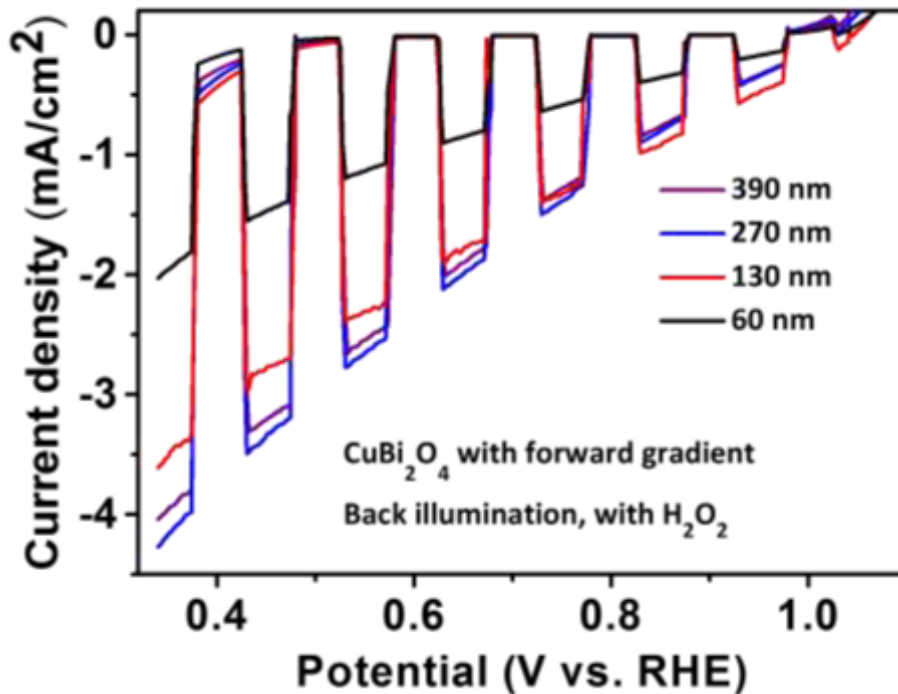


Figure S B5. LSV scans for CuBi_2O_4 films with a forward gradient at different film thicknesses measured in 0.3 M K_2SO_4 and 0.2 M phosphate buffer (pH 6.65) with H_2O_2 added as an electron scavenger under back illumination.

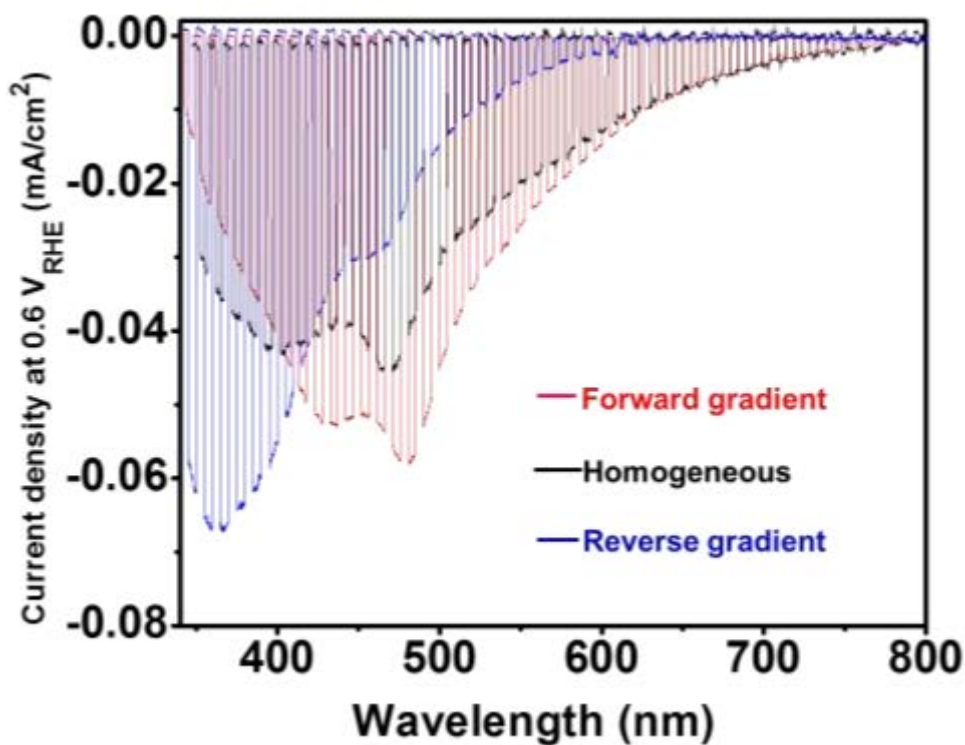


Figure S B6. Dark and light current density for IPCE measurements of ~ 270 nm CuBi_2O_4 films (a) with a forward gradient, (b) without a gradient (homogeneous), and (c) with a reverse gradient. The measurements were performed at a potential of 0.6 V vs RHE in a solution of 0.3 M K_2SO_4 and 0.2 M phosphate buffer (pH 6.65) with H_2O_2 under back illumination.

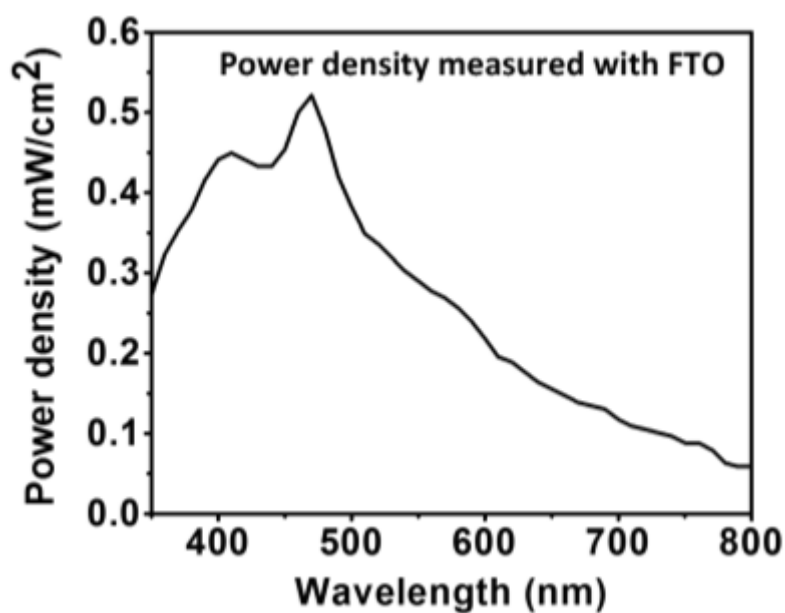


Figure S B7. Power spectra for back illumination IPCE measurements measured with an FTO substrate.

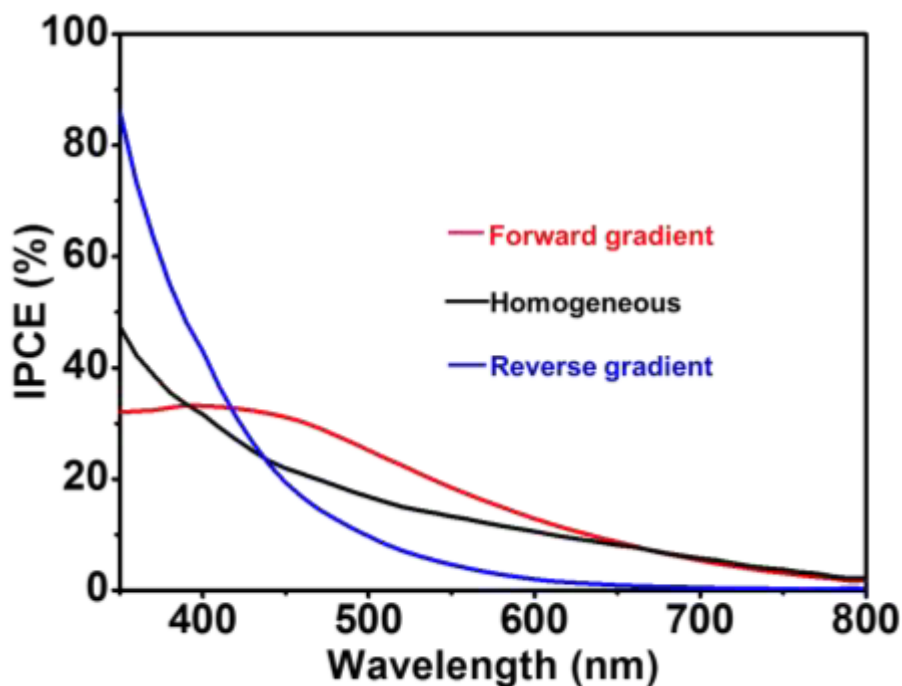


Figure S B8. IPCE spectra for ~ 270 nm CuBi_2O_4 films (a) with a forward gradient, (b) without a gradient (homogeneous), and (c) with a reverse gradient. The measurements were performed at a potential of 0.6 V vs RHE in a solution of 0.3 M K_2SO_4 and 0.2 M phosphate buffer (pH 6.65) with H_2O_2 under back illumination.

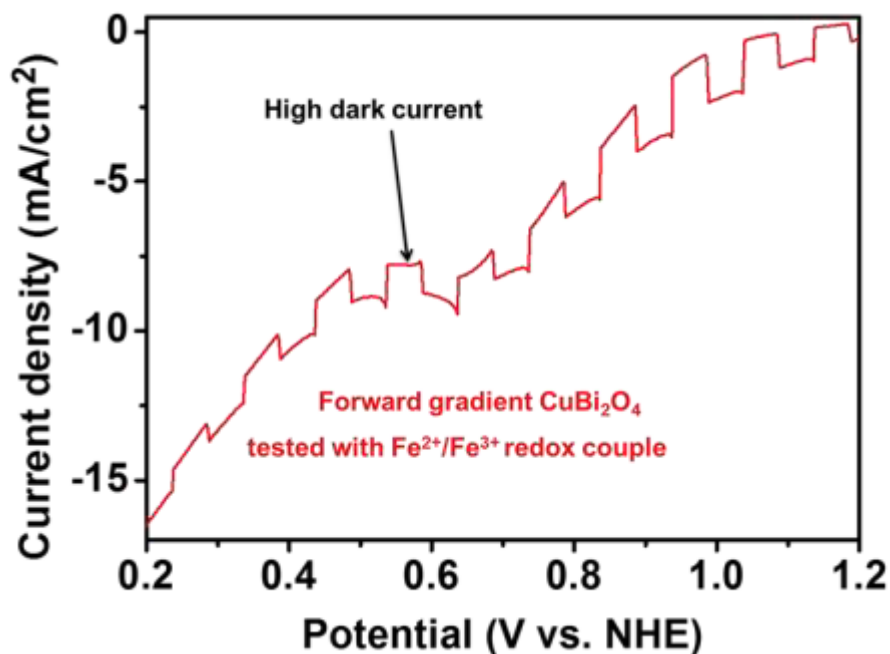


Figure S B9. LSV scans for a ~ 270 nm CuBi_2O_4 film with a forward gradient measured with 35 mM FeCl_2 and 0.1 M FeCl_3 ($\text{Fe}^{2+}/\text{Fe}^{3+}$ redox couple) in acetonitrile under back illumination.

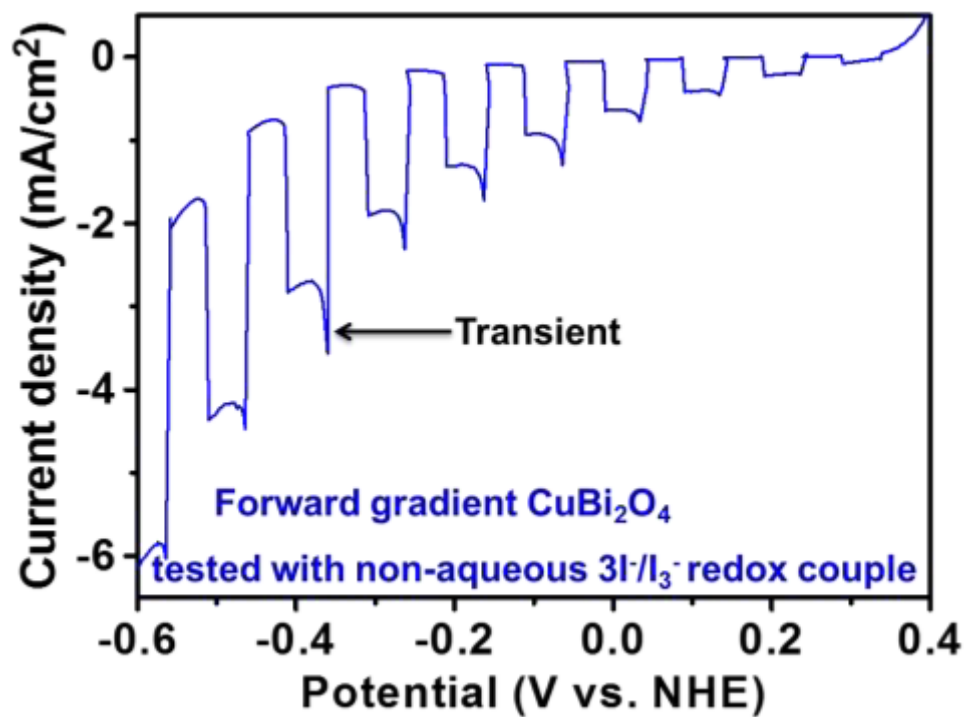
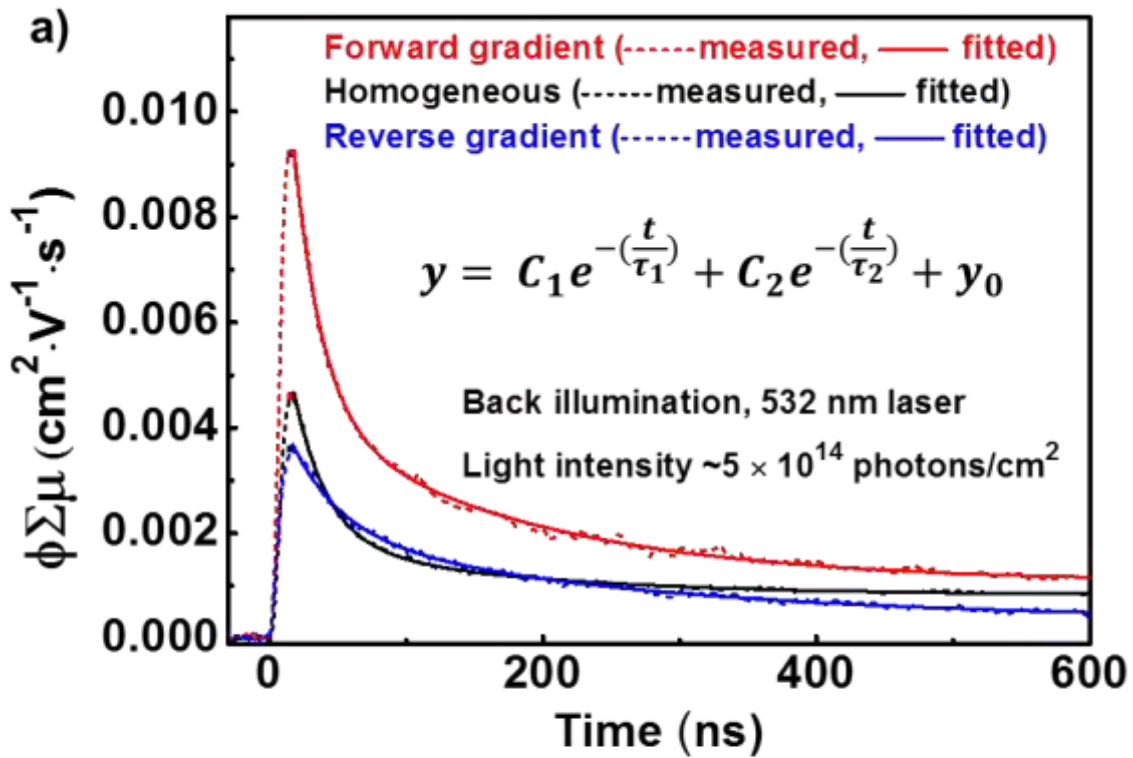


Figure S B10. LSV scans for a ~ 270 nm CuBi_2O_4 film with a forward gradient measured with 25 mM I_2 and 0.25 M NaI ($3\text{I}^-/\text{I}_3^-$ redox couple) in acetonitrile under back illumination.



b)	Parameters	Value	Standard Error
Forward gradient	y_0 (cm ⁻² V ⁻¹ s ⁻¹)	9.1×10^{-4}	2.0×10^{-4}
	C_1 (cm ⁻² V ⁻¹ s ⁻¹)	1.0×10^{-2}	1.4×10^{-3}
	τ_1 (ns)	20.2	3.6
	C_2 (cm ⁻² V ⁻¹ s ⁻¹)	3.2×10^{-3}	7.1×10^{-4}
	τ_2 (ns)	142.6	5.5
Homogeneous	y_0 (cm ⁻² V ⁻¹ s ⁻¹)	7.6×10^{-4}	3.6×10^{-5}
	C_1 (cm ⁻² V ⁻¹ s ⁻¹)	6.3×10^{-3}	2.1×10^{-4}
	τ_1 (ns)	22.7	0.7
	C_2 (cm ⁻² V ⁻¹ s ⁻¹)	1.2×10^{-3}	3.5×10^{-5}
	τ_2 (ns)	153.0	10.4
Reverse gradient	y_0 (cm ⁻² V ⁻¹ s ⁻¹)	2.7×10^{-4}	6.7×10^{-6}
	C_1 (cm ⁻² V ⁻¹ s ⁻¹)	2.2×10^{-3}	1.5×10^{-5}
	τ_1 (ns)	35.0	1.3
	C_2 (cm ⁻² V ⁻¹ s ⁻¹)	1.4×10^{-3}	5.0×10^{-6}
	τ_2 (ns)	237.2	6.3

Figure S B11. (a) TRMC fitting for ~ 270 nm CuBi₂O₄ films deposited on quartz substrates with forward gradient, without gradient (homogeneous), and with reverse gradient, (b) fitting parameters and standard errors.

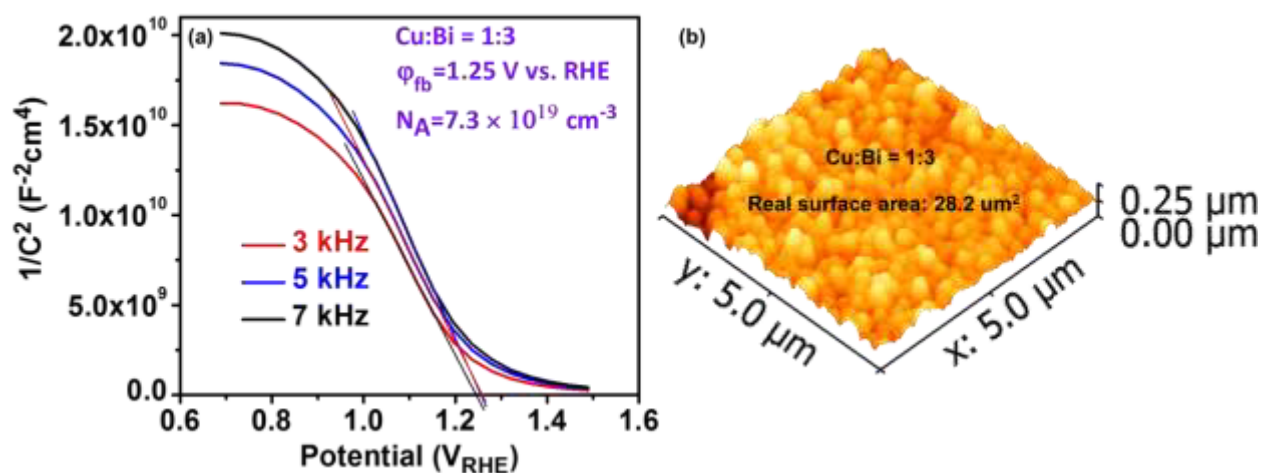


Figure S B12. (a) Mott-Schottky plot for a ~ 270 nm Cu-deficient CuBi_2O_4 photocathode (sprayed using 15 mM $\text{Cu}(\text{NO}_3)_2 \cdot 3\text{H}_2\text{O}$ and 45 mM $\text{Bi}(\text{NO}_3)_3 \cdot 5\text{H}_2\text{O}$ in 1 : 9 acetic acid and ethanol with 5 % TEOF and 1 % PEG on FTO at 450 °C) measured in 0.3 M K_2SO_4 and 0.2 M phosphate buffer (pH 6.65) at 3 kHz, 5 kHz, and 7 kHz, (b) Surface area estimated by AFM.

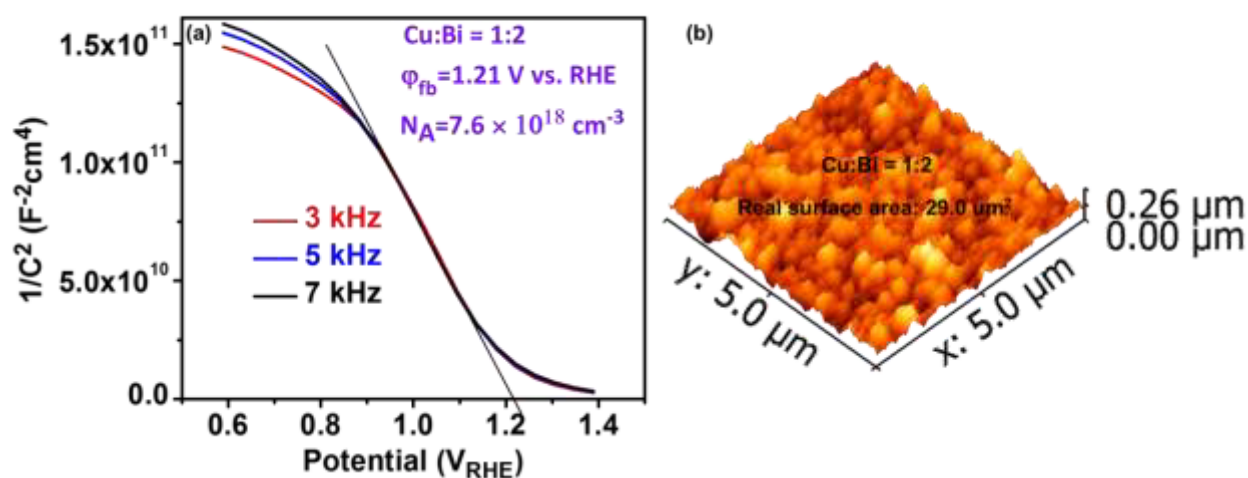


Figure S B13. (a) Mott-Schottky plot for a ~ 270 nm stoichiometric CuBi_2O_4 photocathode (sprayed using 20 mM $\text{Cu}(\text{NO}_3)_2 \cdot 3\text{H}_2\text{O}$ and 40 mM $\text{Bi}(\text{NO}_3)_3 \cdot 5\text{H}_2\text{O}$ in 1 : 9 acetic acid and ethanol with 5 % TEOF and 1 % PEG on FTO at 450 °C) measured in 0.3 M K_2SO_4 and 0.2 M phosphate buffer (pH 6.65) at 3 kHz, 5 kHz, and 7 kHz. (b) Surface area estimated by AFM.

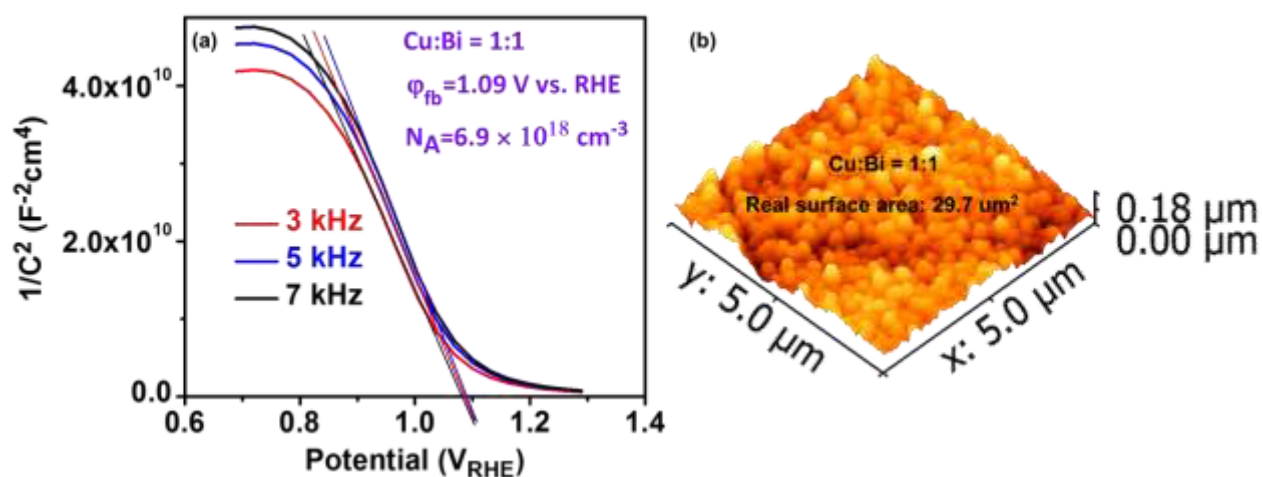


Figure S B14. (a) Mott-Schottky plot for a $\sim 270 \text{ nm}$ Cu-rich CuBi_2O_4 photocathode (sprayed using 30 mM $\text{Cu}(\text{NO}_3)_2 \cdot 3\text{H}_2\text{O}$ and 30 mM $\text{Bi}(\text{NO}_3)_3 \cdot 5\text{H}_2\text{O}$ in $1 : 9$ acetic acid and ethanol with 5% TEOF and 1% PEG on FTO at $450 \text{ }^\circ\text{C}$) measured in 0.3 M K_2SO_4 and 0.2 M phosphate buffer (pH 6.65) at 3 kHz , 5 kHz , and 7 kHz , (b) Surface area estimated by AFM.



Figure S B15. Photo of gas bubbles observed on the photocathode surface during the stability test.

Appendix C: Supplemental Information for Direct Current Magnetron Sputtering of Photoactive BiVO₄: Role of Stoichiometry on Grain Size, Structure, Carrier Mobility and Lifetime

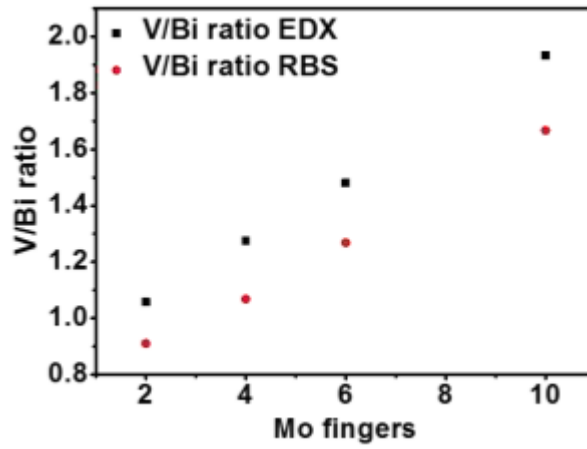


Figure S C1. V : Bi ratio measured by RBS and EDX for Mo-doped BiVO₄ with different Mo content. A correction factor of 0.85 was determined.

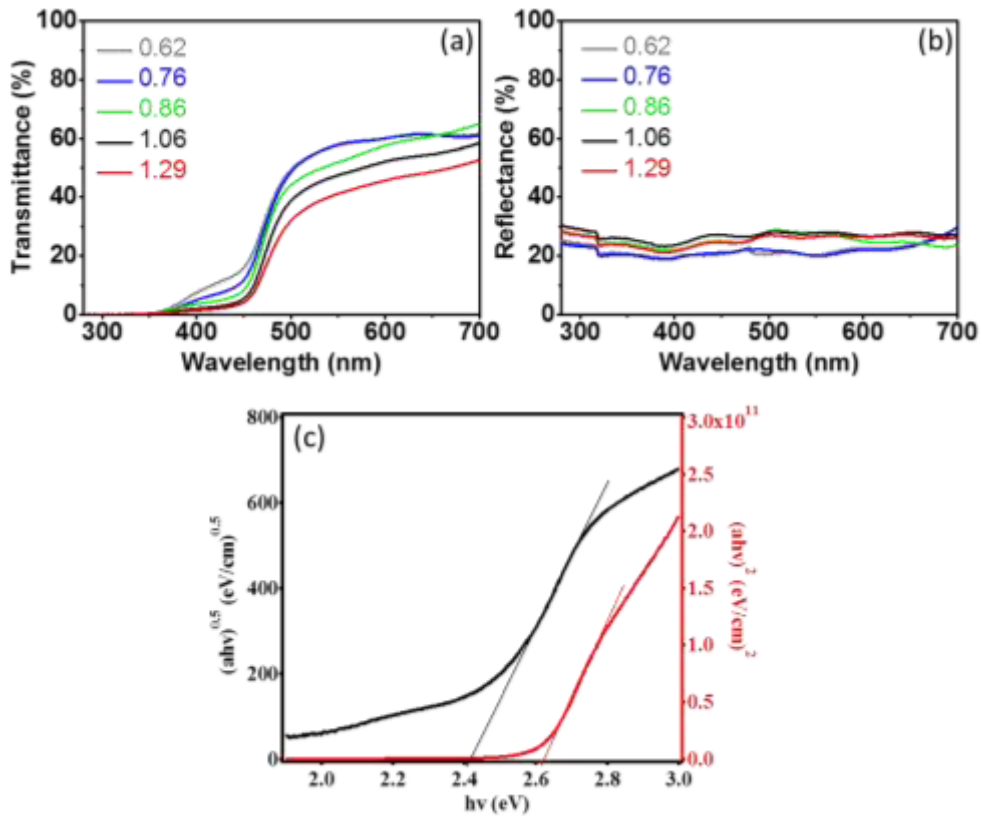


Figure S C2. UV-vis spectroscopy of BiVO₄ samples with different V : Bi ratio (a) transmittance; (b) reflectance; (c) Tauc plot for allowed indirect transitions, black curve and direct transitions of BiVO₄.

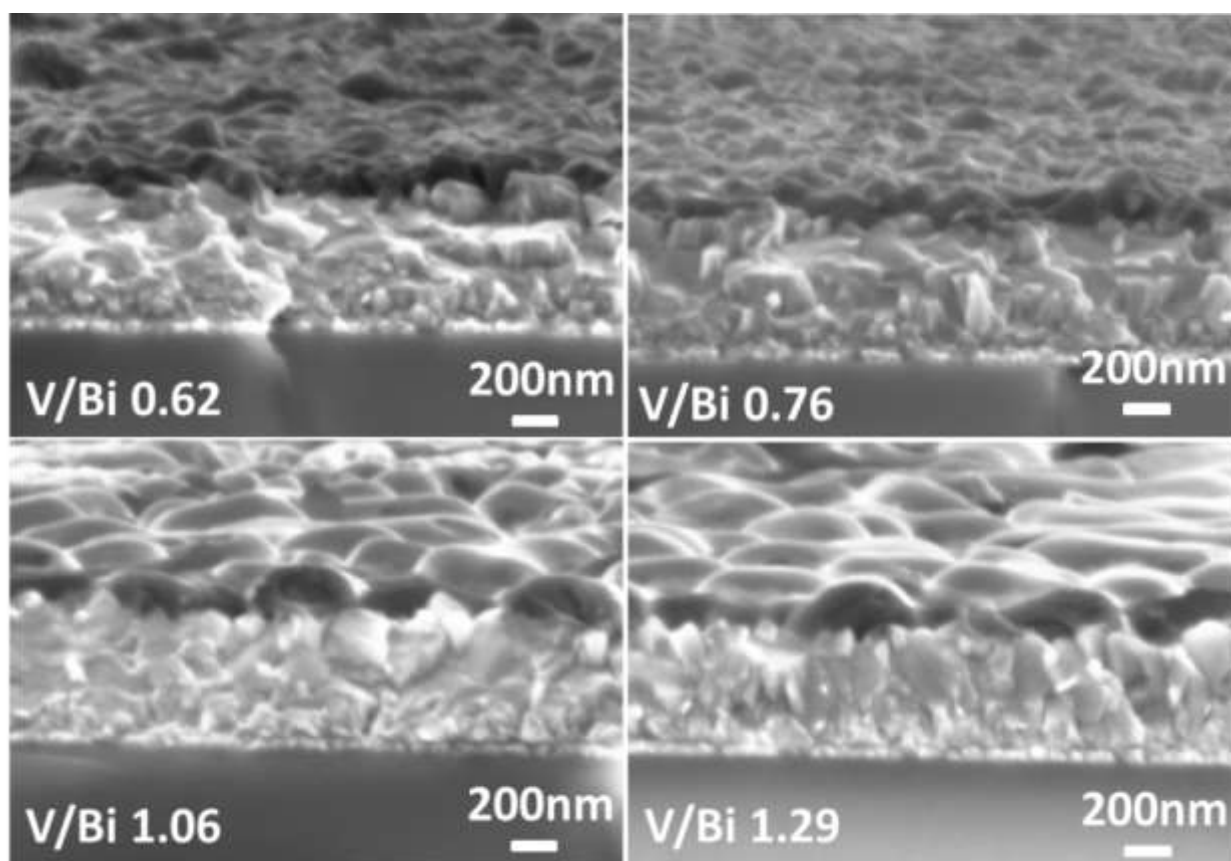


Figure S C3. Cross section SEM images of ~ 180 nm BiVO_4 films with various stoichiometries.

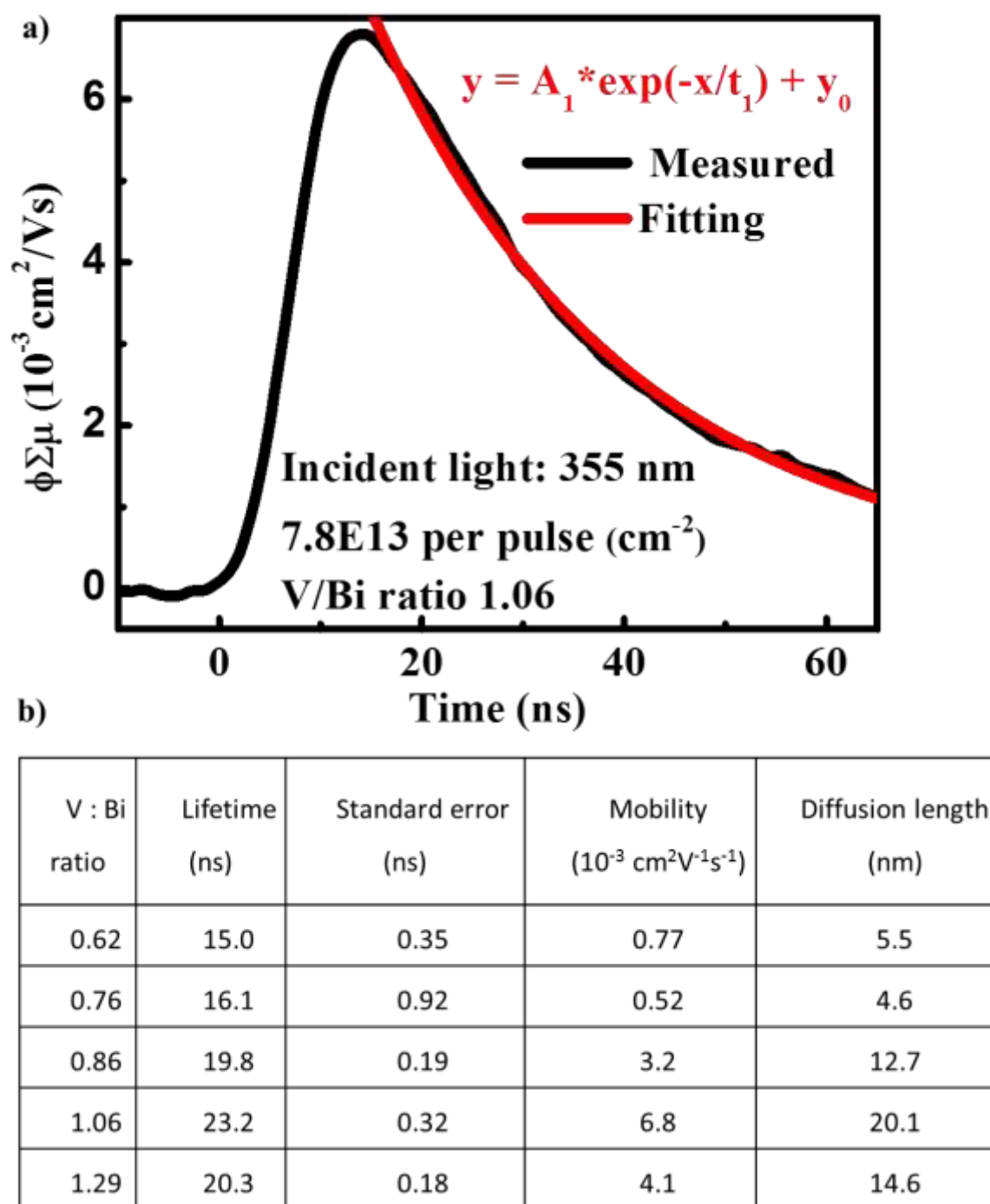


Figure S C4. (a) TRMC signal and lifetime fitting for a ~ 180 nm BiVO_4 film with a V : Bi ratio of 1.06; (b) lifetime, mobility, and diffusion length for ~ 180 nm BiVO_4 films with various stoichiometries.

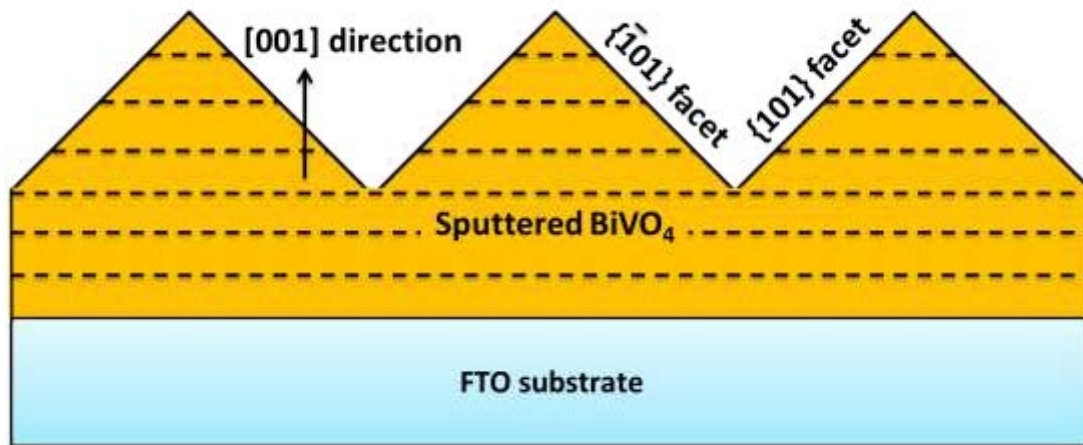


Figure S C5. A simplified illustration of BiVO₄ films with preferred growth along [001] direction but with dominant exposed {101} and {01} facets.

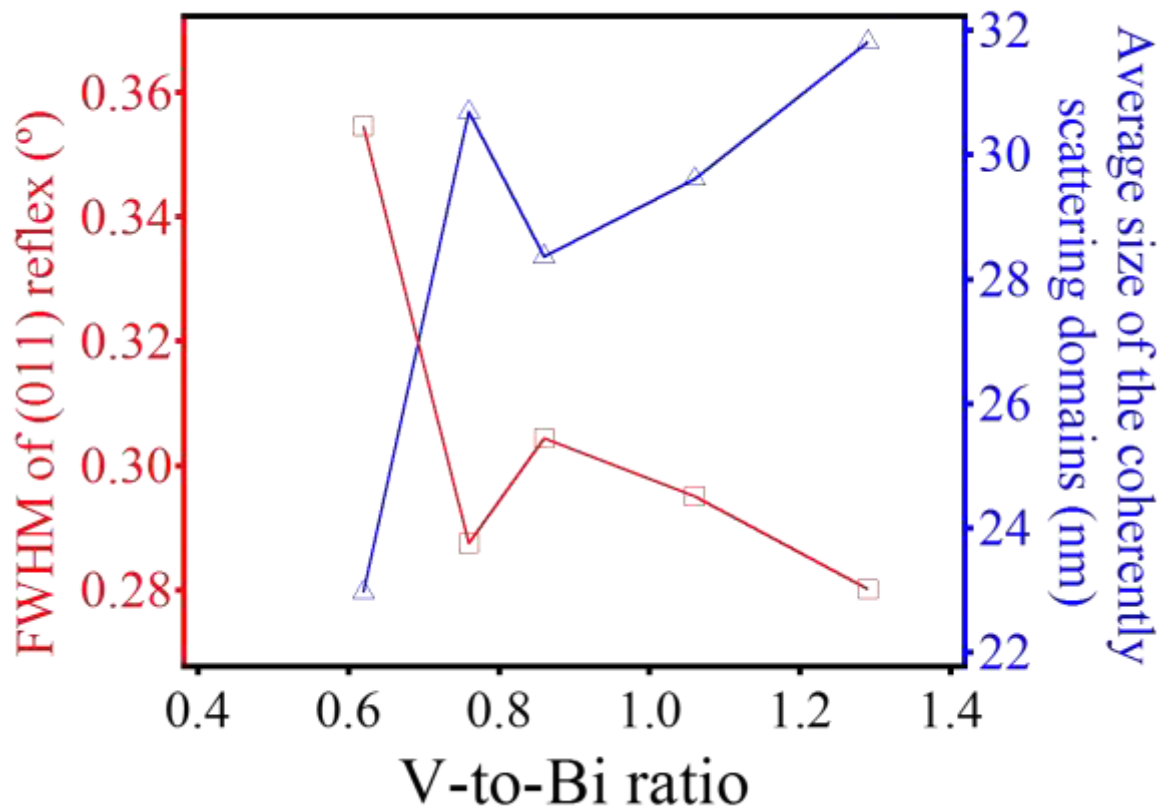


Figure S C6. Average size of the crystallite size estimated from the full width at half maximum (FWHM) of the (011) reflex of the monoclinic BiVO₄.

Appendix C

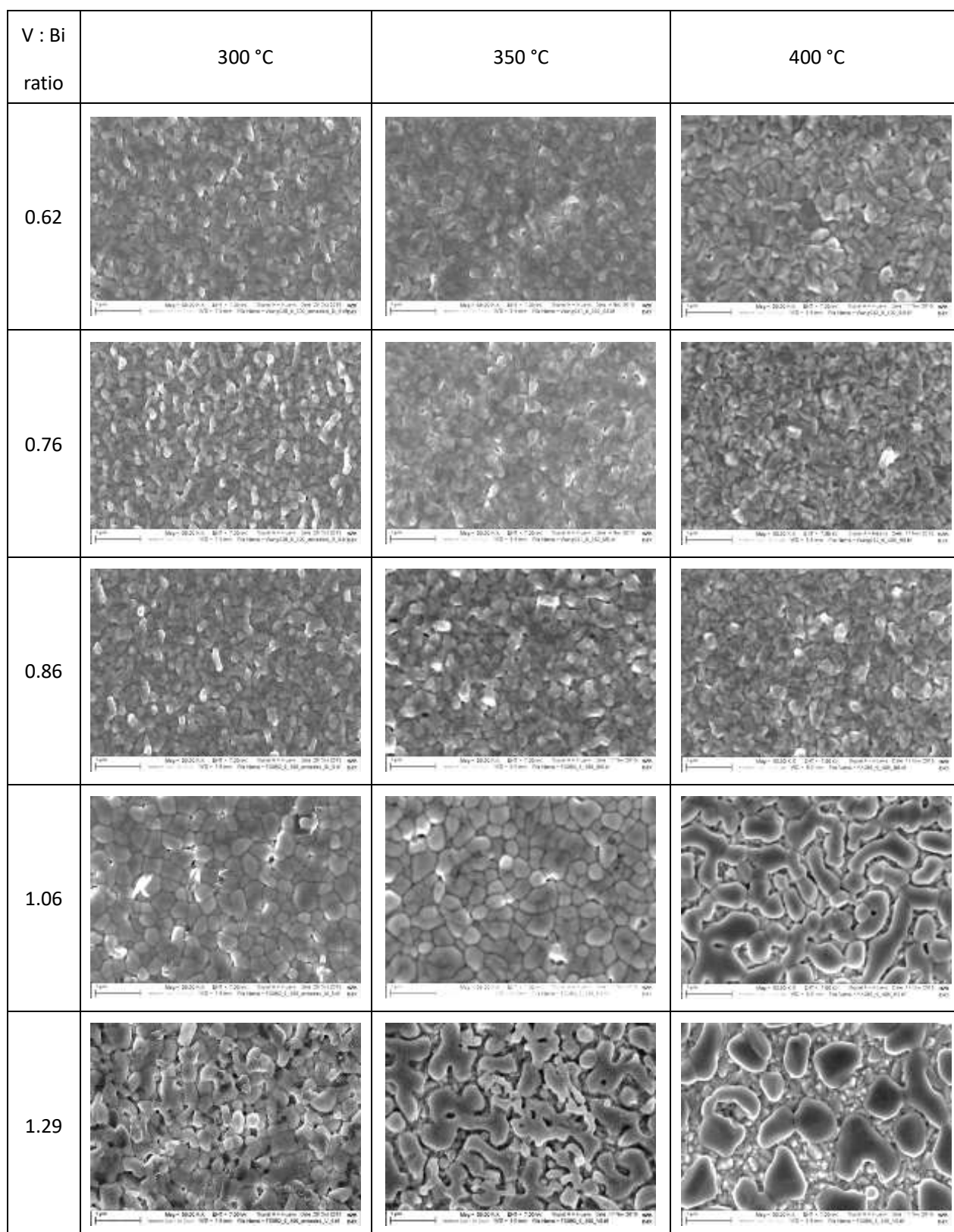


Figure S C7. SEM images of ~ 180 nm BiVO_4 films deposited at 300, 350 and 400 °C with different V-to-Bi ratios.

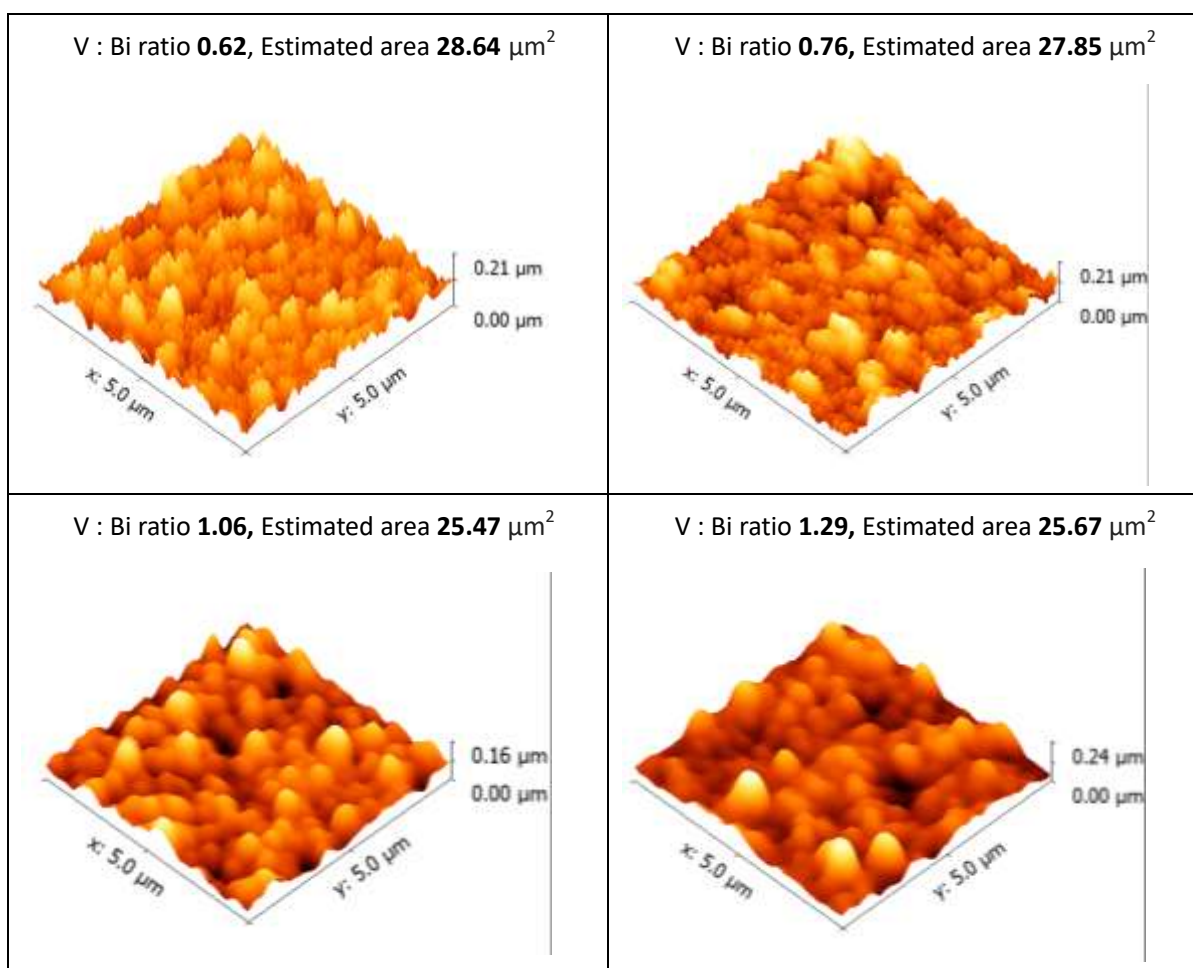


Figure S C8. AFM images of ~ 180 nm BiVO_4 thin films deposited at 300°C with different V-to-Bi ratios (a) V-to-Bi ratios 0.62, calculated surface area $28.64 \mu\text{m}^2$, (b) V-to-Bi ratios 0.76, calculated surface area $27.85 \mu\text{m}^2$, (c) V-to-Bi ratios 1.06, calculated surface area $25.47 \mu\text{m}^2$, (d) V-to-Bi ratios 1.26, calculated surface area $25.67 \mu\text{m}^2$. All the AFM images were measured on an area of 5 μm times 5 μm .

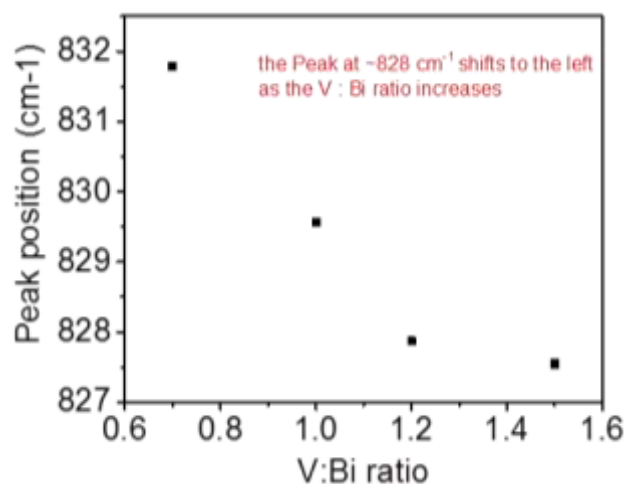


Figure S C9. Raman shift of the peak at $\sim 828 \text{ cm}^{-1}$ for BiVO_4 films as a function of V:Bi ratio.

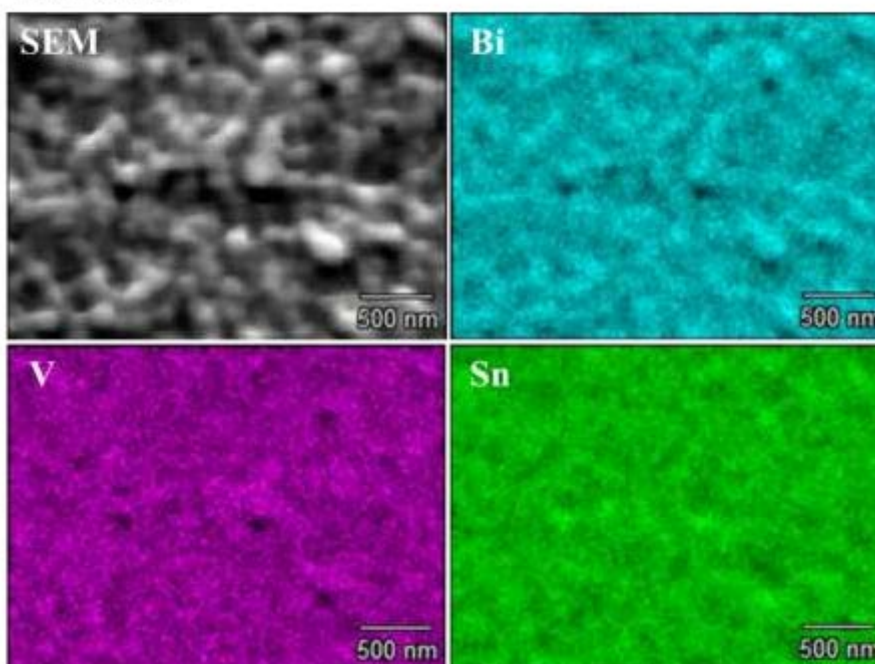
V:Bi=0.76

Figure S C10. EDX mapping of a ~ 180 nm BiVO_4 film deposited at 300°C with a V : Bi ratio of 0.76. Shown are an SEM picture as well as the elemental mappings of Bi, V, and Sn (from the back contact layer $\text{SnO}_2:\text{F}$).

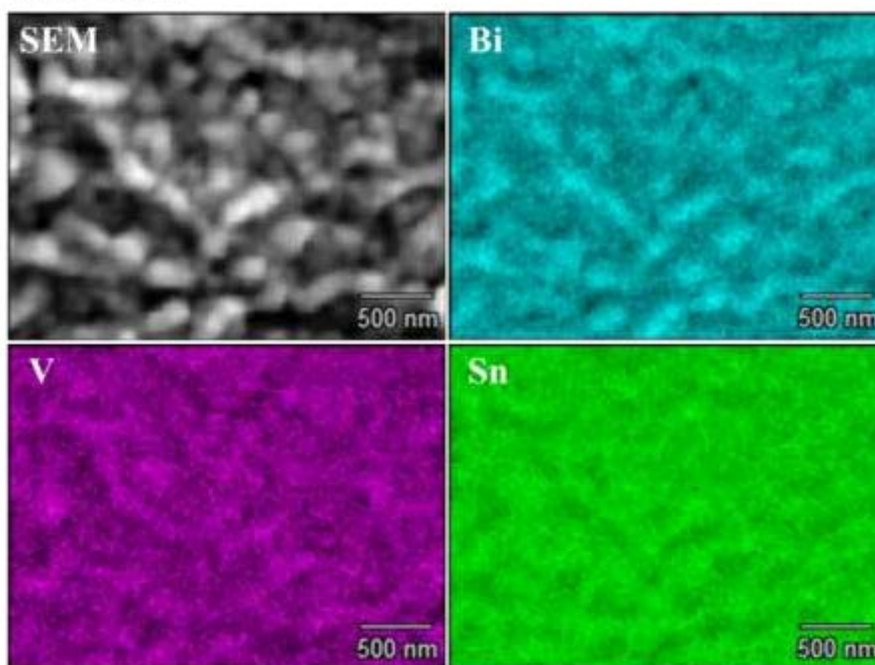
V:Bi=0.86

Figure S C11. EDX mapping of a ~ 180 nm BiVO_4 film deposited at 300°C with a V : Bi ratio of 0.86. Shown are an SEM picture as well as the elemental mappings of Bi, V, and Sn (from the back contact layer $\text{SnO}_2:\text{F}$).

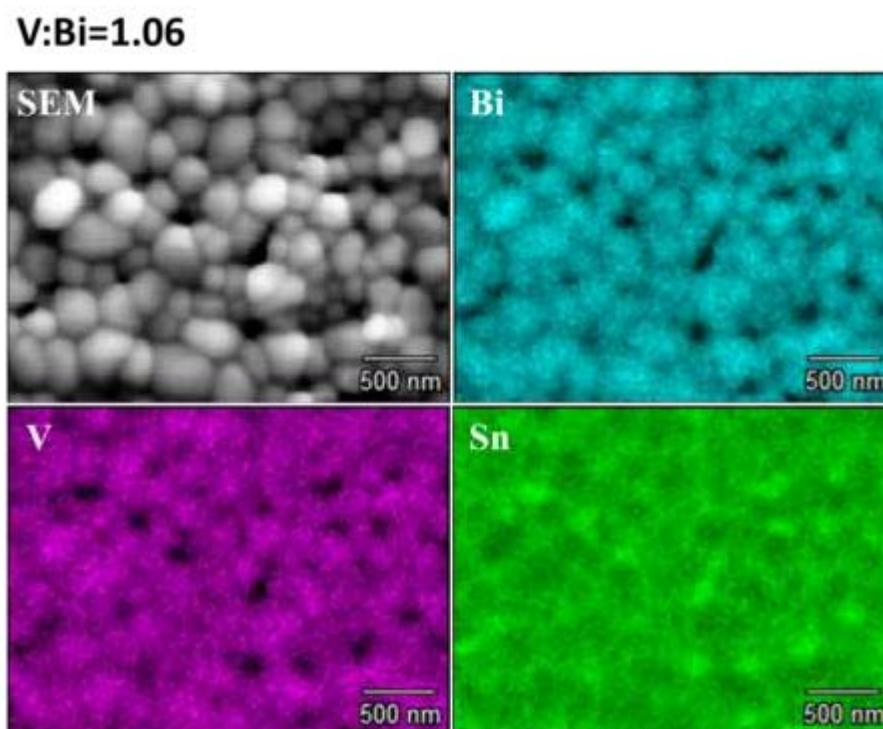


Figure S C12. EDX mapping of a ~ 180 nm BiVO_4 film deposited at 300°C with a V : Bi ratio of 1.06. Shown are an SEM picture as well as the elemental mappings of Bi, V, and Sn (from the back contact layer $\text{SnO}_2:\text{F}$).

List of Publications

1. **Wang, F.**; Chemseddine, A.; Abdi, F. F.; van de Krol, R.; Berglund, S. P. *J. Mater. Chem. A*. **2017**, *5*, 12838-12847.
2. **Wang, F.**; Septina, W.; Chemseddine, A.; Abdi, F. F.; Friedrich, D.; Bogdanoff, P.; van de Krol, R.; Tilley, S. D.; Berglund, S. P. *J. Am. Chem. Soc.* **2017**, **accepted**.
3. **Wang, F.**; Ellmer, K. et al. Reactively magnetron sputtered photoactive BiVO₄ films: structure-stoichiometry-electronic property relationships, **2017**, **prepared**.
4. Xi, L.; **Wang, F.**; Schwanke, C.; Abdi, Fatwa F. F.; Gornak, R.; Fiechter, S.; Ellmer, K.; van de Krol, R.; Lange, K. M. In Situ Structural Study of MnPi Modified BiVO₄ Photoanodes by Soft X-ray Absorption Spectroscopy. *J. Phys. Chem. C*, **2017**, *121*, 19668-19676.
5. **Wang, F.**; Berglund, S. P. et al. Charge carrier dynamics and recombination in dense CuBi₂O₄ films, **in preparation**.
6. Hirst, J.; **Wang, F.**; Berglund, S. P.; Eichberger, R. et al. Defects study in CuBi₂O₄ by photo induced absorption spectroscopy, **in preparation**.
7. Berglund, S. P.; Krause, M.; **Wang, F.** et al. Na-doped CuBi₂O₄ with improved conductivity and photoelectrochemical activity, **in preparation**.

Acknowledgement

I would like to thank my advisors Dr. Sean P. Berglund and Prof. Roel van de Krol for their advice and guidance. Thanks Prof. Roel van de Krol for offering me the excellent opportunity to pursue my PhD at EE-IF, and providing all the facilities and professional guidance. Sean is specially acknowledged for helping me drafting the research plan, providing invaluable advices, supporting my ideas and helping me in any possible way to explore them. Thanks Sean also for believing me, and allowing me the space and freedom that I need for independent thinking.

Thanks Karim for creating a very comfortable working environment for me and offering all the facilities on the 4th floor. It is really enjoyable to discuss solution chemistry with you.

Fatwa is gratefully acknowledged for teaching me the necessary skills in PEC and helping me going through the difficulties. Mr. Ellmer and Karsten are acknowledged for their assistance in establishing the magnetron sputtering system. Other group members at EE-IF are also acknowledged for their help in material characterization and data analysis, especially Sebastian, Dennis, Peter, Jiwook, and Yimeng.

Thanks Hagen and Moritz for their kind help with the translation of the abstract.

I deeply appreciate my wife Tingting Sun for her encouragement, support, quiet patience, enormous sacrifice and companionship during the past 3 years. Thanks Tingting also for bringing our little angle to my life. Xuanxuan, your beautiful smile makes every day full of love. I thank my parents in law and my parents for taking good care of Xuanxuan when I was writing my thesis.

Last but not least, I would like to acknowledge the Oversea Study Program of the Guangzhou Elite Project (GEP JY201308, Guangzhou, China) for providing me financial support, and thank the project managers, especially Ms. Huiting Mai, for their assistance during my PhD.

Bibliography

- (1) Hsia-San Shu, F. *University of California, San Diego*. **2008**, 1-41.
- (2) BP Statistical Review of World Energy.
<http://www.bp.com/en/global/corporate/energy-economics/statistical-review-of-world-energy.html>.
- (3) Zhong, W.; Haigh, J. D. *Weather*. **2013**, *68* (4), 100-105.
- (4) P. K. Tans; Ralph. Trends in Atmospheric Carbon Dioxide. www.esrl.noaa.gov/gmd/ccgg/trends/.
- (5) North, G. R.; Biondi, F.; Bloomfield, P.; Christy, J.; Cuffey, K.; Dickinson, R.; Druffel, E.; Nychka, D.; Otto-Bliesner, B.; Roberts, N. *The National Academies Press*. **2006**, 145.
- (6) Stocker, T. F.; Qin, D.; Plattner, G.-K.; Tignor, M.; Allen, S. K.; Boschung, J.; Nauels, A.; Xia, Y.; Bex, V.; Midgley, P. M. *Intergovernmental Panel on Climate Change, Working Group I Contribution to the IPCC Fifth Assessment Report (AR5)(Cambridge Univ Press, New York)*. **2013**.
- (7) Huaman, R. N. E.; Jun, T. X. *Renewable and Sustainable Energy Reviews*. **2014**, *31*, 368-385.
- (8) Hansen, J.; Ruedy, R.; Sato, M.; Lo, K. *Rev. Geophys*. **2010**, *48* (4).
- (9) Mathiesen, B. V.; Lund, H.; Karlsson, K. *Applied Energy*. **2011**, *88* (2), 488-501.
- (10) Barbier, E. *Renewable and Sustainable Energy Reviews*. **2002**, *6* (1), 3-65.
- (11) Jafari, T.; Moharreri, E.; Amin, A. S.; Miao, R.; Song, W.; Suib, S. L. *Molecules*. **2016**, *21* (7), 900.
- (12) van de Krol, R.; Grätzel, M., *Photoelectrochemical hydrogen production*. Springer: **2012**; Vol. 90.
- (13) Lewis, N. S.; Nocera, D. G. *Proceedings of the National Academy of Sciences*. **2006**, *103* (43), 15729-15735.
- (14) C. Philibert. *International Energy Agency*. **2014**.
- (15) Parida, B.; Iniyar, S.; Goic, R. *Renewable and sustainable energy reviews*. **2011**, *15* (3), 1625-1636.
- (16) Xie, W.; Dai, Y.; Wang, R.; Sumathy, K. *Renewable and Sustainable Energy Reviews*. **2011**, *15* (6), 2588-2606.
- (17) Turner, J. A. *Science*. **2004**, *305* (5686), 972-974.
- (18) Melián, E. P.; Díaz, O. G.; Méndez, A. O.; López, C. R.; Suárez, M. N.; Rodríguez, J. D.; Navío, J.; Hevia, D. F.; Peña, J. P. *Int. J. Hydrogen Energy*. **2013**, *38* (5), 2144-2155.
- (19) Dunn, S. *Int. J. Hydrogen Energy*. **2002**, *27* (3), 235-264.
- (20) Veziroğlu, T. N.; Şahi, S. *Energy Convers. Manage*. **2008**, *49* (7), 1820-1831.
- (21) Rajeshwar, K.; McConnell, R.; Licht, S. *Toward a renewable energy future*. Springer: New York. **2008**.
- (22) Grimes, C. A.; Varghese, O. K.; Ranjan, S., Hydrogen generation by water splitting. In *Light, Water, Hydrogen*, Springer: **2008**; pp 35-113.
- (23) Schröder, V.; Emonts, B.; Janßen, H.; Schulze, H. P. *Chemical engineering & technology*. **2004**, *27* (8), 847-851.
- (24) James, B. D.; Baum, G. N.; Perez, J.; Baum, K. N. *Technoeconomic analysis of photoelectrochemical (PEC) hydrogen production*; Directed Technologies, Inc., Arlington, VA (United States): **2009**.
- (25) Keable, J.; Holcroft, B., Economic and Business Perspectives. In *Photoelectrochemical Hydrogen Production*, Springer: **2012**; pp 277-292.

- (26) Hund, F., *History of quantum theory*. **1980**.
- (27) Center, R. R. D. *ASTM G173-03 Tables*. **2016**.
- (28) Kahn, A. *Materials Horizons*. **2016**, 3 (1), 7-10.
- (29) Weber, M. F.; Dignam, M. *Int. J. Hydrogen Energy*. **1986**, 11 (4), 225-232.
- (30) Murphy, A.; Barnes, P.; Randeniya, L.; Plumb, I.; Grey, I.; Horne, M.; Glasscock, J. *Int. J. Hydrogen Energy*. **2006**, 31 (14), 1999-2017.
- (31) Bolton, J. R.; Strickler, S. J.; Connolly, J. S. *Nature*. **1985**, 316 (6028), 495-500.
- (32) Bolton, J. R.; Hall, D. O. *Annual Review of Energy*. **1979**, 4 (1), 353-401.
- (33) Shangguan, W.; Yoshida, A. *J. Phys. Chem. B*. **2002**, 106 (47), 12227-12230.
- (34) Paracchino, A.; Laporte, V.; Sivula, K.; Grätzel, M.; Thimsen, E. *Nature Materials*. **2011**, 10 (6), 456-461.
- (35) Moriya, M.; Minegishi, T.; Kumagai, H.; Katayama, M.; Kubota, J.; Domen, K. *J. Am. Chem. Soc.* **2013**, 135 (10), 3733-3735.
- (36) Huang, Q.; Ye, Z.; Xiao, X. *J. Mater. Chem. A*. **2015**, 3 (31), 15824-15837.
- (37) Seitz, L. C.; Chen, Z.; Forman, A. J.; Pinaud, B. A.; Benck, J. D.; Jaramillo, T. F. *ChemSusChem*. **2014**, 7 (5), 1372-1385.
- (38) Sivula, K.; Van De Krol, R. *Nature Reviews Materials*. **2016**, 1, 15010.
- (39) Böckris, J.; Reddy, A.; Gamboa-Aldeco, M. *Modern Electrochemistry, 2A: Fundamentals of Electrodeics*. **2000**.
- (40) Luo, J.; Steier, L.; Son, M.-K.; Schreier, M.; Mayer, M. T.; Grätzel, M. *Nano Lett.* **2016**, 16 (3), 1848-1857.
- (41) Choi, J.; Song, J. T.; Jang, H. S.; Choi, M.-J.; Sim, D. M.; Yim, S.; Lim, H.; Jung, Y. S.; Oh, J. *ELECTRON MATER LETT.* **2017**, 13 (1), 57-65.
- (42) Berglund, S. P.; Abdi, F. F.; Bogdanoff, P.; Chemseddine, A.; Friedrich, D.; van de Krol, R. *Chem. Mater.* **2016**, 28 (12), 4231-4242.
- (43) Wang, F.; Chemseddine, A.; Abdi, F.; van de Krol, R.; Berglund, S. P. *J. Mater. Chem. A*. **2017**, 5, 12838-12847.
- (44) Spathis, P.; Poullos, I. *Corros. Sci.* **1995**, 37 (5), 673-680.
- (45) Gerischer, H. *Journal of Electroanalytical Chemistry and Interfacial Electrochemistry*. **1977**, 82 (1-2), 133-143.
- (46) Park, S.-M.; Barber, M. E. *J. Electroanal. Chem. Interfacial Electrochem.* **1979**, 99 (1), 67-75.
- (47) Morrison, S. R., *Electrochemistry at semiconductor and oxidized metal electrodes*. **1980**.
- (48) Bak, T.; Nowotny, J.; Rekas, M.; Sorrell, C. *Int. J. Hydrogen Energy*. **2002**, 27 (10), 991-1022.
- (49) Bhatt, M. D.; Lee, J. S. *J. Mater. Chem. A*. **2015**, 3 (20), 10632-10659.
- (50) Septina, W.; Prabhakar, R. R.; Wick, R.; Moehl, T.; Tilley, S. D. *Chem. Mater.* **2017**, 29 (4), 1735-1743.
- (51) Navarro, R. M.; Alvarez-Galvan, M. C.; de la Mano, J. A. V.; Al-Zahrani, S. M.; Fierro, J. L. G. *Energy Environ Sci.* **2010**, 3 (12), 1865-1882.
- (52) Chen, X.; Shen, S.; Guo, L.; Mao, S. S. *Chem. Rev.* **2010**, 110 (11), 6503-6570.

- (53) Boddy, P. J. *Electrochem. Soc.* **1968**, *115* (2), 199-203.
- (54) Fujishima, A.; Honda, K. *Nature*. **1972**, *238* (5358), 37-38.
- (55) Jiang, C.; Moniz, S. J.; Wang, A.; Zhang, T.; Tang, J. *Chem. Soc. Rev.* **2017**.
- (56) Sivula, K.; Le Formal, F.; Grätzel, M. *ChemSusChem*. **2011**, *4* (4), 432-449.
- (57) Cristino, V.; Caramori, S.; Argazzi, R.; Meda, L.; Marra, G. L.; Bignozzi, C. A. *Langmuir*. **2011**, *27* (11), 7276-7284.
- (58) Abdi, F. F.; Han, L.; Smets, A. H.; Zeman, M.; Dam, B.; van de Krol, R. *Nat. Commun.* **2013**, *4*, 2195.
- (59) Joshi, U. A., New Cu (I)-Based p-Type Semiconducting Metal Oxides for Solar-to-Fuel Conversion: Investigation and Challenges. In *Materials and Processes for Solar Fuel Production*, Springer: **2014**; pp 97-112.
- (60) Prévot, M. S.; Guijarro, N.; Sivula, K. *ChemSusChem*. **2015**, *8* (8), 1359-1367.
- (61) Yu, Q.; Meng, X.; Wang, T.; Li, P.; Liu, L.; Chang, K.; Liu, G.; Ye, J. *Chem. Commun.* **2015**, *51* (17), 3630-3633.
- (62) Matsumoto, Y.; Omae, M.; Sugiyama, K.; Sato, E. *Journal of Physical Chemistry*. **1987**, *91* (3), 577-581.
- (63) Joshi, U. A.; Maggard, P. A. *J. Phys. Chem. Lett.* **2012**, *3* (11), 1577-1581.
- (64) Wolfe, C. M.; Stillman, G.; Lindley, W. *J. Appl. Phys.* **1970**, *41* (7), 3088-3091.
- (65) Khaselev, O.; Turner, J. A. *Science*. **1998**, *280* (5362), 425-427.
- (66) Lee, M. H.; Takei, K.; Zhang, J.; Kapadia, R.; Zheng, M.; Chen, Y. Z.; Nah, J.; Matthews, T. S.; Chueh, Y. L.; Ager, J. W. *Angew. Chem. Int. Ed.* **2012**, *51* (43), 10760-10764.
- (67) Ziegler, J.; Fertig, D.; Kaiser, B.; Jaegermann, W.; Blug, M.; Hoch, S.; Busse, J. *Energy Procedia*. **2012**, *22*, 108-113.
- (68) Kocha, S. S.; Turner, J. A. *J. Electrochem. Soc.* **1995**, *142* (8), 2625-2630.
- (69) Kamimura, J.; Bogdanoff, P.; Lähnemann, J.; Hauswald, C.; Geelhaar, L.; Fiechter, S.; Riechert, H. *J. Am. Chem. Soc.* **2013**, *135* (28), 10242-10245.
- (70) Licht, S.; Wang, B.; Mukerji, S.; Soga, T.; Umeno, M.; Tributsch, H. *J. Phys. Chem. B*. **2000**, *104* (38), 8920-8924.
- (71) Liu, C.; Sun, J.; Tang, J.; Yang, P. *Nano Lett.* **2012**, *12* (10), 5407-5411.
- (72) Walter, M. G.; Warren, E. L.; McKone, J. R.; Boettcher, S. W.; Mi, Q.; Santori, E. A.; Lewis, N. S. *Chemical reviews*. **2010**, *110* (11), 6446-6473.
- (73) Gratzel, M. *Nature*. **2001**, *414* (6861), 338.
- (74) Huang, Q.; Li, Q.; Xiao, X. *J. Phys. Chem. C*. **2014**, *118* (5), 2306-2311.
- (75) Mathew, X.; Bansal, A.; Turner, J.; Dhere, R.; Mathews, N.; Sebastian, P. *J. New Mater. Electrochem. Syst.* **2002**, *5* (2), 149-154.
- (76) Ahmed, S.; Reuter, K. B.; Gunawan, O.; Guo, L.; Romankiw, L. T.; Deligianni, H. *Advanced Energy Materials*. **2012**, *2* (2), 253-259.
- (77) Kushiya, K.; Ohtake, Y.; Yamada, A.; Konagai, M. *Jpn. J. Appl. Phys.* **1994**, *33* (12R), 6599.

- (78) Scheer, R.; Walter, T.; Schock, H.; Fearheiley, M.; Lewerenz, H. *Applied Physics Letters*. **1993**, *63* (24), 3294-3296.
- (79) Yokoyama, D.; Minegishi, T.; Jimbo, K.; Hisatomi, T.; Ma, G.; Katayama, M.; Kubota, J.; Katagiri, H.; Domen, K. *Applied physics express*. **2010**, *3* (10), 101202.
- (80) Luo, J.; Li, Z.; Nishiwaki, S.; Schreier, M.; Mayer, M. T.; Cendula, P.; Lee, Y. H.; Fu, K.; Cao, A.; Nazeeruddin, M. K. *Advanced Energy Materials*. **2015**, *5* (24).
- (81) Septina, W.; Ikeda, S.; Harada, T.; Minegishi, T.; Domen, K.; Matsumura, M. *Chem. Commun.* **2014**, *50* (64), 8941-8943.
- (82) Goetzberger, A.; Knobloch, J.; Voss, B., *Crystalline silicon solar cells*. Wiley Online Library: **1998**.
- (83) Ma, Q.-B.; Ziegler, J.; Kaiser, B.; Fertig, D.; Calvet, W.; Murugasen, E.; Jaegermann, W. *Int. J. Hydrogen Energy*. **2014**, *39* (4), 1623-1629.
- (84) Kargar, A.; Kim, S. J.; Allameh, P.; Choi, C.; Park, N.; Jeong, H.; Pak, Y.; Jung, G. Y.; Pan, X.; Wang, D. *Adv. Funct. Mater.* **2015**, *25* (17), 2609-2615.
- (85) Ding, C.; Qin, W.; Wang, N.; Liu, G.; Wang, Z.; Yan, P.; Shi, J.; Li, C. *Physical Chemistry Chemical Physics*. **2014**, *16* (29), 15608-15614.
- (86) Hou, Y.; Abrams, B. L.; Vesborg, P. C.; Björketun, M. E.; Herbst, K.; Bech, L.; Setti, A. M.; Damsgaard, C. D.; Pedersen, T.; Hansen, O. *Nature materials*. **2011**, *10* (6), 434.
- (87) Xu, H.; Ouyang, S.; Liu, L.; Reunchan, P.; Umezawa, N.; Ye, J. *J. Mater. Chem. A*. **2014**, *2* (32), 12642-12661.
- (88) Asahi, R.; Morikawa, T.; Ohwaki, T.; Aoki, K.; Taga, Y. *Science*. **2001**, *293* (5528), 269-271.
- (89) Piskunov, S.; Lisovski, O.; Begens, J.; Bocharov, D.; Zhukovskii, Y. F.; Wessel, M.; Spohr, E. *J. Phys. Chem. C*. **2015**, *119* (32), 18686-18696.
- (90) Pendlebury, S. R.; Wang, X.; Le Formal, F.; Cornuz, M.; Kafizas, A.; Tilley, S. D.; Grätzel, M.; Durrant, J. R. *J. Am. Chem. Soc.* **2014**, *136* (28), 9854-9857.
- (91) Barroso, M.; Pendlebury, S. R.; Cowan, A. J.; Durrant, J. R. *Chemical Science*. **2013**, *4* (7), 2724-2734.
- (92) Barroso, M.; Cowan, A. J.; Pendlebury, S. R.; Grätzel, M.; Klug, D. R.; Durrant, J. R. *J. Am. Chem. Soc.* **2011**, *133* (38), 14868-14871.
- (93) Cesar, I.; Kay, A.; Gonzalez Martinez, J. A.; Grätzel, M. *J. Am. Chem. Soc.* **2006**, *128* (14), 4582-4583.
- (94) Dotan, H.; Kfir, O.; Sharlin, E.; Blank, O.; Gross, M.; Dumchin, I.; Ankonina, G.; Rothschild, A. *Nature Materials*. **2013**, *12* (2), 158.
- (95) Noufi, R.; Tench, D. *J. Electrochem. Soc.* **1980**, *127* (1), 188-190.
- (96) Ellis, A. B.; Bolts, J. M.; Wrighton, M. S. *J. Electrochem. Soc.* **1977**, *124* (10), 1603-1607.
- (97) Pareek, A.; Purbia, R.; Paik, P.; Hebalkar, N. Y.; Kim, H. G.; Borse, P. H. *Int. J. Hydrogen Energy*. **2014**, *39* (9), 4170-4180.
- (98) Tokunaga, S.; Kato, H.; Kudo, A. *Chemistry of Materials*. **2001**, *13* (12), 4624-4628.
- (99) Yu, J.; Kudo, A. *Adv. Funct. Mater.* **2006**, *16* (16), 2163-2169.
- (100) Suarez, C. M.; Hernández, S.; Russo, N. *Applied Catalysis A: General*. **2015**, *504*, 158-170.

- (101) Chen, Z.; Jaramillo, T. F.; Deutsch, T. G.; Kleiman-Shwarscstein, A.; Forman, A. J.; Gaillard, N.; Garland, R.; Takanahe, K.; Heske, C.; Sunkara, M. *J. Mater. Res.* **2010**, *25* (01), 3-16.
- (102) Arai, T.; Konishi, Y.; Iwasaki, Y.; Sugihara, H.; Sayama, K. *J. Comb. Chem.* **2007**, *9* (4), 574-581.
- (103) Ong, E.; Kwei, G.; Robinson, R.; Ramakrishna, B.; Von Dreele, R. *Phys. Rev. B.* **1990**, *42* (7), 4255.
- (104) Henmi, C. *Mineralogical Magazine.* **1995**, *59* (396), 545-548.
- (105) Sharma, G.; Zhao, Z.; Sarker, P.; Nail, B. A.; Wang, J.; Huda, M. N.; Osterloh, F. E. *J. Mater. Chem. A.* **2016**, *4*, 2936-2942.
- (106) Hahn, N. T.; Holmberg, V. C.; Korgel, B. A.; Mullins, C. B. *J. Phys. Chem. C.* **2012**, *116* (10), 6459-6466.
- (107) Kang, D.; Hill, J. C.; Park, Y.; Choi, K.-S. *Chem. Mater.* **2016**, *28* (12), 4331-4340.
- (108) Sean P. Berglund, F. F. A., Peter Bogdanoff, Abdelkrim Chemseddine, Dennis Friedrich, and Roel van de Krol. *Chemistry of Materials.* **2016**.
- (109) Gomes, W.; Vanmaekelbergh, D. *Electrochim. Acta.* **1996**, *41* (7-8), 967-973.
- (110) Granér, F.; Sillén, L. G. *Nature.* **1947**, *160* (4073), 715-715.
- (111) Nolin, B.; Jones, R. N. *Can. J. Chem.* **1956**, *34* (10), 1382-1391.
- (112) Huang, H.; He, Y.; Li, X.; Li, M.; Zeng, C.; Dong, F.; Du, X.; Zhang, T.; Zhang, Y. *J. Mater. Chem. A.* **2015**, *3* (48), 24547-24556.
- (113) Udvardi, B.; Kovács, I. J.; Fancsik, T.; Kónya, P.; Bátor, M.; Stercel, F.; Falus, G.; Szalai, Z. *Appl. Spectrosc.* **2016**, 1-12.
- (114) Calvar, N.; Gonzalez, B.; Dominguez, A. *Chem. Eng. Process.* **2007**, *46* (12), 1317-1323.
- (115) Kesslin, G.; Bradshaw, R. *Ind. Eng. Chem. Prod. Res. Dev.* **1966**, *5* (1), 27-29.
- (116) Perednis, D.; Gauckler, L. J. *J. Electroceram.* **2005**, *14* (2), 103-111.
- (117) Perednis, D. Thin film deposition by spray pyrolysis and the application in solid oxide fuel cells. Diss., Naturwissenschaften ETH Zürich, Nr. 15190, **2003**.
- (118) Wang, L. S.; Zhou, Y. H.; Quan, Z. W.; Lin, J. *Mater. Lett.* **2005**, *59* (10), 1130-1133.
- (119) Azizian, S.; Hemmati, M. *J. Chem. Eng. Data.* **2003**, *48* (3), 662-663.
- (120) Rahbari-Sisakht, M.; Taghizadeh, M.; Eliassi, A. *J. Chem. Eng. Data.* **2003**, *48* (5), 1221-1224.
- (121) Meek, T.; Von Roedern, B.; Clem, P.; Hanrahan, R. *Mater. Lett.* **2005**, *59* (8), 1085-1088.
- (122) Meinert, M.; Reiss, G. *J. Phys.: Condens. Matter.* **2014**, *26* (11), 115503.
- (123) Park, H. S.; Lee, C.-Y.; Reisner, E. *Phys. Chem. Chem. Phys.* **2014**, *16* (41), 22462-22465.
- (124) Berglund, S. P.; Lee, H. C.; Núñez, P. D.; Bard, A. J.; Mullins, C. B. *Phys. Chem. Chem. Phys.* **2013**, *15* (13), 4554-4565.
- (125) Daipayan Roy, G. F. S., Mohammad Kabir Hossaina, Csaba Janáky, Krishnan Rajeshwar. *Catal. Today.* **2017**.
- (126) Wood, D.; Tauc, J. *Phys. Rev. B.* **1972**, *5* (8), 3144.
- (127) Boschloo, G.; Fitzmaurice, D. *J. Phys. Chem. B.* **1999**, *103* (12), 2228-2231.

- (128) Chen, X.; Liu, L.; Peter, Y. Y.; Mao, S. S. *Science*. **2011**, *331* (6018), 746-750.
- (129) Zhang, B.; Zhang, X.; Xiao, X.; Shen, Y. *ACS Appl. Mater. Interfaces*. **2016**, *8* (3), 1606-1614.
- (130) Li, J.; Peter, L. *J. Electroanal. Chem. Interfacial Electrochem*. **1985**, *182* (2), 399-411.
- (131) Schneider, J.; Bahnemann, D. W. *J. Phys. Chem. Lett*. **2013**, *4* (20), 3479-3483.
- (132) Cao, D.; Nasori, N.; Wang, Z.; Mi, Y.; Wen, L.; Yang, Y.; Qu, S.; Wang, Z.; Lei, Y. *J. Mater. Chem. A*. **2016**, *4*, 8995-9001.
- (133) Hong, S. J.; Lee, S.; Jang, J. S.; Lee, J. S. *Energy Environ Sci*. **2011**, *4* (5), 1781-1787.
- (134) Saito, R.; Miseki, Y.; Sayama, K. *Chem. Commun*. **2012**, *48* (32), 3833-3835.
- (135) Zhang, K.; Shi, X.-J.; Kim, J. K.; Park, J. H. *Phys. Chem. Chem. Phys*. **2012**, *14* (31), 11119-11124.
- (136) Saad, M.; Kassis, A. *Sol. Energy Mater. Sol. Cells*. **2003**, *79* (4), 507-517.
- (137) Abdi, F. F.; Savenije, T. J.; May, M. M.; Dam, B.; van de Krol, R. *The Journal of Physical Chemistry Letters*. **2013**, *4* (16), 2752-2757.
- (138) Ziwrtsch, M.; Müller, S. n.; Hempel, H.; Unold, T.; Abdi, F. F.; van de Krol, R.; Friedrich, D.; Eichberger, R. *ACS Energy Lett*. **2016**, *1* (5), 888-894.
- (139) Fuxian Wang, A. C., Fatwa F. Abdi, Roel van de Krol, Sean P. Berglund. *Journal of Materials Chemistry A*. **2017**, *5*, 12838.
- (140) Kroeze, J. E.; Savenije, T. J.; Warman, J. M. *Journal of the American Chemical Society*. **2004**, *126* (24), 7608-7618.
- (141) Kunst, M.; Beck, G. *J. Appl. Phys*. **1986**, *60* (10), 3558-3566.
- (142) Savenije, T. J.; Ferguson, A. J.; Kopidakis, N.; Rumbles, G. *The Journal of Physical Chemistry C*. **2013**, *117* (46), 24085-24103.
- (143) Infelta, P. P.; De Haas, M. P.; Warman, J. M. *Radiat. Phys. Chem*. **1977**, *10* (5-6), 353-365.
- (144) Hazra, S.; Ghosh, A. *J. Appl. Phys*. **1998**, *84* (2), 987-992.
- (145) Cole, K. S.; Cole, R. H. *J. Chem. Phys*. **1941**, *9* (4), 341-351.
- (146) Ghose, J.; Kanungo, A. *J. Therm. Anal. Calorim*. **1981**, *20* (2), 459-462.
- (147) Popović, Z. V.; Kliche, G.; Cardona, M.; Liu, R. *Phys. Rev. B*. **1990**, *41* (6), 3824-3828.
- (148) Yuvaraj, S.; Karthikeyan, K.; Kalpana, D.; Lee, Y. S.; Selvan, R. K. *J. Colloid Interface Sci*. **2016**, *469*, 47-56.
- (149) Zhang, F.; Saxena, S. *Appl. Phys. Lett*. **2006**, *88* (14), 141926.
- (150) Hagemann, H.; Bill, H.; Walker, E.; François, M. *Solid state communications*. **1990**, *73* (6), 447-451.
- (151) Anderman, M.; Kennedy, J. H. *J. Electrochem. Soc*. **1984**, *131* (1), 21-26.
- (152) Hardee, K. L.; Bard, A. J. *J. Electrochem. Soc*. **1977**, *124* (2), 215-224.
- (153) Abdi, F. F.; Berglund, S. P. *J. Phys. D: Appl. Phys*. **2017**, *50* (19), 193002.
- (154) Mei, B.; Pedersen, T.; Malacrida, P.; Bae, D.; Frydendal, R.; Hansen, O.; Vesborg, P. C.; Seger, B.; Chorkendorff, I. *J. Phys. Chem. C*. **2015**, *119* (27), 15019-15027.

- (155) Seger, B.; Pedersen, T.; Laursen, A. B.; Vesborg, P. C.; Hansen, O.; Chorkendorff, I. *J. Am. Chem. Soc.* **2013**, *135* (3), 1057-1064.
- (156) Pihosh, Y.; Turkevych, I.; Mawatari, K.; Uemura, J.; Kazoe, Y.; Kosar, S.; Makita, K.; Sugaya, T.; Matsui, T.; Fujita, D. *Scientific reports.* **2015**, *5*.
- (157) Sleight, A. W.; Chen, H. Y.; Ferretti, A.; Cox, D. E. *Mater. Res. Bull.* **1979**, *14* (12), 1571-1581.
- (158) Kudo, A.; Omori, K.; Kato, H. *J. Am. Chem. Soc.* **1999**, *121* (49), 11459-11467.
- (159) Zhao, Z.; Luo, W.; Li, Z.; Zou, Z. *Phys. Lett. A.* **2010**, *374* (48), 4919-4927.
- (160) Walsh, A.; Yan, Y.; Huda, M. N.; Al-Jassim, M. M.; Wei, S.-H. *Chem. Mater.* **2009**, *21* (3), 547-551.
- (161) Chatchai, P.; Murakami, Y.; Kishioka, S.-y.; Nosaka, A.; Nosaka, Y. *Electrochem. Solid-State Lett.* **2008**, *11* (6), H160-H163.
- (162) Chen, S.; Wang, L.-W. *Chem. Mater.* **2012**, *24* (18), 3659-3666.
- (163) Park, Y.; McDonald, K. J.; Choi, K.-S. *Chem. Soc. Rev.* **2013**, *42* (6), 2321-2337.
- (164) Zhao, Z.; Li, Z.; Zou, Z. *Phys. Chem. Chem. Phys.* **2011**, *13* (10), 4746-4753.
- (165) Zhang, L.; Chen, D.; Jiao, X. *J. Phys. Chem. B.* **2006**, *110* (6), 2668-2673.
- (166) Yu, J.; Kudo, A. *Chem. Lett.* **2005**, *34* (6), 850-851.
- (167) Obregón, S.; Caballero, A.; Colón, G. *Applied Catalysis B: Environmental.* **2012**, *117*, 59-66.
- (168) Luo, W.; Yang, Z.; Li, Z.; Zhang, J.; Liu, J.; Zhao, Z.; Wang, Z.; Yan, S.; Yu, T.; Zou, Z. *Energy Environ Sci.* **2011**, *4* (10), 4046-4051.
- (169) Chemseddine, A.; Ullrich, K.; Mete, T.; Abdi, F.; van de Krol, R. *J. Mater. Chem. A.* **2016**, *4*, 1723-1728.
- (170) Su, J.; Guo, L.; Bao, N.; Grimes, C. A. *Nano Letters.* **2011**, *11* (5), 1928-1933.
- (171) Abdi, F. F.; Firet, N.; Dabirian, A.; van de Krol, R. In *Spray-deposited Co-Pi Catalyzed BiVO₄: a low-cost route towards highly efficient photoanodes*, MRS Proceedings, Cambridge Univ Press: 2012; pp mrss12-1446-u02-05.
- (172) Dunkle, S. S.; Helmich, R. J.; Suslick, K. S. *J. Phys. Chem. C.* **2009**, *113* (28), 11980-11983.
- (173) Berglund, S. P.; Flaherty, D. W.; Hahn, N. T.; Bard, A. J.; Mullins, C. B. *The Journal of Physical Chemistry C.* **2011**, *115* (9), 3794-3802.
- (174) Seabold, J. A.; Choi, K.-S. *J. Am. Chem. Soc.* **2012**, *134* (4), 2186-2192.
- (175) Ding, C.; Shi, J.; Wang, D.; Wang, Z.; Wang, N.; Liu, G.; Xiong, F.; Li, C. *Phys. Chem. Chem. Phys.* **2013**, *15* (13), 4589-4595.
- (176) Pinaud, B. A.; Benck, J. D.; Seitz, L. C.; Forman, A. J.; Chen, Z.; Deutsch, T. G.; James, B. D.; Baum, K. N.; Baum, G. N.; Ardo, S.; Wang, H.; Miller, E.; Jaramillo, T. F. *Env. Sci. Techn.* **2013**, *6*, 1983-2002.
- (177) Kukla, R. *Surface & Coatings Technology.* **1997**, *93* (1), 1-6.
- (178) Musil, J.; Baroch, P.; Vlček, J.; Nam, K.; Han, J. *Thin Solid Films.* **2005**, *475* (1), 208-218.
- (179) Ellmer, K. *Low Temperature Plasmas. Fundamentals, Technologies and Techniques.* **2008**, *2*, 101.
- (180) Safi, I. *Surf. Coat. Technol.* **2000**, *127* (2), 203-218.
- (181) Tien, L.-C.; Liou, Y.-H. *Surface & Coatings Technology.* **2015**, *265*, 1-6.

- (182) Olsson, M. K.; Macak, K.; Graf, W. *Surface & Coatings Technology*. **2000**, *124* (1), 85-85.
- (183) Sittinger, V.; Szyszka, B.; Hong, R. J.; Werner, W.; Ruske, M.; Lopp, A., *New cost effective ZnO: Al films deposited by large area reactive magnetron sputtering*. **2003**; p 503-506.
- (184) Chen, L.; Alarcón-Lladó, E.; Hettick, M.; Sharp, I. D.; Lin, Y.; Javey, A.; Ager, J. W. *The Journal of Physical Chemistry C*. **2013**, *117* (42), 21635-21642.
- (185) Thalluri, S. M.; Rojas, R. M.; Rivera, O. D.; Hernández, S.; Russo, N.; Rodil, S. E. *Physical Chemistry Chemical Physics*. **2015**, *17* (27), 17821-17827.
- (186) Gong, H.; Freudenberg, N.; Nie, M.; van de Krol, R.; Ellmer, K. *AIP Advances*. **2016**, *6* (4), 045108.
- (187) Mahan, J. E.; Vantomme, A. *Phys. Rev. B*. **2000**, *61* (12), 8516-8525.
- (188) Depla, D.; Strijckmans, K.; De Gryse, R. *Surf. Coat. Technol.* **2014**, *258*, 1011-1015.
- (189) Gurvitch, M. *Journal of Vacuum Science & Technology A*. **1984**, *2* (4), 1550-1551.
- (190) Jeynes, C.; Peng, N.; Barradas, N.; Gwilliam, R. *Nuclear Instruments and Methods in Physics Research Section B: Beam Interactions with Materials and Atoms*. **2006**, *249* (1), 482-485.
- (191) Mighell, A. D. *Journal of research of the National Institute of Standards and Technology*. **2002**, *107* (4), 373.
- (192) Munprom, R.; Salvador, P. A.; Rohrer, G. S. *J. Mater. Chem. A*. **2015**, *3* (5), 2370-2377.
- (193) Sleight, A.; Chen, H.-Y.; Ferretti, A.; Cox, D. *Mater. Res. Bull.* **1979**, *14* (12), 1571-1581.
- (194) Liu, G.; Jimmy, C. Y.; Lu, G. Q. M.; Cheng, H.-M. *Chem. Commun.* **2011**, *47* (24), 6763-6783.
- (195) Liu, T.; Zhou, X.; Dupuis, M.; Li, C. *Phys. Chem. Chem. Phys.* **2015**, *17* (36), 23503-23510.
- (196) Pan, J.; Liu, G.; Lu, G. Q. M.; Cheng, H. M. *Angew. Chem. Int. Ed.* **2011**, *50* (9), 2133-2137.
- (197) Wang, D.; Jiang, H.; Zong, X.; Xu, Q.; Ma, Y.; Li, G.; Li, C. *Chemistry—A European Journal*. **2011**, *17* (4), 1275-1282.
- (198) Yang, H. G.; Sun, C. H.; Qiao, S. Z.; Zou, J.; Liu, G.; Smith, S. C.; Cheng, H. M.; Lu, G. Q. *Nature*. **2008**, *453* (7195), 638-641.
- (199) Kashida, S.; Hori, T.; Nakamura, K. *J. Phys. Soc. Jpn.* **1994**, *63* (12), 4422-4426.
- (200) Touboul, M.; Lokaj, J.; Tessier, L.; Kettman, V.; Vrabel, V. *Acta Crystallographica Section C-Crystal Structure Communications*. **1992**, *48*, 1176-1179.
- (201) Li, R.; Zhang, F.; Wang, D.; Yang, J.; Li, M.; Zhu, J.; Zhou, X.; Han, H.; Li, C. *Nat. Commun.* **2013**, *4*, 1432.
- (202) Xi, G.; Ye, J. *Chem. Commun.* **2010**, *46* (11), 1893-1895.
- (203) Mathian, G.; Amzil, H.; Zehaf, M.; Crest, J.; Psaila, E.; Martinuzzi, S.; Oualid, J. *Solid-State Electron.* **1983**, *26* (2), 131-141.
- (204) Yoneda, H.; Ueda, K.-i.; Aikawa, Y.; Baba, K.; Shohata, N. *J. Appl. Phys.* **1998**, *83* (3), 1730-1733.
- (205) Ghosh, A. K.; Fishman, C.; Feng, T. *J. Appl. Phys.* **1980**, *51* (1), 446-454.
- (206) Guo, X.; Zhang, Z. *Acta Mater.* **2003**, *51* (9), 2539-2547.
- (207) Dall'Antonia, L. H.; de Tacconi, N. R.; Chanmanee, W.; Timmaji, H.; Myung, N.; Rajeshwar, K. *Electrochem. Solid State Lett.* **2010**, *13* (5), D29-D32.

- (208) Yu, J. Q.; Kudo, A. *Adv. Funct. Mater.* **2006**, *16* (16), 2163-2169.
- (209) Barreca, D.; Depero, L.; Noto, V. D.; Rizzi, G.; Sangaletti, L.; Tondello, E. *Chem. Mater.* **1999**, *11* (2), 255-261.
- (210) Sangaletti, L.; Depero, L.; Allieri, B.; Groppelli, S.; Sberveglieri, G. In *Effects of oxygen stoichiometry on the structural properties of W-Ti-O thin films*, Mater. Sci. Forum, Trans Tech Publ: 1998; pp 472-477.
- (211) Helander, M. G.; Greiner, M.; Wang, Z.; Tang, W.; Lu, Z. *Journal of Vacuum Science & Technology A: Vacuum, Surfaces, and Films.* **2011**, *29* (1), 011019.
- (212) Kumar, B.; Llorente, M.; Froehlich, J.; Dang, T.; Sathrum, A.; Kubiak, C. P. *Annu. Rev. Phys. Chem.* **2012**, *63*, 541-569.
- (213) Liu, C.; Colón, B. C.; Ziesack, M.; Silver, P. A.; Nocera, D. G. *Science.* **2016**, *352* (6290), 1210-1213.